Stony Brook University

Electrocatalysts for Ethanol Oxidation in Direct Ethanol Fuel Cell (DEFC)

A Dissertation Presented

by

Meng Li

to

The Graduate School

in Partial fulfillment of the

Requirements

for the Degree of

Doctor of Philosophy

in

Materials Science and Engineering

Stony Brook University

August 2011

Stony Brook University

THE GRADUATE SCHOOL

Meng Li

We, the dissertation committee for the above candidate for the
Doctor of Philosophy degree,
hereby recommend acceptance of this dissertation.

Dr. Radoslav Adzic, Advisor
Chemistry Department, Brookhaven National Laboratory

Dr. Jonathan Sokolov, Chair
Materials Science and Engineering Department

Dr. Gary Halada, Member
Materials Science and Engineering Department

Dr. Nebojsa Marinkovic, Outside Member
Department of Chemical Engineering, University of Delaware

This dissertation is accepted by the Graduate School

Lawrence Martin

Dean of the Graduate School

Abstract of the Dissertation

Electrocatalysts for Ethanol Oxidation in Direct Ethanol Fuel Cell (DEFC)

by

Meng Li

Doctor in Philosophy

in

Materials Science and Engineering

Stony Brook University

2011

Ethanol, with its high energy density, likely production from renewable sources, ease of storage and distribution, is almost the ideal combustible for fuel cells wherein its chemical energy can be converted directly into electrical energy. However, commercialization of direct ethanol fuel cells (DEFC) has been impeded by ethanol's slow, inefficient oxidation even at the best electrocatalysts.

We synthesized a ternary Pt-Rh-SnO_2 electrocatalyst that is capable of splitting C-C bond and oxidizing ethanol to CO_2 with high efficiency. A model catalyst, $RhSnO_2$/Pt(111), was first prepared by depositing Rh and SnO_2 nanoclusters on Pt(111) single crystal surface; and then carbon-supported $PtRhSnO_2$ nanoparticle catalysts were synthesized by a seeded growth approach. Both showed unprecedented activity for ethanol oxidation reaction (EOR) with the onset of reaction occurring at low overpotentials. *In situ* infrared reflection-absorption spectra (IRRAS) obtained during EOR with both $RhSnO_2$/Pt(111) and $PtRhSnO_2$/C indicate CO_2 is the major product and it also demonstrate that we successfully split C-C bond at room temperature.

A density functional theory (DFT) investigation of ethanol decomposition was carried out over a model RhPt/SnO_2(110) catalyst, and results suggest the optimal pathway leading to C-C bond breaking is: CH_3CH_2OH→ *CH_3CH_2O+H* → *CH_2CH_2O+2H* → *CH_2+*CH_2O+2H*. *In situ* X-ray absorption spectroscopy (XAS) study was conducted and the results indicate that the PtRh surface is only slightly oxidized. EXAFS fitting results revealed structure information like the particle size and bond distance. These results were corroborated by those obtained using XRD, HADDF-STEM, EDS, and ICP-OES. PtRhSnO_2/C electrocatalysts with a moderate Rh content, i.e. Pt/Rh = 2/1 and 3/1, showed highest EOR activity and selectivity towards C-C bond splitting.

Pt-Ir-SnO_2/C electrocatalyst with atomic ratio Pt:Ir:Sn of 1:1:1 demonstrated a moderately enhanced capability in C-C bond cleavage. Ir-based electrocatalysts (Ir, Ir-Sn, Ir-Ru) were prepared using a simple thermal decomposition method and Ir-Sn/C exhibited high EOR activity at low overpotentials. Pt monolayer deposited on Au(111) substrate and carbon-supported Au@Pt core-shell nanoparticle electrocatalyst both demonstrated enhanced activity in the electro-oxidation of methanol and ethanol.

In summary, our findings potentially resolve the major impediment hindering the development of practical DEFCs and open new possibilities for studies of C-C bond splitting in variety of important reactions.

To My Parents

Table of Contents

List of Figures

List of Tables

List of Symbols

AC	Aberration-corrected
AEM	Anion exchange membrane
Au@Pt	Au-Pt core-shell
BF	Bright field
CA	Chronoamperometry
CCM	Catalyst-coated-membrane
CHP	Combined heat and power
CV	Cyclic voltammetry
DEFC	Direct ethanol fuel cell
DF	Dark field
DFAFC	Direct formic acid fuel cell
DFT	Density functional theory
DMFC	Direct methanol fuel cell
EDS	Energy disperse X-ray spectroscopy
ECSA	Electrochemical active surface area
EELS	Electron energy loss spectroscopy
EOR	Ethanol oxidation reaction
EtOH	Ethanol
EXAFS	Extended X-ray absorption fine structure
fcc	Face centered cubic
FT	Fourier transform
FTIR	Fourier transform infrared spectroscopy

GC	Glassy carbon
HADDF	High-angle annular dark-field
HOR	Hydrogen oxidation reaction
ICP-OES	Inductively coupled plasma-optical emission spectroscopy
IR	Infrared
IRRAS	Infrared reflection-absorption spectroscopy
KMC	Kinetic Monte Carlo
ML	Monolayer
MOR	Methanol oxidation reaction
MtOH	Methanol
M/C	Carbon supported metal nanoparticles
NP	Nanoparticle
OCP	Open circuit potential
ORR	Oxygen reduction reaction
PDOS	Partial density of states
PEM	Proton exchange membrane
PESK	Quaternized poly(phthalazinone ether sulfone ketone)
PTFE	Polytetrafluoroethylene
PZC	Potential at the point of zero charge
QPES-C	Quaternized polyether sulfone cardo
STM	Scanning tunneling microscopy
STEM	Scanning transmission electron microscopy
TEM	Transmission electron microscopy

UPD	Underpotential deposition
VW	Volmer-Weber
XANES	X-ray absorption near edge spectroscopy
XAS	X-ray absorption spectroscopy
XRD	X-ray diffraction
α	Absorption coefficient
E	Potential
F	Faraday constant (96487 C mol^{-1})
G	Gibbs free energy
j	Current density
R	Reflectivity
T	Temperature

Acknowledgements

I would like to thank my advisor Dr. Radoslav Adzic and for his guidance and support throughout my Ph.D. program.

I would also like to thank Dr. Jonathan Sokolov, Dr. Gary Halada, and Dr. Nebojsa Marinkovic for their serving on committee.

My colleagues and friends Dr. Andrzej Kowal, Dr. Kotaro Sasaki, Dr. Wei-Ping Zhou, Dr. Miomir Vukmirovic, Dr. Yun Cai, Dr. Ping Liu, Dr. Qi Wang, Dr. YongMan Choi, Dr. Wei-Fu Chen, and Kurian Kuttiyiel offered invaluable assistance during my research at BNL, which I appreciate a lot.

I would express special thanks to my boyfriend Shubo Zhang, and my parents in China, for their constant support, encouragement, and understanding.

I would also like to thank Department of Materials Science and Engineering, Stony Brook University for the full scholarship. I appreciate the research sponsorship from US Department of Energy: Basic Energy Science and Energy Efficiency and Renewable Energy.

Chapter 1: INTRODUCTION

Fuel cells are among those oldest energy conversion systems known to men and in the middle of the 19th century, Sir William Grove has discovered the basic principle of fuel cells [1]. In a fuel cell, electricity is generated from the reactions of a fuel (hydrogen, natural gas, methanol, ethanol, hydrocarbons, etc.) and an oxidant (oxygen) on two electrodes in an electrochemical cell and in this way the chemical energy of the fuel and oxidant is directly converted to electric energy. Nowadays finite resources of fossil fuels and environmental concerns, like global warming, have stimulated broad interests in developing alternative power sources. Compared to conventional thermal engines, fuel cells possess superior characteristics such as high efficiency, no environmental pollution, and continuous, quiet operation as long as reactants are supplied. Therefore, fuel cells have been widely accepted to be very promising power sources for both portable and residential applications.

Hydrogen is the most convenient fuel for fuel cell applications, because of its fast oxidation kinetics and the high efficiency of a hydrogen/oxygen fuel cell; however, hydrogen is not a primary fuel, meaning it has to be produced from other sources, such as, natural gas reforming, oil or coal gasification, and water electrolysis. The clean and efficient production of hydrogen and the difficulties with its storage and large-scale distribution have greatly hindered the wider application and commercialization of hydrogen-fed fuel cells [2-3]. Therefore, alcohols (e.g. methanol, ethanol, etc.) are considered as potential alternatives to hydrogen, because they are liquid under ambient temperature and pressure, which greatly simplifies their storage and distribution. Moreover, alcohols have a high energy density (6-9kWhkg^{-1}) and they can be

obtained from renewable sources (e.g. bioethanol from biomass) [4]. Compared to methanol, ethanol possesses advantages such as low toxicity, easy logistics, likely production in large quantities from renewable sources, and higher energy density (8.0 and 6.1kWhkg^{-1}, for ethanol and methanol, respectively). Therefore, the direct ethanol fuel cell (DEFC) could afford an excellent alternative solution to energy-generation problems, and entail major improvements in the prospects for a renewable energy economy. [5-7]

1.1 Fuel Cell Basics

1.1.1 Working Principles of a Fuel Cell

The basic structure and working principle are similar for all fuel cells [8]. Two electrodes, anode and cathode, are separated by electrolyte and connected through an external circuit. At the anode, the fuel ((hydrogen, natural gas, methanol, ethanol, etc.) is oxidized with the help of the electrocatalyst, producing electrons (e^-) and protons (H^+). Electrons transfer to the cathode through the external circuit, resulting in an electrical current, and protons diffuse to the cathode through the electrolyte. At the cathode, the oxidant (air or pure oxygen) is reduced by these electrons to form anions, which meet protons to form water. Figure 1.1 shows a schematic diagram of a typical H_2/O_2 fuel cell.

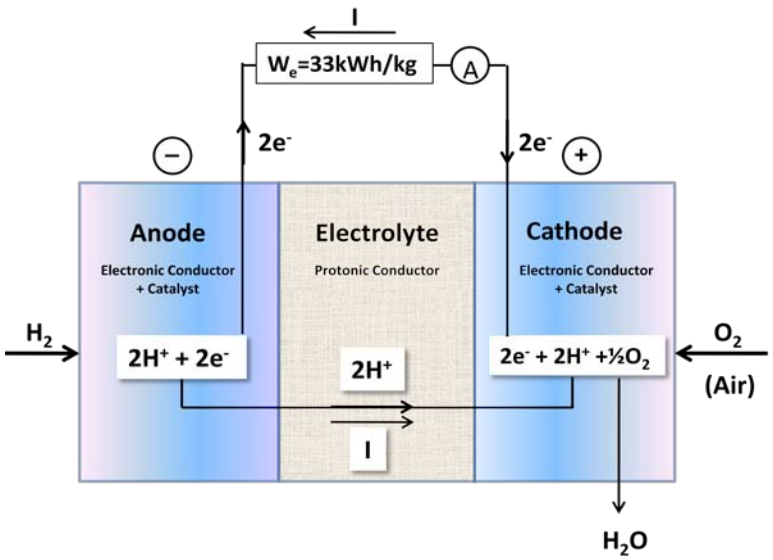

Figure 1.1 Schematic diagram of a typical H_2/O_2 fuel cell.

1.1.2 Thermodynamics of Fuel Cells

In a fuel cell the Gibbs free energy (ΔG) of an electrochemical reaction is converted into electrical energy in the form of an electrical current. Thus, the maximum electrical work (W_e) obtained in a fuel cell is equal to the change of the Gibbs free energy (ΔG) of the electrochemical reaction [9]:

$$W_e = \Delta G = -n_e FE \tag{1.1}$$

where n_e is the number of electrons involved in the reaction, F is the Faraday constant and F = 96485C/mol, and E is the potential difference between two electrodes, which is also the ideal potential of the electrochemical cell versus the standard hydrogen electrode (SHE).

For a cell operating at standard pressure (1atm) and at temperature T:

$$\Delta G_0 = -n_e FE_0 \tag{1.2}$$

Where ΔG_0 is the standard Gibbs free energy and E_0 is the standard potential.

For a general cell reaction:

$$\alpha A + \beta B = \gamma C + \delta D \tag{1.3}$$

The Gibbs free energy change of this cell reaction can be expressed as:

$$\Delta G = \Delta G_0 + RT \ln \frac{[C]^{\gamma}[D]^{\chi}}{[A]^{\alpha}[B]^{\beta}} \tag{1.4}$$

Where ΔG_0 is the standard Gibbs free energy; [A], [B], [C] and [D] are the concentration of species A, B, C and D, respectively. Substituting equation (1.4) to (1.1) gives Nernst's equation:

$$E = E_0 + \frac{RT}{nF} \ln \frac{[C]^{\gamma}[D]^{\chi}}{[A]^{\alpha}[B]^{\beta}} \tag{1.5}$$

In the case of a H_2/O_2 PEM fuel cell, the overall reaction:

$$2H_2 + O_2 \rightarrow 2H_2O \tag{1.6}$$

Based on the Nernst equation, the ideal performance of this cell can be calculated as:

$$E = E_0 - \frac{RT}{4F} \ln \frac{P_{H_2O}{}^2}{P_{H_2}{}^2 P_{O_2}} \tag{1.7}$$

Thus, the ideal potential of this H_2/O_2 fuel cell is 1.23V with liquid water product, or 1.18V with gaseous water product.

1.1.3 Actual Performance of Fuel Cells

Figure 1.2 shows a characteristic PEMFC cell voltage – current density curve, and there are four zones associated with the following energy losses [10]:

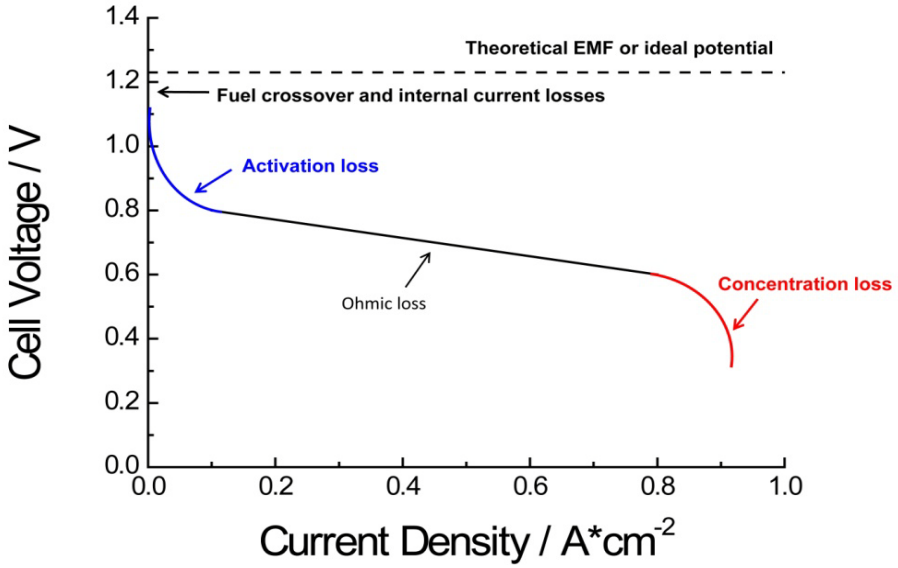

Figure 1.2 A typical PEM fuel cell current-voltage characteristic curve.

(1) Under working conditions, even the open circuit potential (OCP) is lower than the Nernstian value, and it is caused by fuel crossover and internal current losses. A small part of the fuel can permeate through the polymer membrane and reach the cathode, lowering cathode potential and also the cell's efficiency. Liquid fuels usually diffuse through membranes easily than hydrogen fuel. On the other hand, a small amount of electrons can also migrate through the membrane to the cathode, generating internal current. The fuel crossover and internal current do not have a significant effect the cell's operating efficiency, but they do cause a considerable drop in OCP.

(2) Activation loss is the rapid initial voltage drop, caused by the sluggish reaction kinetics on both electrodes. In a proton exchange membrane fuel cell (PEMFC), activation loss accounts for the major energy loss, thus, better electrocatalysts need to be developed to improve reaction kinetics particulary for the cathode and to decrease the activation loss.

(3) Ohmic loss corresponds to the linear voltage drop, due to the resistance to the ion flow in

the electrolyte and also the resistance to the electron flow through the electrode. A thinner electrolyte with higher ion conductivity can reduce the ohmic polarization. Less separation of electrode electrocatalysts and better contact between the backing layer and the bipolar plates can also help reduce the ohmic loss.

(4) Concentration loss is the rapid voltage drop in high current density region, and it is caused by the decrease of the reactants' concentration on electrocatalysts surface at high overpontentials.

1.1.4 Classification of Fuel Cells

Fuel cells are usually divided into five types based on the electrolyte employed, and a second grouping can be done according to the operating temperatures: low-temperature and high-temperature fuel cells. Table 1.1 [11-12] shows the basic information of all these systems. Low-temperature fuel cells include the proton exchange membrane fuel cell (PEMFC), the alkaline fuel cell (AFC), and the phosphoric acid fuel cell (PAFC). High-temperature fuel cells include the molten carbonate fuel cell (MCFC) and the solid oxide fuel cell (SOFC).

The proton exchange membrane fuel cells (PEMFC), also called solid polymer electrolyte fuel cell (SPEFC), use a proton exchange polymer membrane as electrolyte and they operate at relatively low temperature (~80ºC). Thus, high activity electrocatalysts are the only way to solve the problem of slow reaction rates and till now Pt and its alloy are still the best electrocatalysts. Besides hydrogen, liquid fuels (methanol, ethanol, formic acid, etc.) can also be directly used in PEMFCs, and the ethanol-fed PEMFC is also called direct ethanol fuel cell (DEFC). PEMFCs are very attractive for automobile and other mobile applications, because of its simple structure, compactness and low temperature operation.

The alkaline fuel cells (AFC) use alkaline solution (usually KOH) as the electrolyte and they operate at a temperature range from 100 ~ 250ºC. One advantage of AFCs is that a wide range of non-precious electrocatalysts (e.g. Ni, Ag, metal oxide, spinels, etc.) can be used at both electrodes instead of the expensive Pt-based electrocatalysts. CO_2 is a poison in AFCs because it reacts with KOH electrolyte and forms K_2CO_3. AFCs have been used in space mission by NASA since the mid-1960s.

The phosphoric acid fuel cells (PAFC) use concentrated H_3PO_4 (up to 100%) contained in a Teflon-bonded silicon carbide matrix as the electrolyte, and operate at a temperature range of 150~200ºC. Pt-based electrocatalysts are used in both electrodes. Water management is not so difficult in PAFCs because concentrated acid minimizes the water vapor pressure. Another main advantage of PAFCs is the high CO tolerance (up to 1.5%). PAFCs are the first commercial fuel cells and they are typically used for stationary power generation and backup power sources, with a combined heat and power efficiency of about 80%.

The molten carbonate fuel cells (MCFC) use a molten mixture of alkali metal carbonates suspended in a chemically inert $LiAlO_2$ matrix as the electrolyte, and operate at high temperatures around 650ºC. Non-precious metals can serve as electrocatalysts because of the high operation temperature and the overall cell efficiency can reach up to 85%. The main problem of MCFCs is under such high temperature there are severe cell components corrosion and even breakdown.

The solid oxide fuel cells (SOFC) use an oxide ion-conducting ceramic material as the electrolyte, and operate at around 1000ºC. Similar to the MCFC, because of high operation temperature non-noble metals can work as electrocatalysts but the durability is not satisfactory. Typically, the anode is Ni-ZrO_2 cermet, and the cathode is Sr-doped $LaMnO_3$. Overall fuel use

efficiencies could reach 80 – 85%.

Table 1.1: Comparison of different Fuel Cells [11-12]

	AFC	PEMFC	PAFC	MCFC	SOFC
Operation Temperature	<100 ºC	60~120 ºC	160~220 ºC	600~800 ºC	800~1000 ºC
Anode Reaction	$H_2 + 2OH^- \rightarrow 2H_2O + 2e^-$	$H_2 \rightarrow 2H^+ + 2e^-$	$H_2 \rightarrow 2H^+ + 2e^-$	$H_2 + CO_3^{2-} \rightarrow H_2O + CO_2 + 2e^-$	$H_2 + O^{2-} \rightarrow H_2O + 2e^-$
Cathode Reaction	$\frac{1}{2}O_2 + H_2O + 2e^- \rightarrow 2OH^-$	$\frac{1}{2}O_2 + 2H^+ + 2e^- \rightarrow H_2O$	$\frac{1}{2}O_2 + 2H^+ + 2e^- \rightarrow H_2O$	$\frac{1}{2}O_2 + CO_2 + 2e^- \rightarrow CO_3^{2-}$	$\frac{1}{2}O_2 + 2e^- \rightarrow O^{2-}$
Applications	Transportation Space Military Energy storage systems		Combined heat and power for decentralized stationary power systems	Combined heat and power for stationary decentralized systems and for transportation (trains, boats,…)	
Released Power	Small plants 5 – 150kW modular	Small plants 5 – 250kW modular	Small – medium sized plants 50kW – 11MW	Small power plants 100kW – 2MW	Small power plants 100 – 250kW
Charge Carrier in the Electrolyte	OH^-	H^+	H^+	CO_3^{2-}	O^{2-}

1.2 Direct Ethanol Fuel Cell (DEFC)

1.2.1 Proton Exchange Membrane Fuel Cell (PEMFC)

PEMFCs have been actively studied due to the simple structure, low operating temperature, high power density and quick start-up and their potential applications in vehicles, portable electronics and combined heat and power (CHP) systems. The development of highly active and

low Pt content electrocatalysts is crucial in PEMFCs. [13]

A PEMFC stack consists of a number of elementary cells, which is called the membrane electrode assembly (MEA). As illustrated in Figure 1.3, one MEA consists of a proton exchange membrane sandwiched by the fuel anode and the oxygen cathode. Carbon-supported nanoparticle electrocatalysts are fixed on a porous and conductive material such as carbon fiber paper or carbon cloth, forming the gas diffusion layer or electrode substrate. The gas diffusion layer can provide mechanical support, diffuse the gas, and connect the catalysts layer to the current collector. In manufacturing, the fixed electrodes are then hot pressed on each side of the electrolyte membrane to form the complete MEA. A MEA is usually around a few hundred micrometers thick, and it delivers a cell voltage of 0.5-0.9V, depending on the working current density. Many elementary cells are electrically connected by bipolar plates, and are assembled together in series and in parallel to form a PEMFC stack.

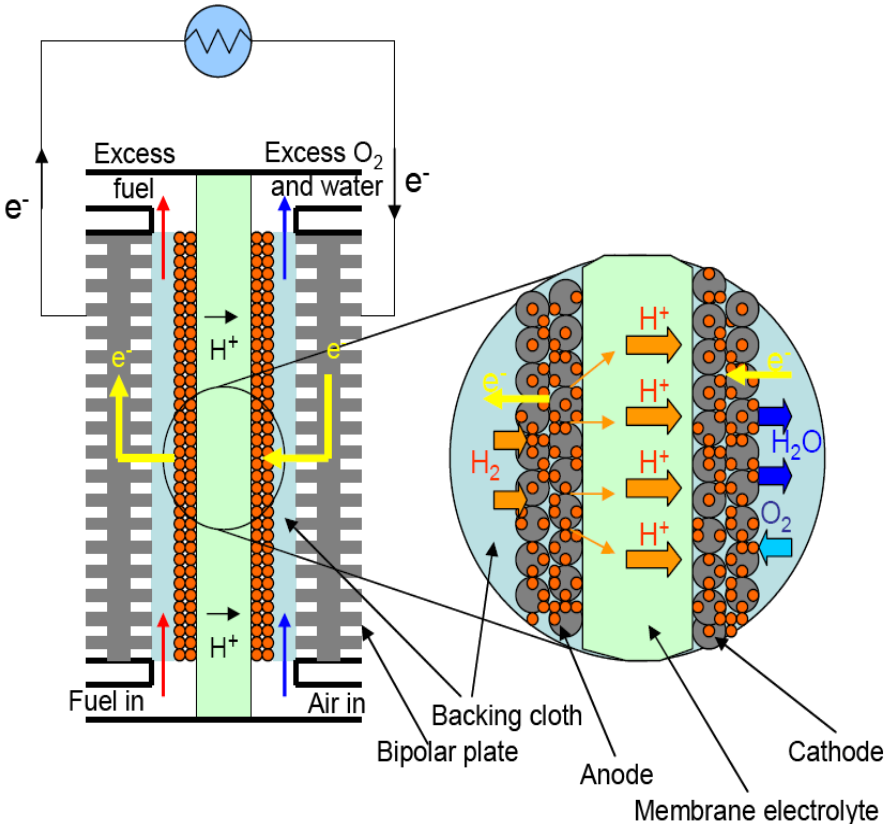

Figure 1.3 Schematic illustration of a typical PEMFC

The proton exchange membrane (PEM) in the MEA allows rapid proton transport and also acts as an electronic insulator and gas barrier between two electrodes. The most studied and operated polymer membrane in PEMFCs is Nafion by DuPont. As shown in Figure 1.4, Nafion consists of a poly-tetrafluoroethylene (PTFE) backbone and side chains ending with sulphonic acid $-SO_3H$. The $-SO_3H$ group is ionically bonded and that means the end is actually $-SO_3^-$, which is highly hydrophilic and absorbs lots of water. In these hydrated regions protons are weakly attached to the $-SO_3^-$ group and they can move, which explains how the Nafion film works as the conductor of proton. In addition, Nafion is mechanically strong and it can be fabricated into very thin films, down to 50μm.

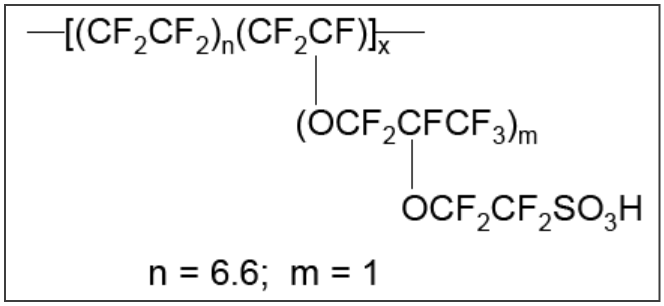

Figure 1.4 The Nafion Membrane by DuPont

Electocatalysis is one of the main problems need to be solved before the commercialization of PEMFCs. [14-17] Current electrocatalysts are still suffering from low activity, insufficient stability and high cost. At the low operating temperature (20-80°C) of common PEMFCs, kinetics of the involved electrochemical reactions, such as oxygen reduction reaction (ORR) at the cathode and fuel oxidation at the anode, is still slow. Increasing the working temperature from 80 to 150°C could strongly increase the reaction rates by a factor of 100 to 1000 due to thermal activation. But the hash working environment under high temperature could harm all cell components and cause their degradation. Currently the best electrocatalysts for both the anode and cathode reactions are still Pt and its alloys. Pt-based nanoparticles (2~10nm) are dispersed on conductive support such as Vulcan XC72 carbon to improve catalyst utilization. Figure 1.5 shows typical TEM images of a state-of-art carbon-supported Pt nanoparticle electrocatalysts (46.4 wt.%) from Tanaka Kikinzoku (TKK) international inc. Currently carbon-supported nanoparticle electrocatalysts show insufficient stability due to particle agglomeration and carbon support corrosion. The investigation of new electrocatalysts, with lower Pt content, that are more active and stable for oxygen reduction and fuel oxidation is thus an important point for the development of practicle PEMFCs.

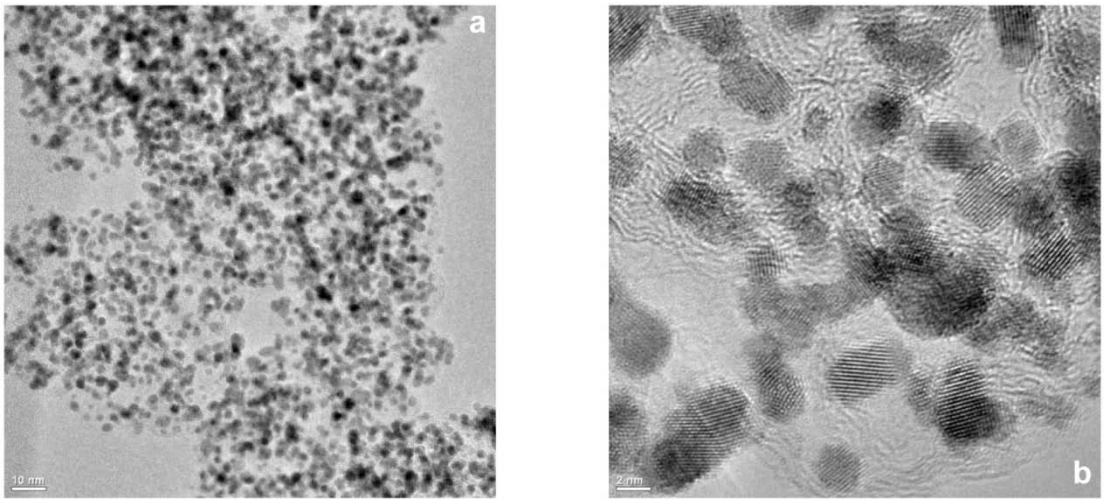

Figure 1.5 Typical TEM images of a carbon-supported Pt nanoparticle electrocatalyst (46.4 wt.%) from TKK Inc.

The bipolar plates are usually made from graphite or corrosion-resistant metal plates, they separate electrodes of neighboring MEAs (one anode of a cell and one cathode of the other), and play the following roles: i) to provide electrical conductivity; ii) to allow the distributions of reactants (hydrogen and oxygen gases, and/or liquids fuels) to the electrocatalysts sites and the evacuation the reaction products (H_2O and CO_2 in the case of alcohol fuels) through the distribution channels; iii) to evacuate excess heat for thermal management purpose.

PEMFCs are usually operated under temperatures lower than 100ºC and at atmospheric pressure, which means water is produced as a liquid here. Therefore, water management [18-19] is crucial here and the cell must operate under perfect conditions – neither flooded, nor dry. The ionic conductivity of the electrolyte is only high when the membrane is sufficiently hydrated. Maintaining high water content is also important while operating at high current densities (approximately $1Acm^{-2}$). However, too much water can adversely impact the mass transport of reactants to the catalytic sites due to the flooding in the electrocatalyst layers.

Hydrogen is the most studied fuel in PEMFCs because the kinetics of hydrogen oxidation

reaction (HOR) is very fast and it requires negligible overpotentials. Even though hydrogen is ideal fuel for PEMFCs, there are considerable problems needed to be solved in the production, purgation, transportation, distribution and storage of gaseous hydrogen. [2-3] Thus, liquid fuels such as formic acid, methanol, ethanol and dimethyl ether are considered as promising candidates to replace hydrogen as the fuel for PEMFCs.

1.2.2 Direct Ethanol Fuel Cell (DEFC)

The direct alcohol fuel cell (DAFC) is a subcategory of PEMFCs, where hydrogen fuel is replaced by an alcohol (methanol, ethanol, etc.). The direct methanol fuel cell (DMFC) gained most attention at first because methanol is the simplest alcohol (with only one carbon atom) and its electrocatalysis is also the simplest. But it cannot be ignored that methanol is a toxic compound and a pollutant. Thus, ethanol becomes a very promising substitute because it is less toxic. Similar to methanol, ethanol is liquid, which simplifies its storage and distribution; and it also, possesses a high theoretical mass energy density (6.1 and 8.0 kWh/kg for methanol and ethanol, respectively). Moreover, ethanol can be obtained from biomass, which is to say, the employment of bio-generated ethanol as the fuel will not change the natural balance of carbon dioxide (CO_2) in the atmosphere.

The direact ethanol fuel cell (DEFC) transforms chemical energy in ethanol molecules directly into electricity, without a fuel processor to produce hydrogen first from ethanol reforming [16-17]. As shown in Figure 1.6, in a DEFC, the ethanol aqueous solutions are fed to the anode compartment, where ethanol can be oxidized to CO_2 and H_2O releasing simultaneously protons and electrons with the help of the anode electrocatlysts. Protons are then transported to

the cathode through the membrane; while electrons flow through an external circuit to the cathode, forming electrical current. At the cathode the oxidant (air or pure oxygen) reacts with the protons and electrons transported from the anode to produce water. Not like the H_2/O_2 PEMFC, the main activation loss in DEFCs is due to the slow reaction kinetics of ethanol electro-oxidation in the anode.

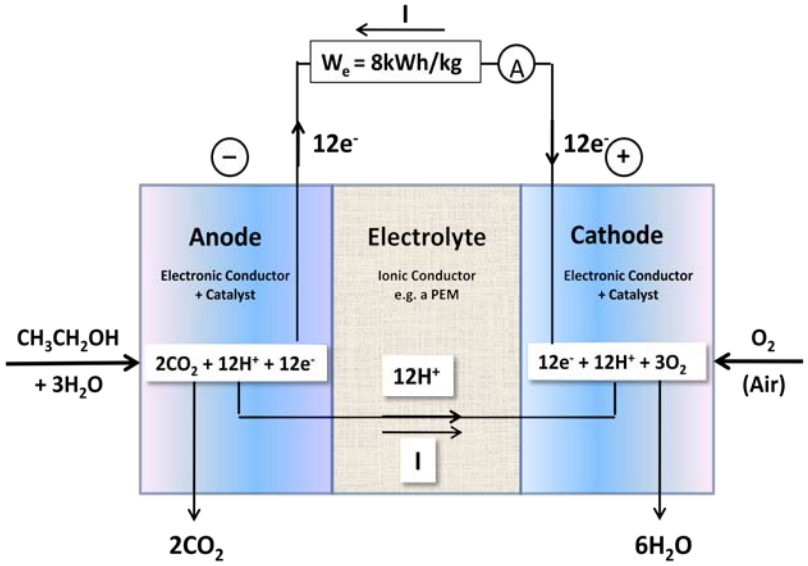

Figure 1.6 Schematic Diagram of a DEFC

Ethanol oxidation reaction (EOR) occurs at the anode of a DEFC, producing CO_2 and H_2O, in the case of ethanol total oxidation:

$$C_2H_5OH + 3H_2O \rightarrow 2CO_2 + 12H^+ + 12e^- \qquad E_0^1 = 0.085V \text{ vs. SHE} \qquad (1.8)$$

Oxygen reduction reaction (ORR) happens at the cathode of a DEFC:

$$3O_2 + 12H^+ + 12e^- \rightarrow 6H_2O \qquad E_0^2 = 1.229V \text{ vs. SHE} \qquad (1.9)$$

where E_i^o are the standard electrode potentials versus standard hydrogen electrode (SHE), thus the standard cell voltage is:

$$E_0 = E_0^2 - E_0^1 = 1.229 - 0.085 = 1.144V \qquad (1.10)$$

These give the following overall reaction:

$$C_2H_5OH + 3O_2 \rightarrow 2CO_2 + 3H_2O \tag{1.11}$$

The theoretical energy efficiency of a DEFC, under reversible standard conditions, is defined as the ratio between the maximum electrical energy produced ($W_e = \Delta G_0 = -n_e F E_0$) and the heat of combustion ($\Delta H_0 = -1366 kJ / mol$): [5]

$$\varepsilon_{cell}^{rev} = \frac{W_e}{-\Delta H_0} = \frac{n_e F E_0}{-\Delta H_0} = \frac{12 \times 96485 \times 1.144}{-(-1366 \times 10^3)} = 0.97 \tag{1.12}$$

where $n_e = 12$, the number of exchanged electrons per one ethanol molecule in the case of ethanol total oxidation to CO_2.

However, practical energy efficiency of a DEFC is much lower than the theoretical energy efficiency. Under working conditions, with a current density j, the cell voltage E(j) is lower than E^0, because of the overvoltage required for both electrode reactions and also the ohmic drop. In addition, most ethanol molecules cannot be completely oxidized to CO_2, with the exchange of 12 electrons per molecule; in contrast, the dominant EOR products are acetic acid ($n_e = 4$) and acetaldehyde ($n_e = 2$) [20]. Moreover, part of ethanol could crossover [10, 21] through the polymer membrane and reaches cathode compartment, which results in a lowered cathode potential because both ORR and EOR are taking place at the same electrode. Ethanol crossover causes a reduction in the cell voltage and a further decrease in the voltage efficiency. Song et al. [21] found that the ethanol permeated to the cathode exhibited a less serious effect on the cell performance than that of methanol fuel cell because of both its smaller permeability through polymer membrane and its slower electrochemical oxidation kinetics over platinum cathode.

Carbon supported platinum nanopartices electrocatalyst is the most commonly used anode

electrocatalyst in low temperature fuel cells; however, pure platinum is not the ideal anodic catalyst for DEFCs because it will be rapidly poisoned by the strongly adsorbed species coming from the dissociative adsorption of ethanol. Current studies mainly focus on developing multifunctional electrocatalysts to mitigate the poisoning of platinum through the addition of co-catalysts, particularly ruthenium and tin, to platinum. Regarding the catalysts stability issue in DEFCs, Song et al. [22] suggested that the decay of the DEFC's performance during life time test could be mainly attributed to the following reasons: (i) the delamination of the catalyst layer from the electrolyte membrane due to the different swelling degree between the catalyst layer and the electrolyte with ethanol aqueous solution, (ii) the agglomeration of electrocatalysts, (iii) the destruction of the anode catalyst, and (iv) ethanol crossover from the anode to the cathode through the electrolyte.

There are two ways for the MEA fabrication in DEFCs [23-24]. The first method is to fix electrocatalysts onto the membrane to form catalyst-coated-membrane (CCM) first and then produce MEA by hot-pressing the CCM with diffusion layers. Another one is the separate electrode method, in which the catalysts ink with Nafion is firstly being spread onto the diffusion layer to form electrode and then fixed to one side of the membrane by hot-pressing process.

1.2.3 Solid Alkaline Membrane Fuel Cell (SAMFC)

The reaction rate of both EOR and ORR is higher in alkaline than in acidic media, so that to develop an ethanol-fed solid alkaline membrane fuel cell (SAMFC), with an anion exchange membrane (AEM) instead of a PEM, can bring new opportunities in DEFCs [25-26]. The development of inexpensive electrocatalysts with good activity and stability, and an AEM with sufficient anion conductivity and stability are critical in ethanol-fed SAMFCs.

The most studied anode electrocatalysts for ethanol-fed fuel cells, in both acidic and alkaline media, are based on Pt-Sn and Pt-Ru, and their better performance compared to pure Pt has been attributed to the bi-functional mechanism and/or the electronic effect [27-28]. In alkaline media, Pd-based electrocatalysts demonstrate slightly better EOR activity compared to Pt-based ones [29]. It has been reported by Shen et al. [30] that Pd/C could be improved by the addition of nanocrystalline oxides such as CeO_2, Co_3O_4, Mn_3O_4, NiO, etc. The authors found such oxide-promoted Pd-based electrocatalysts were superior to Pt-based ones in both EOR activity and poison tolerance, and particularly a Pd-NiO/C catalyst showed a 300mV negative shift of reaction onset potential compared to the Pt/C catalyst. Non-precious electrocatalysts such as nano-strctured Fe-Co-Ni alloy [31-32] have been developed for SAMFC applications, and show reasonably good activity. Ethanol-fed SAMFCs based on Fe-Co-Ni alloy catalysts delivered powder density as high as 30~40mWcm^{-2} at room temperature and up to 60mWcm^{-2} at 80°C. However, the catalysts stability is still unsatisfactory due to the slow formation of an oxide layer on the catalyst surface.

Non-platinum electrocatalysts have been extensively studied for ORR in alkaline medium [33-42]. They are made from other noble metals such as palladium [33] and ruthenium [34]. Non-precious electrocatalysts such as iron-porphyrin or phthalocyanie catalysts [35-36], nickel and cobalt catalysts, nickel-cobalt-spinel catalysts [37-39], and manganese oxide-based electrocatalysts [40-42] have also been developed. The main issue of non-precious electrocatalysts is still the relatively low durability, and the ORR mechanisms on these catalysts still remain unclear.

In SAMFCs, the electrolyte membrane is another key component besides electrocatalysts, and generally AEMs are based on quaternary ammonium groups as anion-exchange groups to transport ionic species (e.g. hydroxyl ion, OH^-, in an AEM) [43]. Chloromethylated aromatic

polymer of the polycondndensation type, for instance, the quaternized poly(phthalazinone ether sulfone ketone) membrane (PESK) by Fang and Shen [44], and quaternized polyether sulfone cardo polymer (QPES-C) by Li et al. [45-46], are generally used to produce strongly alkaline AEMs. Another important class of AEMs is prepared from perfluorinated backbone polymers, such as the commercially available ADP-Morgane membrane by Solvay which consists of a cross-linked fluorinated polymer carring quaternary ammonium as exchange groups. The major issue in AEMs is to improve their durability in strong alkaline environment because the conductive groups could decompose in concentrated alkaline solution following the Hofmann degradation reaction [47] and in SAMFCs the pH may increase up to 14 during fuel cell operation.

1.3 Electrocatalysis of Fuel Cell Reactions

1.3.1 Electrocatalytic Oxidation of Hydrogen

The reaction rate of the hydrogen oxidation reaction (HOR), as measured by the exchange current density i_0 (i.e. the current density at the equilibrium potential) greatly depends on the electrode materials. The reaction mechanisms of hydrogen oxidation reaction (HOR) have been extensively studied [48-49] and there are three elementary reaction steps for the HOR on a Pt electrode in acid solutions [50-52]:

$$2Pt + H_2 \rightarrow 2Pt - H_{ads} \qquad \text{Tafel reaction} \qquad (1.13)$$

$$Pt + H_2 \rightarrow Pt - H_{ads} + H^+ + e^- \qquad \text{Heyrovsky reaction} \qquad (1.14)$$

$$Pt - H_{ads} \rightarrow Pt + H^+ + e^- \qquad \text{Volmer reaction} \qquad (1.15)$$

With an overall HOR reaction:

$$H_2 \rightarrow 2H^+ + 2e^- \quad (1.16)$$

In summary, there are two reaction pathways in HOR, and in the Tafel-Volmer pathway, the dissociative adsorption of a H_2 molecule results in two adsorbed hydrogen atom (H_{ads}), followed by two separate one-electron oxidation of H_{ads}. While in the Heyrovsky-Volmer pathway, dissociation of one H_2 molecule forms one H_{ads} simultaneously with a one-electron oxidation to H^+, followed by another one-electron oxidation of the H_{ads}. Wang et al. [53] developed a dual-pathway kinetic equation to describe the reaction mechanism, and they demonstrated that a fast, inversed exponential increasing of kinetic current at the low overpotential region occurs through the Tafel-Volmer pathway, while a much more gradual current rise in the overpotential region higher than 50 mV involves the Heyrovsky-Volmer pathway.

HOR on a Pt electrode has extremely fast kinetics, however, trace amount of carbon monoxide inevitably exists in H_2 produced from steam reforming of natural gas, and CO can poison Pt anode electrocatalysts, causing a significant decrease in cell's efficiency. Pt-Ru alloy electrocatalysts show improved CO tolerance because Ru can provide RuOH species for the oxidation of CO to CO_2, according to the bi-functional mechanism. A Pt/Ru/C electrocatalyst comprising a sub-monolayer of Pt deposited on carbon-supported Ru nanoparticles was prepared by the electroless (spontaneous) deposition of Pt on Ru, and the novel electrocatalyst greatly reduced the loading of Pt [54].

1.3.2 Electrocatalytic Oxidation of Formic Acid

Direct formic acid fuel cell (DFAFC) is an interesting subject because formic acid has faster oxidation kinetics than methanol and ethanol [55-57]. Pt-based and Pd-based electrocatalysts are the most studied formic acid oxidation catalysts. Pd-based electrocatalysts show a very high

initial activity due to the free of CO formation, but their durability is not satisfactory [58-60]. Pure Pt is easily poisoned by adsorbed CO, a reaction intermediate, and Pt can be modified by sub-monolayer of foreign metal such as Pb, Bi, Sb, etc. [55, 61-64].

There are three possible reaction pathways proposed for formic acid oxidation [55, 65-67]:

(i) $HCOOH^{*} \rightarrow COOH^{*} + H^{+} + e^{-} \rightarrow CO_2 + 2H^{+} + 2e^{-}$ direct pathway (1.17)

where hydrogen atom (dehydrogenation) is removed first from the C-H bond forming hydroxy carbonyl, and then a second H is removed from the O-H bond to produce CO_2;

(ii) $HCOOH^{*} \rightarrow HCOO^{*} + H^{+} + e^{-} \rightarrow CO_2 + 2H^{+} + 2e^{-}$ formate pathway (1.18)

where the dehydrogenation first occurs to O-H bond forming formate, and then to C-H bond to produce CO_2;

(iii) $HCOOH^{*} \rightarrow CO^{*} + H_2O \rightarrow CO_2 + 2H^{+} + 2e^{-}$ indirect pathway (1.19)

where adsorbed CO (CO^{*}) is produced from non-Faradaic dehydration of formic acid, and then oxidized to CO_2.

Both (i) and (ii) are accomplished by dehydrogenation (via different intermediates) to form CO_2 directly without the formation of adsorbed CO, so (i) and (ii) are sometimes referred to "direct pathway" jointly.

1.3.3 Electrocatalytic Oxidation of Methanol

Methanol oxidation reaction (MOR) on a pure Pt electrode forms many adsorbed species and reaction intermediates, among them adsorbed CO can block Pt sites [68-70]. The overvoltage on pure Pt is relatively high (0.3~0.5V), therefore lots of efforts have been made to improve Pt and Pt-Ru electrocatalysts lead to the best performance. The promotional effect of Ru has been ascribed to the bi-functional mechanism, according to which Pt sites serve for the dissociative

chemisorptions of methanol to CO_{ads}, while Ru sites activate and dissociate water molecules, forming adsorbed hydroxyl species (OH). The oxidation of CO_{ads} by the adsorbed OH becomes the rate-determining step. The multi-step reaction can be described as the following: [71]

$$Pt + CH_3OH \rightarrow Pt - CH_3OH_{ads} \quad (1.20)$$

$$Pt - CH_3OH_{ads} \rightarrow Pt - CHO_{ads} + 3H^+ + 3e^- \quad (1.21)$$

$$Pt - CHO_{ads} \rightarrow Pt - CO_{ads} + H^+ + e^- \quad (1.22)$$

$$Ru + H_2O \rightarrow Ru - OH_{ads} + H^+ + e^- \quad (1.23)$$

Therefore, the overall reaction of methanol oxidation to CO_2 is as below:

$$CH_3OH + H_2O \rightarrow CO_2 + 6H^+ + 6e^- \quad (1.24)$$

PtRu alloy electrocatalysts are commercially available and currently used in DMFC. Lamy et al. [71] showed the PtRu alloy catalyst with atomic ratio Pt:Ru between 3:1 to 4:1 gave the best current yield and power densities. Pt_{ML}/Ru/C electrocatalyst was developed by Sasaki et al. [72] showed a fourfold higher Pt mass activity compared to the commercial PtRu/C catalyst. Some Pt-Ru-based trimetallic electrocatalysts, such as Pt-Ru-Mo, has been synthesized and shows enhanced catalytic activity compared to PtRu catalysts.

1.3.4 Electrocatalytic Oxidation of Ethanol

The electro-oxidation of ethanol takes place through complex parallel pathways (Figure 1.7) and is far more complicated than the case of hydrogen. The ethanol electro-oxidation mechanism has studied by means of various techniques, such as differential electrochemical mass spectrometry (DEMS), in situ Fourier transform infrared spectroscopy (FTIRS), electrochemical thermal desorption mass spectroscopy (ECTDMS), surface enhanced infrared absorption

spectroscopy with attenuated total reflection (SEIRAS-ATR), etc. [73-82]. There is a number of adsorbed species resulting from the oxidation of ethanol on a platinum electrode in acid solution and almost all researchers agree that carbon dioxide (CO_2), acetaldehyde (CH_3CHO), and acetic acid (CH_3COOH) are the main products of the oxidation of ethanol in acidic solution. Breaking the C-C bond for a total oxidation to CO_2 is the major problem in ethanol electrocatalysis. The parallel reactions cause a considerable lowering of the fuel efficiently utilization to generate electricity.

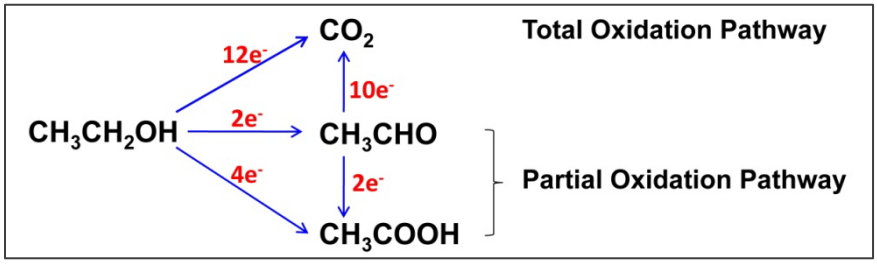

Figure 1.7 Parallel reaction pathways in ethanol electro-oxidation.

Based on the foregoing work, the global oxidation mechanism of ethanol in acid solution can be summarized in the following parallel reactions:

$$C_2H_5OH \rightarrow \left[C_2H_5OH\right]_{ad} \rightarrow C1_{ad}, C2_{ad} \rightarrow CO_2 \qquad \text{(Total oxidation)} \qquad (1.25)$$

$$C_2H_5OH \rightarrow \left[C_2H_5OH\right]_{ad} \rightarrow CH_3CHO \rightarrow CH_3COOH \qquad \text{(Partial oxidation)} \qquad (1.26)$$

The mechanism of ethanol oxidation includes two separate processes, which are adsorption and oxidation. The first step involves dissociative adsorption of ethanol on the electrode's surface and this process does not happen until the surface is free of H atoms (e.g. near 0.2V vs. RHE for a polycrystalline platinum). The next step requires the reaction between the adsorbed intermediates and the oxygen-containing species (OH_{ad}, from the dissociation of water) to

generate CO_2. Unfortunately, OH_{ad} can only form fast at potentials above 0.6V on platinum catalysts, which means that the high overpotential needed for ethanol oxidation. Furthermore, the kinetics of ethanol oxidation is more sluggish than methanol oxidation because the number of electrons exchanged doubles and the activation of the C-C bonds is more difficult than that of the C-H bonds. [83] The formation of CO_2 goes through two adsorbed intermediates $C1_{ad}$ and $C2_{ad}$, which represent fragments with one and two carbon atoms, respectively.

1.3.5 Electrocatalytic Reduction of Oxygen

Oxygen reduction reaction (ORR) is also a multi-electron transfer reaction with several steps and intermediate species [84-89]. ORR mainly occurs via two possible pathways: the "direct" four-electron reduction pathway leading to the formation of water, and the "peroxide" two-electron pathway, giving hydrogen peroxide. ORR on Pt-family metals occurs by the parallel mechanism with predominantly the four-electron reduction, which can be written as follows:

$$Pt + O_2 \rightarrow Pt - O_{2ads} \tag{1.27}$$

$$Pt - O_{2ads} + H^+ + e^- \rightarrow Pt - O_2 + Pt - OH_{ads} \tag{1.28}$$

$$Pt - O_{ads} + H^+ + e^- \rightarrow Pt - OH_{ads} \tag{1.29}$$

$$2Pt - OH_{ads} + 2H^+ + 2e^- \rightarrow 2Pt + 2H_2O \tag{1.30}$$

The overall reaction for ORR is:

$$O_2 + 4H^+ + 4e^- \rightarrow 2H_2O \tag{1.31}$$

On pure Pt, ORR requires a relatively high overvoltage, ca. 0.3V, and it accounts for the main activation loss in a H_2/O_2 fuel cell. Therefore, Pt is alloyed with a transition metal (Co, Ni, Fe, Cu, ect.) to gain improved activity. Pt monolayer electrocatalysts are a new class of catalysts

developed by Adzic et al., and their Pt mass-specific activity was up to twenty times higher than the state-of-the-art commercial Pt/C catalysts [90-92].

1.4 Brief Review of Electrocatalysts in DEFCs

1.4.1 Anode Electrocatalysts for Ethanol Electro-oxidation

At low temperature fuel cells, carbon supported platinum or platinum alloys are used as anode catalysts because of its specific electronic properties that facilitate many reactions. Since catalysis is a surface effect, the catalyst needs to have the highest possible surface area. Hence, platinum nanoparticles are dispersed on a conductive support as carbon (e.g. Vulcan XC72). Pure platinum, however, is not the most efficient anodic catalyst for the direct ethanol fuel cell. Indeed, the electro-oxidation of a partially oxygenated organic molecule, such as ethanol, can only be performed with a multifunctional electrocatalyst. Platinum itself is known to be rapidly poisoned on its surface by strongly adsorbed species coming from the dissociative adsorption of ethanol. Moreover, pure Pt catalysts show very low selectivity to ethanol total oxidation to CO_2, with dominant EOR products of acetic acid and acetaldehyde.

1.4.1.1 PtRu-Based Electrocatalysts

The more extensively investigated anode materials for DEFCs are the binary Pt-Ru/C and Pt-Sn/C and those related ternary Pt-Ru-based and Pt-Sn-based catalysts. These multifunctional electrocatalysts show superior activity in ethanol electro-oxidation reaction with respect to platinum alone, which was mainly attributed to the bifunctional effect (promoted mechanism) and to the electronic interaction between platinum and alloyed metals (intrinsic mechanism) [71, 93-95]. According to the promoted mechanism, the oxidation of the strongly adsorbed oxygen-

containing species is facilitated in the presence of Ru (Sn) oxides by supplying oxygen atoms at an adjacent site at a lower potential than that accomplished by pure Pt. The intrinsic mechanism postulates that the presence of Ru (Sn) modifies the electronic structure of Pt, and, as a consequence, the adsorption of oxygen-containing species.

Pt-Ru catalysts have been proved to be very active in methanol oxidation, thus, they also received much attention in ethanol oxidation [96-99]. Carbon-supported PtRu nanoparticle catalysts can be produced by impregnation and colloids methods. The impregnation method is a simple procedure; however, the carbon-supported metal nanoparticles obtained have a large average size and a broad distribution. The colloidal methods have the advantage to produce very small and homogeneously distributed carbon-supported metal nanoparticles but their methodologies are very complex. In summary, the obtained PtRu/C electrocatalysts showed higher and more durable electrocatalytic activities for ethanol oxidation than a comparative Pt/C catalyst.

The composition of Pt-Ru catalysts is an important parameter influencing the ethanol oxidation. Lamy et al. [98] observed a poor activity of Pt-Ru (Pt: Ru atomic ratio = 4:1) for the ethanol oxidation at room temperature. Camara et al. [99] investigated the catalytic activity for ethanol oxidation as a function of the atomic composition of PtRu electrodeposits and the results revealed that the catalytic activity of PtRu towards the ethanol oxidation reaction is strongly dependent on the Ru content. There is a relatively narrow range of PtRu compositions that present a high rate of ethanol oxidation and the optimum Pt:Ru composition was 60:40. The authors claimed that at low Ru concentration, there are not enough Ru sites to effectively assist the oxidation of adsorbed residues and the oxidation current remains almost at the levels obtained for pure Pt. A Pt:Ru ratio of 60:40 seemed to present a site distribution close to the optimum for ethanol electro-oxidation. Ru concentrations higher than ca. 40% caused the current

to fall and this effect can be rationalized in terms of an inhibition of ethanol adsorption, which was probably due to the diminution of Pt sites.

Regarding the oxidation mechanism of ethanol, controversial opinions exist. Schmidt et al. [100] observed that the formation of chemisorbed species coming from dissociated ethanol is partially inhibited by the presence of Ru and the reaction favors the oxidation pathway through weakly adsorbed species. In agreement with this result, Camara et al. [99] found that the dissociative adsorption of ethanol seems to be inhibited by Ru and the authors claimed that this effect is because of the diminution of neighboring Pt sites, which are necessary for the scission of the C-C bond. On the other hand, according to Fujiwara et al. [80], the promoter action of Ru seems to enhance the oxidation of strongly-bound adsorbed intermediates to give a higher relative yield of CO_2 than on pure Pt.

Some research work was also conducted to modify Pt-Ru catalysts. A third metal (W, Ni, Mo, Pb, etc. [101-107]) or even metal oxide (RuO_2, IrO_2, etc. [108]) were added to Pt-Ru catalysts and those Pt-Ru-based ternary catalysts showed superior catalytic activities than Pt-Ru catalysts.

1.4.1.2 PtSn-Based Electrocatalysts

It was found that Sn could also promote the electrocatalytic activity of platinum to ethanol oxidation and works even better than Ru. According to V. Radmilovic et al. [109], platinum and tin form five bimetallic intermetallic phases, which are Pt_2Sn_3, $PtSn_2$, PtSn, $PtSn_2$ and $PtSn_4$. Polyol method [110-111] and "Bönneman" method [98] were utilized to synthesize Pt-Sn/C or Pt-SnO_x/C catalysts. The effect of the atomic composition of tin was investigated in Lamy et al. [98], and the authors found an optimum composition for Pt-Sn/C electrocatalysts. With 10 at.% in Sn, the electrocatalytic activity observed was greatly enhanced mainly at low potentials. Smallest enhancements existed also for higher Sn contents (20 at.%), but for contents in Sn greater than

25–30 at.%, the EOR activity decreased in comparison to pure platinum.

Assuming that ethanol adsorption takes place only on Pt sites, OH species can be formed on Sn at lower potentials [112-113], which will help to oxidize the adsorbed intermediate species like Pt-CO-CH_3 to CH_3COOH and Pt-CO to CO_2 respectively, according to the bifunctional mechanism [69]. In Pt-Sn/C catalyst, Jiang et al. [111] claimed that the lattice parameter of Pt was dilated because Sn alloyed with Pt. In the study of methanol oxidation reaction on Pt-Sn/C catalysts, it was believed that the dilatation of lattice parameter of Pt inhibited the ability of Pt to adsorb methanol and dissociate C-H bonds [`114]. According to the Zhou et al. [115], suitable dilatation of Pt crystalline lattice constant might be favorable to ethanol adsorption, while overdilatation of lattice constant would inhibit the adsorption and dissociation of ethanol due to the complete alloy of Pt and Sn. For the Pt-Sn/C, the ethanolic residues could not be removed from Pt active sites smoothly because of the lack of oxygen-containing species around Pt active sites. However, for $PtSnO_x$/C the electro-oxidation residues could react with the oxygen-containing resulting from tin oxide in the vicinity of Pt particles to free Pt active sites. On the basis of the above discussion, it was deduced that an ideal PtSn electrocatalyst for ethanol electro-oxidation could be that Pt alloyed tin to a suitable degree with tin existing partially as an oxide.

Pt-Sn-based systems like Pt-Sn-Ni, Pt-Sn-Rh, Pt-Sn-Ru, etc. [116-120] were also studied to improve the electrocatalytic activity.

Other catalysts including Pt-M (where M represent metals other than Ru or Sn, e.g., W, Pd, Rh, Re, Mo, Ti, Ce, etc. [121-122]) and Pt-MO (where MO represent a metal oxide like WO_3, TiO_2, CeO_2, etc. [123-125]) have also been investigated in ethanol electro-oxidation.

1.4.1.3 Non-Platinum Electroatalysts

Non-Pt catalysts such as Ir and Rh based catalysts [126-129] have also been investigated for ethanol oxidation reaction, and there have been some are interesting and reasonably promising results. Lamy et al. carried out *in situ* FTIR study on polycrystalline Ir and Rh electrodes, and showed ethanol oxidation on Ir leading selectively to either acetic acid or acetaldehyde, which Rh is a better catalyst in the total oxidation of ethanol to CO_2 [126]. Cao et al. studied carbon-supported Ir_3Sn nanoparticle electrocatalyst, and the fuel cell test results showed that the overall performance of Ir_3Sn/C was comparable to that the Pt_3Sn/C catalyst [128].

1.4.2 Cathode Electrocatalysts in Direct Ethanol Fuel Cells (DEFC)

Oxygen reduction reaction (ORR) happens at the cathode of DEFC. However, the requirements for cathode catalysts for DEFC include not only a high activity for ORR but also a high ethanol tolerance. Some alloys of the first-row transition metals present a higher activity for ORR than platinum in low temperature fuel cell operated on hydrogen. For instance, Pt-based binary catalysts, such PtCr and PtNi, are less sensitive to the presence of alcohol than pure Pt. The enhancement in ORR activity observed when using supported Pt-M alloy electrocatalysts was ascribed to both geometric (decrease of the Pt-Pt bond distance) and electronic factors (increase of Pt d-electron vacancy). [130]

On cathode catalysts ethanol adsorption and oxygen adsorption are competing with each other for the surface sites. The dissociative chemisorption of ethanol requires the existence of several adjacent Pt ensembles and the presence of atoms of the second metal around Pt active sites could block ethanol adsorption on Pt sites because of the dilution effect.

1.5 Electrocatalysts for Ethanol Oxidation – The Subject of the Research in This Dissertation

As discussed in previous sections, the finite resources of fossil fuels, along with environmental concerns are stimulating a broad intensive search for alternative energy sources. The direct ethanol oxidation fuel cell (DEFC) could afford an excellent alternative solution to energy-generation problems, and entail major improvements in the prospects for a renewable energy economy. As a fuel, ethanol has several almost ideal properties [5]: It is non-toxic liquid, easy to store and transport; it can be produced from renewable sources; and, it has a high energy density of 8.0kWh/kg. In principle, in DEFCs, its chemical energy can be converted directly into electricity with high efficiency if it is oxidized to CO_2 in an exchange of 12 electrons.

However, so far, one property of ethanol has impeded its use in fuel cells. Its oxidation kinetics, even on the best available electrocatalysts, is slow and incomplete, i.e., it does not finally yield CO_2, indicating that the C-C bond is not broken in that reaction at practical potentials. The origin of this behavior lies in the large activation energy required for rupturing this bond, thereby necessitating high anodic potentials for Pt-based anodes, presently the main anode electrocatalysts used in low-temperature fuel cells. This requirement renders impractical fuel cells with such anodes. Platinum frequently is alloyed with Ru, Sn, or other metals to provide oxygen-containing species for oxidizing strongly bound intermediate (blocking species) in the oxidation of small organic molecules [96-99, 109-111]. Apparently, the best binary catalysts for ethanol oxidation in acid environments are Pt–Sn alloys; however, spectroscopic studies have demonstrated that adding Sn to Pt inhibits the splitting of C-C bonds [131-132]. To date, no Pt-alloy has proven sufficiently efficacious in oxidizing ethanol to support its application in DEFCs. In

summary, the major challenge for the electrocatalysis of ethanol is to achieve its total oxidation to CO_2 at low overpotentials, and the focus of this dissertation is to develop effective electrocatalysts for oxidizing ethanol to CO_2.

Ternary Pt-Rh-SnO_2 Electrocatalysts

We designed the Pt-Rh-SnO_2 ternary electrocatalyst for ethanol oxidation starting from three constituents having the specific properties to perform certain functions in the catalytic reaction, and expecting certain synergy between them, as often observed in similar systems. Thus, Pt was selected because its bare surface is essential for ethanol adsorption and the abstraction and oxidation of H atoms in ethanol molecules, SnO_2 was chosen to provide oxygen containing species (OH) to oxidize strongly bound intermediates, such as CO, and finally, we elected Rh to help in splitting C-C bond, as some data from UHV studies suggested [133]. This ternary electrocatalyst has been found capabable of splitting C-C bond and oxidizing ethanol to CO_2 in this dissertation study.

A model catalyst, $RhSnO_2$/Pt(111), was first prepared by depositing Rh and SnO_2 nanoclusters on Pt(111) surface; and then carbon-supported $PtRhSnO_2$ nanoparticle electrocatalysts were synthesized using a cation-adsorption-reduction-adatom-galvanic displacement method. The catalysts were characterized by inductively coupled plasma-optical emission spectroscopy (ICP-OES), X-ray diffraction (XRD) and transmission electron microscope (TEM). A set of electrochemical techniques including cyclic voltammetry (CV), chronoamperometry (CA), and potetniostatic polarization were employed to investigate the catalytic performance of the ternary catalyst. *In situ* infrared reflection absorption spectroscopy (IRRAS) studies were carried out to determine the reaction intermediates and product

distribution. *In situ* X-ray absorption spectroscopy (XAS) measurements were conducted and the results revealed information of oxidation state (X-ray absorption near edge spectroscopy (XANES)) and structural information like bond length and coordination number (extended X-ray absorption fine structure (EXAFS)).

Carbon-supported Pt, Rh, PtRh, $PtSnO_2$, $RhSnO_2$, PtRh, and $PtRhSnO_2$ nanoparticle electrocatalysts were synthesized using a facile polyol approach. A combination of electrochemical and *in situ* spectroscopic studies was carried out to study the role of each element played in the ternary Pt-Rh-SnO_2 electrocatalyst.

Our findings open new possibilities for studies of C-C bond splitting in variety of important reactions, while this ternary Pt-Rh-SnO_2 electrocatalyst holds great promise for resolving the major impediment to developing efficient direct ethanol fuel cells (DEFC) – i.e., the very slow, partial oxidation of ethanol by existing electrocatalysts.

Carbon-Supported MM'/SnO_2 (MM' = PtRh, PtIr, IrRh, PtIrRh) NP Electrocatalysts

Rh is one of the rarest and the most costly element in earth, Ir is therefore studied as an alternative to Rh. Ir and Rh are in the same group, and they share similar properties, including the same number of unpaired d electrons and similar oxyphilicity.

We discuss our DFT calculation guided design, syntheses, and characterization of MM'/SnO_2 nanoparticles (NPs) consisting of multi-metallic nanoislands (MM' = PtRh, PtIr, IrRh, PtIrRh) deposited on SnO_2 NP cores, which provide active metal-metal oxide interface and are synthetic analogues of the PtRh/SnO_2(110) model catalyst in our density functional theory (DFT) study. We first employed a range of characterization techniques, including XRD, aberration-corrected scanning transmission electron microscopy (AC-STEM) with complementary dark

field (DF) and bright field (BF) imaging, energy disperse X-ray spectroscopy (EDS) and *in situ* XAS, to establish the composition and architecture of the synthesized MM'/SnO_2 NPs. Carbon-supported MM'/SnO_2 electrocatalysts with different compositions were prepared using a seeded growth approach and investigated utilizing a combination of electrochemical methods and *in situ* IRRAS to establish the composition-reactivity and composition-selectivity correlations.

Ir-Based (Ir, Ir-Ru, and Ir-Sn) Electrocatalysts

The catalytic property of Ir-based electrocatalysts in ethanol electro-oxidation are studied, we employe a combination of high resolution transmission electron microscope (HRTEM), electrochemical methods, *in situ* IRRAS, along with *in situ* XAS, to improve our understanding of pure Ir and Ir-based binary electrocatalysts (Ir-Ru and Ir-Sn) in ethanol electrocatalysis. The Ir-based binary electrocatalysts were prepared using a simple thermal decomposition method. We demonstrated that Ir-based electrocatalysts exhibited much higher EOR activity compared to pure Pt in low over-potential region of 0.1V-0.6V, and Ir-Sn displayed most profoundly enhanced activity among the Ir-based catalysts. The promotional effect of Sn is likely due to both bi-functional effect and electronic effect. Our *in situ* infrared studies also revealed that ethanol adsorbed mainly as C2 species on Ir-based catalysts and the dominant EOR pathway is partial oxidation pathway forming CH_3COOH.

Pt Monolayer Electrocatalysts

Pt monolayer catalysts hold great potential in fuel cell applications due to the low Pt content and the possibility of fine tuning catalytic properties of Pt by electronic and geometric effects introduced by the substrate metal (or alloy) and the lateral effects of the neighboring

metal atoms [134]. In oxygen reduction reaction (ORR) the Pt mass-specific activity of the new Pt monolayer electrocatalysts was up to twenty times higher than the state-of-the-art commercial Pt/C catalysts. Inspired by our success in ORR, we studied the application of Pt monolayer catalysts in the oxidation of alcohols (methanol and ethanol), and in this dissertation we discussed our results from Pt monolayer deposited on gold substrates.

Pt monolayer deposited on Au(111) was prepared by displacing a Cu underpotential deposition (UPD) layer, and carbon-supported Au@Pt core-shell nanparticle electrocatalyst was synthesized using a microemulsion method [135]. A combination of electrochemical and *in situ* IRRAS study was carried out to investigate the catalytic properties of Pt monolayer modified by the underlaying Au substrates.

Chapter 2: EXPERIMENTAL & TECHNIQUES

2.1 Preparation of Single Crystals

2.1.1 Mechanical Polishing & Annealing

Noble metal single crystals including Pt(111), Rh(111) and Au(111) were employed in this thesis. The single crystals were 11mm and 8mm in diameter, obtained from Metal Crystals and Oxides, Cambridge, England. The single crystal surfaces were oriented to better than 0.2°. The crystal was polished with diamond pastes and alumina powder of 1μm size gradually down to 0.05μm to receive a mirror-like finishing. After polishing, the crystal was first rinsed by ultrapure water, and then ultrasonically cleaned with ultrapure water for 2 minutes to remove the contaminants left on the surface, and thoroughly cleaned by copious ultrapure water again.

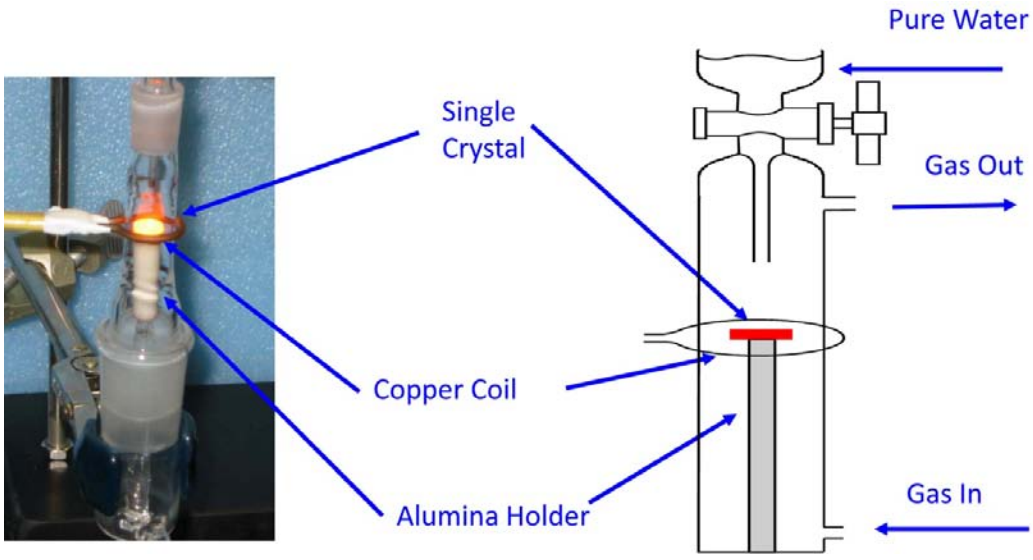

Figure 2.1 Induction heating system for single crystal surface preparation. (with M. B. Vukmirovic)

After mechanical polishing, the crystal was then transferred into the induction heating system (shown in Figure 2.1) for annealing. The purpose of annealing the single crystal was to relax the strain and disorder in surface atomic layers generated during polishing. The crystal was placed on an alumina holder inside a quartz tube, and ultrapure argon (or 5% H_2 in Ar) was purged through the quartz tube. Ar gas purging was started 30 minutes before the heating, to ensure an oxygen-free atmosphere. The crystal was heated inductively via a copper coil around the quartz tube by the use of a high frequency generator HU 2000, and cooling water flowed through the coil during the heating. Heating was conducted for 10min, and then the crystal was cooled under ultrapure argon atmosphere. After cooled down to room temperature, the crystal was protected by a drop of ultra-pure water and was mounted either on a holder for work in a "hanging meniscus" configuration in a regular electrochemical cell or in the FTIR cell.

Besides induction heating, flame annealing can also be used for the preparation of Pt(111) and Au(111) single crystals. After mechanically polishing, the crystals were annealed in air with a H_2 flame. The annealing temperatures were about 1500°C and 800°C for Pt(111) and Au(111) respectively. The annealing was carried out for 5~10 minutes. Special caution should be exercised when annealing Au due to its relatively low melting temperature. After flame annealing, Pt(111) crystal was cooled down under 5% H_2 in Ar and Au (111) was cooled in ultrapure Ar gas. After cooled to room temperature, the single crystal surface was terminated by a droplet of ultrapure water to prevent contamination, and transferred to an electrochemical cell or FTIR cell for further studies.

2.1.2 Electrochemical Polishing of Au(111) Single Crystal

Instead of annealing, Au(111) surface can be electrochemically polished to remove the disordered surface atomic layers [136]. The electrochemical polishing of Au(111) single crystal involved the anodic DC treatment in a two-electrode cell with a Pt foil as cathode, and the temperature was kept constant at 60°C during the polishing. The polishing electrolyte consisted of acetic acid, ethylene glycol and concentrated hydrochloric acid with a volume ratio of 3:2:1. The crystal was anodized for 10~15s at a DC current density of 2.5Acm^{-2} for several times until a bright and shiny surface was obtained. After polishing, the crystal was rinsed by ultrapure water first, and then left in 50% nitric acid at 60°C for about 10min to remove contaminates, and the crystal was thoroughly rinsed with pure water again. Sometimes a flame annealing was followed to ensure the surface quality.

2.2 Metal Monolayer Deposition

2.2.1 Metal Monolayer Deposition on a Metal Substrate

Metal monolayer can be deposited on selected metal substrates by galvanic displacement of a pre-deposited Cu monolayer, and this approach was developed by Adzic et al [91, 137-139]. As illustrated in Figure 2.2a, first, a Cu pseudomorphic monolayer was deposited on a noble metal (e.g. Pt, Pd, Au, etc.) surface through the under potential deposition (UPD) from a solution containing 50mM $CuSO_4$ and 50mM H_2SO_4; second, the electrode covered by this Cu monolayer was emersed from the plating solution and rinsed with ultrapure water to remove Cu^{2+} from the solution film; third, the electrode was placed into a deaerated noble metal ion solution (e.g. 1mM

K_2PtCl_4 + 50mM H_2SO_4) and after 2 min immersion to completely replace Cu by this noble metal (e.g. Pt), the electrode was rinsed by ultrapure water again to remove the noble metal ions (e.g. Pt^{2+}) from the solution film. All these procedures were carried out in a multi-compartment electrochemical cell (Figure 2.2b) purged with Ar to prevent the oxidation of Cu adatoms in contact with O_2. Figure 2.2c displays the scanning tunneling microscopy (STM) image of the Pt monolayer deposit on a Pd(111) surface, and one can find the deposit consists of two-dimensional interconnected Pt islands, with several holes between the islands and also a few sites with Pt atoms in the second layer [138]. Figure 2.2d shows a typical Z contrast image from high-angle annular dark field (HAADF) scanning transmission electron microscopy (STEM) show a bright Pt shell on a relatively darker Pd nanoparticle, signifying the formation of a core/shell structure [139].

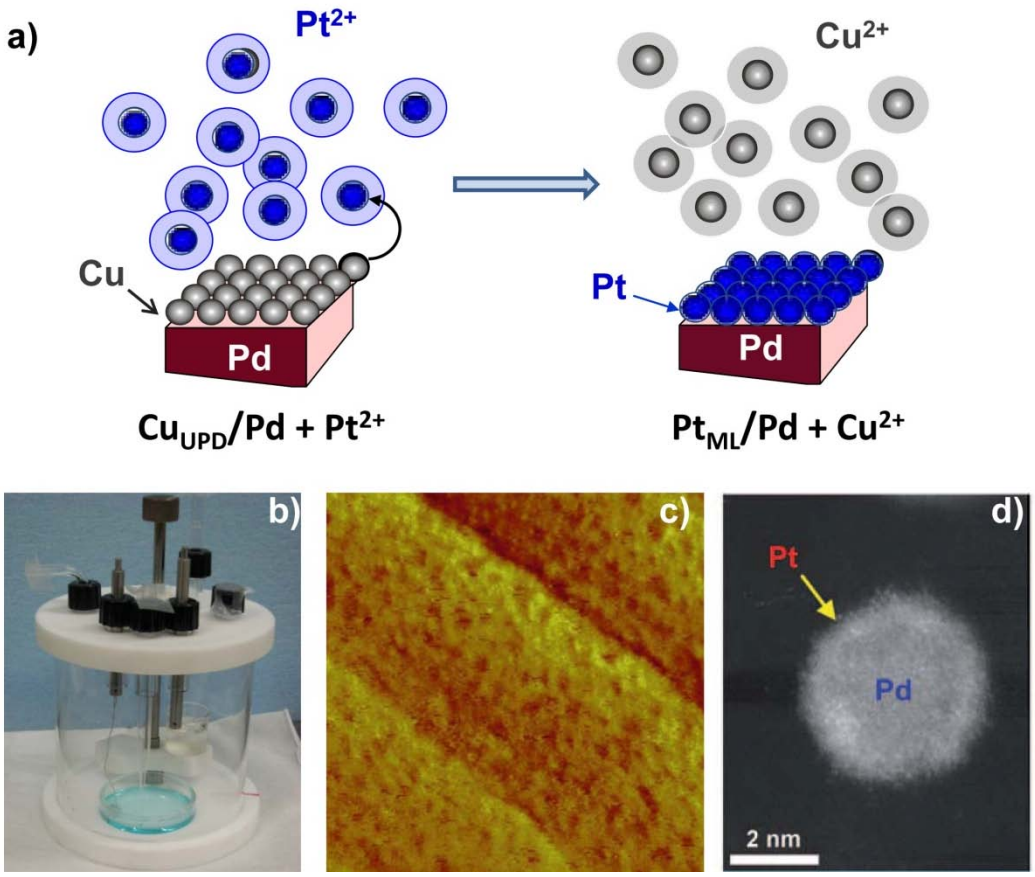

Figure 2.2 (a) Illustration of the Pt monolayer deposition on a Pd substrate by galvanic displacement of a Cu UPD layer. (b) Picture of the mulit-compartment cell used for metal monolayer deposition by galvanic displacement of a Cu monolayer. (c) A STM image, 50 nm × 50 nm, of the Pt monolayer deposited on a Pd(111) surface. The electrode potential is 0.8 V in 0.1 M $HClO_4$; the tunneling current is 1.24nA. (d) A typical HAADF image of the sample of Pt monolayer shell on a Pd core nanoparticle, the Pt_{ML}/Pd/C electrocatalyst.

2.1.2 Cation – Adsorption – Reduction – Adatom – Displacement – Deposition

Another approach was developed by Adzic et al. [140] to deposit a metal adlayer on a metal oxide substrate. As we know, when the pH value is higher than that of the point of zero charge, the metal oxide surface will be negatively charged. Thus, positively charged cation can be adsorbed on the oxide surface.

The procedures were illustrated by Figure 2.3. First, cations (e.g. Pb^{2+}, Zn^{2+} Cu^{2+}, Bi^{3+}, etc.)

were absorbed on the metal oxide surface (e.g. SnO_2); second, the absorbed cations (e.g. Pb^{2+}) were reduced to metallic state through electrochemical or chemical reduction to form a metal adlayer (e.g. Pb^0); third, the electrode covered with metal adlayer (e.g. Pb^0) was immersed into a deaerated noble metal ion solution (e.g. 1mM K_2PtCl_4 + 50mM H_2SO_4) to completely displace Pb adatoms by this noble metal atoms (e.g. Pt). All these procedures were also carried out in the multi-compartment electrochemical cell purged with Ar to prevent the oxidation of Pb adatoms in contact with O_2. $PtRhSnO_2/C$ electrocatalyst was prepared by displacing Pb adatoms on SnO_2/C by Pt and Rh atoms (Section 3.1.2).

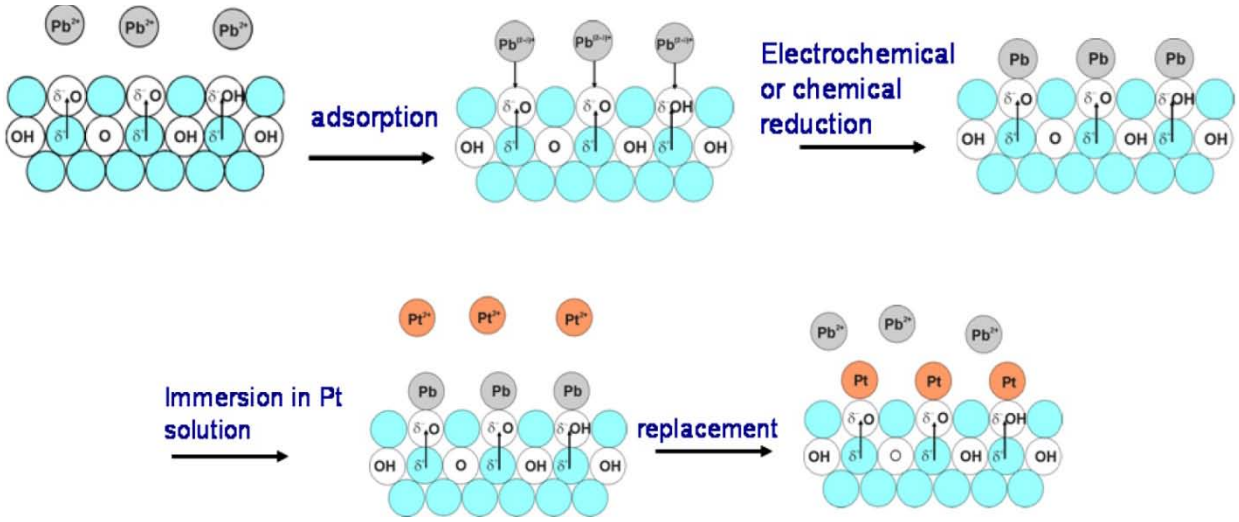

Figure 2.3 Illustration of the cation – adsorption – reduction – adatom – galvanic displacement-deposition method for Pt deposition on a metal oxide substrate by displacing a Pb adlayer.

2.3 Syntheses of Electrocatalysts for Ethanol Oxidation

2.3.1 Rh-SnO_2/Pt(111) and Pt-SnO_2/Rh(111) Model Catalysts

Pt(111) single crystal was prepared by mechanical polishing, followed by induction annealing, as described in Section 2.1. Rh and SnO_2 nanoclusters modified Pt(111) surface was prepared according to the following procedures. Half monolayer of rhodium was deposited on the Pt(111) by displacing 3/4 monolayer of underpotentially deposited (UPD) Cu. One droplet of $SnCl_4$ solution containing two monolayer amount equivalent Sn^{4+} was placed on the 1/2ML Rh modified Pt(111) surface and after dried in air, the crystal was heated in 200ºC in air for half an hour to thermally oxidize $SnCl_4$ to SnO_2 nanoclusters. Figure 2.4 shows the procedures of preparing 2ML SnO_2-1/2ML Rh/Pt(111) electrode (denoted as Rh-SnO_2/Pt(111) hereafter).

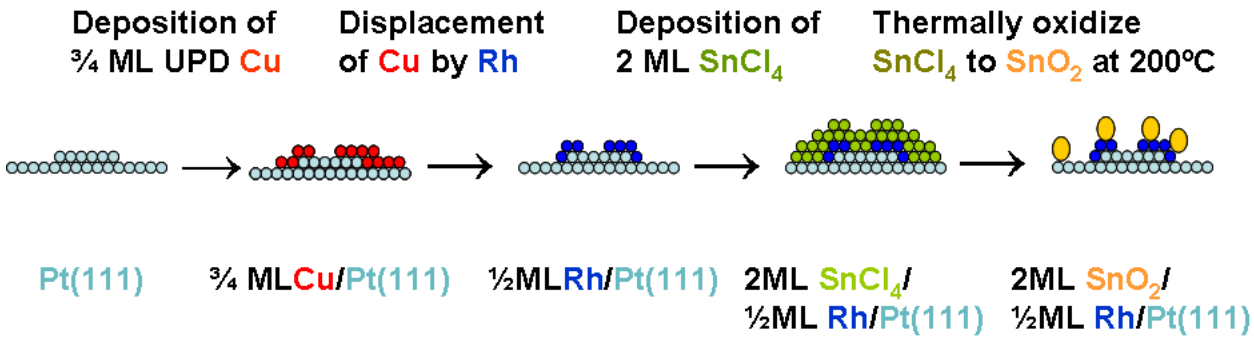

Figure 2.4 The procedures of preparing 2ML SnO_2-1/2ML Rh/Pt (111) electrode.

The assembly of Rh-Pt-SnO_2 ternary system was prepared on Rh(111) surface through a different method. Pt was reduced by $NaBH_4$ on SnO_2 particles obtained using sol-gel method and the obtained Pt-SnO_2 particles were suspended in water. One drop of this suspension containing one monolayer equivalent amount of Pt and two monolayer equivalent amount of SnO_2 was

dropped on Rh(111) electrode and after dried in air, the obtained 2ML SnO_2-1ML Pt-Rh(111) electrode (denoted as Pt-SnO_2/Rh(111) hereafter) was employed in later study.

2.3.2 Syntheses of Ternary Pt-Rh-SnO_2/C Electrocatalysts

2.3.2.1 Preparation of SnO_2 Nanoparticles (NPs)

SnO_2 NPs were prepared by the sol-gel method [141]. In a typical synthesis, ammonia water $NH_3 \cdot H_2O$ (15%) was added into 0.1M $SnCl_4 \cdot 5H_20$ solution dropwise where white precipitate appeared immediately. The white precipitate was washed by pure water for 5 times to remove the remaining ions and was then collected by centrifuge. The obtained solid was dried at 50ºC in air for one day to remove moisture and then grinded by mill.

In the typical polyol synthesis [142] of SnO_2 NPs, 0.2 g of $SnCl_2 \cdot 2H_2O$ (dissolved in 10 mL of EG) was added to a mixture of EG and water (volumetric ratio of 99:1) which was hosted in a round-bottom flask. The solution was refluxed at 190ºC for 40min with constant stirring with oxygen flowing all the time during the synthesis. During the preparation, under elevated temperature, Sn was reduced by ethylene glycol, and then immediately oxidized to SnO_2 by oxygen. The resulted SnO_2 NPs was dispersed and stabilized by ethylene glycol, and formed clear colloid with a light yellow color.

2.3.3.2 Preparation of Pt/C, Rh/C, SnO_2/C, PtRh/C, PtSnO_2/C, RhSnO_2/C and PtRhSnO_2/C Electrocatalysts by a Facile Polyol Approach

In this thesis, a modified polyol method was employed to synthesize a series of nanoparticles including Pt, Rh, SnO_2, PtRh, PtSnO_2, RhSnO_2, and PtRhSnO_2 (Figure 2.5).

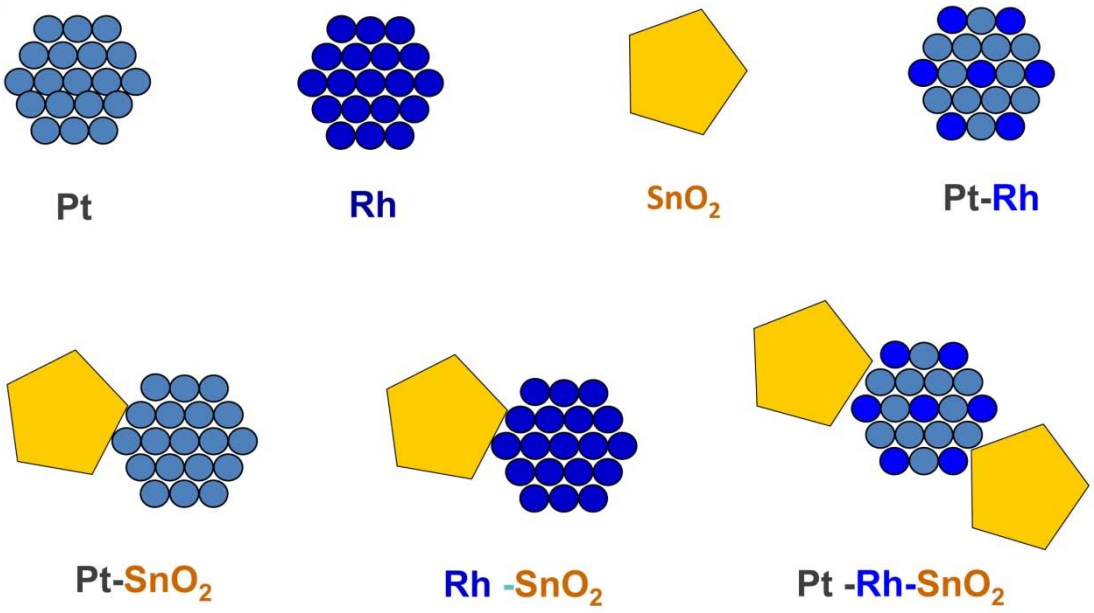

Figure 2.5 Polyol syntheses of different nanoparticle electrocatalysts: Pt/C, Rh/C, SnO_2/C, PtRh/C, $PtSnO_2$/C, $RhSnO_2$/C, and $PtRhSnO_2$/C

The nanoparticle electrocatalysts have been made using a sequential synthetic approach with SnO_2 nanoparticles being formed first and then Pt, Rh or PtRh nanoparticles were reduced in a the second step. SnO_2 nanoparticles were prepared by heating calculated amount of $SnCl_2{\cdot}2H_2O$ dissolved in the mixture of ethylene glycol (EG) and water (H_2O) with volumetric ratio 99:1 at 190ºC for 1h. The resulted SnO_2 colloid with light yellow color was cooled to room temperature, then suitable amounts of $H_2PtCl_6{\cdot}6H_2O$, and/or $RhCl_3$ were dissolved in EG and then added into SnO_2 colloid. The temperature of the mixture was quickly ramped to 60 ºC and then slowly brought to 130 ºC with a temperature ramp of around 1 ºC/min and kept at 130ºC for 2h, with argon flowing in the flask. The resulted black colloid was cooled to room temperature, then calculated amount of Vulcan carbon black was added, and the mixture was stirred overnight. The resulted slurry was filtered, washed with copious ultrapure water, and the precipitate was dried in a vacuum oven at 80°C overnight. The catalysts were annealed in argon at 200°C for 1h to remove remained EG. All the electrocatalysts were prepared with a 40% loading on Vulcan

carbon support.

2.3.3.3 Preparation of Pt-Rh-SnO_2/C Electrocatalysts with Varied Pt:Rh:Sn Ratios Using a Co-reduction Approach

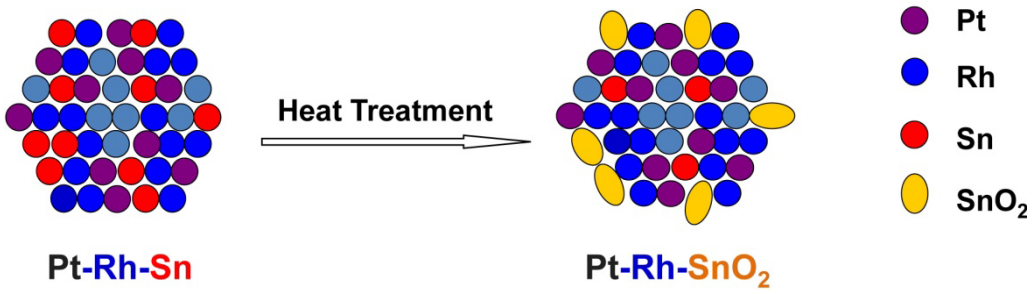

Figure 2.6 Synthesis of Pt-Rh-SnO_2/C electrocatalysts by a co-reduction approach

The Pt-Rh-SnO_2/C catalysts were synthesized using a co-reduction approach, followed by thermal treatment. In a typical procedure, the calculated amount of respective metal precursors, $H_2PtCl_6 \cdot 6H_2O$, $RhCl_3$ and $SnCl_2 \cdot 2H_2O$ were dissolved in a mixture of ethylene glycol (EG) and water. After addition of the appropriate amount of Vulcan XC-72R carbon black, the suspension was stirred overnight to form a uniform suspension. Concentrated NaOH solution (50wt.% in water) was used to raise pH value to 13. The mixture was heated to 180ºC and kept constant for 3h to ensure a complete reaction. After cooling to room temperature concentrated sulfuric acid (98% H_2SO_4) was added to adjust the pH value to neutral. The resulted slurry was filtered, washed with copious distilled water, and the precipitate was dried in a vacuum oven at 80°C overnight. The electrocatalysts were annealed in air at 200°C for 1h to remove remained EG and also oxidize the resulting Sn phase to SnO_2. The resultant Pt-Rh-SnO_2/C catalysts have nominal Pt:Rh:Sn atomic ratio of 3:1:x, with x values varied from 2 to 6; and all the electrocatalysts were prepared with a 20% noble metal loading.

2.3.3.4 Carbon-Supported MM'/SnO_2 (MM' = PtRh, PtIr, IrRh, and PtRhIr) Nanoparticle Electrocatalysts

The MM'/SnO_2 NP electrocatalysts have been made using a seeded growth approach with SnO_2 nanoparticles being formed first and then multi-metallic PtRh, PtIr, IrRh or PtIrRh nanoislands being co-reduced on SnO_2 substrates afterwards. Chemicals, $PtCl_4$, $RhCl_3$, $(NH_4)_2IrCl_6$, $SnCl_2{\cdot}2H_2O$, ethylene glycol (EG), sodium hydroxide (NaOH) were purchased and used as received.

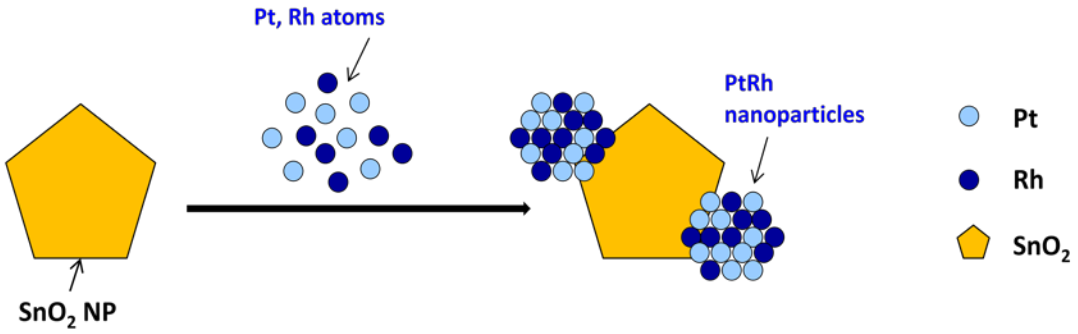

Figure 2.7 The PtRh/SnO_2 nanoparticle synthesis from a seeded growth approach

Synthesis of SnO_2 NPs

In a typical procedure, calculated amounts of $SnCl_2{\cdot}2H_2O$ was dissolved in the mixture of 99ml ethylene glycol (EG) and 1ml water (H_2O) to form a clear solution. Temperature was ramped to 190ºC and was kept there for 1h with oxygen flowing in the flask. The resulted SnO_2 colloid with light yellow color was then cooled to room temperature.

PtRh/SnO_2 NPs

Suitable amounts of $PtCl_4$ and $RhCl_3$ were dissolved in 40mL EG first and then added into

SnO_2 colloid. Concentrated NaOH solution (10M in water) was used to raise pH value to 13. The mixture was heated to 50 ºC first and then slowly brought to 130 ºC with a temperature ramp of around 1ºC/min and kept in 130ºC for 2h. After cooling to room temperature concentrated sulfuric acid (98% H_2SO_4) was added to adjust the pH value to neutral. The reaction was carried out under argon atmosphere. Four PtRh/SnO_2 NP catalysts with atomic ratio Pt:Rh:Sn of 1:1:1, 1:1/2:1, 1:1/3:1 and 1:1/4:1 were prepared.

PtIr/SnO_2 NPs, IrRh/SnO_2 & PtIrRh/SnO_2 NPs

Three categories of electrocatalysts, PtIr/SnO_2, IrRh/SnO_2 and PtIrRh/SnO_2, were synthesized in a similar fashion. Three PtIr/SnO_2 NP catalysts with atomic ratio Pt:Ir:Sn of 1:1:1, 1:1/2:1 and 1:1/4:1, one IrRh/SnO_2 NP catalyst with atomic ratio Ir:Rh:Sn of 1:1:1 and one PtIrRh/SnO_2 NP catalyst with atomic ratio Pt:Ir:Rh:Sn of 1:1:1:1 were prepared.

Preparation of Carbon-Supported Electrocatalysts

The resulted black colloid was cooled to room temperature, then calculated amount of Vulcan carbon black was added, and the mixture was stirred overnight. The resulted slurry was filtered, washed with copious distilled water, and the precipitate was dried in a vacuum oven at 80°C overnight. The catalysts were annealed in argon at 200°C for 1h to remove remained EG. All above electrocatalysts were prepared with a 40% loading on Vulcan carbon support.

2.3.3.5 Ir-Based Electrocatalysts (Ir, Ir-Ru, and Ir-Sn)

A Ir/C sample (10wt.%) from ETEK were used without further treatment in this thesis. Binary Ir-Ru and Ir-Sn electrocatalysts were prepared using a simple thermodecomposition approach. In a typical procedure, calculated amounts of respective metal precursors, $(NH_4)_2IrCl_6$, $RuCl_3$ and/or $SnCl_4 \cdot 5H_2O$ were dissolved in 20mL water first to form concentrated solution, and

then 140mg Vulcan carbon was added. The mixture was stirred for 2h to form a uniform suspension, and then the temperature was raised to around 90°C to evaporate all water and form metal salts impregnated carbon. These impregnated carbons were placed into a quartz glass boat in a tube furnace with a flowing atmosphere of 15% H_2 in Ar, and heated to 400°C, where it was held for 1h. During the calcination, metal salts decomposed and formed carbon supported nanoparticles. The resultant Ir-based binary catalysts have nominal atomic ratio Ir:M (Ru and Sn) of 9:0.5, 9:1 and 9:2, and all binary catalysts were prepared with a total metal loading of 30%.

2.3.3.6 Pt Monolayer Deposited on Au Substrates

Platinum monlayer deposited on gold substrates was studied in this thesis. Au(111) single crystal was prepared by the mechanical polishing, electrochemical polishing and flame annealing to received a mirror-like finishing. Pt_{ML}/Au(111) was prepared by galvanic displacement of one UPD Cu layer on Au(111).

A carbon-supported Au@Pt core-shell nanoparticle electrocatalyst consisting of a Au-rich core and a Pt-rich shell was prepared by microemulsion approach, and the details can be find in Reference 138. $Ru_{1/2ML}$/Au@Pt/C was prepared by displacing half monolayer of Cu deposited on the Au@Pt core-shell NPs.

2.4 Electrochemical Measurements

A VoltaLab PGZ100 potentiostat was used in this thesis for the electrochemical measurements in a standard three-electrode electrochemical cell. The electrocatalysts were ultrasonically mixed with ethanol/water solution (volume ratio 1:1) to form uniform ink and

10μL ink was pipetted onto the polished glassy carbon (GC) disk to form a homogenous thin catalyst layer. Electrochemical measurements including cyclic voltammetry (CV), chronoamperometry (CA) and potentiostatic polarization in ethanol-containing electrolyte were carried out to determine the EOR activity of these electrocatalysts. All the potentials given in this thesis were referenced to that of the reversible hydrogen electrode (RHE) unless as addressed.

In electrochemical experiments, a leak-free Ag/AgCl, 3M Cl^- reference electrode was used with a double –junction reference chamber (Cypress, Lawrence, KS) and a platinum flag was used as counter electrode. Electrochemical measurements were performed at room temperature, which was approximately 20ºC, and at elevated temperature, such as 60°C.

2.5 *In Situ* Infrared Reflection-Absorption Spectroscopy (IRRAS)

Infrared spectroscopy is a very powerful tool for characterizing the chemical composition of a given system and has been widely used in understanding surface electrochemical processes [143-146]. However, the major solvent in electrochemical systems is water, which has a very large IR absorption and therefore hinders the application of infrared spectroscopy. Several improvements have been achieved to increase the signal-to-noise ratios and minimize the interference from the solution [147-148]. In this thesis, the *in situ* infrared reflection absorption spectroscopy (IRRAS) with thin layer configuration was used to characterizing the electrode/solution interface.

As shown in Figure 2.8a, in order to reduce the strong IR absorption from the bulk solution, the electrode is pushed against the ZnSe prism forming a thin solution layer (1-10μm) between the electrode and prism. The IR beam passing through the prism and the thin solution layer, is reflected at the electrode/electrolyte interface. One advantage is in this mode, both the electrode

surface and the whole solution layer are probed and the information of solution species can be obtained. Moreover, both single crystals and polycrystals can be used as working electrode in IRRAS. However, it is not suitable for time-resolved reaction studies because the mass transport is hindered between the thin layer and the bulk solution. Species consumed or generated at the electrode surface can not be easily replaced from or diffused to the bulk solution. In addition, it is not suitable for kinetics study either because of the high resistivity, uneven potential distribution, as well as the hindered mass transport. Even the thin layer configuration has limited the absorption from solution greatly; the solution background is still about three orders of magnitude stronger than the signal from absorbates and difficult to be subtracted completely.

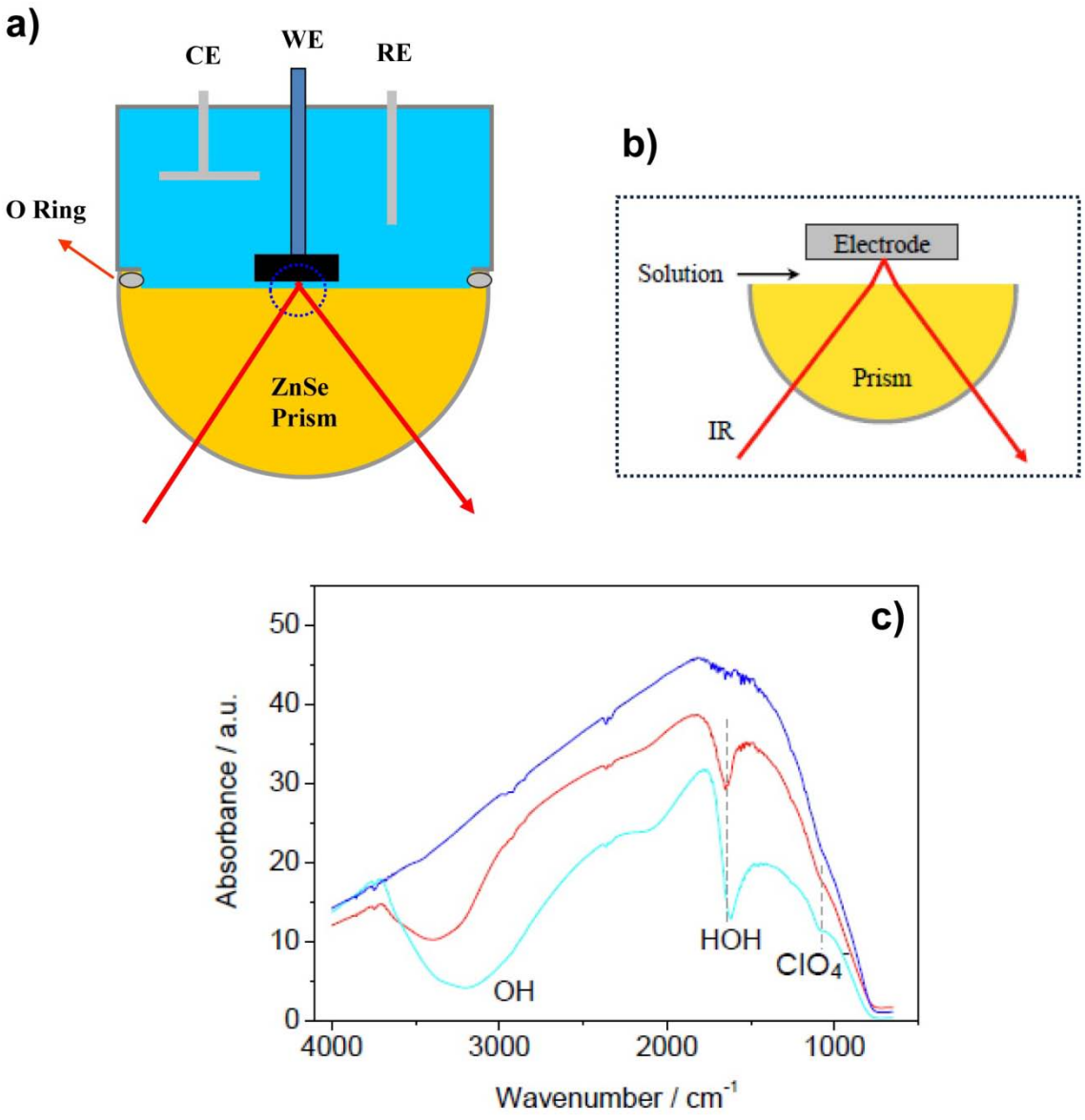

Figure 2.8 (a) Schematic illustration of the thin layer IRRAS used to examine the electrode/electrolyte interface. (b) IR beam reflected at Electrode/electrolyte interface. (c) Background spectra (single beam) of a ZnSe hemisphere measured with the external reflection: without solution (blue line), with 0.1M $HClO_4$ solution in the FTIR cell (cyan line), and Pt(111) electrode pushed against the ZnSe prism in 0.1M $HClO_4$ solution with a thin-layer IRRAS configuration (red line).

Figure 2.8c displays the IR spectra collected under the thin-layer configuration. One can find signal dropped after the FTIR cell was filled with electrolyte (0.1M $HClO_4$) due to the absorption from liquid water, and the IR signal increased when a Pt(111) electrode was pushed against the prism and a thin-layer was created.

In situ IRRAS experiments were performed using a Nicolet Nexus 670 FT-IR spectrometer equipped with a MCT detector cooled with liquid nitrogen. No polarization discrimination was utilized. Spectra ware given in absorbance units defined as $A = -\log\left(R/R_0\right)$, where R and R_0 represent the reflected IR intensities corresponding to the sample- and reference-single beam spectrum, respectively. All experiments were carried out at room temperature, which was approximately 20ºC.

For ethanol oxidation and methanol oxidation experiments, the spectra resolution was set to $8cm^{-1}$ and 128 interferograms were co-added for each spectrum. The reference spectrum was collected at 0.05V vs. RHE, in the alcohol containing electrolyte. Both modified single crystal surfaces and carbon supported nanoparticle electrocatalysts were employed as working electrode.

2.6 *In Situ* X-ray Absorption Spectroscopy (XAS)

X-ray absorption spectroscopy (XAS) provides the details of how x-rays are absorbed by an atom at energies near and above the core-level binding energies of that atom. More specifically, XAS spectra are graphs of the absorption coefficient of a given material versus the incident x-ray photon energies. The probability of x-ray absorption is due to the chemical and physical state of that atom; hence, XAS spectrum contains valuable information like the chemical state of that atom as well as local atomic structure. XAS can be used in a variety of systems and bulk physical environment.

Typically XAS spectrum begins before an absorption edge of the element we study and continues to about 1000eV above the edge. The entire spectrum is divided to two regimes: x-ray absorption near edge spectroscopy (XANES) and extended x-ray absorption fine-structure

(EXAFS) (as shown in Figure 2.9). Typically, XANES refers the range from the threshold of the absorption edge to around 50eV higher while EXAFS considers the rest of the absorption spectrum, which reaches much higher x-ray energies. XANES and EXAFS actually have the same physical origin and contain slightly different physical information. XANES is strongly sensitive to formal oxidation state and coordination chemistry (e.g., octahedral, tetrahedral coordination) of the absorbing atom, while the EXAFS is used to determine the distances, coordination number and species of the neighbors of the absorbing atom [49].

Figure 2.10 is a block plot of XAS experimental set up. It consists of a synchrotron light source, a double-crystal monochromator, electrochemical cell with sample, ionization chamber detectors for monitoring the intensities of the beam for the inlet (I_0), fluorescence (I_f), and transmission (I_t), and a data acquisition system.

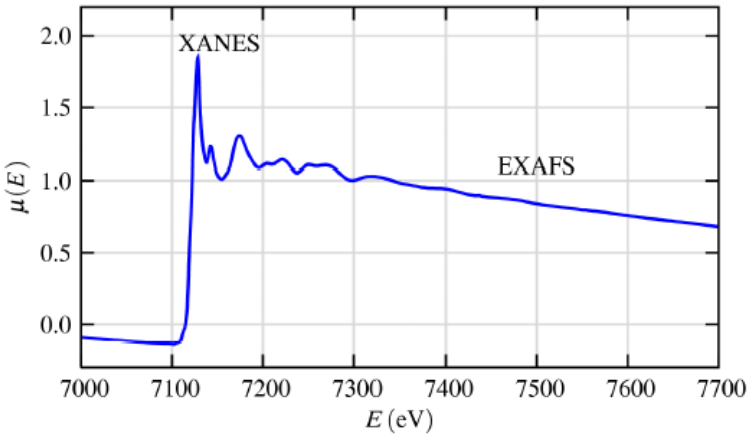

Figure 2.9 A typical x-ray absorption spectrum with XANES and EXAFS regimes

The electrochemical cell employed for X-ray absorption near edge structure spectroscopy (XANES) data acquisition is illustrated in Figure 2.11. A thin electrocatalyst film (working electrode), a proton exchange membrane (Nafion 117, DuPont Chemical Co.), and a carbon

counter electrode (Grafoil, Union Carbide Corp.) were sandwiched and held in PTFE gaskets, and all the cell components were clamped tightly by two acrylic plastic bodies with and O-ring. The membrane is needed to prevent gas crossover form the counter electrode which interferes with the electrochemical measurements. Electrical contact was made through Pt and Au leads that were pressed against the anode and cathode electrodes, respectively. A reference electrode (Ag/AgCl, 3M Cl^-) was inserted in a compartment machined in one of the acrylic blocks. 1M $HClO_4$ was added to the cell as the electrolyte. A VoltaLab PGZ402 potentiostat was used to control the potential. XANES measurements were carried out at the National Synchrotron Light Source (NSLS), Brookhaven National Laboratory (BNL) using Beam Line X18B.

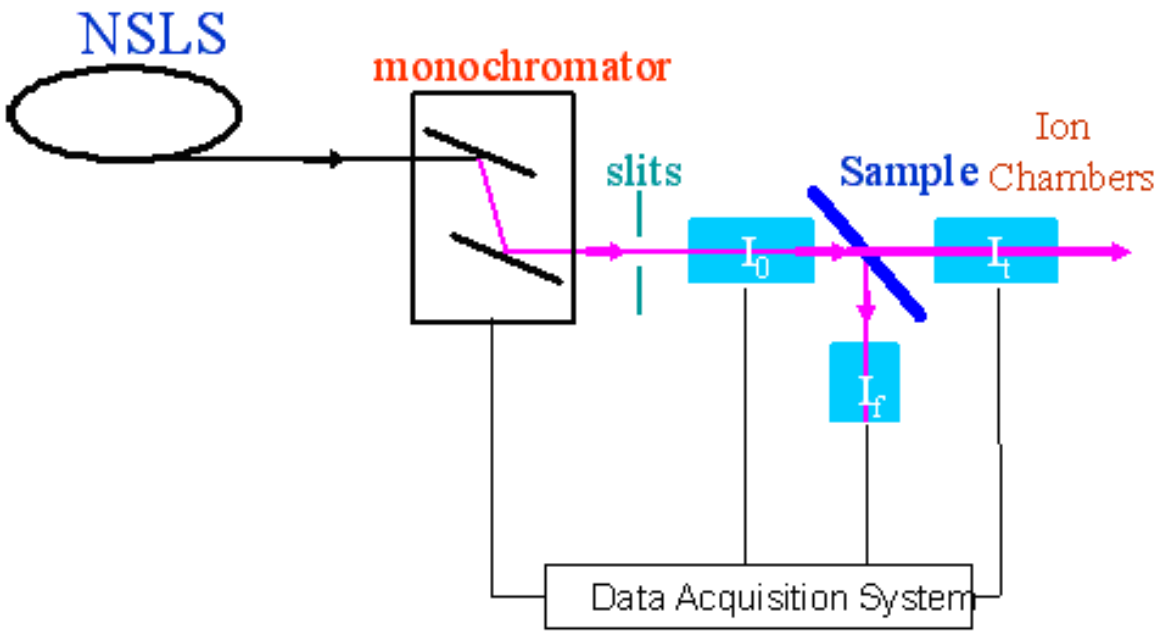

Figure 2.10 Experimental setup for X-ray absorption measurements

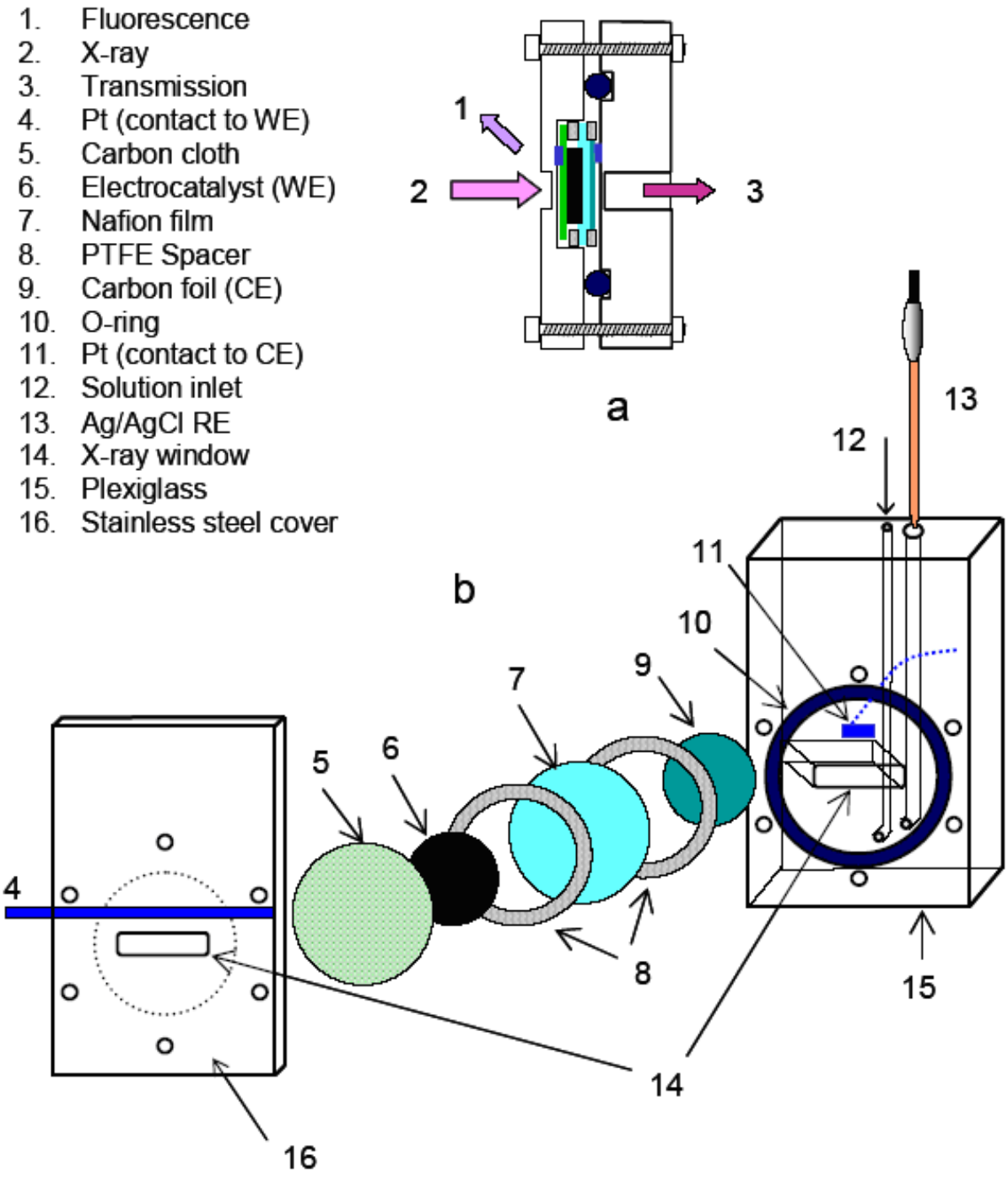

Figure 2.11 Schematic diagram of the in situ electrochemical cell used to obtain the XAS spectra. (a) Cell assembly; (b) Divided cell parts

2.7 Physical Characterization

Powder x-ray diffraction (XRD) measurements were conducted with a Phillips 3100 diffractometer using Cu Kα radiation (1.54056Å). Samples for analyses were prepared by loading the catalyst slurries onto a glass slide, followed by drying in air. Diffraction patterns were collected from 20º to 80º at a scanning rate of 0.6º per minute with a step size of 0.02º. XRD was also conducted at beamline X7B at National Synchrotron Light Source (NSLS), Brookhaven National Laboratory (BNL), with a wavelength of 0.3184nm.

For the transmission electron microspcopy (TEM) measurements we used a JEOL-3000F STEM/TEM, equipped with a Schottky field-emission source operated at 300 KeV, at Materials Science and Condensed Matter Physics Department in BNL. The sample was prepared by placing one drop of the catalyst slurry on a holey carbon covered copper grid (EMS, Hatfield, PA). High resolution-sanning transmission electron microscope (HR-STEM) was operated using a dedicated Hitachi 2700C STEM microscope at Center for Functional Nanomaterials in BNL to determine the catalyst morphology and particle size distribution [149]. An inner-collection-angle of 45mrad and out-collection-angle of 242mrad was used with a convergence angle of electron probe about 27mrad.

The actual chemical composition of these Pt-Rh-SnO_2/C electrocatalysts was studied by inductively coupled plasma optically emission spectroscopy (ICP-OES). Samples were sonicated 15 minutes with aqua regia, heated gently 5 minutes, let stand for about two hours, then diluted to a known volume. Then samples were filtered through a 0.2μm filter and analyzed. The ICP-OES analyses were performed using the Perkin Elmer Optima 3000DV instrument. Electron energy loss spectroscopy (EELS) was employed to determine the composition of different single nanoparticles. The energy resolution of EELS is 0.9eV.

2.8 Density Functional Theory (DFT) Calculations (with Ping Liu)

The unrestricted DFT calculations were carried out using the DMol3 code by Delley27. The ionic cores were described by effective core potentials, with a numerical basis set and the GRA-RPBE functional to describe the exchange and correlation. SnO_2(110) was modeled by means of the supercell approach with three O_Sn_O layer slabs and an 11 Å vacuum between the slabs. The top O_S_O layer of SnO2 substrate, the Rh and Pt atoms on the surface and the adsorbates were allowed to fully relax. Transition states were identified using the combination of synchronous transitmethods and eigenvector following Reference 150.

Chapter 3: RESULTS & DISCUSSION

3.1 Ternary Pt-Rh-SnO_2 Electrocatalysts for Oxidizing Ethanol to Carbon Dioxide [140]

As discussed in Chapter 1, ethanol is an almost ideal combustible for fuel cell applications; however, commercialization of direct ethanol fuel cells (DEFC) has been impeded by ethanol's slow, inefficient oxidation even at the best electrocatalysts. Developing the electrocatalysts for ethanol oxidation to CO_2 that break the C-C bond has been a major challenge in ethanol electrocatalysis. In this chapter we discuss the results from the study of a ternary Pt-Rh-SnO_2 electrocatalyst capable of oxidizing ethanol to CO_2. Both model catalysts based on Pt(111) and Rh(111) single crystals and carbon-supported Pt-Rh-SnO_2 electrocatalyst have been investigated. Our experiments and density functional theory (DFT) calculations indicate that the electrocatalyst's activity and selectivity are due to the specific property of each of its constituents induced by their interactions.

3.1.1 Rh-SnO_2/Pt(111) and Pt-SnO_2/Rh(111) Model Catalysts

Rh-SnO_2/Pt(111) model catalyst (as illustrated in Figure 3.1a) was prepared by depositing 1/2 ML Rh and 2ML equivalent amount of SnO_2 nanoclusters on Pt(111) single crystal surface. At first different amounts of SnO_2 nanoclusters were deposited on Pt(111), and the anodic polarization curves recorded at ethanol containing electrolyte (Figure 3.1d) showed that the electrode modified by moderate loading of SnO_2 nanoclusters, i.e. 1~2ML-equivalent-amount,

gave enhanced EOR activity compared to bare Pt(111) electrode. When SnO_2 loading was too high, i.e. 5ML or higher, the electrode lost EOR activity because most Pt sites were blocked by SnO_2 nanoclusters. 2ML SnO_2 modified Pt(111) (denoted as 2ML SnO_2/Pt(111) hereafter) possessed the best activity, with the most negative reaction onset potential and the highest oxidation current among the four SnO_2 modified Pt(111) electrodes. 1ML SnO_2/Pt(111) also showed improved EOR activity with respect to Pt(111), but lower than that of 2ML SnO_2 modified Pt(111) because more Pt sites were available on 1ML SnO_2/Pt(111) electrode. The promotional effect from SnO_2 has been attributed to the so called bi-functional effect, where the oxide could chemisorb oxygen containing species such as OH to accelerate the oxidation of poisonous species such as CO on Pt sites [27-28]. Hence, 2ML equivalent amount of SnO_2 was chosen in later studies, and 2ML SnO_2 modified Pt(111) electrode was denoted as SnO_2/Pt(111) hereafter. Figure 3.1b and c show STM images of bare Pt(111) and SnO_2/Pt(111), and one can find that SnO_2 nanoclusters were preferentially formed at Pt edge sites.

1/2ML amount of Rh was specifically chosen to modify Pt(111) because Rh is not active for EOR (shown later), and more Pt sites than Rh sites was necessary for the efficient adsorption of ethanol molecules. Figure 3.1e demonstrates the activity comparison of three electrodes: Pt(111), SnO_2/Pt(111), and Rh-SnO_2/Pt(111), and one see that the ternary electrode showed best EOR activity, despite the fact that it had the least amount of Pt sites. Therefore, Rh is essential in forming the highly active EOR electrocatalyst.

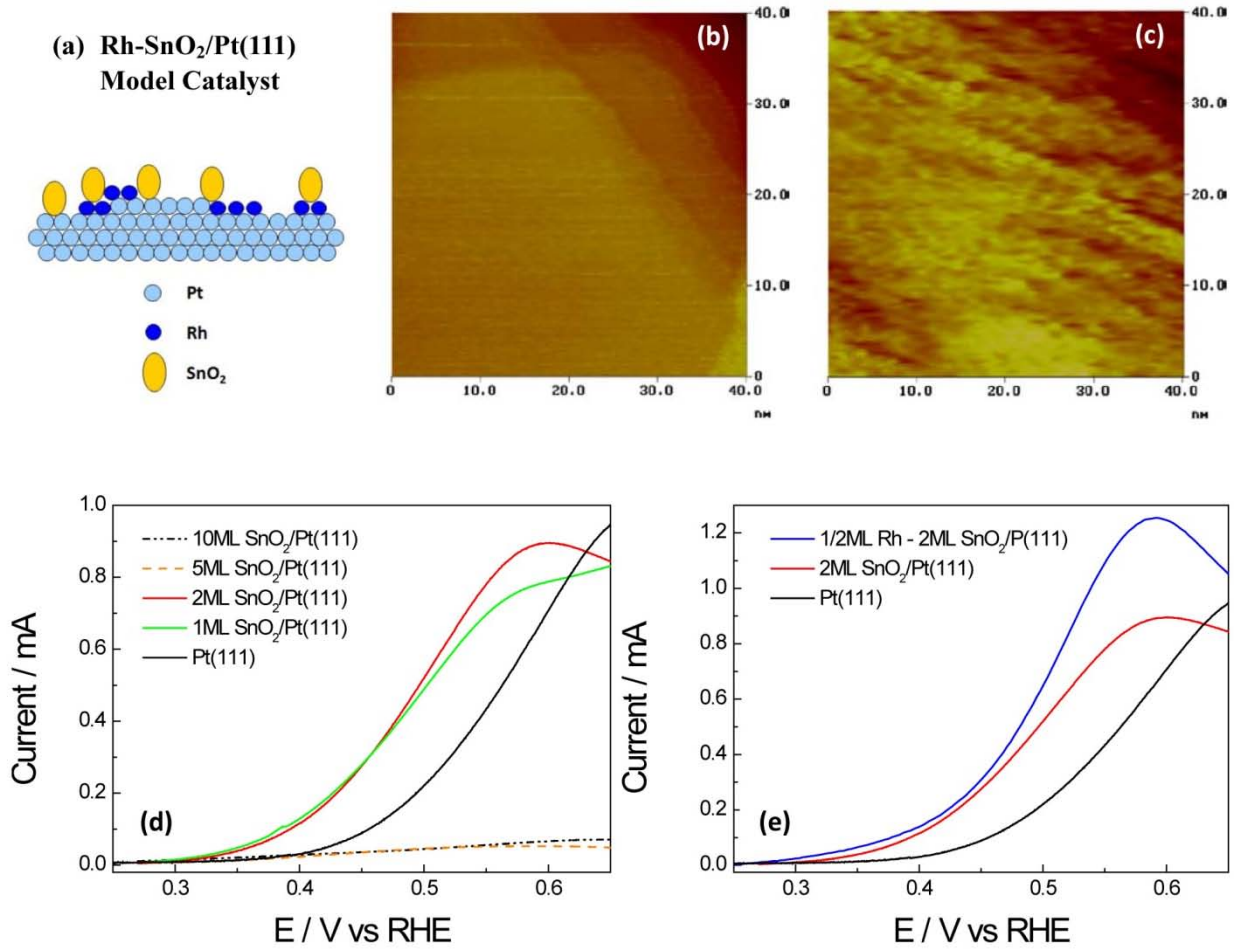

Figure 3.1 (a) Illustration of Rh-SnO_2/Pt(111) model catalyst. STM images of (b) bare Pt(111) and (c) 2ML SnO_2/Pt(111). Anodic polarization curves from (d) four SnO_2 modified Pt(111) electrodes with different SnO_2 loading and bare Pt(111), (e) Rh-SnO_2/Pt(111), SnO_2/Pt(111) and Pt(111). Electrolyte: 0.2M EtOH + 0.1 $HClO_4$, scan rate: 50mV/s. (Work with M. B. Vukmirovic and A. Kowal)

Pt-Sn alloys have been widely recognized as the best binary catalysts for ethanol oxidation in acid environment [98]; however, *in situ* FTIR and on-line DEMS study [132-133] show that the addition of Sn to Pt inhibits the splitting of C-C bonds and only facilitates the ethanol partial oxidation. Therefore, *In situ* IRRAS study were carried out during EOR on the three electrodes: Pt(111), SnO_2/Pt(111) and Rh-SnO_2/Pt(111), to reveal the reaction pathway of ethanol electro-oxidation on the three electrocatalysts.

Table 3.1: *In situ* IRRAS spectra bands assignments [151]

Wavenumber/cm^{-1}	Assignment
2342	CO_2 asymmetric stretching
1715	C=O stretching of CH_3CHO and CH_3COOH in solution
1620-1635	C=O stretching of adsorbed acetaldehyde and acetyl
~1598	H-O-H deformation of adsorbed water
1396-1410	O-C-O stretching of adsorbed acetate
1368, 1108	CH_3 symmetric deformation and C-H wagging in CH_3CHO
~1350	CH_3 in plane bending of adsorbed acetate
1280	C-O stretching of CH_3COOH in solution
1100	Cl-O stretching ClO_4^-
1044	C-O stretching of CH_3CH_2OH
933	C-C-O asymmetric stretching

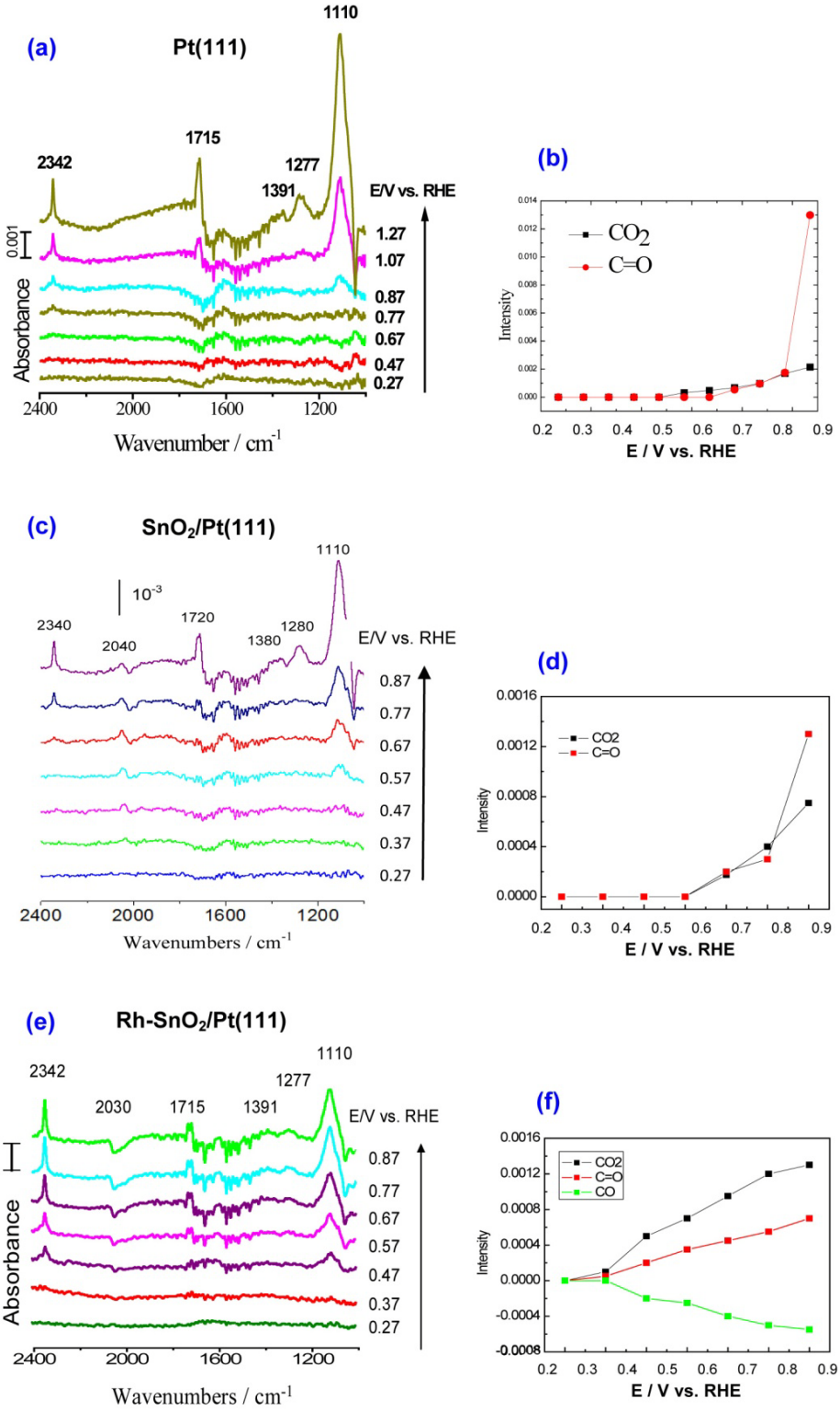

Figure 3.2 *In situ* IRRAS spectra recorded during ethanol oxidation on three different electrodes: (a) Pt(111), (b) SnO_2/Pt(111), and (c) Rh-SnO_2/Pt(111). Electrolyte: 0.1M EtOH + 0.1M $HClO_4$, scan rate: 1mV/s. Variation of band intensities of CO_2 (2342cm^{-1}) and C=O (1715cm^{-1}) from IRRAS spectra versus applied potential on three electrodes: (b) Pt(111), (d) SnO_2/Pt(111), and (f) Rh-SnO_2/Pt(111).

The recorded spectra are shown in Figure 3.2a, c and e, and the frequencies and band assignments are listed in Table 3.1 [151]. The positive potential-dependent peak near 2342cm^{-1} is the signature peak for the asymmetric stretch vibration of CO_2 that appears above 0.77V on Pt(111) and 0.67V on SnO_2/Pt(111), but already is apparent above 0.30V on Rh-SnO_2/Pt(111). The presence of CO_2 indicates the successful cleavage of the C-C bond in ethanol. The bipolar peak at 2030cm^{-1} is assigned to linearly adsorbed CO (CO_L). The band located at around 1715cm^{-1} reflects the stretch vibration of the C=O bond in acetaldehyde and/or acetic acid, both of which are the partial oxidation products. Considerably weaker bands occurred for acetaldehyde at 1715 cm^{-1} and acetic acid at 1277cm^{-1} for the ternary catalyst, confirming the significant decrease of their yield. A high activity of this electrocatalyst was reflected in strong CO_2 bands and negligible CO bands.

In order to better compare the three electrodes, the variation of band intensities of two bands, 2342cm^{-1} (CO_2), and 1715cm^{-1} (C=O in the two partial oxidation products of CH_3COOH and CH_3CHO) versus applied potential are plotted in Figure 3.2 b, d and f. One can find on the ternary Rh-SnO_2/Pt(111) electrode CO_2 was generated at lower potential and in larger quantity than the other two electrodes (Pt(111) and SnO_2/Pt(111)), which highlighted the importance of Rh in splitting C-C bond.

Attempts have been made to study Rh in catalyzing reactions involving C-C bond cleavage in gas phase reactions and DFT calculations [129]. Lamy et al. [126] has shown the polycrystalline Rh electrode can oxidize ethanol with higher efficiency, i.e. more selectively to CO_2, compared to the polycrystalline Ir electrode. Overall speaking, Rh has not been extensively investigated in ethanol electrocatalysis as Pt, so a well ordered Rh(111) single crystal was employed in our study to understand the role of Rh in C-C bond splitting.

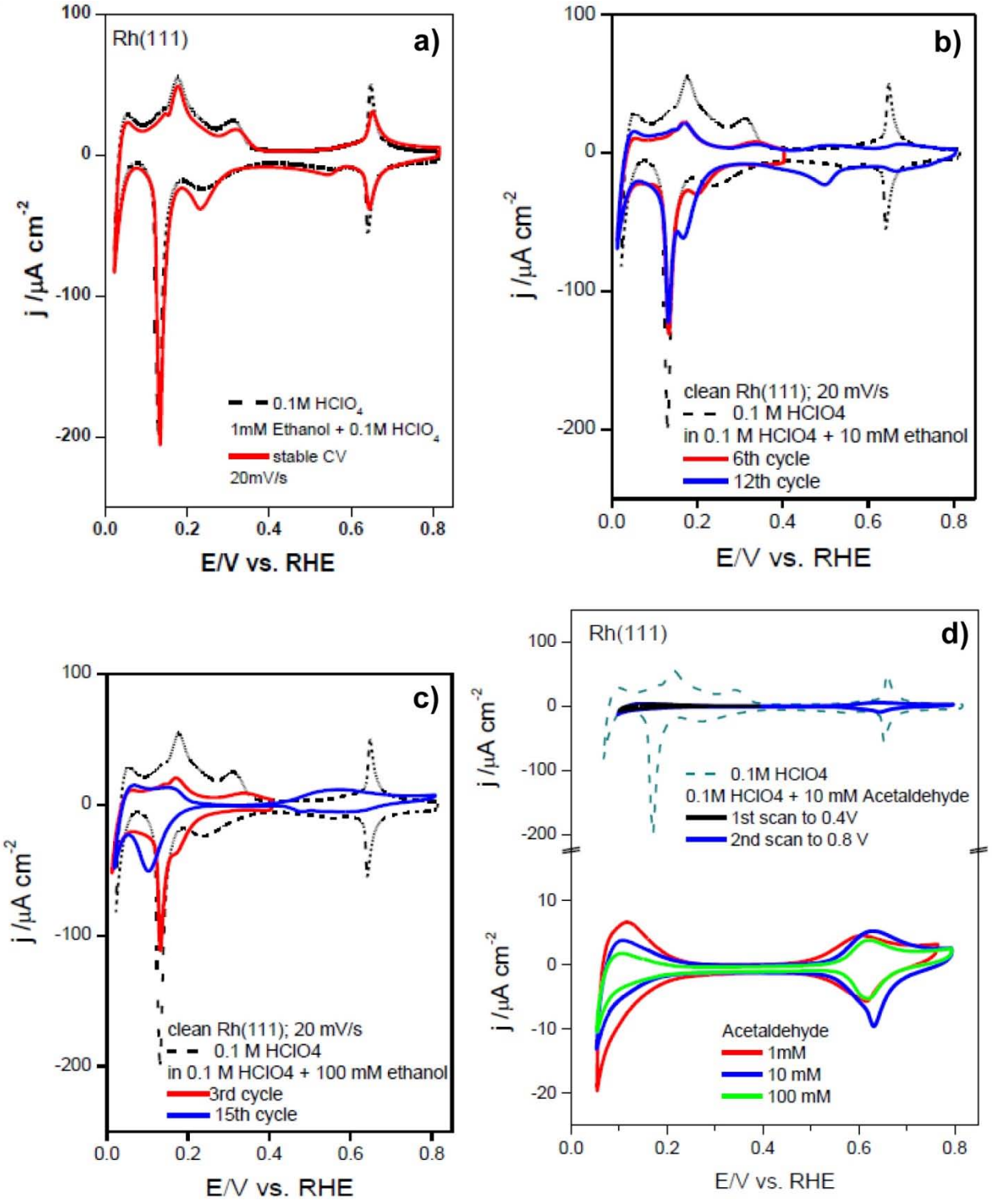

Figure 3.3 CV scans of the Rh(111) single crystal in both base electrolyte of 0.1M $HClO_4$ and ethanol/acetaldehyde containing electrolyte of 0.1M $HClO_4$ with different concentration of ethanol/acetaldehyde: (a) 1mM ethanol, (b) 10mM ethanol, (c) 100mM ethanol, (d) 1mM, 10mM, and 100mM acetaldehyde. Scan rate: 20mV/s. (With W.-P. Zhou)

Figure 3.3a shows CV scans of clean Rh(111) in both base electrolyte (0.1M $HClO_4$) and ethanol containing electrolyte (1mM ethanol + 0.1M $HClO_4$), and one can find the two CV curves are very similar. The hydrogen adsorption/desorption ($H_{ads/des}$) feature and the surface oxide formation/reduction feature preserved in ethanol containing electrolyte, indicating there was only minium ethanol adsorption or oxidation on Rh(111) when the concentration is low, i.e. 1mM. When the ethanol concentration was raised to 10mM (as shown in Figure 3.3b), one can find the $H_{ads/des}$ region shrunk, indicating part of Rh sites were covered with adsorbates from ethanol adsorption. In the oxidation region, the OH formation feature diminished, but there was no obvious current up to 0.8V from the oxidation of adsorbates formed at lower potentials. The CV scans were stable, as the 12^{th} scan was similar to the 6^{th} scan. When the ethanol concentration increased to 100mM (Figure 3.3c), $H_{ads/des}$ region in the 3^{rd} scan was similar to the one in Figure 3.3b, indicating a low saturated coverage of ethanol adsorbates was formed. In the oxidation region, there was a weak oxidation current, suggesting the low EOR activity of Rh(111) electrode. It was worth to notice that the CV was changing with scans, in the 15^{th} scan $H_{ads/des}$ showed further shrinkage and the potential shifted to a lower value compared to the 3^{rd} scan.

DFT studies [129] of ethanol decomposition on Rh(111) showed the dehydrogenative adsorption of ethanol was the rate limiting step of ethanol decomposition on Rh(111) with a high barrier to overcome, and Rh could be poisoned by ethanol decomposition products, i.e. CO and C. Experimentally, the first dehydrogenation forming CH_3CH_2O* occured on Rh(111)at ~220K [152], and the reaction could happen on Pt(111) at 180K [153]. Our electrochemical observation showed good consistency with previous report, Rh(111) showed low EOR activity, due to both of the insufficient ethanol adsorption and the lack of capability to remove the adsorbates.

CV scans of Rh(111) in acetaldehyde containing electrolyte (Figure 3.3d) shows distinct

difference from Figure 3.3a-c with a diminished $H_{ads/des}$ feature, indicating strong adsorption of acetaldehyde on Rh(111). In the oxidation region, there was no obvious oxidation current, and the current was independent of reactant (acetaldehyde) concentration. Hence, acetaldehyde adsorption on Rh(111) formed strong adsorbates and poisoned the surface.

The Rh(111) electrode was further modified by depositing Pt and/or SnO_2 nanoclusters. Figure 3.4 indicates Pt/Rh(111) electrode showed an EOR onset potential of about 0.58V, which was ca. 0.2V more positive compare to Pt(111). We propose that the smaller lattice parameter of Rh compared to that of Pt causes a contraction in the Pt monolayer, and therefore a delayed formation of surface oxidation [134] and a decreased capability to remove poison CO species. Hence, Rh was not chosen as a support to place Pt monolayer in later studies, because of the lattice contraction effect and also its high price. The ternary Pt-SnO_2/Rh(111) electrode possessed the best EOR activity compared to Pt/Rh(111) and bare Rh(111).

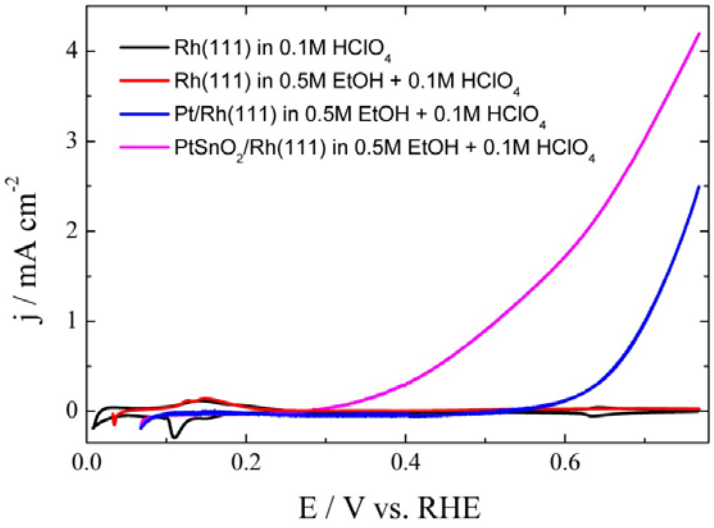

Figure 3.4 Oxidation of ethanol on Rh(111), Pt/Rh(111) and PtSnO_2/Rh(111) in 0.1 M $HClO_4$ with 0.5 M ethanol; sweep rate 20 mV/s.

3.1.2 Carbon-Supported Pt-Rh-SnO_2 Electrocatalyst by a Cation-Adsorption-Reduction-Adatom-Galvanic-Displacement Method

The Rh-SnO_2/Pt(111) and Pt-SnO_2/Rh(111) model catalysts have demonstrated the ternary catalyst have high activity and selectivity towards C-C bond splitting. For the synthesis of the carbon-supported ternary Pt-Rh-SnO_2 nanoparticle electrocatalyst we developed a cation-adsorption-reduction-galvanic-displacement synthetic method that facilitated the controllable deposition of metal atoms on oxide surfaces. Using this method, we placed Pt and Rh atoms on SnO_2 to synthesize the ternary Pt-Rh-SnO_2/C electrocatalyst. The choice of SnO_2 nanoparticles as substrates to place Pt and Rh atoms is because it is expected that the oxide support could: (i) further reduce the total content of noble metals; (ii) modify the electronic properties of Pt and Rh deposits to improve the EOR kinetics; (iii) chemisorb oxygen containing species such as OH that accelerate the oxidation of poison species formed on Pt sites.

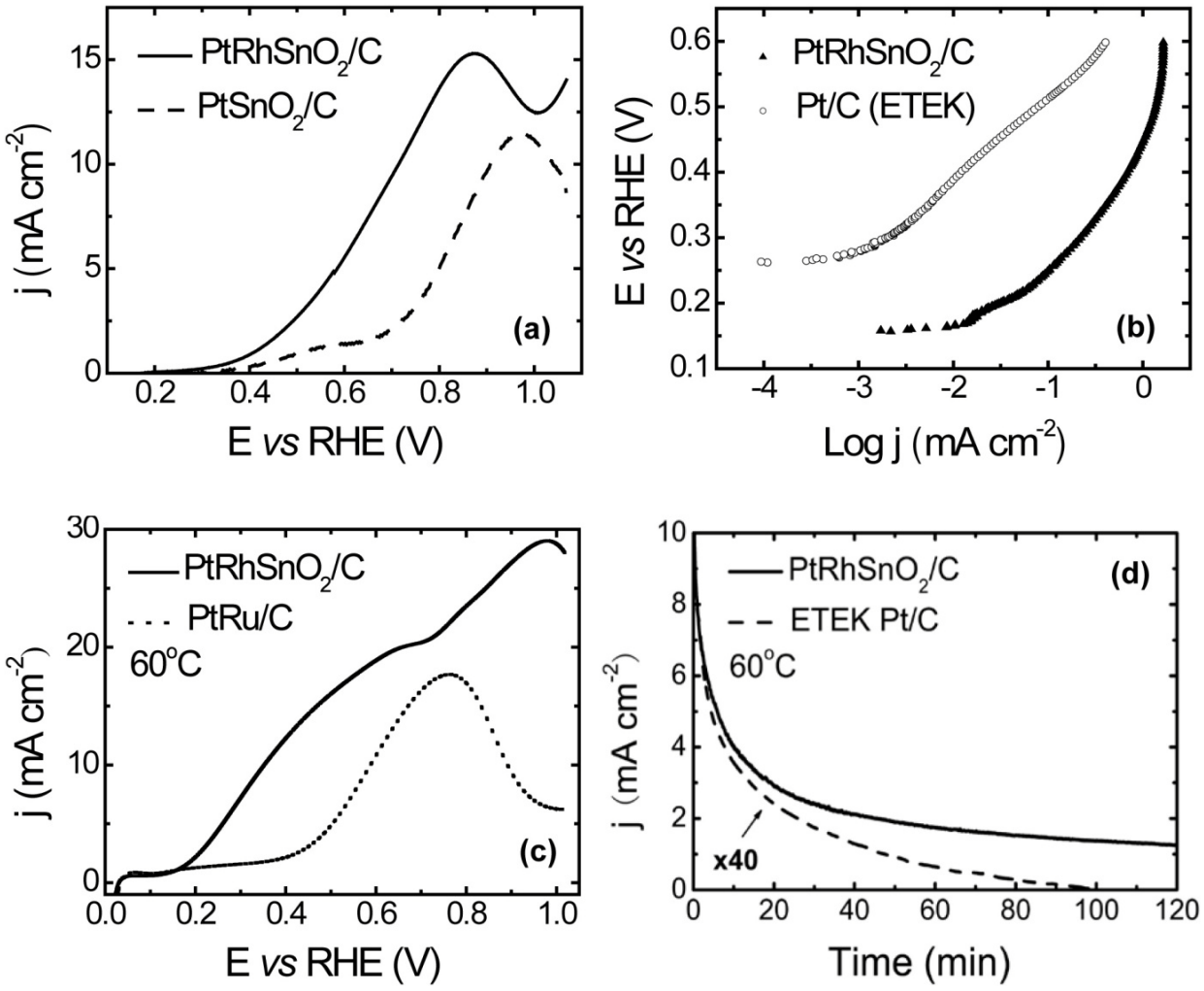

Figure 3.5 Current-potential and current-time polarization curves for comparing the activity of $PtRhSnO_2/C$ with several other catalysts for ethanol oxidation.
(a) Polarization curves for the oxidation of ethanol on $PtRhSnO_2/C$ and $PtSnO_2/C$ thin-film electrocatalysts deposited on a glassy carbon (GC) electrode. Electrocatalysts compositions: $PtRhSnO_2/C$ – ~ 30nmol Pt, 8nmol Rh and 60nmol SnO_2; $PtSnO_2/C$ – ~30nmol Pt and 60nmol SnO_2; electrode surface area is $0.2cm^2$; 0.1M $HClO_4$; 0.2M ethanol; sweep rate is 50mV/s.
(b) Quasi steady-state polarization curves for the oxidation of ethanol on $PtRhSnO_2/C$ and Pt/C (20% Pt on C from E-TEK Co.) electrocatalysts on GC electrode. Electrocatalysts compositions: $PtRhSnO_2/C$ - 25nmol Pt, 16nmol Rh and 25nmol SnO_2; Pt/C - 25nmol Pt; electrode surface area is $0.2cm^2$; 0.1M$HClO_4$; 0.5M ethanol; sweep rate is 1mV/s.
(c) Polarization curves for electrocatalysts for the oxidation of ethanol on $PtRhSnO_2/C$ and PtRu/C (20% PtRu with 1:1 atomic ratio on C E-TEK Co.) at 60ºC. Electrocatalysts compositions: PtRhSnO2/C – 25nmol Pt, 5nmol Rh and 20nmol SnO_2; PtRu/C: 25nmol Pt, Ru: 25nmol, other conditions as in (a).
(d) Chronoamperometry (CA) measurements of ethanol oxidation at 0.45V on $PtRhSnO_2/C$ and Pt/C catalysts at 60°C in 0.5M C_2H_5OH in 0.1 M $HClO_4$. The current for Pt/C is multiplied by 40.

Figure 3.5a shows a considerably higher current of ethanol oxidation, i.e. higher activity,

for the ternary $PtRhSnO_2/C$ electrocatalyst than that of $PtSnO_2/C$, highlighting the importance of the Rh component. Additional tests shows that the activity of $RhSnO_2/C$ (no Pt) electrocatalysts was low (discussed later). Thus, both Pt and Rh at SnO_2 are necessary for an active electrocatalyst. Figure 3.5b shows the comparison between $PtRhSnO_2/C$ electrocatalyst and a commercial Pt/C electrocatalyst lacking Rh and SnO_2 in quasi-steady-state conditions at a sweep rate of 1mV/s. At 0.3 V, the current density for the ternary electrocatalyst is more than two-orders-of magnitude larger than that of the commercial Pt/C electrocatalyst. The Tafel slope of ~120mV can be obtained from that plot, indicating that the first charge transfer is the rate-determining step. Figure 3.5c shows a very high rate of ethanol oxidation of the $PtRhSnO_2/C$ (current density of 7.5 mA/cm^2) at 60°C, *viz.*, the temperature close to that at which DEFCs operate (60-80°C) at the potential of 0.3V. At this same potential, PtRu/C, the common electrocatalyst for ethanol oxidation, has a negligible current density. The chronoamperometric measurements (Figure 3.5d) confirm the high activity of the $PtRhSnO_2/C$ electrocatalyst, which is ~100 times higher than the corresponding activity of Pt/C.

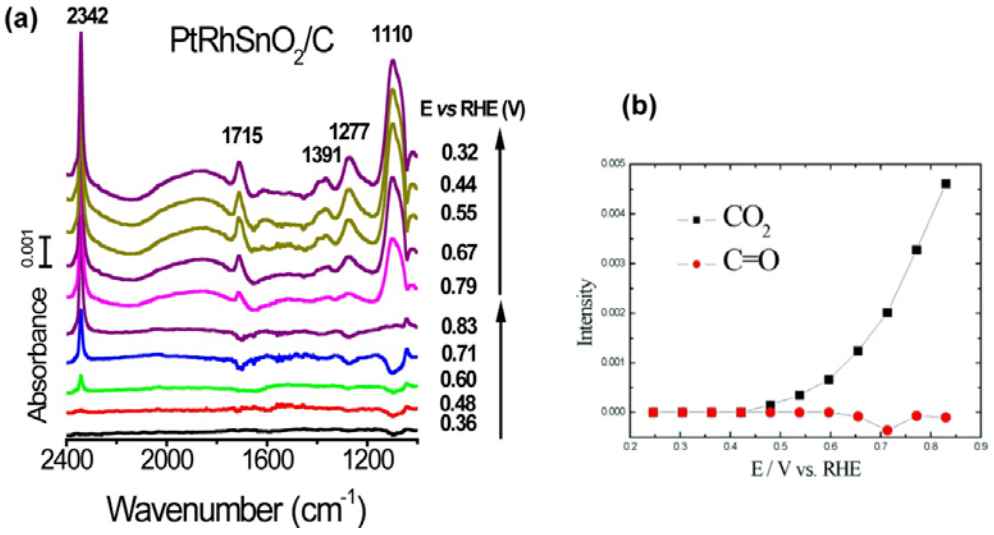

Figure 3.6 (a) *In situ* IRRAS spectra during EOR on $PtRhSnO_2/C$. Electrolyte: 0.1M ethanol in 0.1M $HClO_4$; scan rate: 1mV/s; reference spectrum was taken at 0.05V vs RHE in the same electrolyte. (b) Variation of intensities of CO_2 ($2342cm^{-1}$) and C=O ($1715cm^{-1}$) determined from the IRRAS spectra.

Figure 3.6a shows *in situ* IRRAS spectra collected from $PtRhSnO_2/C$ electrocatalyst during ethanol electron-oxidation, and it can be seen that the ternary nanoparticle electrocatalyst can oxidize ethanol to CO_2 with high efficiency, as indicated by the much higher intensity of CO_2 band ($2340cm^{-1}$) with respect to that of the carbonyl band ($1715cm^{-1}$) from byproducts (acetic acid and/or acetaldehyde).

We determined the structural and electronic properties of PtRhSnO2 electrocatalyst and their potential dependence using *in situ* the x-ray absorption near edge structure (XANES) and extended x-ray absorption fine structure (EXAFS) techniques, and combined them with data obtained by transmission electron microscopy (TEM) and inductively coupled plasma (ICP) analysis. Figures 3.7a and 3.7c shows the Rh K-edge and Pt L3 edge XANES spectra for $PtRhSnO_2/C$, respectively obtained in the potential region from 0.21-1.11V in 1 M $HClO_4$ solution. The main absorption peak at the Rh and Pt edges have a very small potential dependence, indicating that the surfaces were only slightly oxidized, unlike the process that occured with the pure Rh phase. It is likely that OH, that was present on SnO_2 surface in aqueous solutions, causes a shift in surface oxidation of Rh and Pt (Rh-, or Pt-OH formation) to positive potentials induced by the OH-OH repulsion [154]. The adsorption and dissociation of H_2O on SnO_2 has been the subject of a number of studies [155-156]. On oxide surfaces water molecules are adsorbed on metal ions with the transfer of one of the protons to a neighboring oxygen atom. A “carpet” of OH groups mediates the interaction between the oxide surface and the environment. Oxide surfaces behave as non-polarizable interfaces whose electrical state is controlled by the solution’s pH while surface charge of oxides do not depend on the electrode potential.

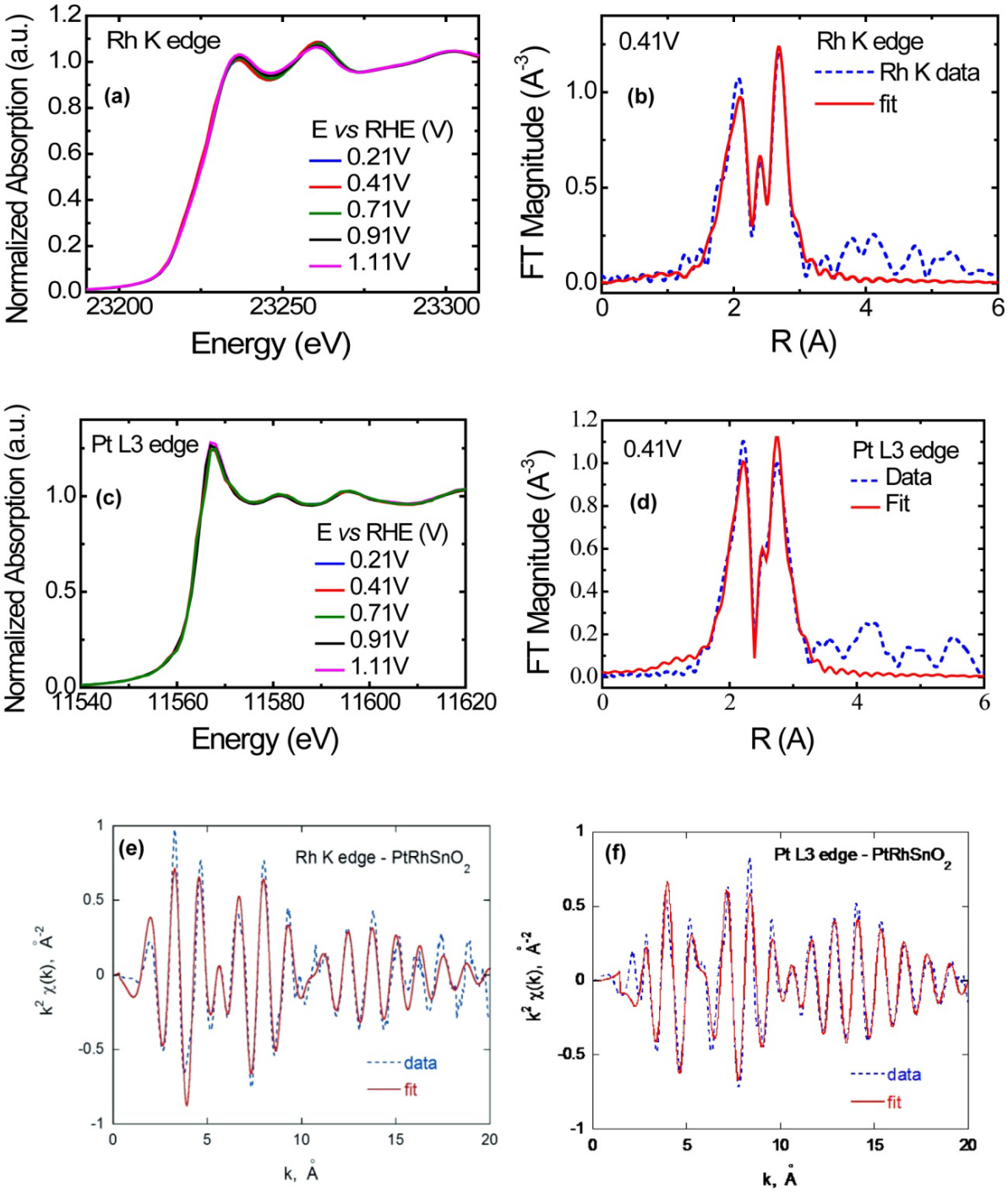

Figure 3.7 *In situ* XANES and EXAFS spectra for determining the structural and electronic properties of $PtRhSnO_2$/C electrocatalyst.
(a), (c) XANES spectra of the Rh K-edge and Pt L3-edge for the $PtRhSnO_2$/C electrocatalyst in 1M $HClO_4$ solution as a function of potential, respectively. Potential settings are indicated in the graph.
(b), (d) Fourier transform magnitudes of the $PtRhSnO_2$/C electrocatalyst in 1M $HClO_4$ solution as a function of potential at the Rh K-edge and Pt L3-edge.
Raw data and fitting in k space of $PtRhSnO_2$/C electrocatalyst under applied potential 0.41V vs. RHE. (e) Rh K edge; (f) Pt L3 edge.

EXAFS spectroscopy measurements with input from TEM studies provide detailed information on the intra-particle composition and degree of alloying of Pt and Rh. Figures 3.7b and 3.7d display the Fourier transform magnitude of the EXAFS data that corresponds to the above XANES spectra at 0.41 V and theoretical signals that are fit to the Rh K-edge and Pt L3-edge data concurrently, by applying physically reasonable constraints. The results of fittings in the k-space of Rh and Pt edges are shown in (Figure 3.7e&f). Measurements of metal-metal (Rh-Pt and Pt-Rh) coordination numbers N_{Rh-Pt} and N_{Pt-Rh} allow us to obtain the average composition of the nanoparticles: $x(Pt)/x(Rh) = N_{Rh-Pt}/N_{Pt-Rh} = 2.1 \pm 0.3$, in a reasonably good agreement with the ICP data $x(Pt):x(Rh) = 1.5 \pm 0.2$. The absolute values of these coordination numbers indicate the same size range (1-3 nm) as obtained by TEM. The obtained Pt-metal and Rh-metal coordination numbers $N_{Pt-M} = N_{Pt-Pt}+N_{Pt-Rh}$ and $N_{Rh-M} = N_{Rh-Rh}+N_{Rh-Pt}$ have similar values (9.5±0.8 and 10.8±0.8, respectively), consistent with homogeneous distribution of Pt and Rh throughout the particles. Additionally, since the N_{Pt-Pt}/N_{Pt-Rh} and N_{Rh-Pt}/N_{Rh-Rh} ratios are found to be consistent, within the uncertainties, with the ratios of Pt and Rh concentrations obtained independently by EXAFS and ICP we conclude that the Pt and Rh form quasi-random alloy. An independent additional evidence toward that conclusion is the similarity between the Pt-Pt, Pt-Rh and Rh-Rh bond lengths found by our EXAFS analysis: 2.743±0.003Å, 2.725±0.004Å, and 2.705±0.005Å, respectively, i.e., characterized by a much smaller spread than between pure Pt (2.775 Å) and Rh (2.689 Å).

3.1.3 DFT Calculations on RhPt/SnO_2(110) Model Catalyst (with P. Liu)

We carried out a DFT investigation of ethanol decomposition over a model RhPt/SnO_2(110) electrocatalyst to obtain additional information on this reaction, in particular on splitting the C-C bond and the roles of Rh, Pt and SnO_2. Rh, at a coverage of 1/4ML on SnO_2(110) generates a metal chain bridging Sn at a coordinatively unsaturated site (Sn_{cus}) and oxygen at bridge sites [162]. The binding energy corresponds, respectively, to -2.82eV/Pt atom and -2.95eV/Rh atom. The co-deposition of Rh and Pt forms an alloy chain along a Sn_{cus} row (Figure 3.8a) with the binding energy of a -3.22eV/metal atom. Figure 3.8a shows water strongly adsorbs on SnO_2 sites undergoing the spontaneous breakage of one of the O-H bonds. In contrast, the Pt or/and Rh sites are much less active and the water molecule stayed intact. Therefore, we assume that SnO_2 sites were saturated by H_2O/OH under the electrochemical condition, thereby weakening the interaction of water with Pt or Rh, which is significant for nanoparticles containing low-coordination sites, that makes them available for ethanol oxidation (Figure 3.8b).

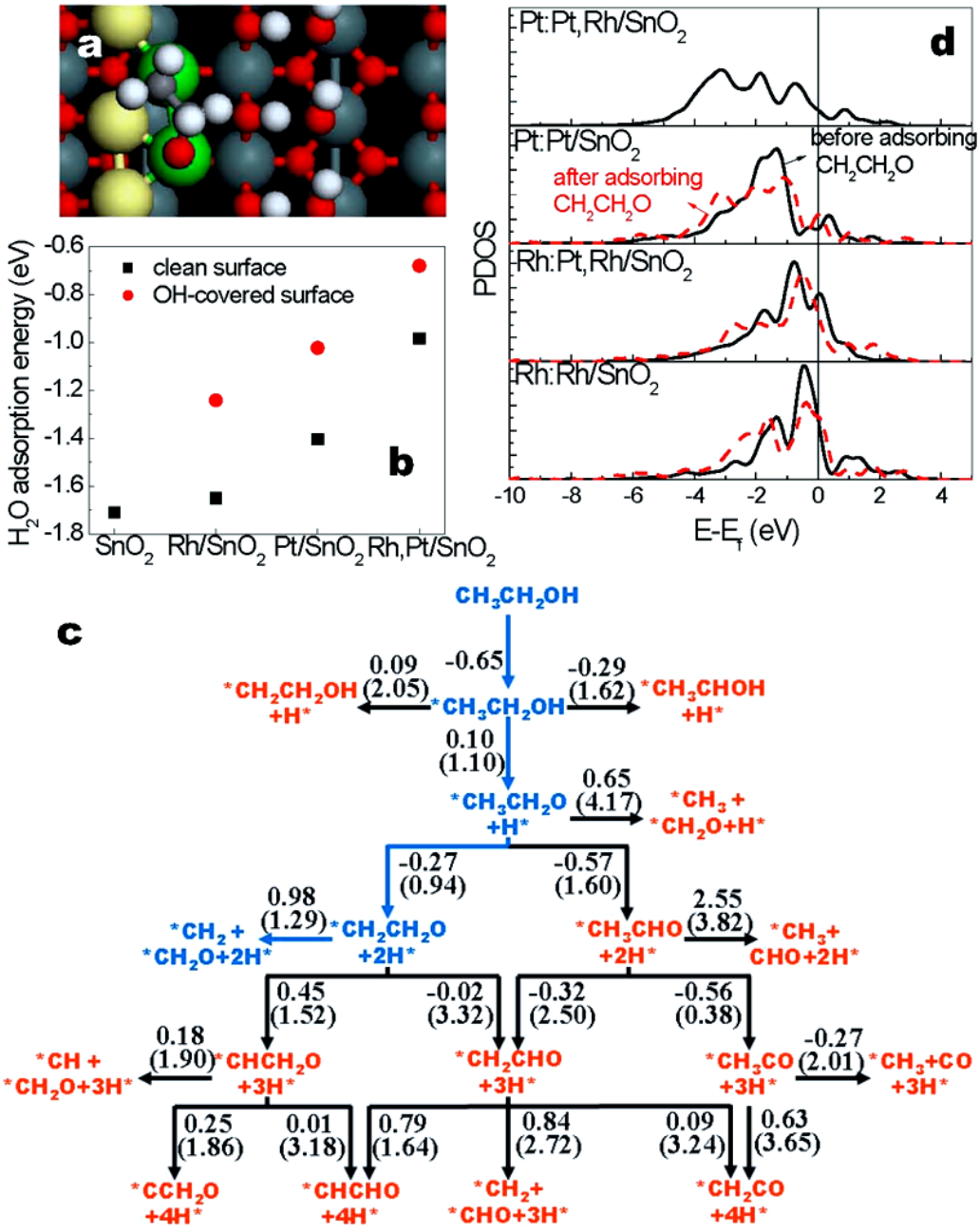

Figure 3.8 Density functional theory investigations of ethanol oxidation on a $RhPt/SnO_2(110)$ surface.
(a) Optimized geometry of CH_2CH_2O adsorption on a $RhPt/SnO_2(110)$ surface. Sn: large grey; Pt: large yellow; Rh: large green; C: small grey; O: small red; H: small white).
(b) DFT calculated adsorption energies of water on the surfaces of $SnO_2(110)$, $Rh/SnO_2(110)$, $Pt/SnO_2(110)$ and Rh,$Pt/SnO_2(110)$ with and without water saturates the SnO_2 sites.
(c) Calculated possible pathways for the C-C bond breaking of ethanol on the $RhPt/SnO_2(110)$ surface. The reaction energies and parenthesized barriers in the figure are expressed in eV.
(d) Calculated partial density of states (PDOS) of d-state of Pt or Rh on the $Rh/SnO_2(110)$, $Pt/SnO_2(110)$ and $RhPt/SnO_2(110)$ surfaces. The solid lines correspond to a bare surface, and the dashed lines represent the case after interacting with CH_2CH_2O.

Further, we considered the possible reaction pathways from gaseous ethanol to C-C bond splitting. Figure 3.8c include the calculated energetics for ethanol decomposition on the $RhPt/SnO_2(110)$ surface with dissociated water saturating the oxide sites. Among all the possibilities, the following is the optimal pathway to C-C bond breaking:

$$*CH_3CH_2OH \rightarrow *CH_3CH_2O+H* \rightarrow *CH_2CH_2O+2H* \rightarrow *CH_2+*CH_2O+2H* \quad (3.1)$$

Here, all adsorbates preferre the pure Rh sites except atomic hydrogen that favors the Rh-Pt hybrid hollow sites. Thus, ethanol decomposition on $RhPt/SnO_2(110)$ occurrs *via* an oxametallacyclic conformation (CH_2CH_2O, Figure 3.8a) that entails direct C-C bond cleavage with a reasonable barrier of 1.29eV. In contrast, the formation of acetaldehyde (CH_3CHO) is not favored, having the barrier higher by 0.66eV, and the barrier for C-C bond breaking in CH_3CHO is highly activated requiring 3.82eV (Figure 3.8c). This agrees with the effect of Rh addition at metal/gas interface [129, 158-160], showing the preference for the CH_2CH_2O conformation. In addition, our calculations show that the barrier to CH_2CH_2O generation decreases in the following sequence: Pt/SnO_2 (1.53eV) > Rh/SnO_2 (0.98eV) $PtRh/SnO_2$ (0.94eV). Thus, the presence of Rh is essential for the formation of CH_2CH_2O. In accordance with the *in situ* IRRAS study, the splitting of the C-C bond does not occur through the pathway involving acetaldehyde. Its negligible coverage, and the evidence of CO involvement in the reaction, mean that this catalyst facilitates a direct splitting of the C-C bond, substantiated by our DFT calculations. Spectra in Figure 3.2 and 3.6, however, do not show evidence for oxametallacycles. The bands that are accessible under our conditions are week (ν(C-H), w(C-H_2)), while CH_2O had the C-O bond parallel to Pt surface, which was not IR active [161] and cannot be seen.

We also calculated the partial density of states (PDOS) of the d-state of the supported Pt and Rh atoms on $SnO_2(110)$ before and after interacting with CH_2CH_2O to gain further

information on bond formation. As Figure 3.8d illustrated, the metal-CH_2CH_2O reaction is dominated by back-donation from the π orbitals of CH_2CH_2O to the d orbital of the metal atoms. Accordingly, Rh obviously is a better choice to stabilize metal-CH_2CH_2O complex than was Pt, which have a high-lying d-band and more unoccupied d-states. In addition, the mixture of Rh and Pt facilitates the occurrence of more empty states of Rh than did Rh alone on SnO_2. The strong interaction between Pt and Rh is accompanied by an electron transfer from Rh to Pt, and more d-states of Rh become available above the Fermi level. Concurrently, the d-states of Pt shifts away from the Fermi-level causing a lower activity of Pt in $PtRh/SnO_2$ than Rh, or even Pt in Pt/SnO_2. Our calculations show that Pt in $PtRh/SnO_2$ weakly interacts with ethanol, and the other dissociated oxygenates and hydrocarbons. It is active only for dissociated H. Thus, the results also imply that slightly increasing the amount of Pt would empty more d-states of Rh, thereby improving the activity for ethanol oxidation, as inferred from our experimental data.

3.1.4 Summary

We synthesized a ternary $PtRhSnO_2/C$ electrocatalyst by depositing platinum and rhodium atoms on carbon-supported tin dioxide nanoparticles that is capable of oxidizing ethanol with high efficiency. This electrocatalyst holds great promise for resolving the impediments to developing practical DEFCs. It effectively splits the C-C bond in ethanol at room temperature in acid solutions, so facilitating its oxidation at low potentials to CO_2, which has not been achieved with existing catalysts. Our experiments and density functional theory (DFT) calculations indicate that the electrocatalyst's activity is due to the specific property of each of its constituents induced by their interactions. These findings help understanding the high activity of Pt-Ru for

methanol oxidation and the lack of it for ethanol oxidation, and point to the way to accomplishing the C-C bond splitting in other catalytic processes.

3.2 Carbon-Supported Ternary Pt-Rh-SnO_2 Electrocatalysts by a Facile Polyol Synthesis

3.2.1 Carbon-Supported Pt, Rh, PtRh, Pt-SnO_2, Rh-SnO_2 and Pt-Rh-SnO_2 Nanoparticle (NP) Catalysts [162]

In the previous section we have demonstrated the ternary Pt-Rh-SnO_2 electrocatalyst can oxidize ethanol to CO_2 at low overpotentials and ambient temperature from both single crystal based model catalysts and carbon-support nanoparticle catalysts studies. In this section, we employed a facile polyol synthesis approach to prepare carbon-supported Pt, Rh, SnO_2, PtRh, $PtSnO_2$, $RhSnO_2$, and $PtRhSnO_2$ nanoparticles electrocatalysts. We used a combination of electrochemical and *in situ* spectroscopic means to gain a fundamental understanding of the synergistic effect between the three constituents: Pt, Rh and SnO_2. We demonstrate that $PtRhSnO_2$ shows best catalytic activity and highest capability in C-C bond cleavage. Very interestingly, byproducts, namely acetaldehyde and acetic acid, are the major EOR products on pure Rh; however, CO_2 is the major EOR product on $RhSnO_2$, despite the fact that $RhSnO_2$ gives lowest current among the six electrocatalysts. $PtSnO_2$ shows enhanced activity with respect to pure Pt; but it only facilitates partial oxidation to acetic acid while the total oxidation pathway is inhibited. PtRh gives a moderate improvement on C-C bond splitting compared to pure Pt and a lowered overall activity. The results establish the role each one plays in the ternary electrocatalyst and shed a light on the designing of active electrocatatlyst oxidizing ethanol to CO_2.

3.2.1.1 Physical Characterization

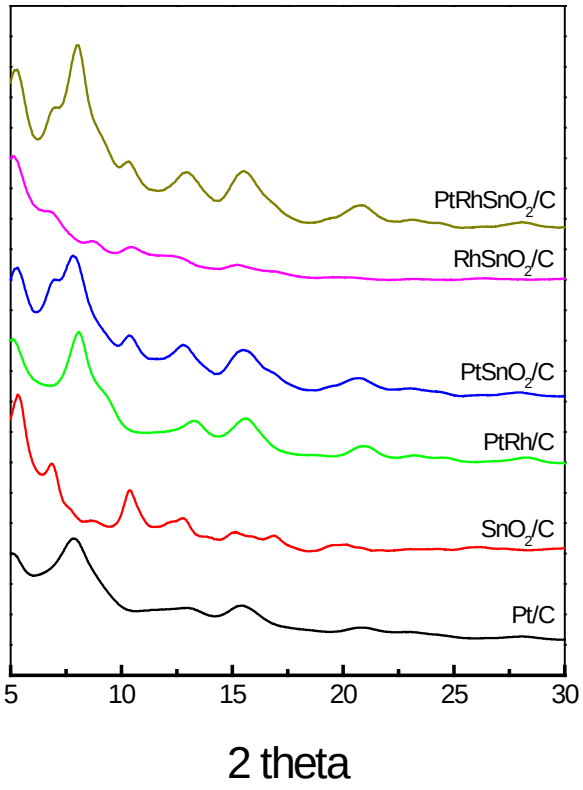

Figure 3.9 XRD profiles of the nanoparticle electrocatalysts prepared by the polyol method: Pt/C, SnO_2/C, PtRh/C, $PtSnO_2$/C, $RhSnO_2$/C, and $PtRhSnO_2$/C.

Figure 3.9 shows XRD spectra of the carbon-supported nanoparticle (NP) electrocatalysts: Pt, SnO_2, PtRh, $PtSnO_2$, $RhSnO_2$, and $PtRhSnO_2$. All the diffraction peaks are clearly broadened, suggesting the formation of very small size or highly amorphous particles from the polyol syntheses. Pt and Rh diffraction peaks cannot be separated in the XRD patterns of PtRh and $PtRhSnO_2$. The PtRh(111) peak positions in PtRh and $PtRhSnO_2$ are in between of Pt(111) peak (from Pt and $PtSnO_2$ XRD patterns) and Rh(111) peak (from $RhSnO_2$ XRD pattern), indicating the formation of Pt-Rh binary alloy, which is consistent with Pt-Rh binary phase diagram. All the XRD peaks could be assigned to Pt, Rh, PtRh alloy or SnO_2, hence the formation of a ternary PtRhSn alloy is unlikely. Similarly, the existence of metallic Sn, separately or in Sn-containing

binary alloys (PtSn or RhSn), is not confirmed. Most probably, the binary PtRh NPs consist of uniform Pt-Rh alloy, $PtSnO_2$ NPs are composed of metallic Pt and oxide SnO_2 NPs, and $RhSnO_2$ are comprised of metallic Rh and oxide SnO_2 NPs. In the ternary $PtRhSnO_2$/C catalyst, it is very likely that Pt and Rh form a uniform alloy, while Sn exists only in SnO_2 phase.

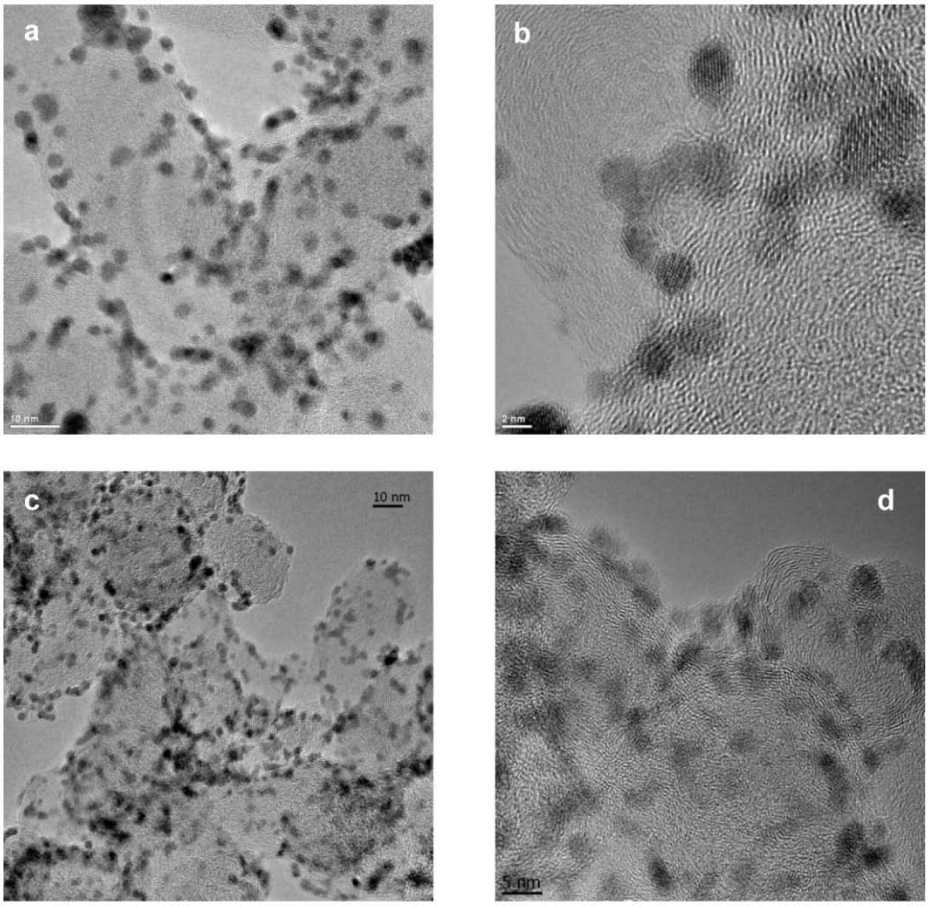

Figure 3.10 Typical TEM images of nanoparticle electrocatalysts: (a) & (b) Pt/C, (c) & (d) $PtRhSnO_2$/C.

Figure 3.10 displays typical TEM images of Pt/C and $PtRhSnO_2$/C electrocatalysts made from polyol syntheses. One can find the electrocatalysts are composed of fine nanoparticles with an average size of about 2nm uniformly dispersed over amorphous carbon support.

3.2.1.2 Electrochemical Measurements

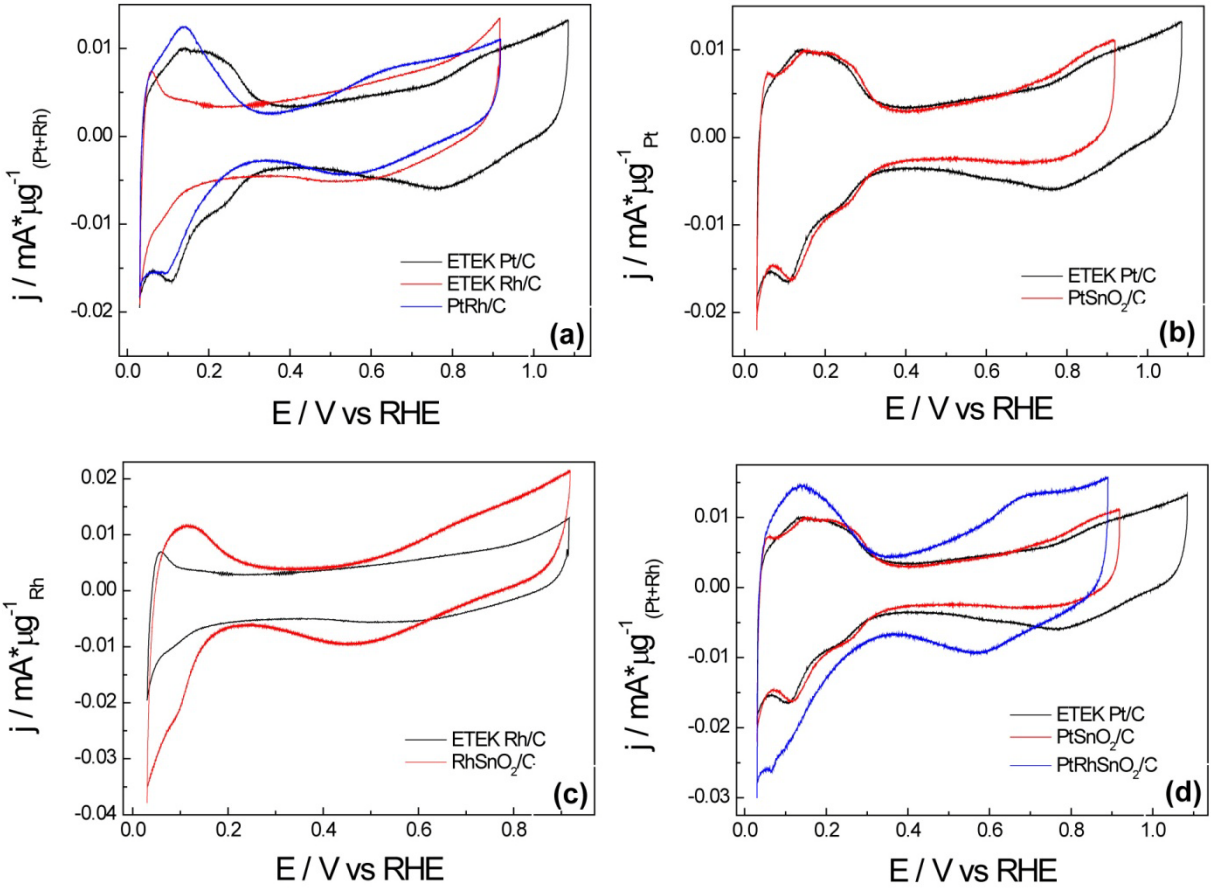

Figure 3.11 CV scans of all NP catalysts in base electrolyte of 0.1M $HClO_4$: a) Pt/C, Rh/C and PtRh/C; b) Pt/C and $PtSnO_2$/C; c) Rh/C and $RhSnO_2$/C and d) Pt/C, $PtSnO_2$/C and $PtRhSnO_2$/C. scan rate: 10mV/s; all current densities are normalized to total noble metal loading (Pt+Rh).

Figure 3.11a shows CV scans of Pt/C, Rh/C and the binary PtRh/C electrocatalysts in 0.1M $HClO_4$ with a scan rate of 10mV/s. The positive limits of potential scans in this study were set to be 0.9V to avoid dissolution of Rh and Sn in all electrocatalysts except for pure Pt. By comparing CV of PtRh with CVs of pure Pt and Rh, one can find the electrochemical behaviors (i.e. the onset potentials of hydrogen adsorption/desorption ($H_{ads/des}$) and surface oxide formation/reduction ($Oxide_{form/red}$)) of PtRh alloy is in between of that of pure Pt and Rh. The uniformity of the binary alloy can be confirmed using techniques like XRD and EXAFS fitting

(shown later), but these techniques provided bulk composition information that does not necessarily correspond to the surface composition. However, surface segregation of one component (Pt or Rh) leading to differences in surface and bulk compositions is expected to be very small in the case of PtRh alloy because of the very close enthalpy of vaporization values of the two elements [73, 163]. The single surface oxide reduction peak shown in the voltammogram of PtRh indicates the formation of homogeneous alloy surface. The $H_{ads/des}$ profile of PtRh is characterized by one single peak, compared to two peaks in pure Pt, and the potential shifts to a more negative value. PtRh alloy surface oxidation commences at more negative potential with respect to that of pure Pt, and potentially the oxygen-containing species could facilitate CO removal and enhance activity based on a bi-functional mechanism.

CVs of Pt/C and $PtSnO_2$/C are given in Figure 3.11b, and the two curves show almost the same characteristics in hydrogen underpotential deposition (UPD) region, which confirms the binary $PtSnO_2$ catalyst consisted of Pt metallic phase and SnO_2 oxide phase while the PtSn alloy formation was unlikely. One can find surface oxidation of $PtSnO_2$ arises at a more negative potential than that of pure Pt. This effect is attributed to the primary oxide (M-OH) spillover from SnO_2 to neighboring Pt sites causing an early oxidation on Pt. Similar effects have been reported on many oxide-supported catalysts [169].

Figure 3.9c displays the CV scans of Rh/C and $RhSnO_2$/C. The two electrocatalysts show big difference of surface area despite the same Rh loading, and it is due to the larger particle size of commercial ETEK Rh/C than $RhSnO_2$/C synthesized by polyol method. The -OH transfer from SnO_2 to Rh could account for the more distinctive feature of surface oxide formation-reduction on $RhSnO_2$ as well.

Figure 3.11d includes CVs of Pt/C, $PtSnO_2$/C and $PtRhSnO_2$/C. The large single peak in

hydrogen UPD region and the more negative $Oxide_{form/red}$ potential in the ternary $PtRhSnO_2/C$ compared with $PtSnO_2/C$ are consistent with what was observed earlier from the CV of PtRh compared to that of pure Pt.

In order to evaluate the activities of these catalysts for ethanol oxidation reaction, anodic polarization scans were carried out on all electrocatalysts in ethanol containing solution with a scan rate of 10mV/s (shown in Figure 3.12).

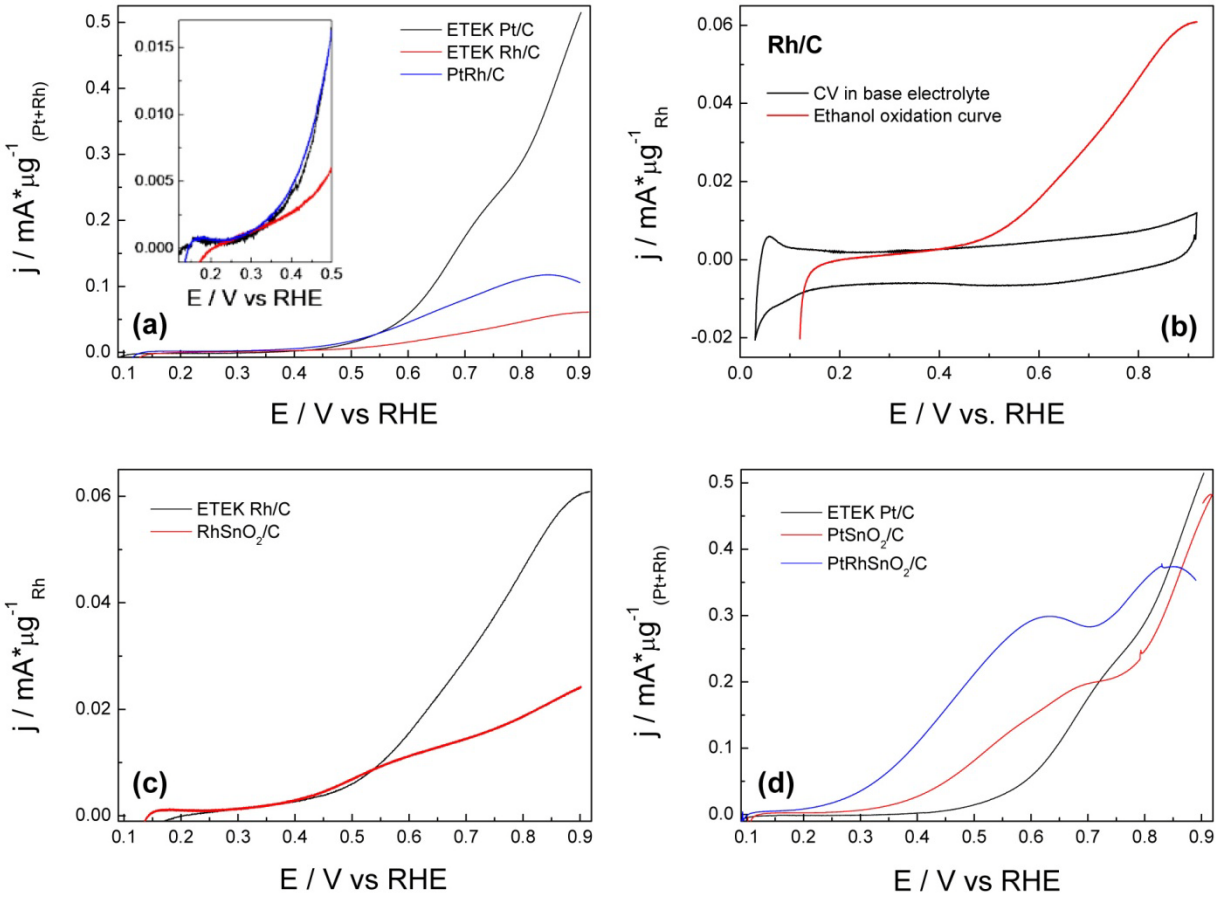

Figure 3.12 Anodic polarization curves in ethanol-containing electrolyte of all electrocatalysts: a) Pt/C, Rh/C and PtRh/C; b) Rh/C with a CV scan in base electrolyte; c) Rh/C and $RhSnO_2/C$ and d) Pt/C, $PtSnO_2/C$ and $PtRhSnO_2/C$. 0.5M EtOH + 0.1M $HClO_4$; scan rate 10mV/s; all current densities are normalized to total noble metal loading (Pt+Rh).

Pure Rh gave a much lower current yield compared to pure Pt (Figure 3.12a), and the two possessed similar reaction onset potential, ca. 0.45V. On Pt, the insufficient activity at potentials

lower than 0.45V is attributed to the blocking of active sites by poisoning species like CO formed from ethanol dissociative adsorption, and the subsequent increase of activity is due to CO removal because of surface oxide formation. The lack of activity on Rh nanoparticles is consistent with our results gained from a well-ordered Rh(111) electrode (Section 3.1.2), and we attributes the low activity to the weak interaction of ethanol molecules and Rh sites, as well as the C and CO poison on Rh sites. PtRh alloy catalyst gave a EOR performance in between of pure Pt and Rh, and the results is consistent with literature [73, 163]. As indicated from earlier CV study, Rh could potentially provide a bi-functional effect because it is capable of activating water with formation of surface oxide species at potential ca. 250mV lower than Pt, but apparently alloying Pt with Rh activity reduced the overall activity. Our Rh(111) single crystal study demonstrated that it is rapidly poisoned by adsorbates from acetaldehyde, one of the major ethanol oxidation products from pure Pt. Hence, Rh sites in PtRh could be easily poisoned. In addition, we attribute the inhibitive influence of Rh on the activity of Pt to both geometric assemble effect and electronic factors. The adsorption and oxidation of one ethanol molecule require multiple active sites, and Rh present in the homogeneous alloy in a substantial amount certainly limits the number of neighboring Pt sites, adversely influencing the activity of the Pt component of the alloy. Moreover, in order for the combination reaction between the carbonaceous adsorbates resulted from ethanol adsorption and the surface oxygen species to proceed fast, either the adsorbates and the surface oxygen species must occupy neighboring adsorption sites, or unhindered surface diffusion of a least one of these species must be possible. It is suspected that surface oxygen species, which are necessary for further oxidizing carbonaceous adsorbates resulted from ethanol adsorption, on Pt are quite mobile; however, Rh can interfere with the surface diffusion of -OH bonded to Pt, thus, introducing a transport-type

limitation. The electronic interaction of Pt and Rh need to be considered as well, because the back donation from Rh d-band electrons to Pt causes a filling of Pt d-band and a lowering of its reactivity.

Figure 3.12b shows CV scans of Rh/C in both base electrolyte and ethanol containing electrolyte. One can find Rh nanoparticles exhibit higher EOR activity compared to the well ordered Rh(111) surface, and it is likely that the defect sites and high index surfaces [165-171] on Rh nanoparticles play a role in enhancing EOR activity.

Figure 3.12c compares polarization curves from Rh/C and $RhSnO_2$/C. On the contrary to Pt/C and $PtSnO_2$/C, $RhSnO_2$ showed lower activity than pure Rh, despite the fact that the $RhSnO_2$ sample possessed much larger effective surface area compared to the commercial Rh catalyst (as indicated in Figure 3.11c). It is hypothesized that ethanol oxidation undergoes different reaction pathways on these two catalysts because of the apparent different kinetics.

Figure 3.12d includes polarization curves from Pt/C, $PtSnO_2$/C and $PtRhSnO_2$/C. $PtSnO_2$ shows enhanced EOR activity compared to pure Pt, and the promotional effect induced by SnO_2 is consistent with previous reported [143]. The addition of SnO_2 shifts reaction onset potential to ca. 0.25V and improves current yield. At potentials higher than 0.7V, $PtSnO_2$ gave lower current than pure Pt, and we ascribe it to the primary oxide spillover from SnO_2 to Pt causing the insufficient active sites for ethanol adsorption. It can be seen that the ternary catalyst further improves the performance of $PtSnO_2$/C with a more negative onset potential and higher current yield. Our previous study (Section 3.1) has shown the synergy between the three constituents causing the high capability to C-C bond splitting in the ternary electrocatalyst.

3.1.2.3 In situ IRRAS Study

In order to gain insight on the reaction mechanisms of ethanol oxidation reaction on these

electrocatalysts, we carried out *in situ* IRRAS studies to reveal the reaction intermediates and products distribution.

Figure 3.13 shows the recorded spectra on the nanoparticle electrocatalysts: Pt, Rh, PtRh, $PtSnO_2$, $RhSnO_2$, and $PtRhSnO_2$. The frequencies and band assignments are listed in Table 3.1. Figure 3.13a displays the IRRAS spectra collected from pure Pt nanoparticles. Carbon dioxide (CO_2), acetic acid (CH_3COOH) and acetaldehyde (CH_3CHO) are the main products of ethanol oxidation in acidic solution, and they can be clearly identified from Figure 3.11a. The positive-going peak near 2343cm^{-1} is attributed to the asymmetric stretch vibration of CO_2, the product of ethanol total oxidation pathway. The bipolar shape band at around 2030cm^{-1} is assigned to linear bond CO, one intermediate believed to be the precursor of CO_2 formation. It is claimed that ethanol does not adsorb on Pt surface at potentials lower than 0.1V [167], so it is CO free in our reference spectrum, which is collected at 0.05V, and formation of a growing band could indicate an accumulation of respective substance. One can see that the intensity of CO band follows a volcano-type behavior, with a low CO intensity at low potentials, and increases with higher potential up to a maximum value which is ca. 0.6V, and a subsequent decay due to increasing CO oxidation and/or decreasing CO formation (C-C bond splitting). CO_2 peak commences at 0.45V and keeps growing with applied potentials. The potential dependence of two peaks supports the proposal that on Pt CO is an intermediate leading to CO_2 formation. The fact that no obvious CO_L peak is seen at Rh/C (Fig. 3.13b) suggests that different absorbates are formed on Rh and Pt. IR spectra generated on Rh nanoparticles indicate that CO_2 is only produced in a very small amount and Rh alone is insufficient to oxidize ethanol to CO_2.

In both spectra (Figure 3.13 a and b) bands of CH_3COOH and CH_3CHO could be clearly indentified. The band located around 1705cm^{-1} can be assigned to the stretch vibration of the

C=O bond, found in both acetaldehyde and acetic acid. Both spectra show the C-O stretching vibration of acetic acid at 1280cm^{-1}, indicating the formation of CH_3COOH on both catalysts. The bands at 1350cm^{-1} and around 1396-1410cm^{-1} are assigned to CH_3 in-plane bending mode and OCO stretching of adsorbed acetate, respectively. These two bands are close and difficult to distinguish. The band observed at 933cm^{-1} is assigned to C-C-O asymmetric stretching of acetaldehyde. The co-existence of total oxidation product and partial oxidation products suggests that the parallel reaction pathways undergo on both Pt and Rh. One can find on both Pt/C and Rh/C electrocatalysts CH_3COOH is the major product. One difference is on Pt/C, the amount of CH_3CHO produced is much lower than CH_3COOH, and the result is consistent with literature report [168]. It is claimed that in the thin-layer configuration and with ethanol concentration of 0.1M, CH_3CHO is likely to be re-adsorbed and be further oxidized to CH_3COOH and/or CO_2. While on Rh/C, there is considerable amount of CH_3CHO produced, and it is in good agreement with our previous finding that Rh is not active in oxidizing CH_3CHO (Figure 3.3). The insufficient capability to further oxidize CH_3CHO could suggest the lack of oxygen-containing species, because both the formation of CO_2 and CH_3COOH requires additional oxygen coupling, and this is consistent with our hypothesis that -OH formation is suppressed on Rh. The band at 1598cm^{-1} is the H-O-H deformation of adsorbed water molecules. The C=O stretching mode of adsorbed acetaldehyde and acetyl around 1620-1635cm^{-1} cannot be resolved because of the presence of the strong water band. The C-H wagging vibration in CH_3CHO, at 1108cm^{-1}, overlaps with the strong band at 1110cm^{-1} of ClO_4^-. The growing Cl-O band from ClO_4^- ions is the consequence of its accumulation in the thin layer cell to compensate the increasingly positive electrode potential.

Fig. 3.13c-e show *in situ* IRRAS spectra gained on the binary catalysts: $PtSnO_2$/C, PtRh/C

and $RhSnO_2$/C. As learned from the electrochemical measurements, SnO_2 improves catalytic activity of Pt, but from IR study we could find the production of CO_2 is actually lower compared with pure Pt. Pt-Sn has been reported as the best binary electrocatalyst for ethanol oxidation. It has been observed that on PtSn [131-132], the CO removal does happen in a potential lower than that on pure Pt; however, CO_2 yield on PtSn is lower than that on pure Pt, which is in agreement with our findings on $PtSnO_2$ that SnO_2 inhibits ethanol dissociative adsorption on Pt and only facilitates partial oxidation pathway.

Despite the fact that PtRh give lower current compared to pure Pt, PtRh show higher capability to split C-C bond than both pure Pt and Rh, as indicated by the stronger CO_2 peak (Figure 3.13 d). It highlights that both Pt and Rh are necessary for C-C bond cleavage.

Contrary to $PtSnO_2$, the addition of SnO_2 into Rh improved catalyst's capability to break C-C bond and CO_2 was the major EOR product on $RhSnO_2$, as indicated in Figure 3.13e. This is rather surprising because the SnO_2 actually tunes the reaction to different pathways in $PtSnO_2$ and $RhSnO_2$.

Infrared spectra on the ternary $PtRhSnO_2$/C catalyst are illustrated in Figure 3.11f, and one can find CO_2 is the major reaction product, which is in consistent with our previous results in Section 3.1. CO_2 is generated in a much larger quantity on $PtRhSnO_2$/C than that on $RhSnO_2$, and it is in agreement with our finding from electrochemical study that $PtRhSnO_2$/C has much higher EOR activity than that of $RhSnO_2$/C.

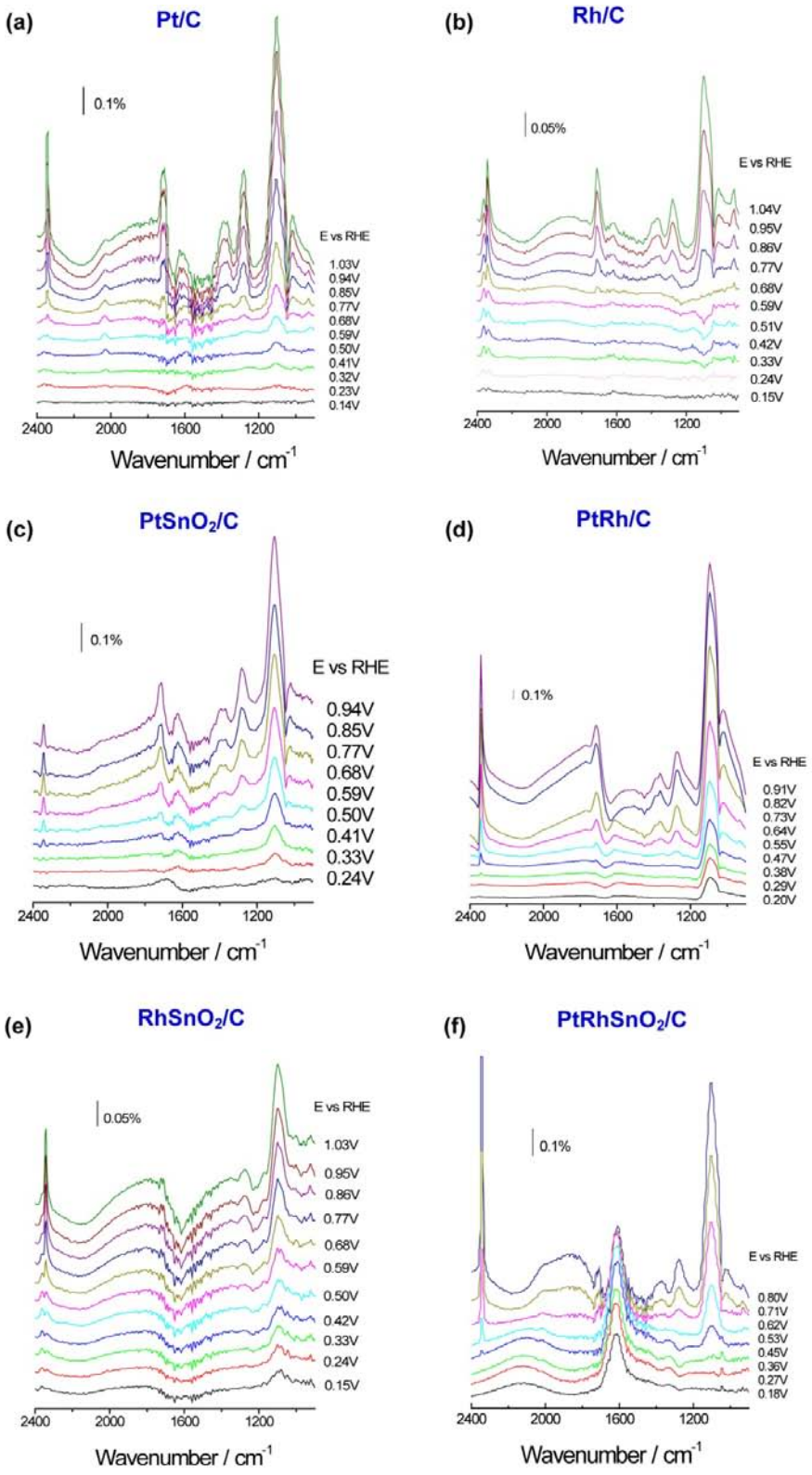

Figure 3.13 *In situ* IRRAS spectra collected during EOR on carbon-supported nanoparticle electrocatalysts: (a) Pt, (b) Rh, (c) $PtSnO_2$, (d) PtRh, (e) $RhSnO_2$, (f) $PtRhSnO_2$.

3.2.1.4 Summary

One motivation of our work was to gain further understanding of the synergistic effect between the three constituents in the ternary $PtRhSnO_2$ electrocatalyst, and the key factor determining its selectivity towards ethanol total oxidation.

We conducted systematic studies on Pt, Rh, PtRh, $PtSnO_2$, $RhSnO_2$ and $PtRhSnO_2$ nanoparticles, and we demonstrate that the activity of above catalysts on ethanol oxidation reaction (EOR) decreases in the order of: $PtRhSnO_2$ > $PtSnO_2$ > Pt > PtRh > Rh > $RhSnO_2$. The catalysts' selectivity towards ethanol total oxidation pathway is examined by *in situ* IRRAS studies and the results indicate CO_2 formation decreases in the order of: $PtRhSnO_2$ ~ $RhSnO_2$ > PtRh > Pt > $PtSnO_2$ ~ Rh.

3.2.1 Ternary Pt-Rh-SnO_2/C Electrocatalysts with Varied Pt:Rh:Sn Ratios [151]

This section presented a detailed study on a series of carbon-supported Pt-Rh-SnO_2 electrocatalysts with atomic Pt:Rh:Sn ratios of 3:1:x, where x varied from 2 to 6. A simple polyol synthesis route was employed to prepare the electrocatalysts, and through this method the active PtRh-SnO_2 interfaces can be created with each single catalyst nanoparticle. This was verified using several structure-sensitive techniques as described below. The structure and morphology of the catalysts were characterized by XRD and HR-STEM. Chemical composition was studied by ICP-OES EELS. The electrochemical properties were evaluated using CV and CA techniques. The selectivity of these electrocatalysts was determined using *in situ* IRRAS. At last *in situ* studies using the XANES and EXAFS revealed information on the structural and electronic properties of Pt-Rh-SnO_2/C electrocatalysts and their potential dependence.

3.2.2.1 Physical Chracterization

The effect of catalyst's composition, i.e. the ratio of Pt:Rh:Sn, has been investigated. Five different Pt-Rh-SnO_2/C catalysts were prepared using polyol method, where the atomic ratio of Pt:Rh:Sn was 3:1:x and x varies from 2 to 6. The 3:1 ratio of Pt:Rh was fixed in this work because the previous theoretical study has shown that higher Pt content relative to that of Rh is likely to facilitate the C-C bond breaking on this system (Section 3.1.3). DFT calculations propose an optimum pathway for C-C bond breaking at the Rh,Pt/SnO_2 interface: *CH_3CH_2OH - *CH_3CH_2O+H* - *CH_2CH_2O+2H* - *CH_2+*CH_2O+2H*. The role of Rh is to adsorb and stabilize the key intermediate CH_2CH_2O in this route, which leads to a cleavage of C-C at a reasonable speed. A back donation from Rh d-band electrons to Pt is proposed, so the presence of Pt could modify the electronic structure of Rh by partially emptying its d-band states and making it strongly bound to CH_2CH_2O. Simultaneously, the activity of Pt is lowered, thus preventing ethanol partial oxidation on Pt sites. Study on binary Pt-Rh electrocatalysts showed that $Pt_{73}Rh_{27}$ produced largest amount of CO_2 among $Pt_{90}Rh_{10}$, $Pt_{73}Rh_{27}$ and $Pt_{55}Rh_{45}$ [73]. Further reasons for using less Rh than Pt are that Rh alone is inactive for ethanol oxidation, and that it was even more expensive than Pt. SnO_2 is considered the suitable tin phase in this system and the activity comes from PtRh/SnO_2 interface. Hence, the atomic ratio of Pt:Rh was fixed to 3:1 and Sn content was manipulated to find the optimal composition.

ICP-OES results for all the Pt-Rh-SnO_2/C electrocatalysts are presented in Table 3.2. It can be seen that each metal in the obtained catalysts is present in a composition close to the nominal one. It is more important to know whether all the three components co-exist at each single catalyst nanoparticle. EELS spectra were taken simultaneously with STEM imaging. Figure 3.14

shows the typical EELS spectra from a single nanoparticle in Pt-Rh-SnO_2/C with atomic ratio Pt:Rh:Sn = 3:1:4 and the insert figure is that particle. At high energy loss region, Pt $M_{4,5}$ absorption edge was clearly seen at 2122eV. At lower energy loss region, C k edge at 284eV, Rh $M_{4,5}$ edge at 307eV and Sn $M_{4,5}$ edges at 484eV were clearly observed from the same nanoparticle. Seven randomly picked nanoparticles were examined by the same method and all of them resolved the three elements. Hence, it can be concluded that all the three components coexist in most of the nanoparticles.

Table 3.2: Metal Content of the Catalysts

Catalysts	Nominal atomic ratio	Nominal metal content (wt.%)			Actual metal content (wt%)		
$PtRhSnO_2$/C	(Pt:Rh:Sn)	Pt	Rh	Sn	Pt	Rh	Sn
Catalyst-1	3:1:2	15.6%	2.7%	6.3%	15.2%	2.1%	5.8%
Catalyst-2	3:1:3	15.0%	2.6%	9.1%	14.8%	2.4%	9.3%
Catalyst-3	3:1:4	14.5%	2.5%	11.7%	14.0%	1.8%	10.7%
Catalyst-4	3:1:5	13.9%	2.4%	14.1%	13.6%	2.4%	14.0%
Catalyst-5	3:1:6	13.4%	2.3%	16.4%	12.7%	1.8%	15.4%

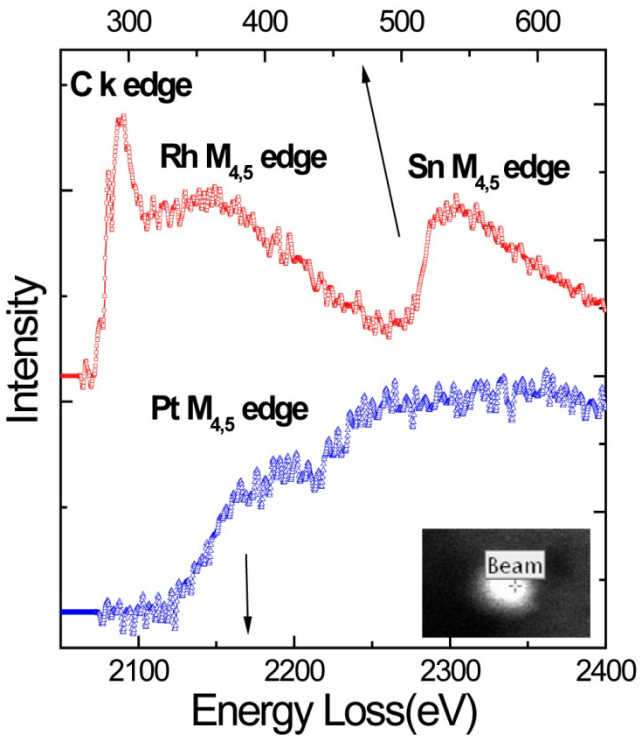

Figure 3.14 Typical EELS spectra from a single nanoparticle in the $PtRhSnO_2/C$ electrocatalyst having the Pt:Rh:Sn = 3:1:4 atomic ratio.

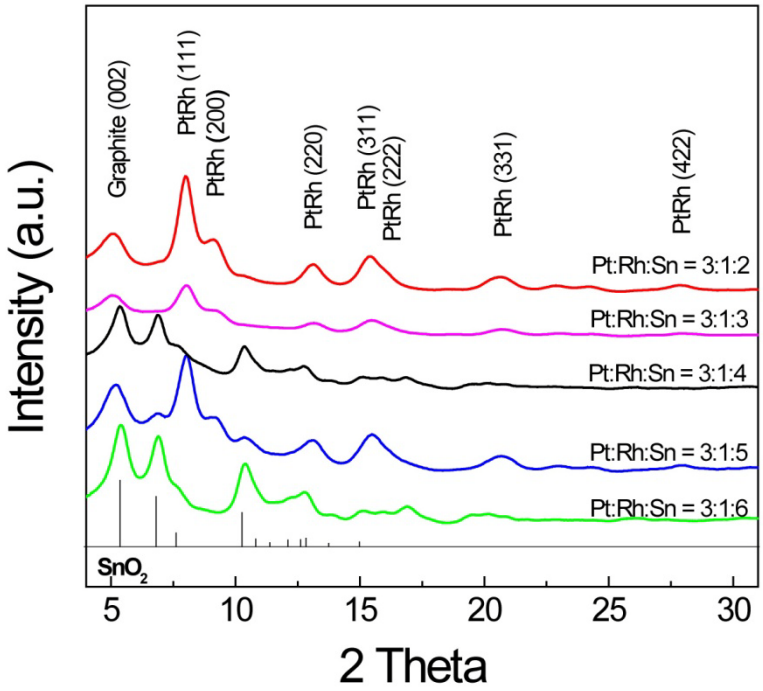

Figure 3.15 XRD patterns of several Pt-Rh-SnO_2/C electrocatalysts with different compositions.

XRD patterns of the Pt-Rh-SnO_2/C electocatalysts are shown in Figure 3.15. The main

diffraction peak positions for SnO_2 (PCPDF 411445) are marked at the bottom. All the diffraction peaks are all clearly broadened, indicating a very small average particle size. Pt and Rh diffraction peaks cannot be resolved separately in any of the XRD patterns. Intrinsically, Pt and Rh have very close diffraction peak positions due to their similar crystalline structure. Both metals crystallize as face-centered cubic (FCC) structure, belong to space group Fm3m, and their lattice constants do not differ considerably (3.9231Å and 3.8031Å, for Pt and Rh, respectively). The similarity in lattice parameters, and the peak broadening due to small particle size, makes it difficult to distinguish Pt from Rh peaks. However, according to Pt-Rh phase diagram [169], the two metals form uniform solid solution at all ratios, so that the absence of doublet in these diffraction peaks is interpreted as the formation of solid solution, as confirmed by EXAFS (see below). All the XRD peaks could be assigned to either PtRh alloy or SnO_2, hence the formation of a ternary alloy is unlikely. Similarly, the existence of metallic Sn, separatedly or Sn-containing binary alloys, is not confirmed. Most probably, Pt and Rh form an alloy, while Sn exists only in SnO_2 phase. When the Sn content is low, like in Catalyst-1 (with Pt:Rh:Sn = 3:1:2 atomic ratio) and Catalyst-2 (with Pt:Rh:Sn = 3:1:3 atomic ratio), no SnO_2 peaks are seen. As the Sn content increases, the SnO_2 peaks are more distinct. Similarly, PtRh peak intensity grow when PtRh content relative to SnO_2 is high.

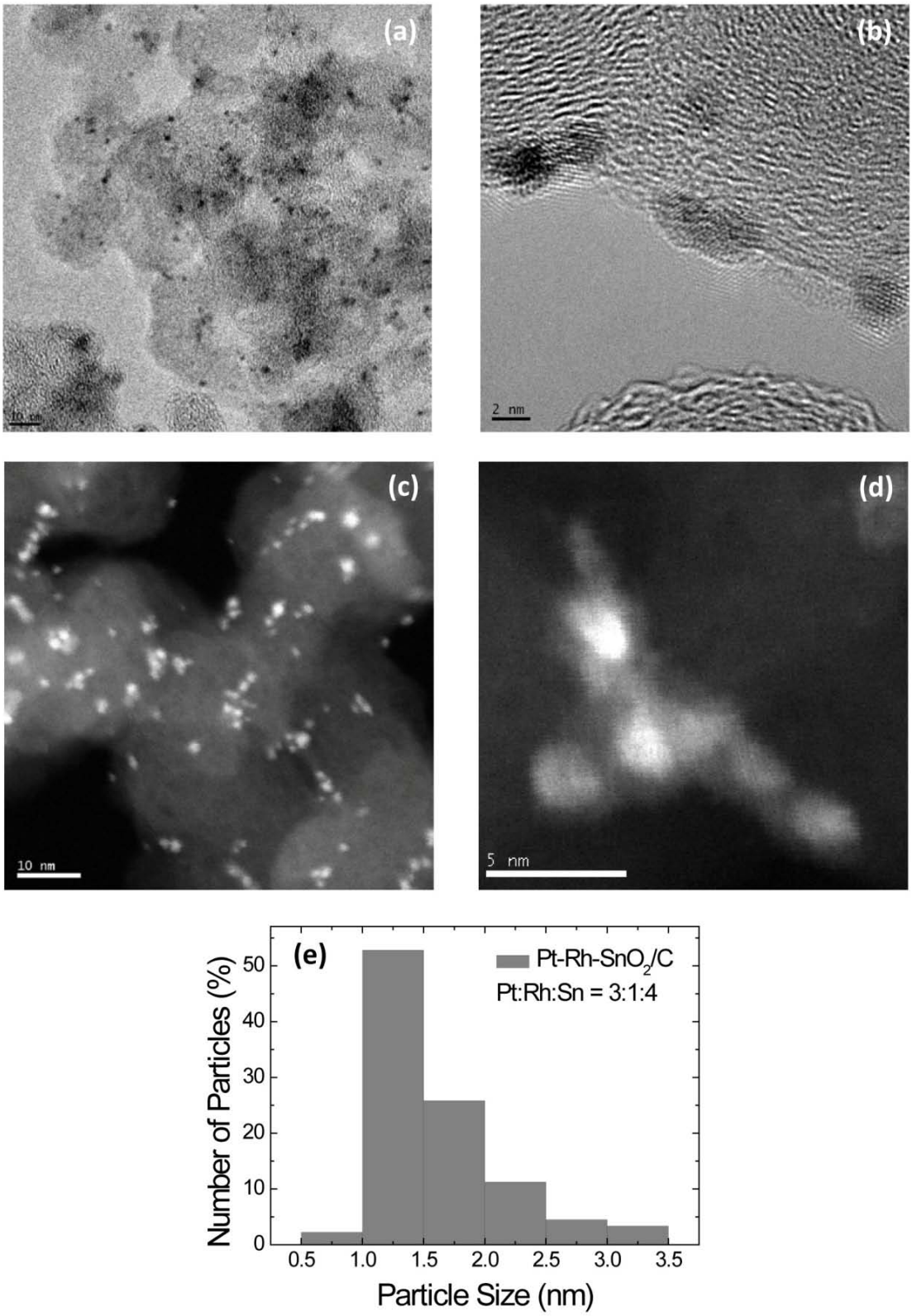

Figure 3.16 Typical TEM (a & b) and STEM images (c & d) and the corresponding particle size distributions (e) of the Pt-Rh-SnO_2/C electrocatalyst with the Pt:Rh:Sn = 3:1:4 atomic ratio.

To evaluate the morphology and particle size distribution, the electrocatalysts were characterized by HR-STEM. Figure 3.16 a and b show two representative TEM images. Figure 3.16 c and d include the typical high angle annular dark-field scanning transmission electron microscope (HAADF-STEM) images from Pt-Rh-SnO_2/C catalyst with atomic ratio of Pt:Rh:Sn = 3:1:4 and histograms of the particle size distribution. In HAADF-STEM images, the field around samples Is dark due to the absence of scattered electrons, and the image contrast Is directly related to atomic numbers. Thus, it is seen that the small bright catalyst nanoparticles uniformly dispersed over the carbon support. The particle size distribution based on the statistics over 300 nanoparticles in STEM images is shown in Figure 3.16e. The nanocatalyst have an average particle size around 1.5nm and a narrow distribution.

3.2.2.2 EOR Activity of Pt-Rh-SnO_2/C Electrocatalysts

The activity of the all the Pt-Rh-SnO_2/C samples was first evaluated in potentiodynamic measurement and Figure 3.17a show the polarization curves of all the catalysts in ethanol-containing electrolyte. Hydrogen adsorption feature is inhibited on all catalysts, indicating strong adsorption of ethanol molecules on the active sites. The profile demonstrates the onset potential of ethanol oxidation is just above 0.1V, a much lower potential compared to that of Pt/C and PtRu/C (0.4V and 0.3V, respectively) [131]. In these measurements the Pt-Rh-SnO_2/C catalyst with atomic ratio Pt:Rh:Sn = 3:1:4 shows the best activity with the most negative EOR reaction onset potential and highest current yield.

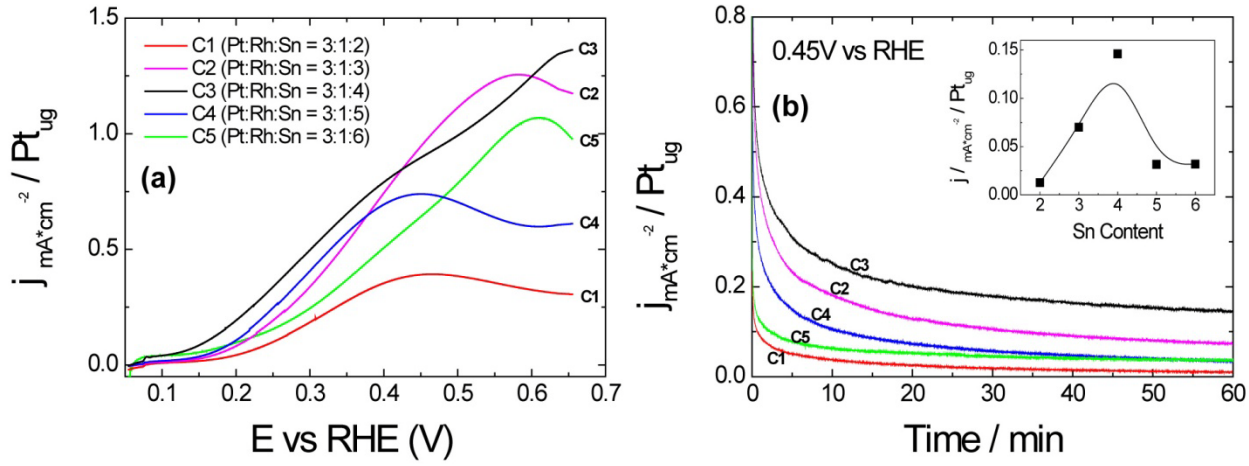

Figure 3.17 (a) Polarization curves of Pt-Rh-SnO_2/C electrocatalysts with a scan rate of 10mV/s^{-1}. (b) Chronoamperometry measurements at 0.45V on Pt-Rh-SnO_2/C catalysts, the insert showed the ethanol oxidation current density after 60min of polarization at 0.45V as a function of the Sn content. The Pt mass specific current densities were employed in the comparison; 0.5M ethanol + 0.1M $HClO_4$; room temperature.

At 0.45V, a potential of technical interest, potentiostatic measurements were carried out to further examine all the electrocatalysts. In all the cases, current drops quickly at the beginning, and then reaches a relatively stable state. The Pt-Rh-SnO_2/C catalyst with Pt:Rh:Sn atomic ratio of 3:1:4 give the highest current yield again. Insert in Figure 3.17b shows the relation of EOR current densities taken after 1h reaction with Sn content in respective Pt-Rh-SnO_2/C electrocatalyst. It can be seen that the ternary catalyst with Pt:Rh:Sn atomic ratio 3:1:4 is the most active; both too high and too low Sn contents causes a decrease in the catalyst's activity. The fact can be interpreted as follows. As shown in XRD and EXAFS (see below) results, PtRh form a metallic alloy, while Sn is found only as SnO_2. EELS study shows the coexistence of all of Pt, Rh and Sn in resulting nanoparticles. Due to the strong interaction between tin and oxygen, Sn has a tendency to segregate to the surface of nanoparticles and forms tin oxide during the annealing in air at 200°C (see section 2.3.3.3). Thus, a high content of Sn has the following consequences: (a) higher content of active PtRh/SnO_2 interface; (b) more OH species for removing reaction intermediates; (c) partial blocking of PtRh active sites; (d) higher resistance of the electrocatalysts due to the semiconducting nature of SnO_2. Among these, the first two factors

lead to higher EOR activity, while the contribution of the latter two lowers it. Hence, the best activity comes from balanced act of all factors, i.e. from a well-tuned content of PtRh and SnO_2.

3.2.2.3 In Situ Infrared Reflection-Absorption Spectroscopy (in situ IRRAS)Study

In situ IRRAS study was carried out to investigate the selectivity of the best Pt-Rh-SnO_2/C catalyst (Catalyst-3 with atomic ratio Pt:Rh:Sn = 3:1:4) and a Pt-SnO_2/C (with atomic ratio Pt:Sn = 3:4) catalyst prepared using the same polyol method. Figure 3.18 shows the recorded spectra from both catalysts during ethanol electro-oxidation. The frequencies and band assignments are listed in Table 3.1. Carbon dioxide (CO_2), acetic acid (CH_3COOH) and acetaldehyde (CH_3CHO) are the main products of ethanol oxidation in acidic solution. The positive-going peak near 2343cm^{-1} is attributed to the asymmetric stretch vibration of CO_2, the product of ethanol total oxidation pathway. It can be observed that the intensity of CO_2 band of Pt-Rh-SnO_2/C is much higher than that of Pt-SnO_2/C, indicating that the addition of Rh enhances the catalyst's capacity to break C-C bond and promotes the ethanol total oxidation. In the spectra on Pt-SnO_2/C, bands of CH_3COOH and CH_3CHO could be clearly indentified. The band located around 1705cm^{-1} can be assigned to the stretch vibration of the C=O bond, found in both acetaldehyde and acetic acid. Both spectra show the C-O stretching vibration of acetic acid at 1280cm^{-1}, indicating the formation of CH_3COOH in both cases. The bands at 1350cm^{-1} and around 1396-1410cm^{-1} are assigned to CH_3 in-plane bending mode and OCO stretching of adsorbed acetate, respectively. These two bands are close and difficult to distinguish. The band observed at 933cm^{-1} is assigned to C-C-O asymmetric stretching of acetaldehyde. The absence of bands at both 933 and 1705cm^{-1} in the case of Pt-Rh-SnO_2/C indicates that CH_3CHO is either not produced or only produced in a very small quantity. There are two possible interpretations for the phenomenon. It can be due to a

higher selectivity towards total oxidation pathway on Pt-Rh-SnO_2/C, or re-adsorption of CH_3CHO at the catalyst in the thin layer configuration, and further oxidation to CH_3COOH. In the latter case, CH_3CHO is the intermediate in the CH_3COOH reaction pathway. The strong band at 1598cm^{-1} is the H-O-H deformation of adsorbed water molecules. This negative-going band indicates a consumption of water during potential excursion. The C=O stretching mode of adsorbed acetaldehyde and acetyl around 1620-1635cm^{-1} cannot be resolved because of the presence of the strong water band. The C-H wagging vibration in CH_3CHO, at 1108cm^{-1}, overlaps with the strong band at 1110cm^{-1} of Cl-O stretching in ClO_4^-. The strong band for ClO_4^- ions is the consequence of its accumulation in the thin layer cell to compensate the increasingly positive electrode potential, and perchlorate accumulation drives water out.

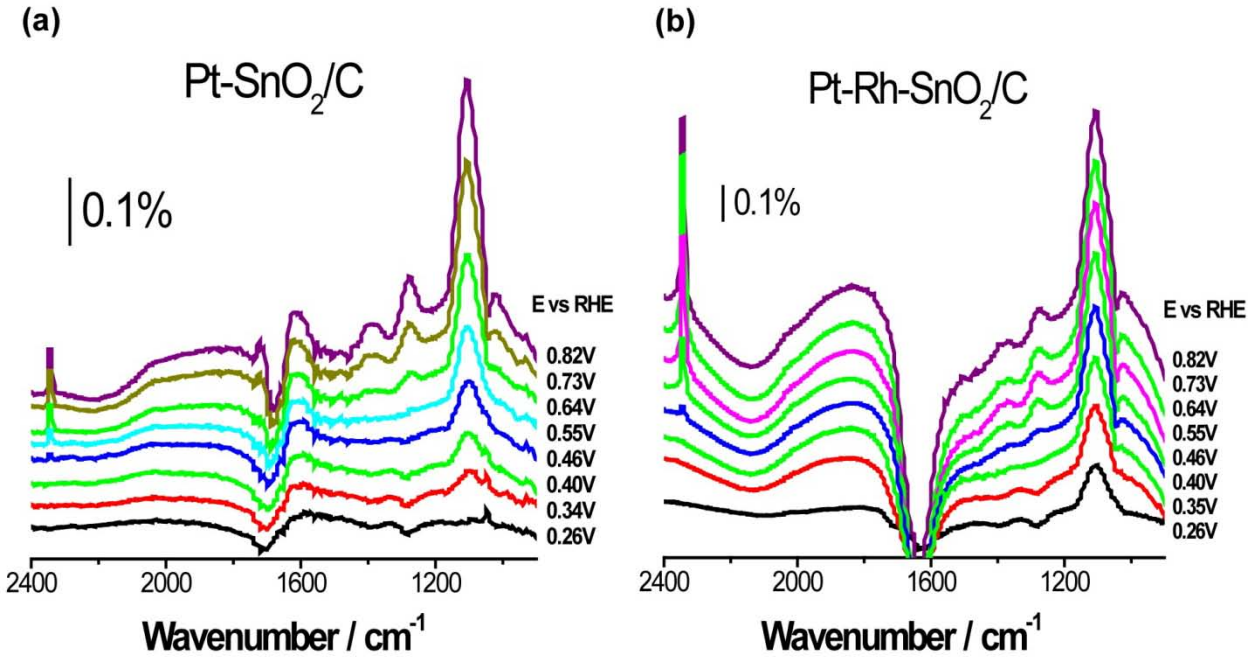

Figure 3.18 *In situ* IRRAS spectra recorded during ethanol oxidation on: (a) Pt-SnO_2/C with the atomic ratio Pt:Sn = 3:4; (b) Pt-Rh-SnO_2/C with the atomic ratio Pt:Rh:Sn = 3:1:4.

Figure 3.19(a) and (b) show the variation of integrated band intensities of CO_2 (2343cm^{-1}), CH_3CHO (933cm^{-1}) and CH_3COOH (1280cm^{-1}) with applied potential for both Pt-Rh-SnO_2/C

and Pt-SnO_2/C samples. It can be clearly seen that on Pt-SnO_2/C the band from CH_3COOH is the strongest band, with band intensity much higher than that of CO_2. On the other hand, CO_2 produces the highest intensity IR band on Pt-Rh-SnO_2/C catalyst. It is interesting to note that on Pt-Rh-SnO_2/C the amount of acetic acid steadily increases with the potential; however, CO_2 production increases to a maximum around 0.8V, and decreases afterwards. That might be the consequence of Pt and Rh oxidation at higher potentials, as the loss of metallic Pt or Rh causes the failure of ternary system, and consequently a weaker capacity to break the C-C bond of ethanol.

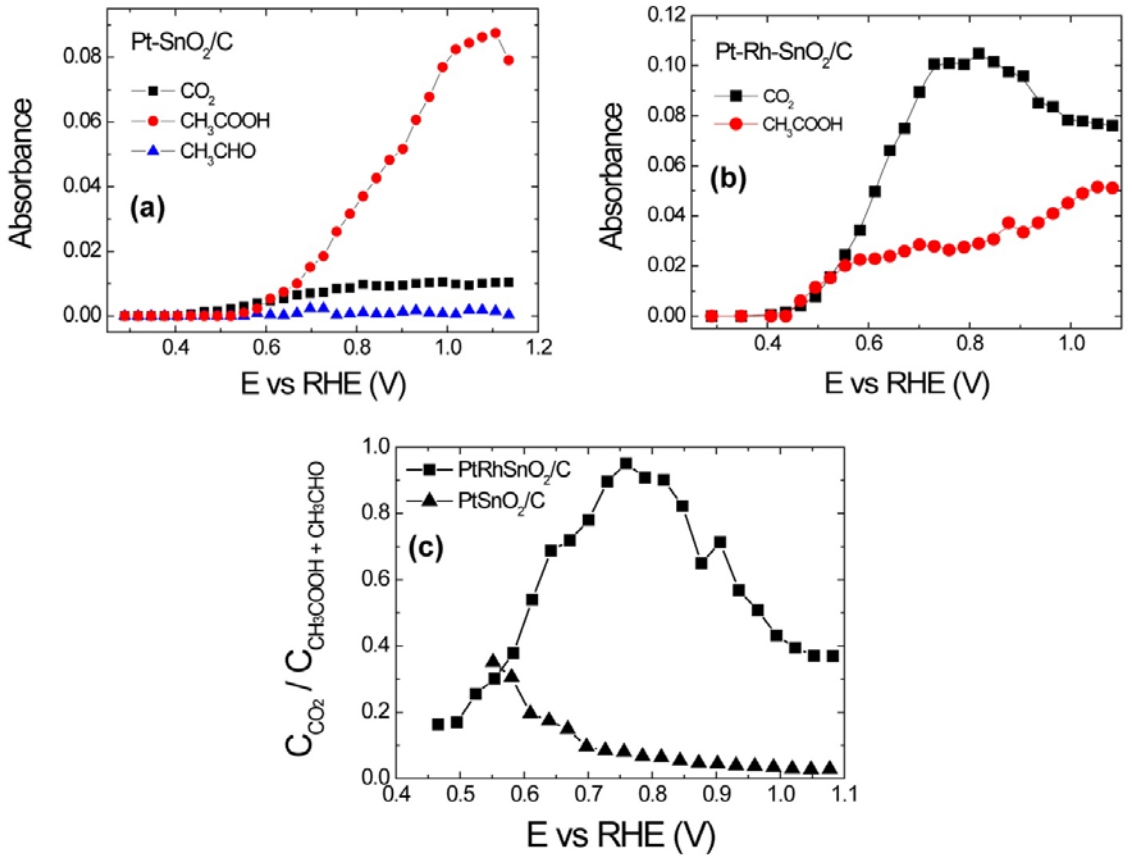

Figure 3.19 (a) Integrated band intensities of CO_2 (2343cm^{-1}), CH_3CHO (933cm^{-1}) and CH_3COOH (1280cm^{-1}) in IRRAS spectra from Pt-SnO_2/C with the atomic ratio Pt:Sn = 3:4; (b) Integrated band intensities of CO_2, CH_3CHO and CH_3COOH from Pt-Rh-SnO_2/C with the atomic ratio Pt:Rh:Sn = 3:1:4; (c) the ratio between charge contribution from total oxidation pathway (C_{CO_2}) and charge contribution from partial oxidation pathway ($C_{CH_3COOH+CH_3CHO}$) versus applied potential on both electrocatalysts.

In order to rationally compare the selectivity of these two electrocatalysts, we plotted the ratio between charge contribution from total oxidation pathway (C_{CO_2}) and charge contribution from partial oxidation pathway ($C_{CH_3COOH+CH_3CHO}$) versus applied potential, and the results are shown in Figure 3.19c. The yield of oxidation products are calculated using respective integrated band intensities, and the amount of a given species Q (mol/cm^2) inside the thin layer cavity follow the relationship [168]

$$Q = \frac{A_i}{\varepsilon_{eff}} \tag{3.2}$$

Where A_i is respective integrated band intensity and ε_{eff} is the value of the effective absorption coefficient. Values of ε_{eff} are taken from the work from Weaver et al.[170-171], and these are 3.5×10^4, 5.8×10^3 and $2.2\times10^3 M^{-1}cm^{-2}$ for CO_2, CH_3COOH and CH_3CHO, respectively. The production of one CO_2, CH_3COOH and CH_3CHO molecule provides 6, 4 and 2 electrons, respectively. Therefore, $C_{CO_2}/C_{CH_3COOH+CH_3CHO}$ are calculated by the equation

$$\frac{C_{CO_2}}{C_{CH_3COOH}+C_{CH_3CHO}} = \frac{6*Q_{CO_2}}{4*Q_{CH_3COOH}+2*Q_{CH_3CHO}} \tag{3.3}$$

As shown in Figure 3.19c, on Pt-Rh-SnO_2/C, C_{CO_2} is comparable to $C_{CH_3COOH+CH_3CHO}$. But on Pt-SnO_2/C, partial oxidation products are responsible to the dominant charge contribution. Hence, the addition of Rh facilitates ethanol total oxidation pathway. Under concurrent configuration it is difficult to obtain exactly the same thin layer condition, and there are both products accumulation and diffusion going on at same time. For different species, the rates are different. CO_2 is the most volatile among the three major products, so we would expect that CO_2 diffuses faster than CH_3COOH and CH_3CHO. We cannot conduct accurate quantitative study on ethanol oxidation products by IRRAS, more investigations like on-line DEMS study will be performed in

the future.

The IR results suggests that there are parallel pathways of EOR in both systems, and the capability of Pt-Rh-SnO_2/C in splitting C-C bonds is much more enhanced compared to that of Pt-SnO_2/C.

3.2.2.4 In Situ X-ray Absorption Spectroscopy (XAS)

In situ XAS study was conducted to elucidate *in situ* changes of Pt-Rh-SnO_2/C catalyst with atomic ratio Pt:Rh:Sn = 3:1:4 under potential control. The XANES spectra of Pt-L3 edge, Rh-K edge and Sn-K edge in the potential region from 0.06-0.91V are shown in Figure 3.20 a, c, and e, respectively. The XANES spectra of Pt and Rh show a potential induced change only at potentials of 0.71V and higher, as observed in the shift of both absorption edge and white line. No obvious change is seen on the spectra at 0.06V and 0.41V. On the other hand, XANES spectra of Sn show no change in the entire potential region, indicating that tin cannot be oxidized or reduced when in the present form.

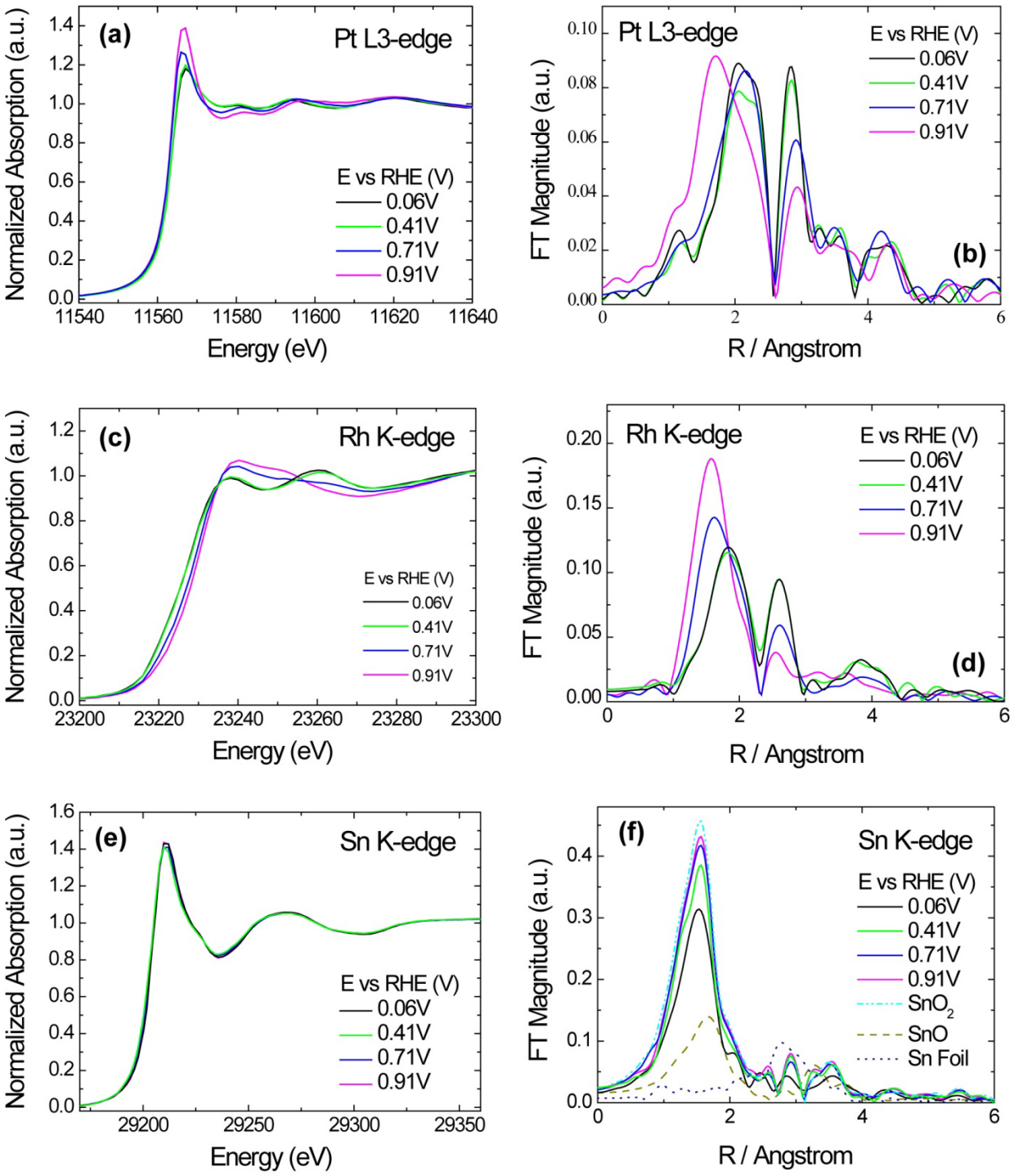

Figure 3.20 XANES spectra (a, c, e) and Fourier transform magnitudes (b, d, f) of Pt L3 edge, Rh K edge and Sn K edge of Pt-Rh-SnO_2/C with the atomic ratio Pt:Rh:Sn = 3:1:4 in 1M $HClO_4$ solution as a function of potential. Potential settings are indicated in the graph.

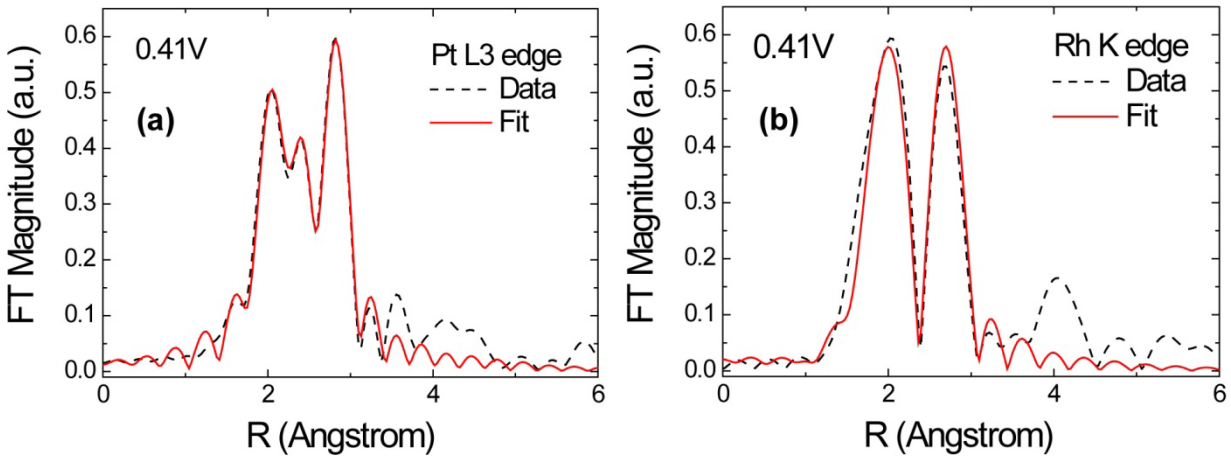

Figure 3.21 Fourier transform magnitudes of Pt-L3 edge (a) and Rh-K edge (b) of Pt-Rh-SnO_2/C with the atomic ratio Pt:Rh:Sn = 3:1:4 electrocatalyst held at 0.41V in 1M $HClO_4$ and the respective first-shell fits. See text for the fitting parameters.

From the Fourier transform magnitudes of Pt-L3 edge shown in Fig. 3.20b, it can be clearly seen that Pt stays in metallic state in the low potential region, whereas Pt-O contribution increases when the applied potential is high. The behavior of Rh is very similar to that of Pt, as shown in Figure 3.20d. Finally, Figure 3.20f shows the comparison of Sn in Pt-Rh-SnO_2/C with standard SnO_2, SnO and metallic Sn foil; it is clearly seen that in the entire potential region, Sn stays in the form of SnO_2.

The first-shell fitting results of the Pt-Rh-SnO_2/C (with Pt:Rh:Sn = 3:1:4 atomic ratio) electrocatalyst at a potential of 0.41V are shown in Figure 3.21 a b. A reasonably good agreement between the fits and the original spectra is seen; the results of coordination numbers and bond lengths are summarized in Table 3.3. In this analysis all parameters except for the passive electron reduction factors ($S_0^2{}_{Pt}$ and $S_0^2{}_{Rh}$) are allowed to vary with no constraints.

Table 3.3: Bond lengths of Pt and Rh metals in the Pt-Rh-SnO_2/C catalyst obtained by EXAFS analysis at 0.41 V and comparison to those of bulk metals.

	Bond length	Coordination number
Pt (bulk)	2.775	12
Rh (bulk)	2.689	12
Pt-Pt	2. 740 $\pm$ 0.004	5.1 $\pm$ 0.9
Rh-Rh	2.683 $\pm$ 0.006	1.9 $\pm$ 0.9
Pt-Rh	2.715 $\pm$ 0.004	1.7 $\pm$ 0.9
Rh-Pt	2.715 $\pm$ 0.004	5.1 $\pm$ 1.0

For an A-B binary solid-solution (random) alloy, the ratio (relative to A atom) of the coordination number $N_{A\text{-}A}$ to $N_{A\text{-}B}$ was equal to the mole fraction ratio x_A/x_B of the elements in the bulk [178] i.e., $N_{A\text{-}A} / N_{A\text{-}B} = x_A / x_B$. Similarly, the ratio for B atom, $N_{B\text{-}B}/N_{B\text{-}A}$ is equal to x_B/x_A. Furthermore, statistical distribution of the two elements is characterized by equal sums of coordination numbers of one metal to that of the other, i.e. $N_{\text{A-M}} = N_{\text{B-M}}$. As seen in Table 3.3, the ratio of coordination numbers $N_{\text{Pt-Pt}} / N_{\text{Pt-Rh}} = 3.0$, is in excellent agreement with the mole fraction ratio $x_{\text{Pt}}/x_{\text{Rh}} = 3$. Concomitantly, the ratio of coordination numbers $N_{\text{Rh-Rh}} / N_{\text{Rh-Pt}}$ is determined to be 0.37, which is also in good agreement with $x_{\text{Rh}}/x_{\text{Pt}} = 0.33$. Furthermore, $N_{\text{Pt-Pt}} + N_{\text{Pt-Rh}} = 6.8$, and $N_{\text{Rh-Rh}} + N_{\text{Rh-Pt}} = 7.0$, thus within the experimental error $N_{\text{Pt-M}} = N_{\text{Rh-M}}$, are consistent with homogeneous distribution of both Pt and Rh atoms throughout the particles without preferential accumulation of one metal around the other. Clearly, the EXAFS analysis demonstrates the formation of homogeneous Pt-Rh random alloy nanoparticles.

The particle size can be estimated from the total coordination numbers of the two metals. Assuming identical lattice constants for Pt and Rh, the average number of atoms in the nanoparticles can be calculated, and the particle size is found to be about 1.4 nm [172], in good agreement with the TEM/STEM data (1.5nm).

3.1.2.5 Summary

A modified polyol method has been employed to synthesize ternary Pt-Rh-SnO_2/C electrocatalysts and to determine the optimal composition by varying atomic ratio of Pt, Rh and Sn. Chemical composition studies confirm that these catalysts are prepared successfully having the actual composition close to the nominal ones, with the coexistence of all the three elements in single catalyst nanoparticles. Structural characterization involving XRD, XAS and HR-STEM techniques reveals a very small particle size and uniform dispersion of these electrocatalysts, comprising metallic PtRh and SnO_2.

Electrochemical measurements reveal the highest activity for ethanol oxidation of the Pt-Rh-SnO_2/C electrocatalyst with atomic ratio Pt:Rh:Sn = 3:1:4. This catalyst (out of five) is characterized by the highest oxidation currents, the least positive reaction onset potential, and the dominant reaction pathway involving the total oxidation to CO_2. Both too low and too high tin content induces a decrease of activity.

For the Pt-SnO_2/C catalyst, with Pt:Sn = 3:4 atomic ratio, acetic acid is the major product. Thus, for the cleavage of C-C bond in ethanol all three constituents are needed and the synergistic effect between them facilitates total oxidation of ethanol, which is facilitated by the formation of PtRh uniform solid solution and the zero oxidation state of Pt and Rh in the potential region below 0.71V. In contrast, Sn exists as SnO_2 in entire potential region.

The data presented in this section corroborates earlier assertion of great potential of this electrocatalyst for resolving major obstacles to development of practical DEFC for a broad range of applications.

3.3 MM'/SnO_2 (MM' = PtRh, PtIr, IrRh, and PtIrRh) Nanoparticle Electrocatalysts for Oxidizing Ethanol to CO_2 [174]

In previous sections we have demonstrated that the ternary Pt-Rh-SnO_2 electrocatalyst has unprecedented activity for ethanol oxidation to CO_2, due to the synergistic effect between the three constituents. However, Rh is one of the rarest and the most costly precious metals, hence, to optimize and reduce Rh content and eventually to replace Rh is of great importance in designing practical ethanol oxidation catalysts. We explored Ir as an alternative to Rh in forming a highly efficient EOR catalyst. Ir is in the same group as Rh, and they have the same number of unpaired d electrons per atom, hence, it is expected that the two may have similar adsorptive and catalytic properties.

In this section we discuss our density functional theory (DFT) calculation guided design, syntheses, and characterization of carbon-supported MM'/SnO_2 nanoparticles (NPs) consisting of multi-metallic nanoislands (MM' = PtRh, PtIr, IrRh, PtIrRh) deposited on SnO_2 NP cores, which provide active metal-metal oxide interface and are synthetic analogues of the PtRh/SnO_2(110) model catalyst in our earlier DFT study (section 3.1.3). We first employed a range of characterization techniques, including XRD, AC-STEM with complementary DF and BF imaging, EDS mapping and *in situ* XAS, to establish the composition and architecture of the synthesized MM'/SnO_2 NPs. Carbon-supported MM'/SnO_2 electrocatalysts with different compositions were prepared using a seeded growth approach and investigated utilizing a combination of electrochemical methods and *in situ* IRRAS to elucidate the correlations between the chemical composition of electrocatalysts and the their performance (activity and selectivity)

in ethanol electro-oxidation. We demonstrate that PtRh/SnO_2/C electrocatalysts with a moderate Rh content, i.e. catalysts with atomic ratio Pt:Rh:Sn = 1:1/2:1 and 1:1/3:1, exhibits very high EOR activity and selectivity towards ethanol complete oxidation to CO_2. PtIr/SnO_2/C and PtIrRh/SnO_2/C catalysts show reasonably good catalytic property, while IrRh/SnO_2 is the poorest EOR catalyst. These findings are of great importance in terms of understanding and designing novel nanostructured materials with substantially improved activity and selectivity in ethanol oxidation.

3.2.1 Physical Characterization

The hetero-nanostructured MM'/SnO_2 NP electrocatalysts comprised of SnO_2 cores decorated with multi-metallic (MM') nanoislands (MM' = PtRh, PtIr, IrRh, or PtIrRh) were prepared as direct analogues of the PtRh/SnO_2(110) model catalyst. SnO_2 NPs were synthesized by modifications of known glycol methods [142], with $SnCl_2$ being reduced forming Sn^0 first by heating in EG and quickly being oxidized to SnO_2 afterwards in the O_2 flow. Multi-metallic nanoislands were subsequently deposited on the preformed SnO_2 seeds using chloride precursors ($PtCl_4$, $RhCl_3$ and/or $(NH_4)_2IrCl_6$) and a seeded growth technique. Most recently, seeded growth has emerged for precisely controlling the morphology and composition of metallic nanostructures that are prepared using solution-phase methods [175-177]. It has been stated that in a system with preexisted core particles the critical energy barrier is generally smaller for heterogenerous nucleation of solute atoms than that for homogeneous one, and if sufficient sites are available for heterogeneous nucleation, both number of critical clusters and nucleation rate should be larger for heterogeneous nucleation than those for heterogenous one [177]. In other

words, the solution atoms nucleate and grow heterogeneously. A range of complex nanostructures have been synthesized in solution phase, such as core-shell, dumbbell, particle-on-particle structures, etc [175-180]. Although most reported cases are metal-on-metal growth, it has been claimed a thin RuO_2 shell covering the Ru^0 core is necessary for Pt coating in the formation of Ru@Pt core-shell nanoparticles [175]. Because of the large lattice mismatch between metals (Pt, Rh and Ir) and SnO_2 NP substrates, metals are expected to grow on those high energy sites of substrate NPs and form islands in order to minimize strain energy, which is the so-called Volmer-Weber (VW) or island growth mode (Figure 3.22a) [181]. The growth of metal nucleus resulted in spherical shape and sometimes chain-like metal nanoislands, as seen in electron microscope images (Figure 3.22 and Figure 3.23). The surfactant-free syntheses were conducted with EG serving as both reducing agent and stabilizer, to retain clean surfaces for electrochemical reactions.

The synthesized carbon-supported MM'/SnO_2 NP catalysts were characterized using multiple analytical methods. The atomic structures and elemental distributions of MM'/SnO_2 NPs were examined using Z-contrast AC-STEM equipped with EDS. Z-contrast STEM is also referred as high-angle annular dark-field (HADDF) STEM or dark-field (DF) STEM, and the brightness in Z-contrast images reflects the HADDF intensity that is approximately proportional to the total number of atoms in the column (or the thickness of the particle) and the square of their average atomic number (Z^2). Figure 3.22b-c show typical Z-contrast images of $PtRh_{1/2}/SnO_2$/C NP electrocatalyst with atomic ratio Pt:Rh:Sn of 1:1/2:1. Our XRD (Figure 3.24) and EDS studies (Figure 3.25) and previous EXAFS studies (Section 3.2.2.4) confirm the formation of PtRh random alloy and SnO_2 oxide in the ternary catalysts. Therefore, PtRh nanoislands appear bright on the dark carbon background and SnO_2 NPs appear as light gray

"rafts" beneath the PtRh nanoislands because Pt has a larger atomic number (Z value) than does Sn. One atomically-resolved STEM image (Figure 3.22b) clearly shows two discrete spherical-shape PtRh nanoislands decorated on an amorphous SnO_2 NP substrate. While in Figure 3.22c, several PtRh nanoclusters form a chain-like nanoisland depositing on a crystalline SnO_2 NP support. Fringes in the SnO_2 NP show a lattice spacing of about 2.78 Å, corresponding to the (011) family of SnO_2 lattice planes. Careful observations over more SnO_2 NPs showed the predominant lattice spacings are 2.78 Å (011 planes) and 3.44 Å, which correspond, within the error of our measurements, to the (110) lattice spacing calculated for SnO_2 (3.35 Å). The study on PtRh nanoclusters shows a dominant fringe spacing of about 2.27 Å, and it corresponded to (111) family of PtRh. Similar studies were carried out on all M/SnO_2/C NP samples, and the results confirm that the obtained nanocatalysts are consisted of multi-metallic (MM' = PtRh, PtIr, IrRh, and PtIrRh) nanoislands decorated over broader SnO_2 NP substrates.

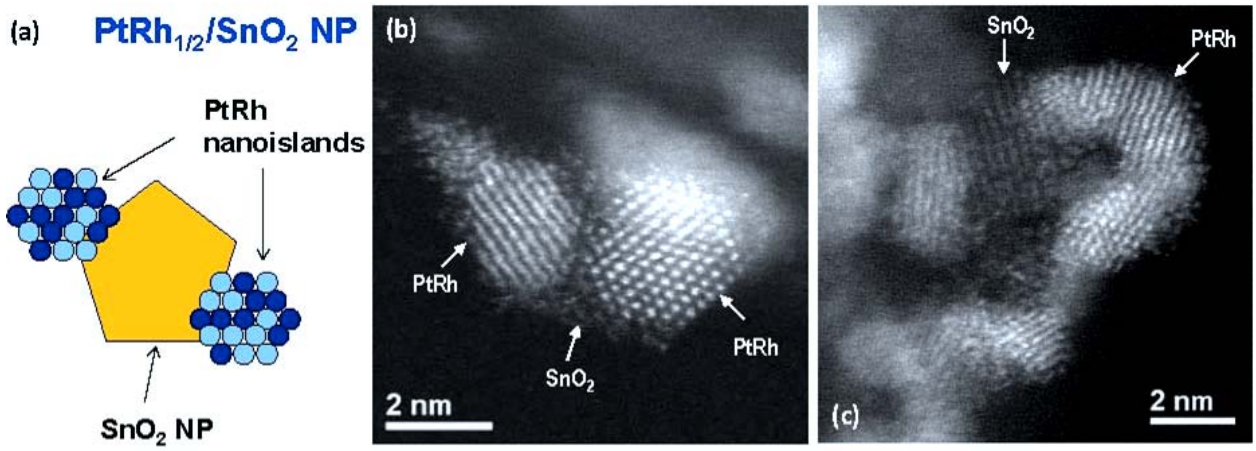

Figure 3.22 (a) Illustration of the $PtRh_{1/2}/SnO_2$ NP from a seeded growth approach. (b)&(c) Typical high resolution Z-contrast AC-STEM images of $PtRh_{1/2}/SnO_2$/C NPs.

Figure 3.23 displays a series of representative DF and BF AC-STEM images from three carbon-supported MM'/SnO_2 NP catalysts: $PtRh_{1/2}/SnO_2$, $PtRh_{1/3}/SnO_2$ and $PtIr/SnO_2$. The bright

multi-metallic nanoislands (PtRh or PtIr) and the gray SnO_2 NP substrates can be clearly resolved from the high-solution DF AC-STEM images (Figure 3.23 (a), (e), and (i)). One can find the PtRh or PtIr nanoislands appear bright on the dark carbon background in the DF images, while they appear dark on the bright carbon background in BF images. The SnO_2 NP substrates appeared as light gray “rafts” beneath the PtRh or PtIr nanoislands in the DF images, they show very little contrast from the carbon support in the BF image, and sometimes SnO_2 NPs are not visible over the carbon background in the BF image. Hence, DF AC-STEM provides a better tool to examine these hetero-nanostructured NPs. Low magnification STEM images (Figure 3.23 (c), (d), (g), (h), (k), and (l)) show an average size of PtRh and PtIr grains of about 2nm.SnO_2 NPs sizes are more difficult to determine because their irregular shapes and amorphous nature, and one can see they are usually in the range of 3-8nm, which is larger than the multimetallic metal nanoislands.

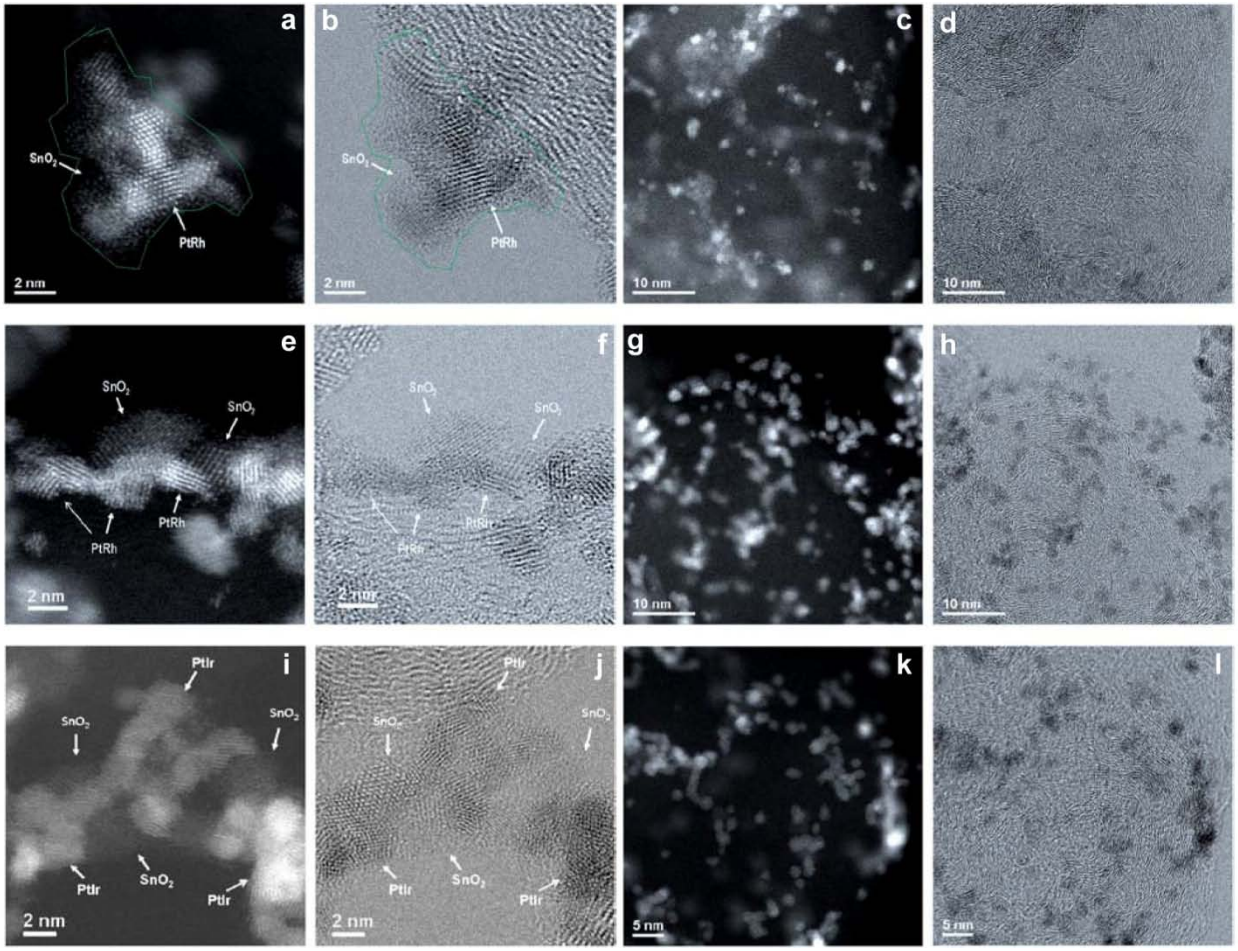

Figure 3.23 Simultaneously recorded DF and BF AC-STEM images of the same area on different carbon-supported MM'/SnO_2 NP electrocatalysts. (a)(b)(c)&(d): $PtRh_{1/2}/SnO_2$; (e)(f)(g)&(h): $PtRh_{1/3}/SnO_2$; and (i)(j)(k)&(l): $PtIr/SnO_2$.

Coupling element-sensitive EDS with DF AC-STEM images offers another way to determine the compositional distribution in MM'/SnO_2 NPs. Figure 3.24a-h show simultaneously recorded Z-contrast AC-STEM images and EDS elemental mapping. Pt-Rh maps (Figure 3.24b&e) suggest that a random alloy is formed, as Pt and Rh signals are overlapping. The O-signal associated with Sn (not shown) confirms that broad rafts are amorphous SnO_2, instead of Sn^0 phase. Pt-Sn maps (Figure 3.24 c&f) demonstrate that PtRh nanoislands are decorating over SnO_2 NP substrates. Similarly, Pt-Ir-Sn map (Figure 3.24h) show PtIr alloy nanoislands are deposited on SnO_2 NP supports. In addition, STEM images (not shown) taken before and after a

6 min EDS map indicated that the samples are beam sensitive to the high energy electron beam; hence, the mapping time was limited to up to 6minutes in all mapping. It has to be noted that the relatively short mapping time (e.g. 6min) limits our ability to acquire high quality EDS maps with sufficient counts to perform reliable quantitative analysis, but maps still show qualitatively the distribution of Sn, Pt, Rh and Ir.

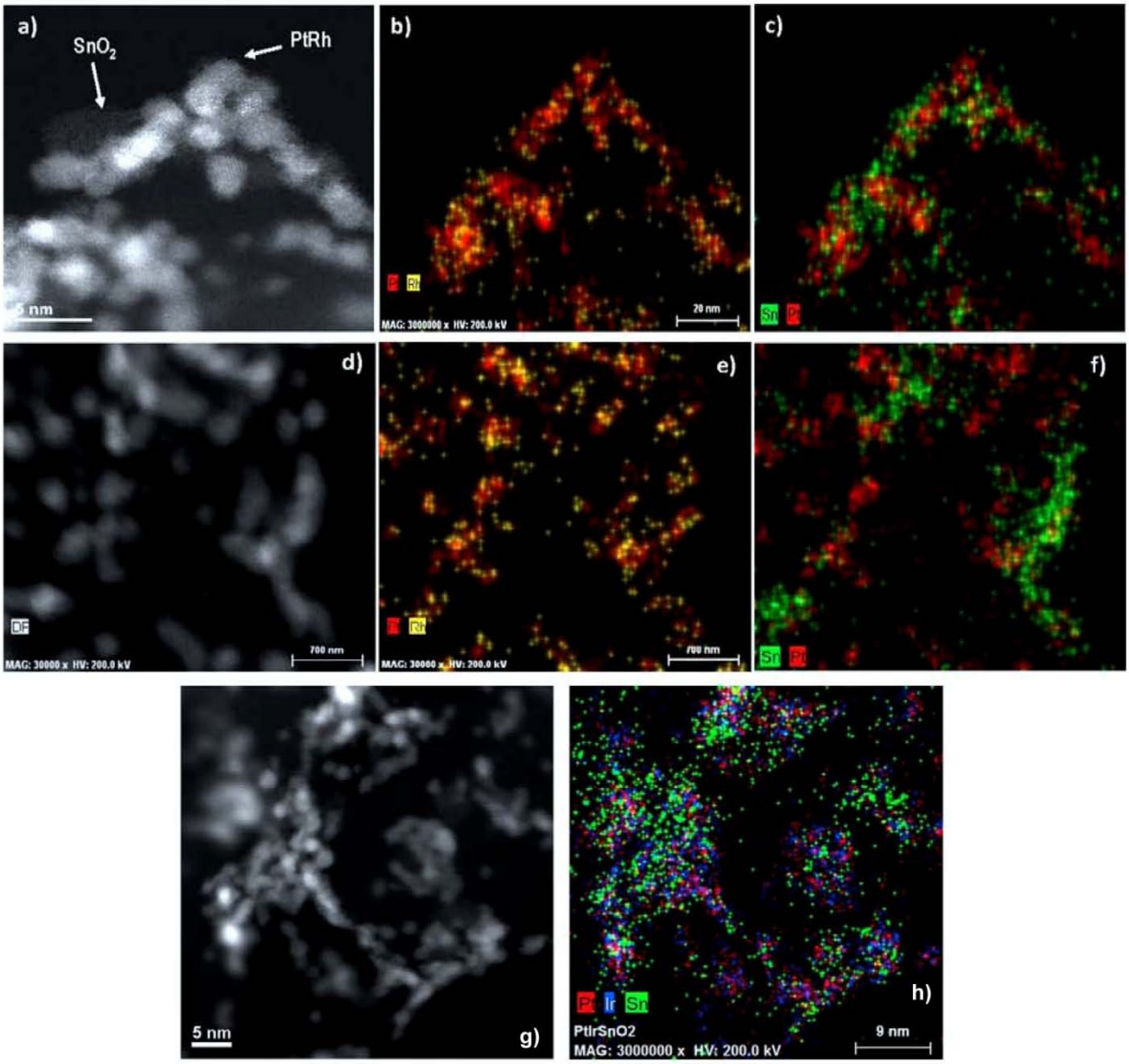

Figure 3.24 DF AC-STEM images and EDS elemental mapping of the same areas on different carbon-supported MM'/SnO_2 NP electrocatalysts. (a)(b)&(c): $PtRh_{1/2}/SnO_2$; (d)(e)&(f): $PtRh_{1/3}/SnO_2$; (g)&(h): $PtIr/SnO_2$.

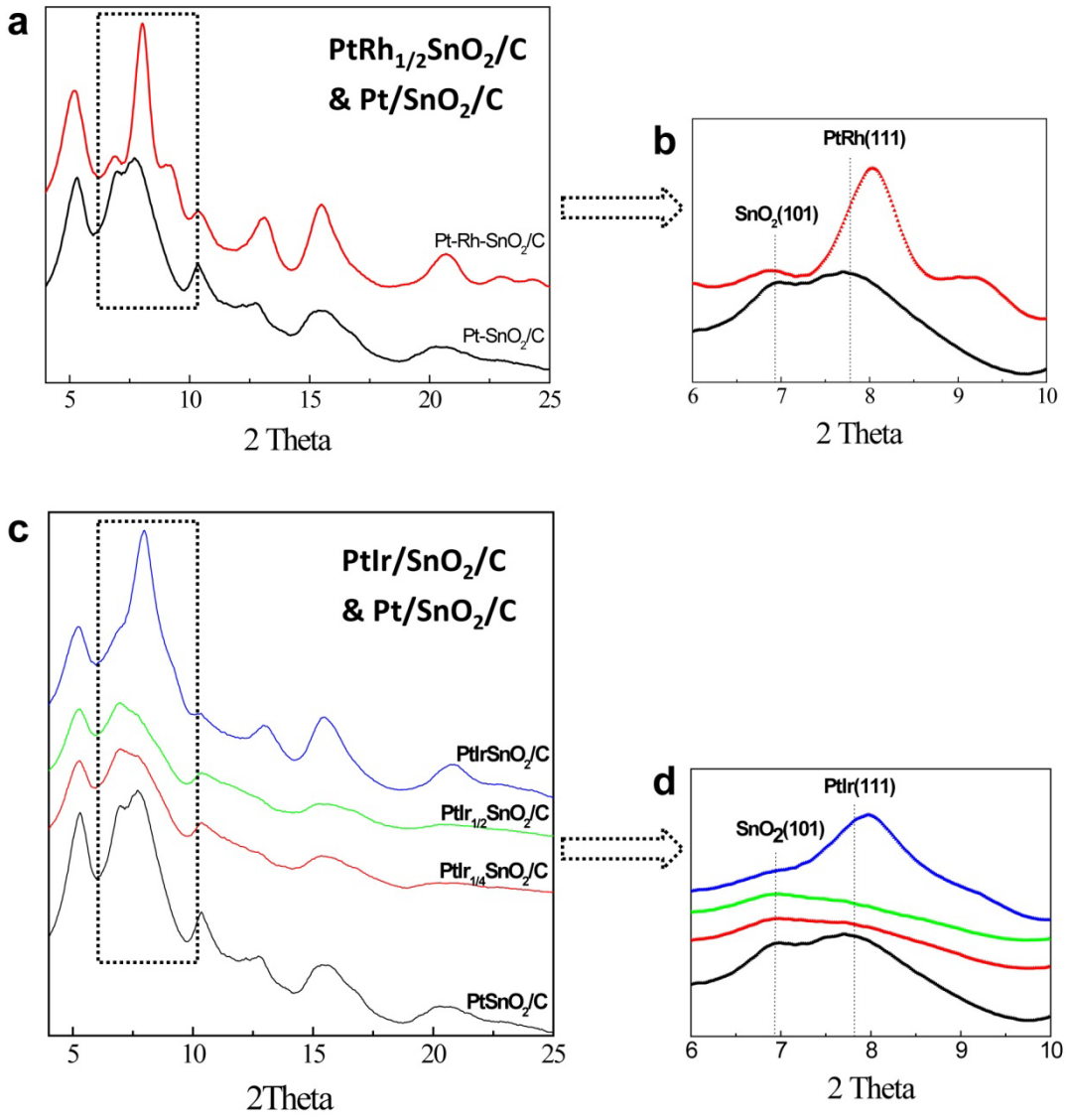

Figure 3.25 XRD profiles of different carbon-supported MM'/SnO_2 NP electrocatalysts. (a)&(b): PtIr/SnO_2 and Pt/SnO_2 NPs; (c)&(d): PtRh/SnO_2 and Pt/SnO_2 NPs.

Figure 3.25 presents XRD profiles of different carbon-supported MM'/SnO_2 (MM' = PtRh and PtIr) NP catalysts. The broadening of diffraction peaks indicates all NP catalysts consisted of nanoparticles with very small particle size, which is consistent with our electron microscope observations. Figure 3.25a displays XRD patterns of $PtRh_{1/2}/SnO_2/C$ electrocatalyst and also Pt/SnO_2/C electrocatalyst (with atomic ratio Pt:Rh of 1:1) prepared from the same method. Similar to our previous study (Figure 3.9 and 3.15), Pt and Rh diffraction peaks cannot be

resolved separately in any of the spectra, suggesting the formation of random PtRh alloy when combined with fitting EXAFS data. More detailed analyses can be found in Section 3.2.2. From Figure 3.25b one can observe the PtRh(111) peak position shifts to higher 2Θ, in consistent with a more compressed lattice due to the smaller radius of Rh atoms compared to Pt atoms (139pm and 134pm, for Pt and Rh atomic radius, respectively). The lattice parameters of the PtRh alloy nanoislands can be determined by refining XRD spectra, and more detailed analyses are undergoing to reveal the correlation between the lattice parameter and the composition.

XRD spectra of three PtIr/SnO_2/C electrocatalysts along with the Pt/SnO_2/C one are presented in Figure 3.25c and d. The cases with iridium component are more complicated because: i) Pt-Rh phase diagram suggests the formation of uniform solid solution at all ratios, while Pt-Ir phase diagram shows the phase segregation at low temperature; ii) EXAFS fitting is insufficient in determining relative distribution of Pt and Ir because their lattice parameters are too close (3.9231Å and 3.8391Å, for Pt and Ir, respectively); iii) the broad and poorly resolved PtIr(111) peaks in Figure 3.25c indicate a more amorphous nature of PtIr nanoislands compared to PtRh ones. However, one can still observe the shift of PtIr(111) peaks to higher 2 Θ values with increasing Ir content, indicating the penetration of Ir atoms to Pt lattice at certain extent.

3.3.2 Electrochemical Measurements

Electrochemical voltammetric measurements were carried out to probe the surface information on the carbon-supported MM'/SnO_2 (MM' = PtRh, PtIr, IrRh, or PtIrRh) electrocatalysts and evaluate their catalytic properties in ethanol electro-oxidation. The four PtRh/SnO_2 electrocatalysts (with atomic ratio Pt:Rh:Sn of 1:1:1, 1:1/2:1, 1:1/3:1, and 1:1/4:1)

were subject to potentiodynamic study to establish composition-reactivity correlation and to optimize Rh content. In order to conduct a close comparison, all current density data shown here were normalized to total noble metal mass, i.e. Pt+Rh+Ir. Therefore, the observed trends in EOR activity directly reflects mass specific reactivity.

Figure 3.26a displays cyclic voltammograms (CV) of PtRh/SnO_2/C catalysts and the CVs showed a systematic variation with the relative Pt/Rh ratio. The surface oxide formation on PtRh/SnO_2 NPs commences at around 0.35V, which is more negative than that observed on pure Pt NPs. With increasing Rh content, one can find a larger current of oxygen adsorption and desorption and the surface oxide reduction peak potential shifts to more negative values. We attribute the variations to the alloy of Rh with Pt because Rh is less noble and more prone to be oxidized compared with Pt. The change in hydrogen adsorption/desorption ($H_{ads/des}$) feature is more complicated due to the existence of oxide substrate. It has been reported that surface hydrogen adsorption could be influenced due to the so-called strong metal support interaction effect (SMSI) [181]. Figure 3.26b presents the anodic polarization curves of all the PtRh/SnO_2/C catalysts in ethanol-containing electrolyte. Hydrogen desorption feature is inhibited on all catalysts, indicating strong adsorption of ethanol molecules on the active sites. The profile demonstrates the onset potential of ethanol oxidation is just above 0.15V, a much lower potential compared to that of Pt/C and PtRu/C (0.4V and 0.3V, respectively) [131]. In these measurements the PtRh/SnO_2 catalysts with atomic ratio Pt:Rh:Sn of 1:1/2:1 and 1:1/3:1 show the best activity with the most negative EOR reaction onset potential and highest current yield. The results suggests a moderate Rh content gives best EOR activity, while too high or too low Rh content causes a lowered activity.

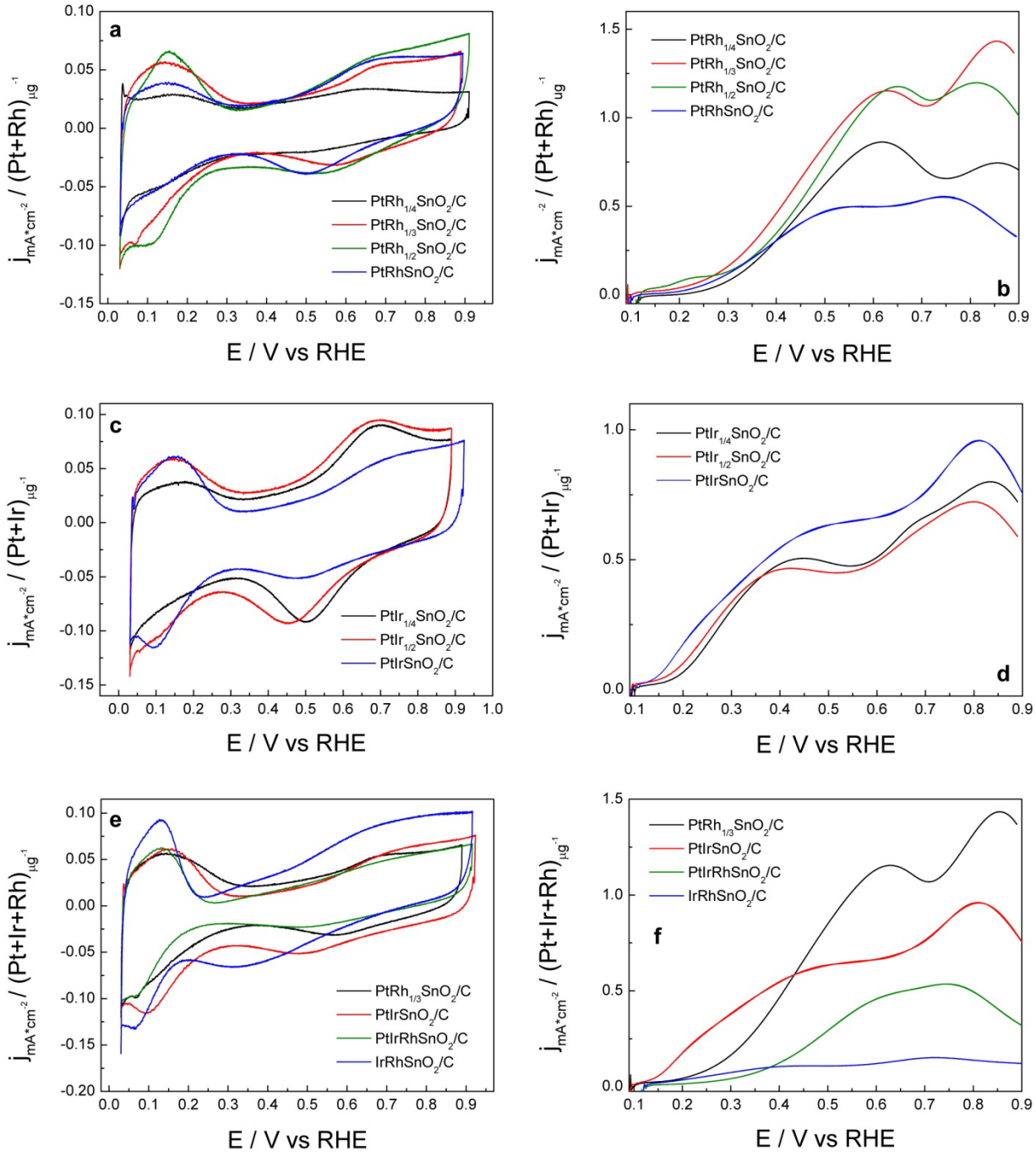

Figure 3.26 (a) Cyclic voltammegram of four $PtRh/SnO_2/C$ electrocatalysts with different Pt/Rh ratios in base electrolyte of 0.1M $HClO_4$ with scan rate: 10mV/s; b) Polarization curves of four $PtRh/SnO_2/C$ electrocatalysts in 0.1M $HClO_4$ with 0.5M ethanol with scan rate: 10mV/C; c) CV scans of three $PtIr/SnO_2/C$ samples with different Pt/Ir ratios; d) Polarization curves of three $PtIr/SnO_2/C$ samples; e) CV scans of $PtRh_{1/3}/SnO_2/C$, $PtIr/SnO_2/C$, $IrRh/SnO_2/C$, and $PtIrRh/SnO_2/C$ catalysts; f) Polarization curves of $PtRh_{1/3}/SnO_2/C$, $PtIr/SnO_2/C$, $IrRh/SnO_2/C$, and $PtIrRh/SnO_2/C$ catalysts. The total noble metal mass (Pt+Rh+Ir) specific current densities were employed in the comparison, and all measurements were carried out in room temperature.

Figure 3.26c and d display CV scans from a series of $PtIr/SnO_2/C$ catalysts (with atomic ratio Pt:Ir:Sn of 1:1:1, 1:1/2:1 and 1:/1/4:1) in both base electrolyte and ethanol-containing electrolyte. Similarly, one can also observe the enhanced surface oxide formation current and the negatively shifted oxide reduction potential with increasing Ir content. The enlarged double layer current is due to the existence of iridium oxide (confirmed by XAS data in Section 3.3.4). $PtIr/SnO_2/C$ catalysts also possess excellent EOR activity like $PtRh/SnO_2$, with a reaction onset potential just above 0.1V and a high current yield. The $PtIr/SnO_2/C$ catalyst with highest Ir content, i.e. atomic ratio Pt:Ir:Sn of 1:1:1, demostrate the best activity, which is different from what was observed in $PtRh/SnO_2$ catalysts. We have observed binary IrSn catalyst (Section 3.4) showed high activity in low potential region, i.e. 0.1V-0.5V; therefore, the high activity exhibited in $PtIr/SnO_2/C$ with highest Ir content can be attributed to the synergy between Ir and Sn elements.

$PtRh/SnO_2$ and $PtIr/SnO_2$ electrocatalysts all show excellent EOR activity and improved capability to split C-C bond in ethanol (shown below); therefore, it is interesting to explore the reactivity and selectivity of $PtIrRh/SnO_2$ and $IrRh/SnO_2$ catalysts in ethanol electro-oxidation. Figure 3.26e includes CV scans of $PtRh_{1/3}/SnO_2/C$ (with atomic ratio Pt:Rh:Sn of 1:1/3:1), $PtIr/SnO_2/C$ (with atomic ratio Pt:Ir:Sn of 1:1:1), $IrRh/SnO_2/C$ (with atomic ratio Ir:Rh:Sn of 1:1:1) and $PtIrRh/SnO_2/C$ (with atomic ratio Pt:Ir:Rh:Sn of 1:1:1:1) catalysts. $IrRh/SnO_2/C$ give the highest oxide formation current and the most negative oxide reduction potential, due to the less nobility possessed by Ir and Rh with respect to Pt. As indicated in Figure 3.26f, the $PtIr/SnO_2$ sample gives lowest EOR onset potential, which is about 50mV more negative compared to that of the $PtRh_{1/3}/SnO_2$ catalyst, but the latter catalyst yields higher EOR current compared to that from $PtIr/SnO_2/C$ when applied potential was higher than ca. 0.42V. The

oxidized iridium tended to segregate on surfaces of PtIr nanoislands, resulting in a relatively higher Ir content in surface than the bulk composition and consequently a lower Pt content in the surface. Iridium is easily oxidized at higher potentials, causing decreased ethanol adsorption and consequently reduced EOR activity. The PtIrRh/SnO_2 catalyst delivers lower current than both $PtRh_{1/3}/SnO_2$/C and PtIr/SnO_2/C, and the IrRh/SnO_2/C catalyst is the poorest one for EOR, which is almost inactive.

In order to fully evaluate the activity and stability of PtRh/SnO_2/C and PtIr/SnO_2/C catalysts in ethanol electro-oxidation, a set of electrochemical techniques, including anodic polarization, quasi-steady-state measurement and chronoamperometric (CA) experiments, were carried out to examine EOR activity of above two best ternary catalysts, $PtRh_{1/3}/SnO_2$/C (with atomic ratio Pt:Rh:Sn of 1:1/3:1) and PtIr/SnO_2/C (with atomic ratio Pt:Ir:Sn of 1:1:1), compared to Pt/SnO_2/C, the best Pt-based binary electrocatalyst. As indicated in Figure 3.27, $PtRh_{1/3}/SnO_2$/C and PtIr/SnO_2/C demonstrates superior performance in ethanol electro-oxidation. Anodic polarization curves (Figure 3.27 a&b) reveal a higher activity of $PtRh_{1/3}/SnO_2$/C and PtIr/SnO_2/C compared to Pt/SnO_2/C due to a lowered reaction onset potential and larger EOR current. Tafel plots and CA curves (Figure 3.27 c-f) indicate a better stability of $PtRh_{1/3}/SnO_2$/C and PtIr/SnO_2/C, as a larger EOR current were produced in prolonged periods of reaction. All the current densities presented here were normalized to Pt mass, as Rh and Ir were considered as active promoter to Pt.

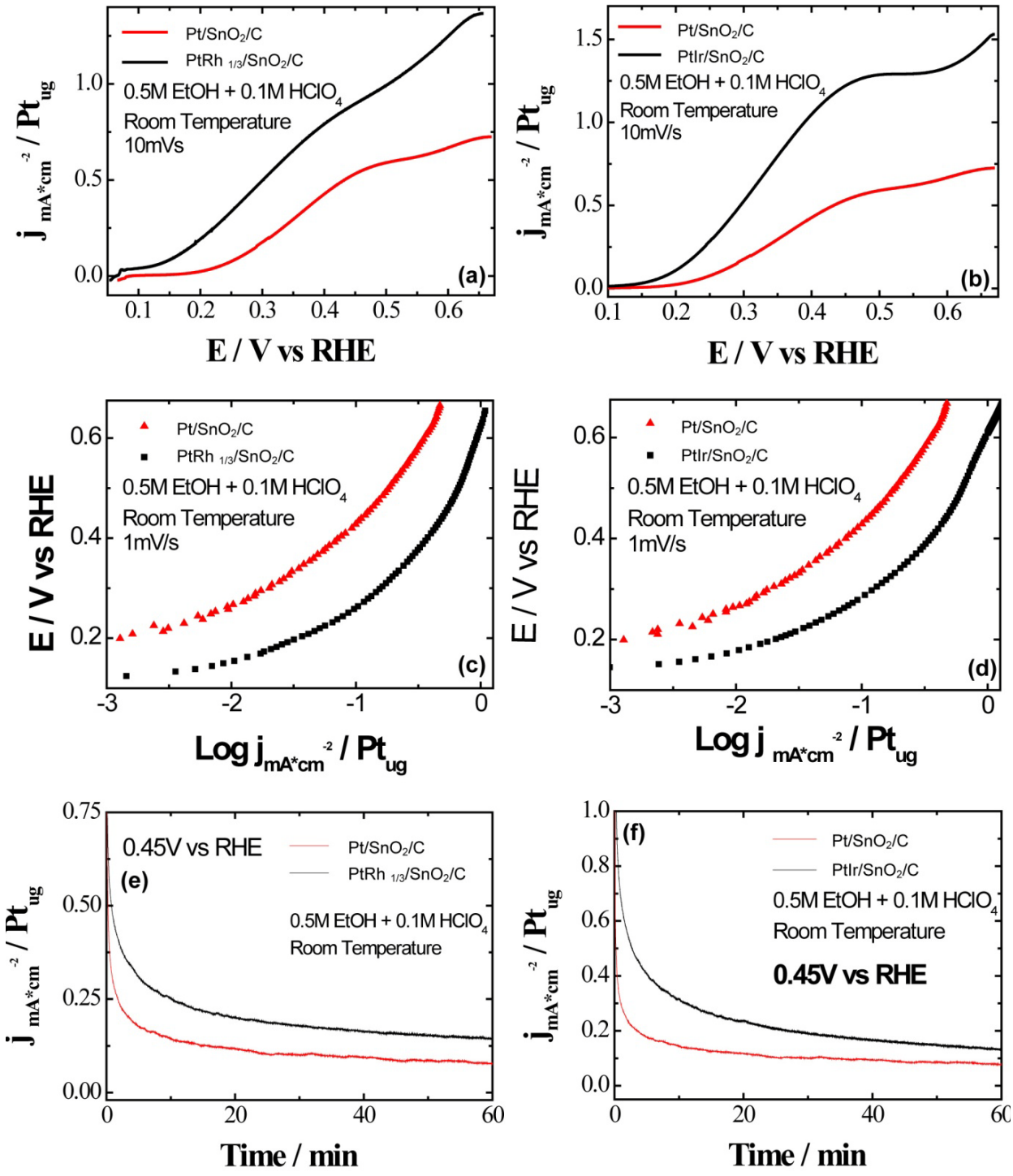

Figure 3.27 Electrochemical characterizations of $PtRh_{1/3}/SnO_2/C$ and $PtIr/SnO_2/C$ electrocatalysts. Anodic polarization curves of $PtRh_{1/3}/SnO_2/C$ & $Pt/SnO_2/C$ (a), and $PtIr/SnO_2/C$ & $Pt/SnO_2/C$ (b), with scan rate of 10mV/s. Tafel plots of $PtRh_{1/3}/SnO_2/C$ & $Pt/SnO_2/C$ (c), and $PtIr/SnO_2/C$ & $Pt/SnO_2/C$ (d), with scan rate of 10mV/s. CA measurements of $PtRh_{1/3}/SnO_2/C$ & $Pt/SnO_2/C$ (e), and $PtIr/SnO_2/C$ & $Pt/SnO_2/C$ (f) under 0.45V versus RHE. Electrolyte: 0.5M ethanol in 0.1M $HClO_4$. All measurements were conducted in room temperature.

3.3.3 *In Situ* IRRAS Studies of Carbon-Supported MM'/SnO_2 Electrocatalysts

3.3.3.1 Carbon-Supported PtRh/SnO_2 NP Electrocatalysts

In order to gain insight on the reaction mechanisms of ethanol electro-oxidation reaction on above catalysts, we carried out *in situ* IRRAS studies to reveal the reaction intermediates and products distribution information. In previous sections our combined theoretical and experimental studies have demonstrated ternary Pt-Rh-SnO_2 system could break C-C bond and fully oxidize ethanol to CO_2. The four PtRh/SnO_2/C electrocatalysts with different Pt/Rh ratios were employed to establish composition-selectivity correlation and to optimize catalysts' composition. It is of great interest because: i) high EOR activity and high selectivity towards CO_2 formation are both essential goals in ethanol electrocatalysis; ii) Rh is a very rare and expensive material and Rh alone is not active for ethanol electro-oxidation.

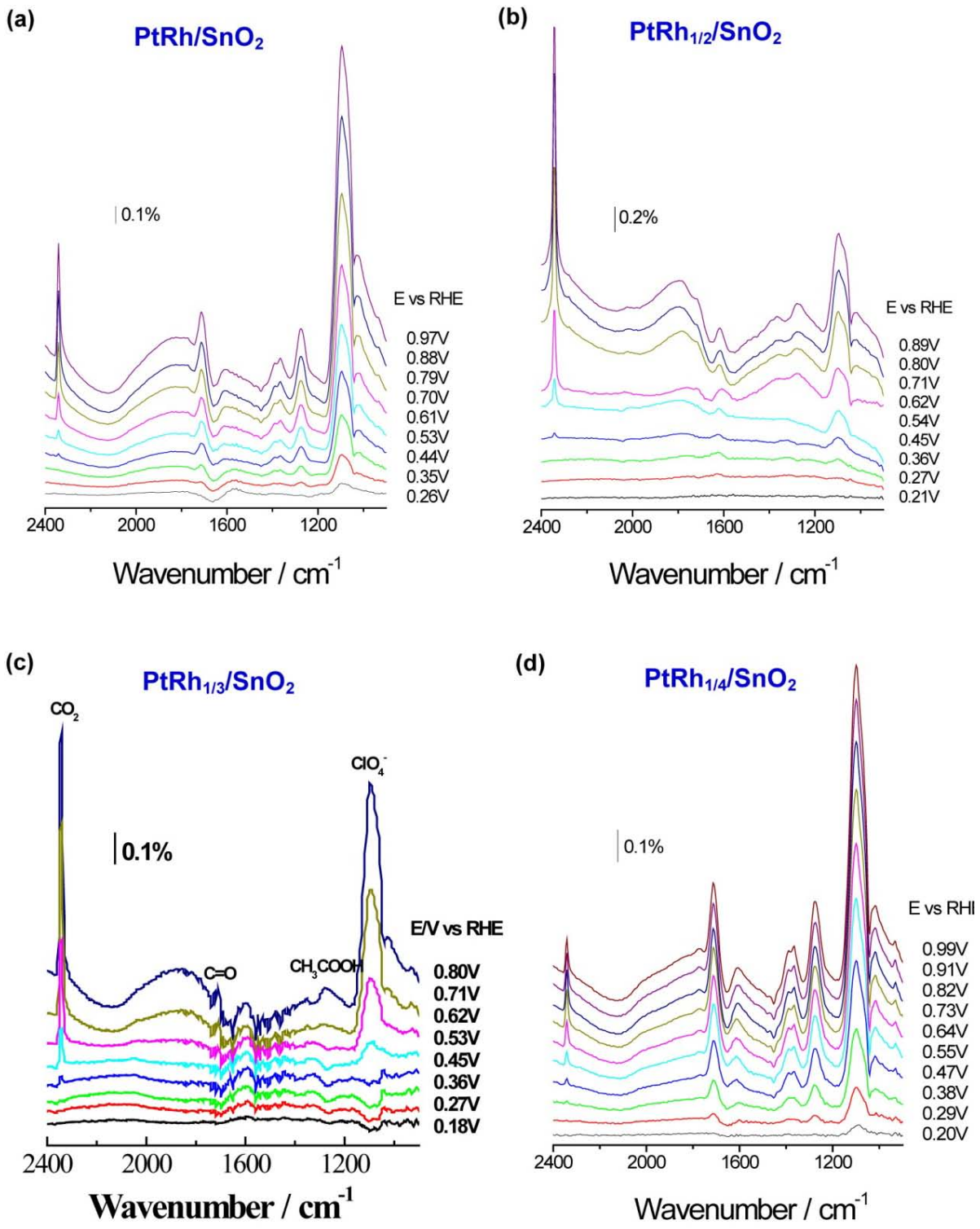

Figure 3.28 *In situ* IRRAS spectra recorded during EOR on four carbon-supported $PtRh/SnO_2$ NP electrocatalysts with different compositions: (a) $PtRh/SnO_2$, (b) $PtRh_{1/2}/SnO_2$, (c) $PtRh_{1/3}/SnO_2$, and (d) $PtRh_{1/4}/SnO_2$.

Figure 3.29a-d show the recorded infrared spectra during ethanol electro-oxidation on four $PtRh/SnO_2/C$ electrocatalysts, and the frequencies and band assignments are listed in Table 3.1. Carbon dioxide (CO_2), acetic acid (CH_3COOH) and acetaldehyde (CH_3CHO) are the main products of ethanol oxidation in acidic solution. The positive-going peak near 2343cm^{-1} is attributed to the asymmetric stretch vibration of CO_2, the product of ethanol total oxidation pathway. It can be observed that CO_2 bands on two $PtRh/SnO_2/C$ catalysts (with atomic ratio Pt:Rh:Sn of 1:1/2:1 and 1:1/3:1) show very high intensity, indicating the formation of large amounts of CO_2. The band located around 1705cm^{-1} can be assigned to the stretch vibration of the C=O bond, found in both acetaldehyde and acetic acid. The band at 1598cm^{-1} represents the H-O-H deformation of adsorbed water molecules. The C=O stretching mode of adsorbed acetaldehyde and acetyl around 1620-1635cm^{-1} cannot be resolved because of the presence of the strong water band. The bands at 1350cm^{-1} and around 1396-1410cm^{-1} are assigned to CH_3 in-plane bending mode and O-C-O stretching of adsorbed acetate, respectively. These two bands are close and difficult to distinguish. A well-defined band at 1280cm^{-1} is the characteristic absorption of C-O stretching in acetic acid, which is usually employed for quantitative analysis of acetic acid. The C-H wagging vibration in CH_3CHO, at 1108cm^{-1}, overlaps with the strong band at 1110cm^{-1} of Cl-O stretching in ClO_4^-. The strong band for ClO_4^- ions is the consequence of its accumulation in the thin layer cell to compensate the increasingly positive electrode potential. The downward band at 1044cm^{-1} is the signature peak for the C-O stretching vibration of CH_3CH_2OH, representing the consumption of ethanol by oxidation. The band observed at 933cm^{-1} is assigned to C-C-O asymmetric stretching of acetaldehyde, which is used for quantification of acetaldehyde in this study.

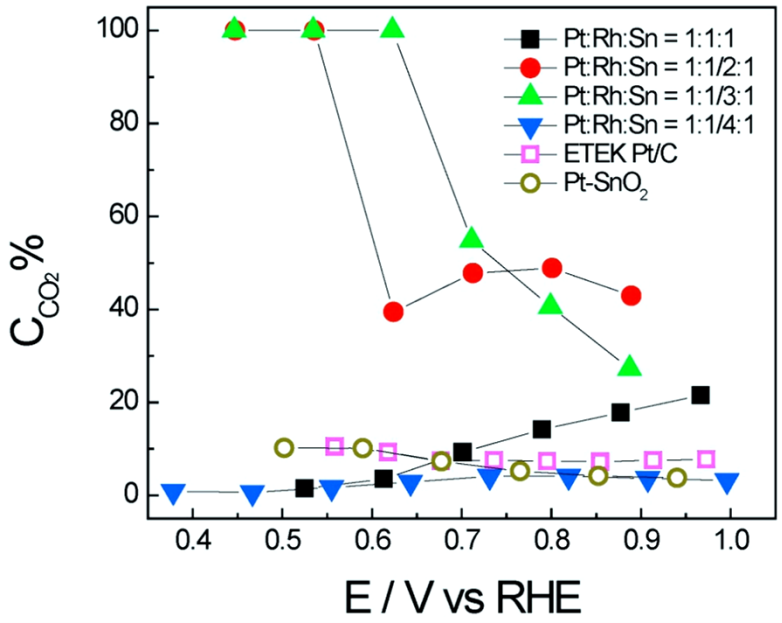

Figure 3.29 The variation of different catalysts' EOR total oxidation current efficiency, i.e. $C_{CO_2} / C_{CO_2+CH_3COOH+CH_3CHO}$, versus applied potential.

In situ IRRAS studies were also carried out on commercial ETEK Pt/C and $Pt/SnO_2/C$ catalysts for comparison reasons (not shown). In order to better compare the selectivity of these four $PtRh/SnO_2$ electrocatalysts, the variation of integrated band intensities of CO_2 (2343cm^{-1}), CH_3CHO (933cm^{-1}) and CH_3COOH (1280cm^{-1}) with applied potential are obtained (not shown). One can find CO_2 produces strongest bands in the spectra of two $PtRh/SnO_2$ catalysts (with atomic ratio Pt:Rh:Sn of 1:1/2:1 and 1:1/3:1), while CH_3COOH bands shows higher intensity on the other two $PtRh/SnO_2$ catalysts (with atomic ratio Pt:Rh:Sn of 1:1:1 and 1:1/4:1). CH_3CHO is only being produced in small amounts at all $PtRh/SnO_2$ catalysts. The EOR total oxidation current efficiency, defined as the ratio between charge contribution from total oxidation pathway (C_{CO2}) and charge contribution from both total oxidation and partial oxidation pathways ($C_{CO2+CH3COOH+CH3CHO}$), could directly represent catalysts' capability to split C-C bond and its variation versus applied potential is shown in Figure 3.29. The quantity of different oxidation products are determined using the same method shown in Section 3.2.2.3. The production of one

CO_2, CH_3COOH and CH_3CHO molecule released 6, 4 and 2 electrons, respectively. Therefore, $C_{CO_2} / C_{CO_2+CH_3COOH+CH_3CHO}$ are calculated following the equation:

$$\frac{C_{CO_2}}{C_{CO_2}+C_{CH_3COOH}+C_{CH_3CHO}} = \frac{6*Q_{CO_2}}{6*Q_{CO_2}+4*Q_{CH_3COOH}+2*Q_{CH_3CHO}} \quad (3.4)$$

One can find in the potential region of practical interest (i.e. lower than 0.7V), the two best $PtRh/SnO_2/C$ catalysts ($PtRh_{1/2}/SnO_2/C$ and $PtRh_{1/3}/SnO_2/C$) could offer above 40% total oxidation current efficiency. As our knowledge, it is above all known ethanol oxidation catalysts. Therefore, catalysts' selectivity highly depended on the composition, i.e. Pt/Rh ratio, and a moderate Rh content yields highest selectivity to CO_2. We attribute this phenomenon to both geometric "ensemble effect" and electronic "ligand effect". DFT calculations propose an optimum pathway for C-C bond breaking at the $Rh,Pt/SnO_2$ interface: $*CH_3CH_2OH \rightarrow *CH_3CHO+H* \rightarrow *CH_2CH_2O+2H* \rightarrow *CH_2+*CH_2O+2H*$. The dehydrogenation process is favored on Pt sites, while C-C bond cleavage preferes Rh sites. One can find multiple adjacent Pt sites are required for abstracting atomic hydrogen in ethanol molecules, therefore, a higher Pt content than Rh content is desired in this system. When Rh content is too low, like in the $PtRh_{1/4}/SnO_2/C$ catalyst, there is not enough Rh sites for the C-C bond splitting reaction. Moreover, the metal-CH_2CH_2O reaction leading to C-C bond breaking is facilitated by back-donation from the π orbitals of CH_2CH_2O to the d orbital of the metal atoms, and Rh is a better candidate than Pt because of its electronic structure. In the mixture of Pt and Rh, the strong interaction between them is accompanied by an electron transfer from Rh to Pt and more d-states of Rh become available above the Fermi level. It suggests that in PtRh system Rh can be more active while Pt becomes more inert, which promotes bond cleavage on Rh sites and at the same time prevents ethanol partial oxidation on Pt sites. Thus, the results imply that a suitably higher

amount of Pt could empty more d-states of Rh, thereby improving the selectivity to total oxidation.

However, it has to be noted that the employment of IRRAS technique in quantitative studies owns several limitations: 1) There are both accumulation and diffusion of EOR products undergoing at the same time, and the amounts being detected really are the total amounts produced subtracted by the amounts that diffused away from the thin-layer. Different products, such as CO_2, CH_3COOH and CH_3CHO, are expected to have different rates when leaving the thin-layer. CO_2 is the most volatile among the three major products, so one would expect that CO_2 diffuses faster than CH_3COOH and CH_3CHO. 2) In the thin-layer, reaction products are likely to be re-adsorbed and further oxidized, which could be different from the case in real fuel cell environment. 3) It is claimed CH_4 could also be an EOR product because part of $-CH_3$ fragments in CH_3CH_2OH molecules are not oxidized to CO_2, and they are reduced to CH_4 in hydrogen UPD potential region and then desorbed from catalyst surface. IRRAS study here appears to be not very useful in detecting CH_4, which could cause an imprecise determination of current efficiency. 4) The instrument sensitivity might be decreased because of: the uneven surface of studied electrodes (prepared by casting NP catalysts ink on an Au disk), the consequently thicker and ununiform thin electrolyte layer, and the strong IR absorption by amorphous carbon support.

On-line differential electrochemical mass spectroscopy (DEMS) has been considered as a quantitative tool to determine ethanol electro-oxidation products. The Pt/SnO_2 catalyst shows lower CO_2 production than that on pure Pt catalyst, which is consistent with literature reports from both on-line DEMS and *in situ* FTIR studies [131-132]. However, the CO_2 production current efficiency on pure Pt, 5~10% as indicated in our IRRAS studies, is considerably higher than the

values determined from DEMS measurements, which are mostly in the range of 2~3%. Moreover, our IRRAS studies observe a very low production of CH_3CHO, while DEMS determines a considerable higher CH_3CHO generation in the same electrolyte. We attribute the different results from two techniques, IRRAS and DEMS, to their different reaction environments: thin-layer cell versus flow cell. In the thin-layer configuration, CH_3CHO is more likely to be re-adsorbed and further oxidized to CO_2 or CH_3COOH, while in the flow-cell setup in DEMS studies, CH_3CHO could easily desorb from catalyst surface once it formed. Nevertheless, on-line DEMS could be a very useful complement to the *in situ* IRRAS study, and currently the DEMS studies are undergoing in our lab to gain more information in catalysts' selectivity.

3.3.3.2 Carbon-Supported $PtIr/SnO_2$ and $PtIrRh/SnO_2$ NP Electrocatalysts

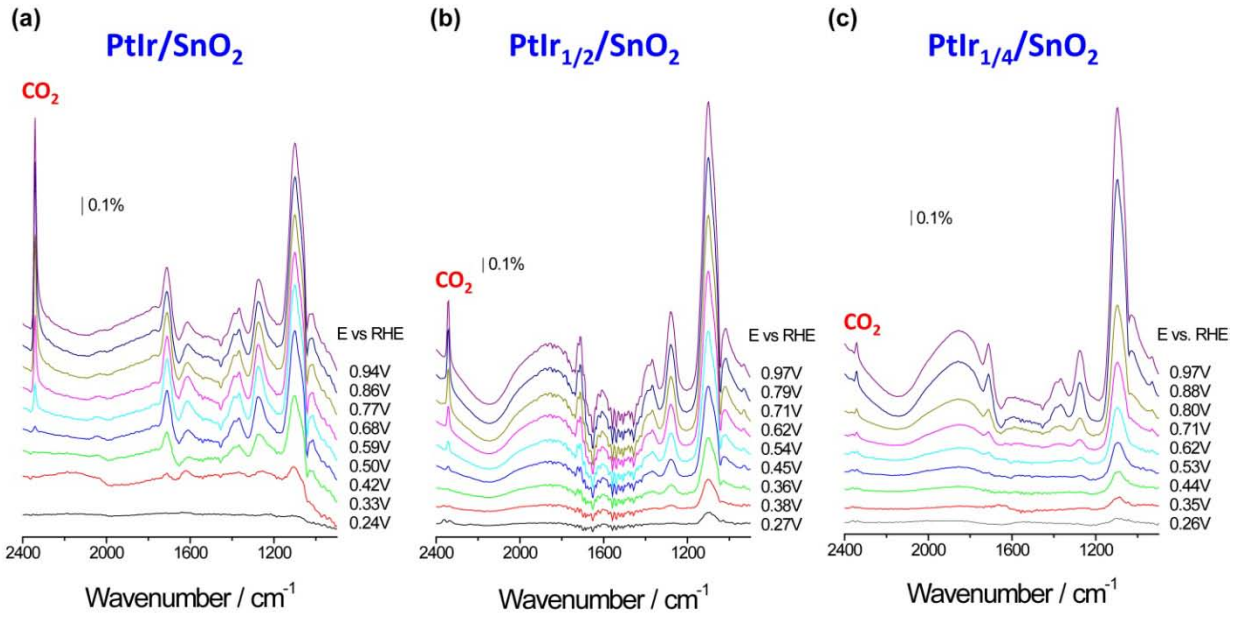

Figure 3.30 *In situ* IRRAS spectra recorded during EOR from all three $PtIr/SnO_2/C$ electrocatalysts with different compositions: (a) $PtIr/SnO_2/C$, (b) $PtIr_{1/2}/SnO_2/C$ and (c) $PtIr_{1/4}/SnO_2/C$.

Figure 3.30a-c display infrared spectra collected from three $PtIr/SnO_2/C$ catalysts:

PtIr/SnO_2/C, $PtIr_{1/2}$/SnO_2/C and $PtIr_{1/4}$/SnO_2/C. Similar to the ones from PtRh/SnO_2/C catalysts, carbon dioxide (CO_2), acetic acid (CH_3COOH) and acetaldehyde (CH_3CHO) are clearly identified from all spectra, suggesting the parallel reaction pathways undergoing on all above PtIr/SnO_2 catalysts. In order to better compare the selectivity of these three electrocatalysts, the variation of integrated band intensities of CO_2 (2343cm^{-1}), CH_3CHO (933cm^{-1}) and CH_3COOH (1280cm^{-1}) with applied potential for all PtIr/SnO_2 catalysts are determined (not shown). Figure 3.31 shows ethanol total oxidation current efficiencies change versus applied potential during ethanol electro-oxidation on three PtIr/SnO_2 catalysts. One can find the catalyst with highest Ir content, PtIr/SnO_2 sample with atomic ratio Pt:Ir:Sn of 1:1:1, gives reasonably enhanced selectivity toward CO_2 formation compared to Pt, while the other two PtIr/SnO_2 NP catalysts show lowered capability in C-C bond splitting compared to pure Pt.

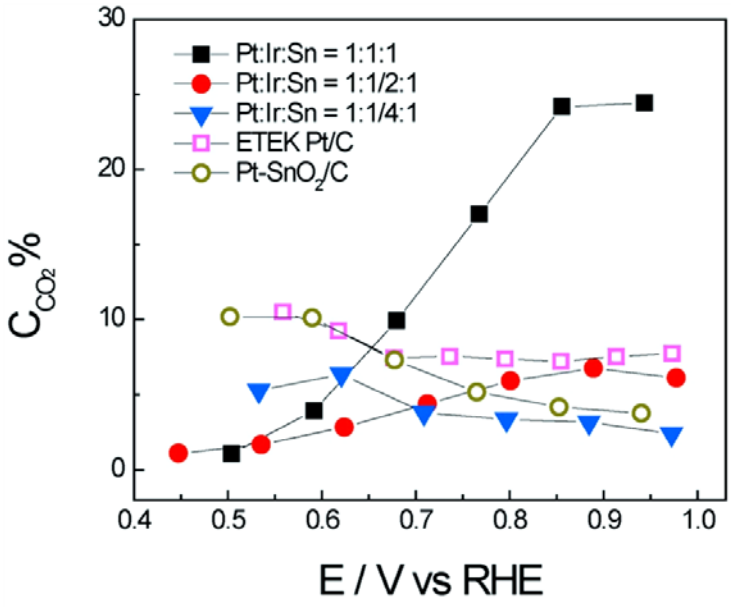

Figure 3.31 The variation of different electrocatalysts' EOR total oxidation current efficiency, i.e. $C_{CO_2} / C_{CO_2+CH_3COOH+CH_3CHO}$, versus applied potential.

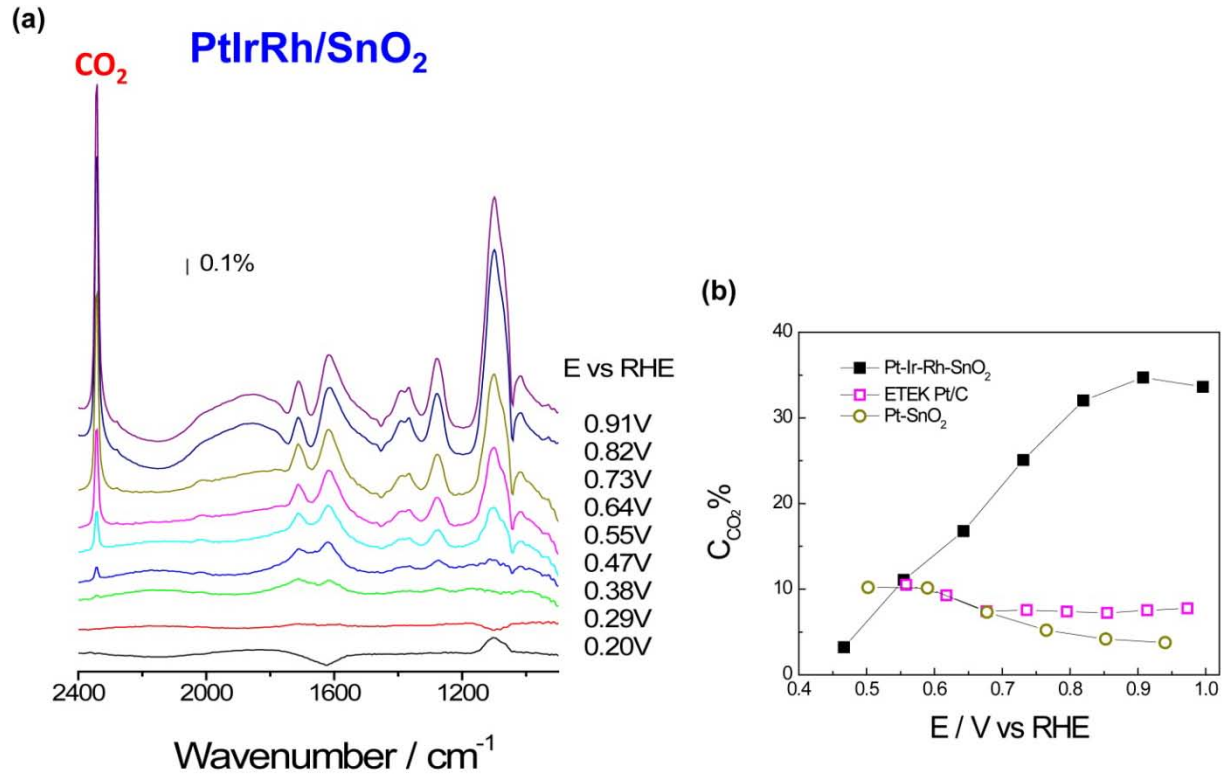

Figure 3.32 *In situ* IRRAS spectra (a) and the variation of EOR total oxidation current efficiency versus applied potential (b) from $PtIrRh/SnO_2/C$ electrocatalyst.

Figure 3.32 a and b show infrared spectra generated on the $PtIrRh/SnO_2/C$ catalyst and its ethanol total oxidation current efficiency determined from the infrared study. At high overpotential, this catalyst gives considerably high CO_2 production rate; however, it is still lower than the best $PtRh/SnO_2$ electrocatalysts. In summary, the CO_2 production efficiency of the catalysts decreases in the order of: $PtRh/SnO_2/C$ (with atomic ratio Pt:Rh:Sn of 1:1/2:1 and 1:1/3:1) > $PtIrRh/SnO_2/C$ (with atomic ratio Pt:Ir:Rh:Sn of 1:1:1:1) > $PtIr/SnO_2/C$ (with atomic ratio Pt:Ir:Sn of 1:1:1).

3.3.4 *In situ* XAS Study of $PtIr/SnO_2/C$ Electrocatalysts

In situ XAS studies of ternary Pt-Rh-SnO_2 electrocatalysts were extensively discussed in

Section 3.1.4 and Section 3.2.2.4, therefore, the results from *in situ* XAS study of $PtIr/SnO_2/C$ electrocatalyst are discussed in this section.

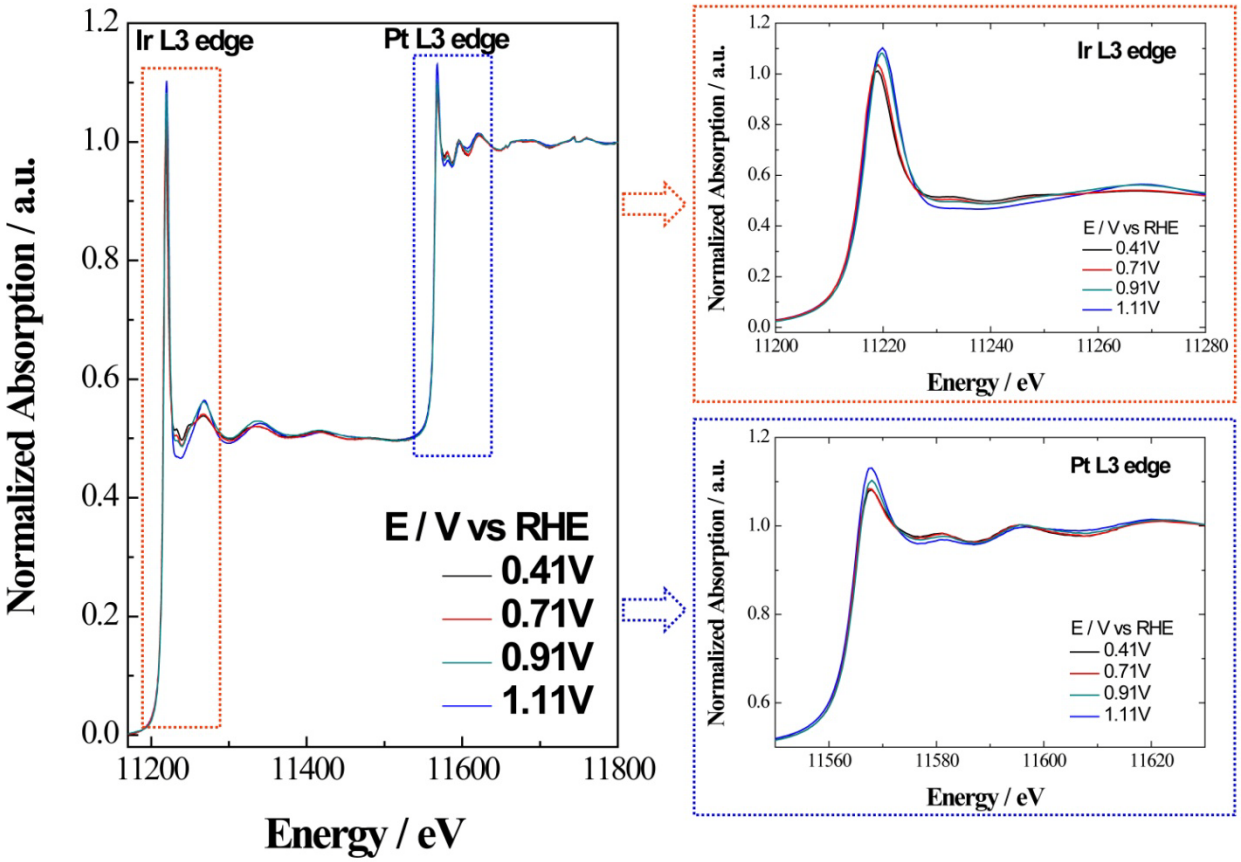

Figure 3.33 *In situ* XANES spectra of Pt L3 and Ir L3 edges of $PtIr/SnO_2/C$ electrocatalyst under different applied potentials.

In situ XANES spectra obtained from $PtIr/SnO_2/C$ electrocatalyst (with atomic ratio Pt:Ir:Sn of 1:1:1) are presented in Figure 3.33. One can see the L3 absorption edges of Pt and Ir are very close; hence the XANES feature of Pt L3 edge have a mixed impact from Ir L3 edge absorption. The much higher white line observed from Ir L3 edge compared to Ir black reference (not shown) at all applied potentials indicate an oxidized state of Ir. Both Ir and Pt spectra show a potential dependence, they start to be more oxidized when potential reached 0.97V and higher.

The absorption heights of Pt-L3 and Ir-L3 are nearly proportional to their contents, so we determine Pt/Ir ratio is 0.95, which is very close to the nominal value of 1.

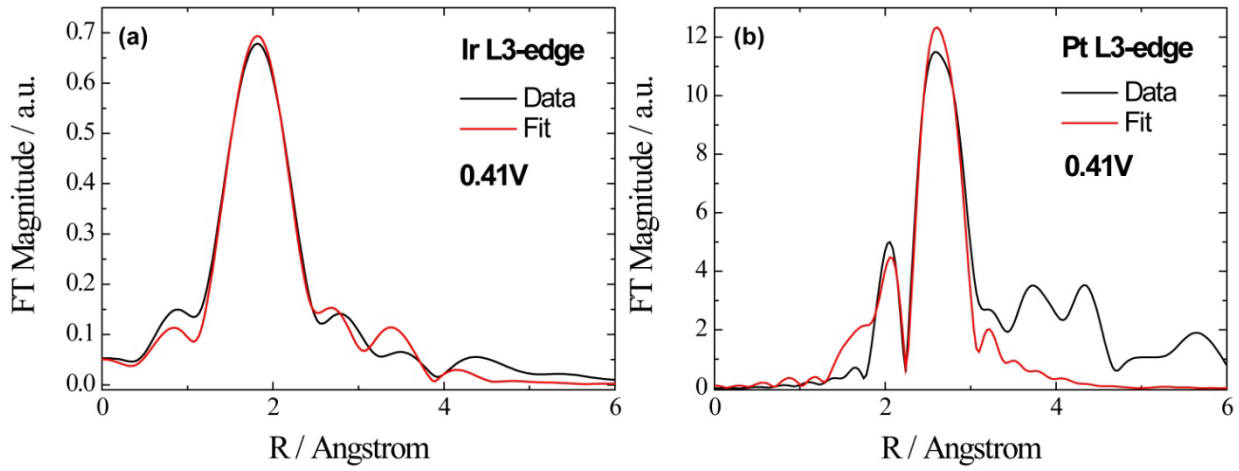

Figure 3.34 Fourier transform magnitudes of Ir-L3 edge (a) and Pt-L3 edge (b) of the $PtIr/SnO_2/C$ catalyst held at 0.41V in 1M $HClO_4$ and the respective first-shell fits. The fitting parameters and constraints are the same as Section 3.2.2.4. (With Q. Wang).

Figure 3.34 display the FT magnitudes of Pt-L3 and Ir-L3 edges and the respective first-shell fits. A reasonably good agreement between the fits and the original spectra is seen; the results of coordination numbers are summarized in Table 3.4. Fitting parameters and constraints are the same as Section 3.2.2.4. In the Ir model set-up, both contribution from metal (Pt and Ir) and oxygen are considered. In the Pt model set-up, influence from Ir is also taken into consideration; hence, there are three contributions: Pt-M (Ir+Pt), Ir-M (Ir+Pt), and Ir-O. Ir fitting results show non-metallic bond dominate over the metallic bond, indicating an oxidized state of Ir. Pt fitting results show Pt-M is predominant while Ir-M and Pt-O also contribute. The contracted Pt-M bond compared to Pt-Pt bond in bulk Pt is due to the influence from both Ir and O.

Table 3.4: EXAFS fitting results

	Coordination Number	Bond Length (Å)
Bulk Pt	12	2.775
Bulk Ir	12	2.7654
Ir-M	3.3 ± 0.6	2.61 ± 0.008
Ir-O	3.0 ± 0.4	2.11 ± 0.01
Pt-M	6.0 ± 1.4	2.75 ± 0.01

3.3.5 Summary

Carbon-supported MM'/SnO_2 NP electrocatalysts comprising SnO_2 NP cores decorated with multi-metallic nanoislands (MM' = PtRh, PtIr, IrRh, PtIrRh) were prepared using a seeded growth approach as synthetic analogues to the PtRh/SnO_2(110) model catalyst in our DFT study. An array of characterization techniques, XRD, HADDF-STEM, EDS and *in situ* XAS, were employed to establish the composition and architecture of the synthesized NPs.

A combination of electrochemical measurements and *in situ* IRRAS technique was used to investigate the catalytic properties of the MM'/SnO_2 NP electrocatalysts for ethanol electro-oxidation. Both EOR reactivity and selectivity towards CO_2 formation of several of these M/SnO_2/C NP catalysts are significantly improved with respect to Pt/C and Pt/SnO_2/C. Among systems studied, PtRh/SnO_2/C electrocatalysts with a suitable Rh content, i.e. catalysts with atomic ratio Pt:Rh:Sn = 1:1/2:1 and 1:1/3:1, exhibit highest EOR activity and selectivity towards ethanol total oxidation, and we attribute this phenomenon to both ensemble effect and ligand effect. PtIr/SnO_2/C catalyst with highest Ir content, i.e. the catalyst with atomic ratio Pt:Ir:Sn = 1:1:1, shows best activity among three PtIr/SnO_2 catalysts. The PtIrRh/SnO_2/C electrocatalyst (with atomic ratio Pt:Ir:Rh:Sn of 1:1:1:1) displays lower activity compared to PtRh/SnO_2/C and PtIr/SnO_2/C electrocatalysts, and the IrRh/SnO_2/C electrocatalyst (with atomic ratio Ir:Rh:Sn of

1:1:1) is the poorest one. The CO_2 production efficiency of the above catalysts decreases in the order of: PtRh/SnO_2 (with atomic ratio Pt:Rh:Sn of 1:1/2:1 and 1:1/3:1) > PtIrRh/SnO_2 (with atomic ratio Pt:Ir:Rh:Sn of 1:1:1:1) > PtIr/SnO_2 (with atomic ratio Pt:Ir:Sn of 1:1:1).

These findings presented in this section are of great importance in terms of understanding and designing novel nanostructured materials with substantially enhanced activity and selectivity in ethanol electro-oxidation.

3.4 Enhanced Catalytic Activity of Ir-Based Electrocatalysts for Ethanol Electro-oxidation at Low Over-potentials [182]

Platinum has been extensively studied for fuel cell electrocatalysis, and it has been learned that during EOR Pt sites are rapidly blocked by poison species, namely CO, from ethanol dissociative adsorption. Platinum is frequently alloyed with a second element to improve its EOR activity based on the bi-functional effect and/or electronic effect, and Pt-Ru and Pt-Sn are the best known Pt-based binary electrocatalysts. Numerous spectroscopic studies demonstrate that acetaldehyde and acetic acid are the main EOR products on Pt, Pt-Ru and Pt-Sn, with carbon dioxide appearing only at extreme over-potentials. In previous sections we discussed a ternary Pt-Rh-SnO_2 electrocatalyst which is effective in splitting the C-C bond in ethanol at room temperature due to the synergistic effect between the three constituents. We also found that Ir together with Sn could modify Pt and the ternary Pt-Ir-SnO_2 electrocatalyst demonstrated a considerably enhanced EOR activity.

On the other hand, the catalytic property of iridium for ethanol electro-oxidation has yet received enough attention; though there have been attempts to compare Ir with Pt [126-128]. Furthermore, for formic acid oxidation, it is reported that single crystal Ir surfaces have different activities for poison formation and for main oxidation reaction [183]. In addition, the catalytic activities of Ir electrodes may depend on the properties and thickness of surface oxide film which, in turn, changes with pH [184-186].

In this section, we employ a combination of electrochemical and *in situ* spectroscopic means to improve our understanding of pure Ir and Ir-based binary electrocatalysts (Ir-Ru and Ir-

Sn) in ethanol electrocatalysis. The Ir-based binary electrocatalysts were prepared using a simple thermal decomposition method, and the morphology of obtained catalysts was characterized by HRTEM. We demonstrate that Ir-based electrocatalysts exhibit much higher EOR activity compared to pure Pt in low over-potential region of 0.1V-0.6V, and Ir-Sn displays most profoundly enhanced activity among the Ir-based catalysts. The promotional effect of Sn is likely due to both bi-functional effect and electronic effect. Our *in situ* infrared studies also reveal that ethanol adsorbs mainly as C2 species on Ir-based catalysts and the dominant EOR pathway is partial oxidation pathway forming CH_3COOH. The results are of great importance in terms of understanding the catalytic properties of iridium and searching novel materials with substantially enhanced catalytic activity in ethanol electro-oxidation.

3.4.1 Physical Characterization

Figure 3.35a-h display typical TEM images of Pt/C, Ir/C, Ir_9Ru_1/C and Ir_9Sn_1/C electrocatalysts. Pt nanoparticles are mostly in spherical shape, with an average size of about 3nm, uniformly distributing over the amorphous carbon support. Ir/C catalyst is also composed of fine spherical nanoparticles evenly dispersed on the carbon support, and Ir/C shows a smaller average particle size of 1~2nm. Binary catalysts, Ir_9Ru_1/C and Ir_9Sn_1/C, exhibit generally larger particle sizes, broader distribution, more irregular shape particles, and certain degree of particle agglomeration. The morphologies of the two binary catalysts are likely caused by the high temperature (400°C) annealing during syntheses, and right now the preparation of these catalysts with a modified low temperature synthetic method is undergoing in our group. For a close comparison of electrochemical features of these catalysts, all current densities data in this study

are normalized to electrochemically active surface area (ECSA) of the catalysts, which are determined from the electric charges of hydrogen adsorption and desorption, assuming the charge of 210μC/cm^2 on Pt and 169μC/cm^2 on Ir [187].

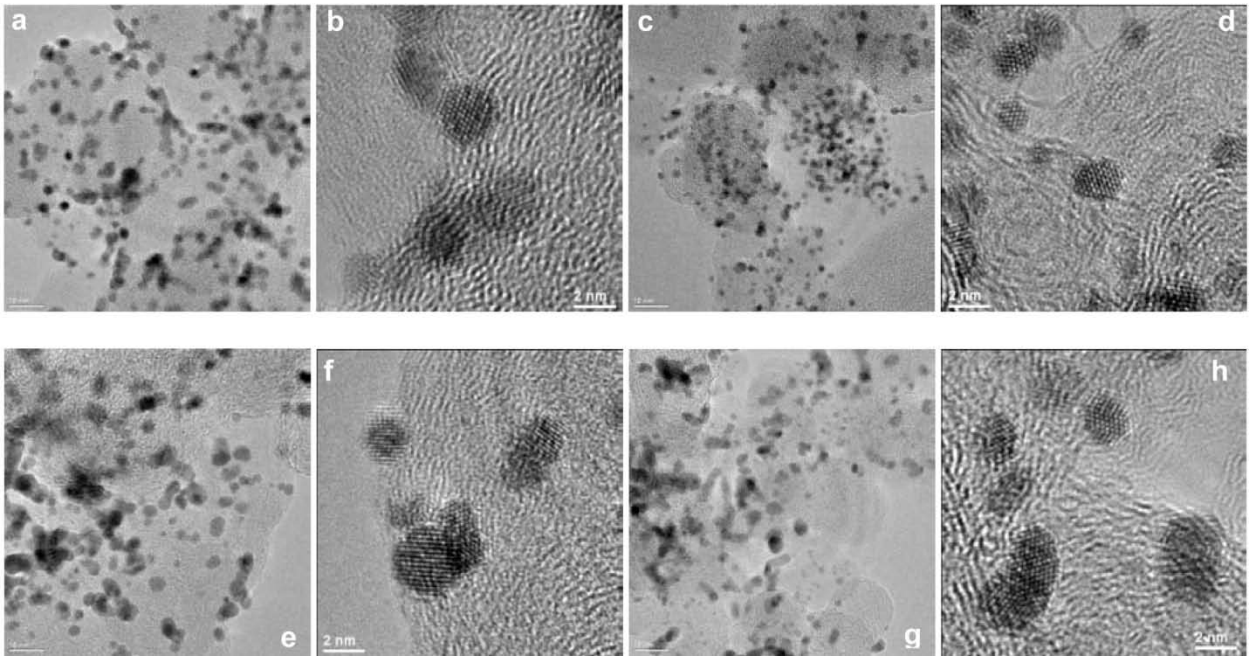

Figure 3.35 Typical TEM images of Pt/C (a&b), Ir/C (c&d), Ir_9Ru_1/C (e&f) and Ir_9Sn_1/C (g&h) electrocatalysts.

3.4.2 Electrochemical Measurements

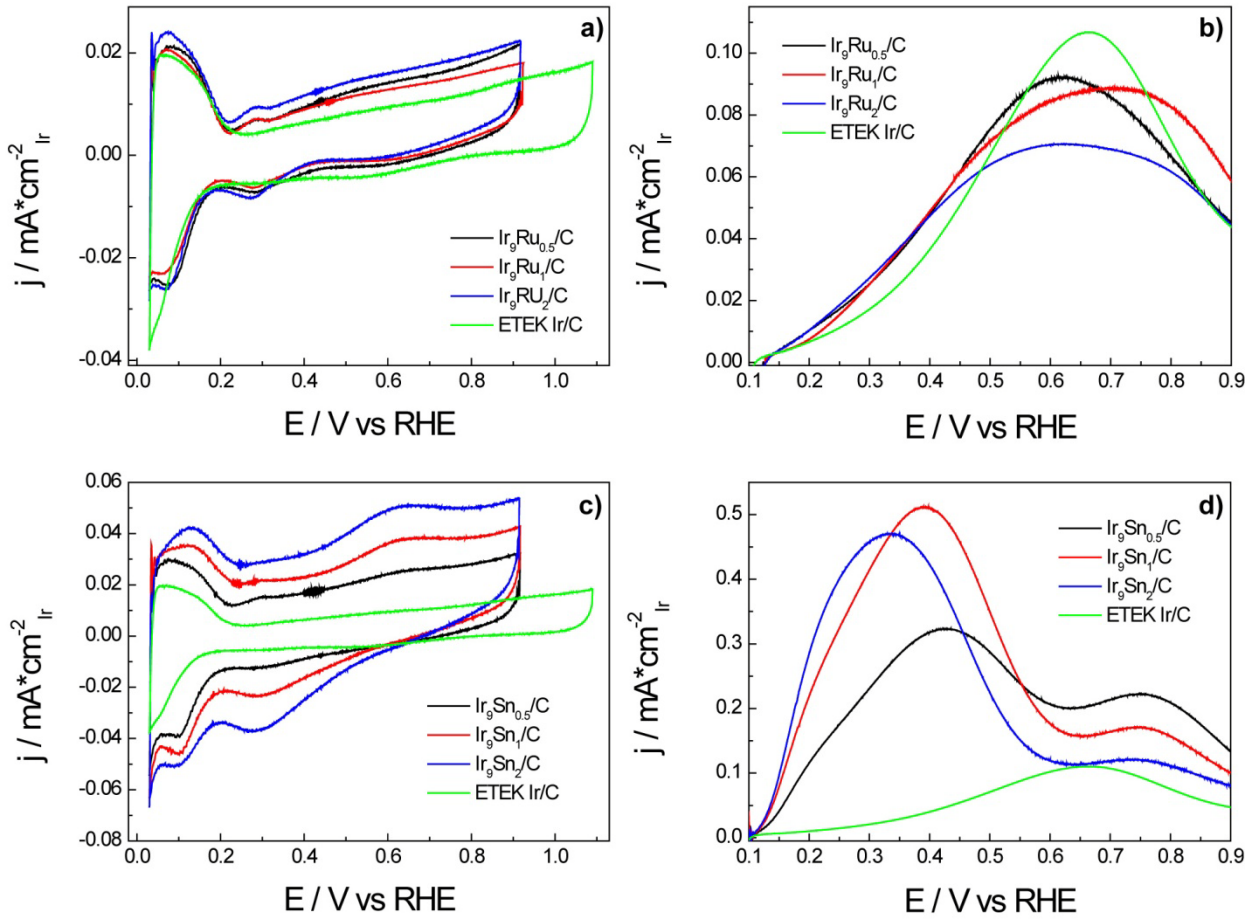

Figure 3.36 CV scans (a&c) in base electrolyte of 0.1M $HClO_4$ and anodic polarization curves (b&d) in ethanol-containing electrolyte of 0.5M ethanol in 0.1M $HClO_4$ of Pt-Ru/C and Pt-Sn/C catalysts with different compositions. Scan rate: 10mV/s.

Ir-Ru and Ir-Sn binary catalysts with three different compositions were synthesized and their activities were compared using potential dynamic measurements. Figure 3.36a and b show CV scans of pure Ir and a series of Ir-Ru binary catalysts with atomic ratio Ir:Ru of 9:0.5, 9:1 and 9:2 in both supporting electrolyte and ethanol containing electrolyte. The electrochemical behavior of the Ir-Ru binary catalysts are not very sensitive to Ru content, CV scans and polarization curves are very similar regardless of Ir/Ru ratio. Ru shows very limited promotional effect to the EOR activity of pure Ir, while it is demonstrated with a much profound promotional effect to pure Pt catalyst in catalyzing ethanol electro-oxidation. In binary Pt-Ru catalyst, Pt

accomplishes the chemisorption of ethanol, whereas Ru forms a surface oxy-hydroxide which subsequently oxidizes the carbonaceous adsorbates. The insufficient enhancement from Ru might indicate a different reaction mechanism on Ir from that on Pt.

Figure 3.36c and d show CV scans of pure Ir and Ir-Sn binary catalysts with atomic ratio Ir:Sn of 9:0.5, 9:1 and 9:2. It can be seen that unlike the case of Ir-Ru, the effect of Sn component is very profound; CV and polarization curves of Ir-Sn catalysts are distinctly different from that of pure Ir. Ir-Sn CV shows increasing double layer capacitance and enlarged $Oxide_{form/red}$ current with higher Sn content. Polarization curves of pure Ir and Ir-Ru catalysts present single oxidation peak centered at around 0.65V in the potential region of 0.1V-0.9V. Even with only 5% Sn content in $Ir_9Sn_{0.5}$ electrocatalyst, polarization curve profile is different from that on pure Ir. While on Ir-Sn catalysts, polarization curves shows the first oxidation peak in 0.35V-0.45V, followed by a second oxidation peak centered at around 0.75V with lower current density. With the increase of Sn content, center of the first oxidation peak shifts to more negative potential, and the peak current of the second peak decreases. It can be seen that Ir-Sn loses most of its activity when the potential is higher than 0.5V, we ascribe it to the intensive surface oxide formation, as indicated from CV, making the surface inactive for ethanol adsorption.

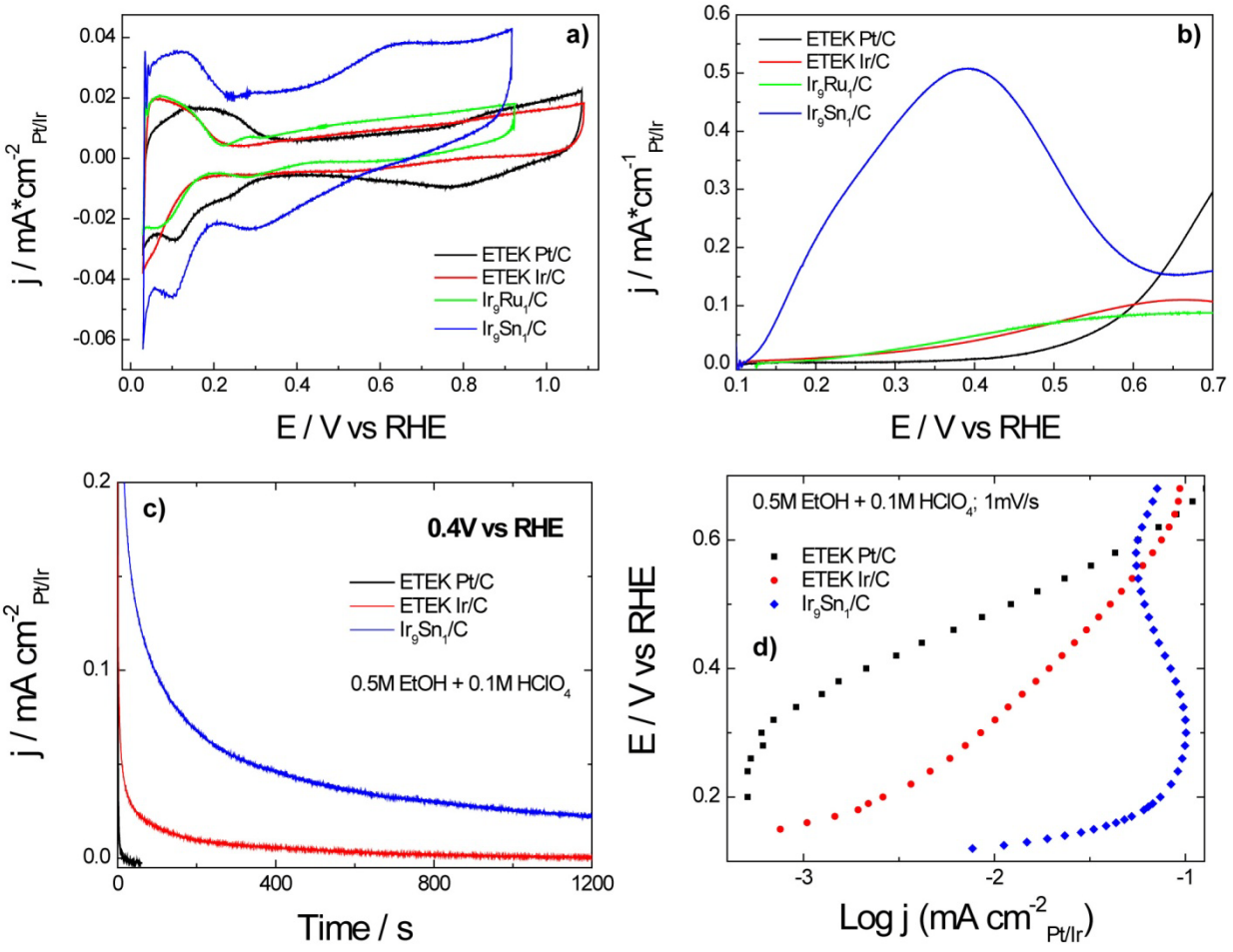

Figure 3.37 (a) CV scans of Pt/C, Ir/C, Ir_9Ru_1/C, and Ir_9Sn_1/C catalysts in base electrolyte of 0.1M $HClO_4$ with a scan rate of 10mV/s. (b) Anodic polarization curves of Pt/C, Ir/C, Ir_9Ru_1/C, and Ir_9Sn_1/C catalysts in ethanol containing electrolyte of 0.5M ethanol in 0.1M $HClO_4$ with a scan rate of 10mV/s. (c) Chronoamerometry measurements from Pt/C, Ir/C, and Ir_9Sn_1/C at 0.4V vs. RHE in 0.5M ethanol in 0.1M $HClO_4$. (d) Tafel plots from Pt/C, Ir/C, and Ir_9Sn_1/C in 0.5M ethanol in 0.1M $HClO_4$ with scan rate of 1mV/s. All measurements were conducted under room temperature.

Figure 3.37a shows cyclic voltammograms (CVs) of Pt/C, Ir/C, Ir_9Ru_1/C and Ir_9Sn_1/C electrocatalysts in 0.1M $HClO_4$ solution. Well-defined hydrogen adsorption/desorption ($H_{ads/des}$), double layer, and surface oxide formation-reduction ($Oxide_{form/red}$) features can be clearly observed from Pt CV. Ir CV shows a pair of $H_{ads/des}$ peaks in the potential region of 0.03V-0.22V, a very small separation between hydrogen adsorption and onset of oxide formation, and a less clearly resolved $Oxide_{form/red}$ feature compared to Pt CV. It is reported that CV of a

polycrystalline Ir electrode exhibited $H_{ads/des}$ process over the potential region 0.05V-0.45V, and the hydrogen UPD region was consisted of 3 pair of $H_{ads/des}$ peaks [126]. The difference between nanoparticle Ir CV and bulk Ir CV could be due to the high density of step and defect sites in small size nanoparticles. Ir_9Ru_1 voltammogram reveals an additional pair of small peaks at around 0.28V, which may be due to its larger particle size and more bulk-like nature, and a slightly higher oxide formation current because of hydrous oxide formation on Ru. Sn shows a more profound influence on Ir compared to Ru, and one can find Ir_9Sn_1 CV has distinctively different characteristics compared to Ir_9Ru_1 and pure Ir, with much larger double layer current and broad $oxide_{form/red}$ peaks, which are likely due to large amount of tin oxide existing in Ir_9Sn_1 catalyst.

The catalysts were subject to potentiodynamic experiments to evaluate their catalytic activity for EOR. Figure 3.37b presents anodic polarization curves on above catalysts in 0.5M ethanol in 0.1M $HClO_4$ solution at room temperature. Ir-based catalysts demonstrate higher activity than that of Pt in low potential region, i.e. less than 0.6V. Pt shows almost no EOR activity at potentials lower than 0.4V where Pt surface is blocked by poison species like CO, and current boosts at potentials higher than 0.5V, which is ascribed to the CO removal due to Pt-OH formation at high over-potential. Ethanol oxidation on pure Ir commences at around 0.15V and a mild increase in current follows. The better performance of Ir compared to Pt might be due to its hydrous surface oxide formation occurs at lower potentials than that of Pt. Ir_9Ru_1 shows slightly higher activity than that of pure Ir, which might be due to the oxygen-containing species further help the removal of surface carbonaceous species. Ir_9Sn_1 catalyst gives significantly enhanced activity in low potential region, with a reaction onset potential of around 0.1V and a much higher current yield. Therefore, in the potentials lower than 0.6V, the catalysts' activity decreases in the

order of Ir_9Sn_1 >> Ir_9Ru_1 ~ Ir > Pt.

Chronoamperometry (CA) and quasi-steady-state measurements were carried out to examine the electrocatalytic activity and stability of the above catalysts under continuous operating condition. Figure 3.37c shows the current-time plots obtained during ethanol oxidation on above catalysts under 0.4V in a 0.5M ethanol in 0.1M $HClO_4$ solution at room temperature. Clearly, the Ir_9Sn_1 electrocatalyst displays much higher activity both at the experimental beginning and after 1000s reaction. After 1000s reaction, the current density was 0.023A*cm^{-2} on Ir_9Sn_1. Pt loses its activity within 60s in this low potential, and Ir shows slightly better performance than Pt. Figure 3.37d displays Tafel plots from above catalysts in quasi-steady-state conditions at a sweep rate of 1mV/s, and one can find at 0.3V, the current density on Ir_9Sn_1 is more than two orders-of-magnitude larger than that of Pt/C. In summary, Ir_9S_1 electrocatalys demonstrate superior EOR performance in low overpotential region.

3.4.3 *In situ* Infrared Reflection-Absoption Spectroscopy (IRRAS) Study

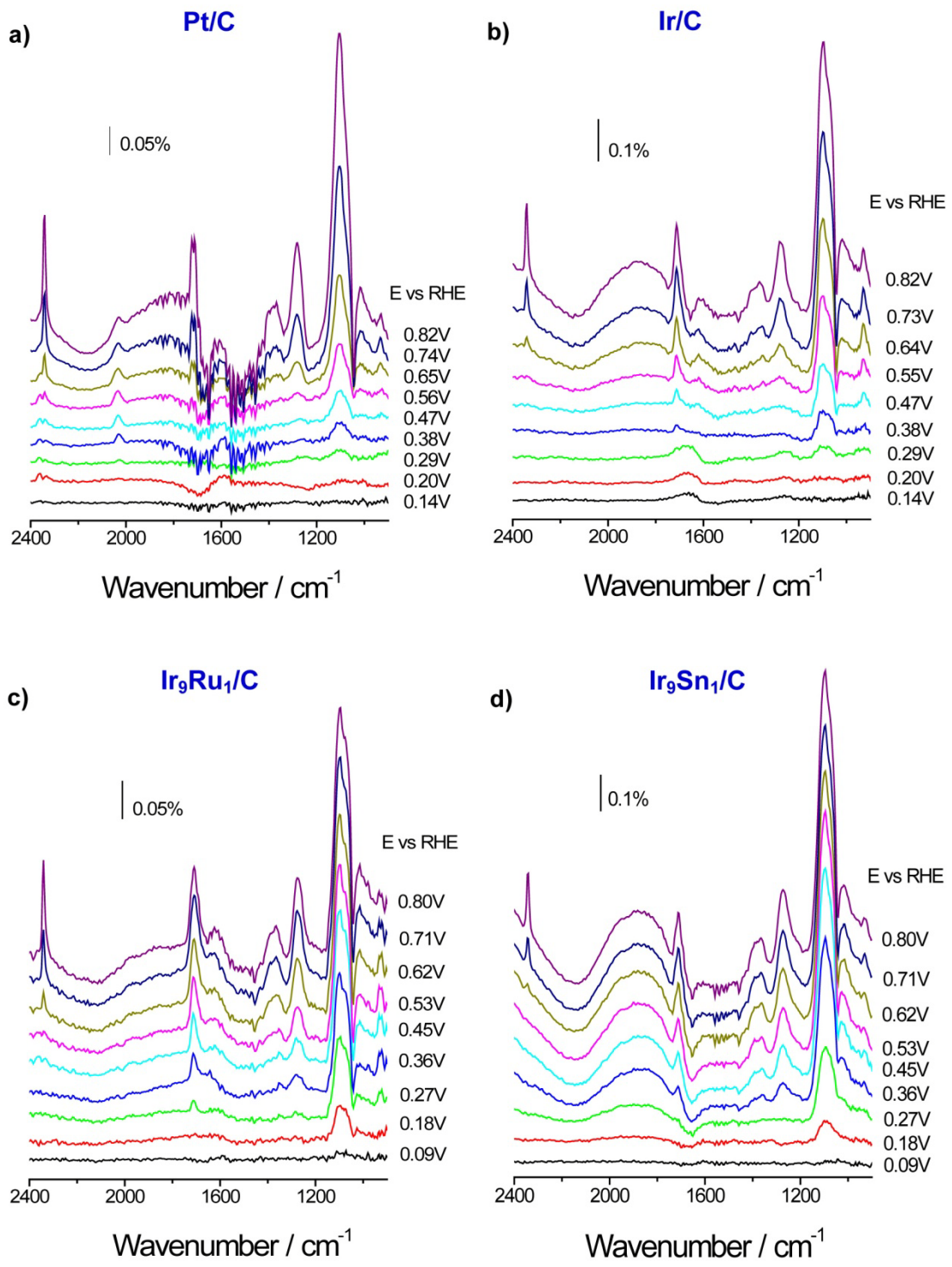

Figure 3.38 *In situ* IRRAS spectra recorded during EOR on different electrocatalysts: (a) Pt/C; (b) Ir/C; (c) Ir_9Ru_1/C; (d) Ir_9Sn_1/C. Electrolyte: 0.1M EtOH + 0.1M $HClO_4$. Scan rate: 1mV/s. Reference speactra were collected at 0.05V vs. RHE in the same electrolyte.

Numerous studies have demonstrated that ethanol electro-oxidation on Pt requires high over-potential and the dominant reaction pathway is partial oxidation pathway leading to the formation of acetic acid and/or acetaldehyde. Few studies have been carried out to investigate the catalytic property of Ir, and to our knowledge, no extensive optical studies of ethanol adsorption and oxidation on Ir-based binary catalysts have been published so far. In order to gain insight on the EOR mechanisms on Ir-based electrocatalysts, we conducted *in situ* IRRAS studies to reveal the reaction intermediates and products distribution information. Figure 3.38 shows the recorded spectra during EOR on Pt/C, Ir/C, Ir_9Ru_1/C and Ir_9Sn_1/C electrocatalysts, and the frequencies and band assignments could refer to Table 3.1. Carbon dioxide (CO_2), acetic acid (CH_3COOH) and acetaldehyde (CH_3CHO) are clearly identified from all spectra, suggesting the parallel reaction pathways undergoing on all above electrocatalysts.

The downward band at 1044cm^{-1} is the signature peak for the C-O stretching vibration of CH_3CH_2OH, representing the consumption of ethanol by oxidation. The positive-going peak near 2343cm^{-1} is attributed to the asymmetric stretch vibration of CO_2, the product of ethanol total oxidation pathway. The bipolar shape band at around 2043cm^{-1} is assigned to linear bound CO, one intermediate believed to be the precursor of CO_2 formation. The band located around 1705cm^{-1} can be assigned to the stretch vibration of the C=O bond, found in both acetaldehyde and acetic acid. A well-defined band at 1280cm^{-1} is the characteristic absorption of C-O stretching in acetic acid, which is usually employed for quantitative analysis of acetic acid. The bands at 1350cm^{-1} and around 1396-1410cm^{-1} are assigned to CH_3 in-plane bending mode and O-C-O stretching of adsorbed acetate, respectively. These two bands are close and difficult to distinguish. The band observed at 933cm^{-1} is assigned to C-C-O asymmetric stretching of acetaldehyde, which could be used for quantification of acetaldehyde. The band at 1598cm^{-1} is

the H-O-H deformation of adsorbed water molecules. The C=O stretching mode of adsorbed acetaldehyde and acetyl around 1620-1635cm^{-1} cannot be resolved because of the presence of the strong water band. The C-H wagging vibration in CH_3CHO, at 1108cm^{-1}, overlaps with the strong band at 1110cm^{-1} of ClO_4^-. The strong band from ClO_4^- ions is the consequence of its accumulation in the thin layer cell to compensate the increasingly positive electrode potential.

One can find the main difference between the spectra on Ir-based catalysts and ones on Pt is that the band at 2043cm^{-1}, the one from CO_L, is only observed on Pt while there is no obvious sign of CO formation during EOR on any Ir-based catalysts, which suggests a different adsorbates formation. The absence of CO indicates less poisoning species and more active sites, which is possibly the reason why ethanol can be oxidized on Ir-based catalysts at much lower over-potential. On the other hand, the absence of both CO and CO_2 at low over-potential region indicates that Ir-based catalysts possesses a limited capability to break C-C band in the same region, and the observed faraday current is likely due to ethanol partial oxidation.

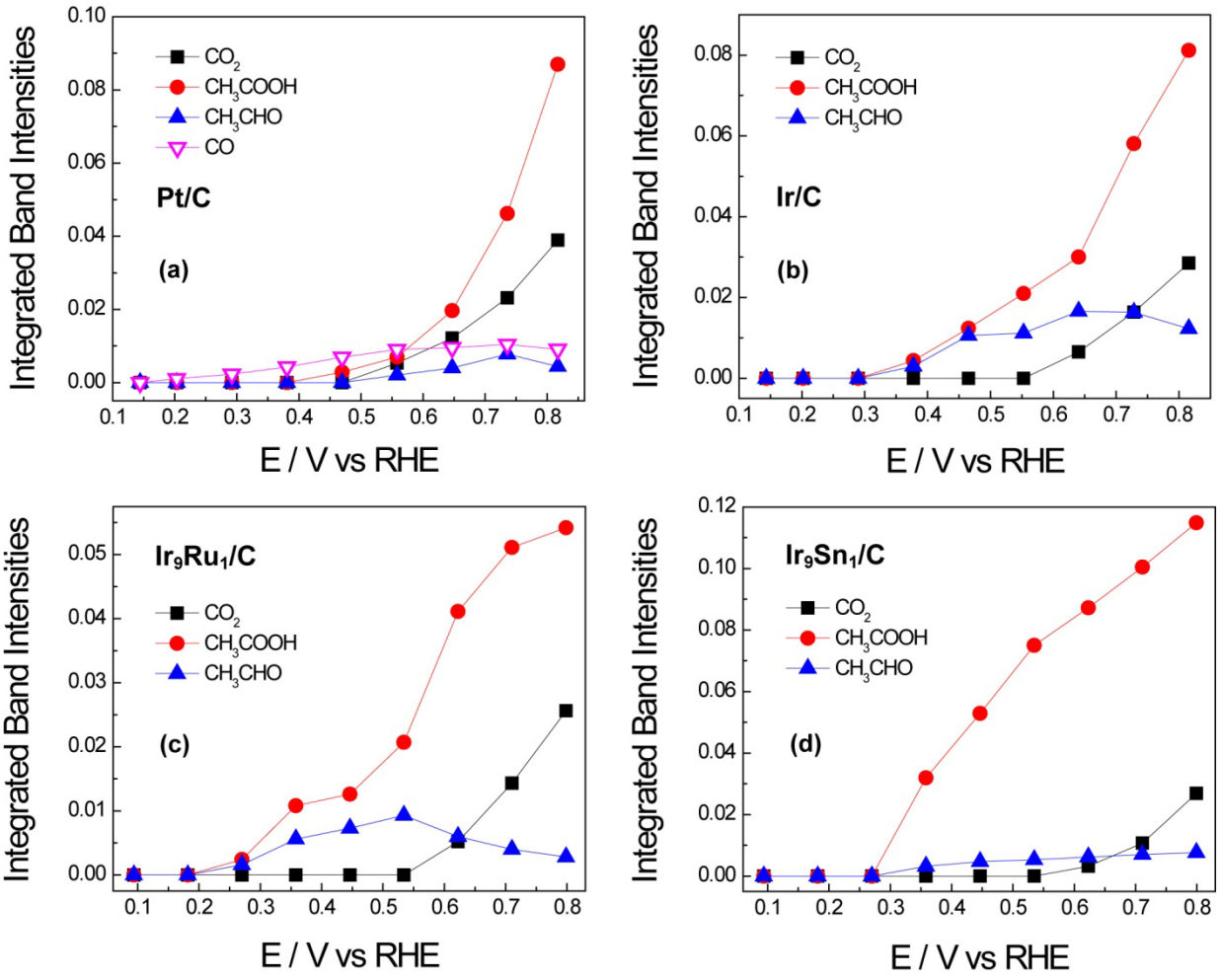

Figure 3.39 Integrated band intensities of three bands: 2343cm^{-1} (CO_2), 1280cm^{-1} (CH_3COOH), and 933cm^{-1} (CH_3CHO) versus applied potential, determined from the spectra shown in Figure 3.38.

Figure 3.39 displays the variation of integrated band intensities of selected bands, representing CO_2, CH_3COOH, CH_3CHO and CO, determined from the *in situ* IRRAS spectra. The band from CH_3COOH is the strongest band in all spectra and the potentials where CH_3COOH bands commence briefly coincide with the emergence of the anodic current in EOR, which both indicate CH_3COOH is the main EOR product on these catalysts. The integrated band intensity change profiles of CO and CO_2 on Pt was in agreement with many other reports, CO band increases with higher potential up to a maximum value at around 0.6V, and decays subsequently due to increasing CO oxidation and/or decreasing CO formation (C-C bond

splitting). CO_2 peak starts to appear at 0.45V and keeps growing with increasing potentials. The potential dependence of two peaks supports the proposal that on Pt adsorbed CO (CO_{ads}) is the intermediate leading to CO_2 formation. The absence of both CO_{ads} and CO_2 in spectra from Ir-based catalysts suggests that C-C bond is not broken in low over-potential region, i.e. less than 0.5V, and a small portion of ethanol molecules are fully oxidized to CO_2 when the applied potential is higher than 0.5V. It can be observed that the quantities of CH_3CHO generated on these catalysts follow the order of: Ir > Ir_9Ru_1 > Pt ~ Ir_9Sn_1. It is claimed that CH_3CHO is likely to be re-adsorbed and be further oxidized to CH_3COOH and/or CO_2, therefore, the insufficient capability to further oxidize CH_3CHO on pure Ir and Ir_9Ru_1 could suggest a fast desorption of CH_3CHO or the lack of oxygen-containing species, because both the formation of CO_2 and CH_3COOH requires additional oxygen coupling. Ir has a stronger affiliation to –OH species than Pt, so the latter propose seems unlikely. Hence, it leads to the conclusion that the higher CH_3CHO amounts are due to a weaker bonding between Ir and CH_3CHO and consequently a less chance to further oxidize it. Both Ru and Sn could activate water and provide oxygen-containing species. So the addition of Ru and Sn could improve catalysts' activity based on the bi-functional mechanism by supplying –OH to oxidize CH_3CHO to CH_3COOH, or to oxidize CO to CO_2. One can see Ir_9Ru_1 shows only slightly higher EOR activity and CH_3COOH production than pure Ir, while the improvement on Ir_9Sn_1 is rather dramatic compared to Ir and Ir_9Ru_1. It suggests that Sn may alter electronic property (as evidenced in following *in situ* XAS study) of Ir and strengthen its bonding to CH_3CHO, making it more prone to be further oxidized to CH_3COOH.

3.4.4 *In situ* X-ray Absoption Spectroscopy (XAS) Study

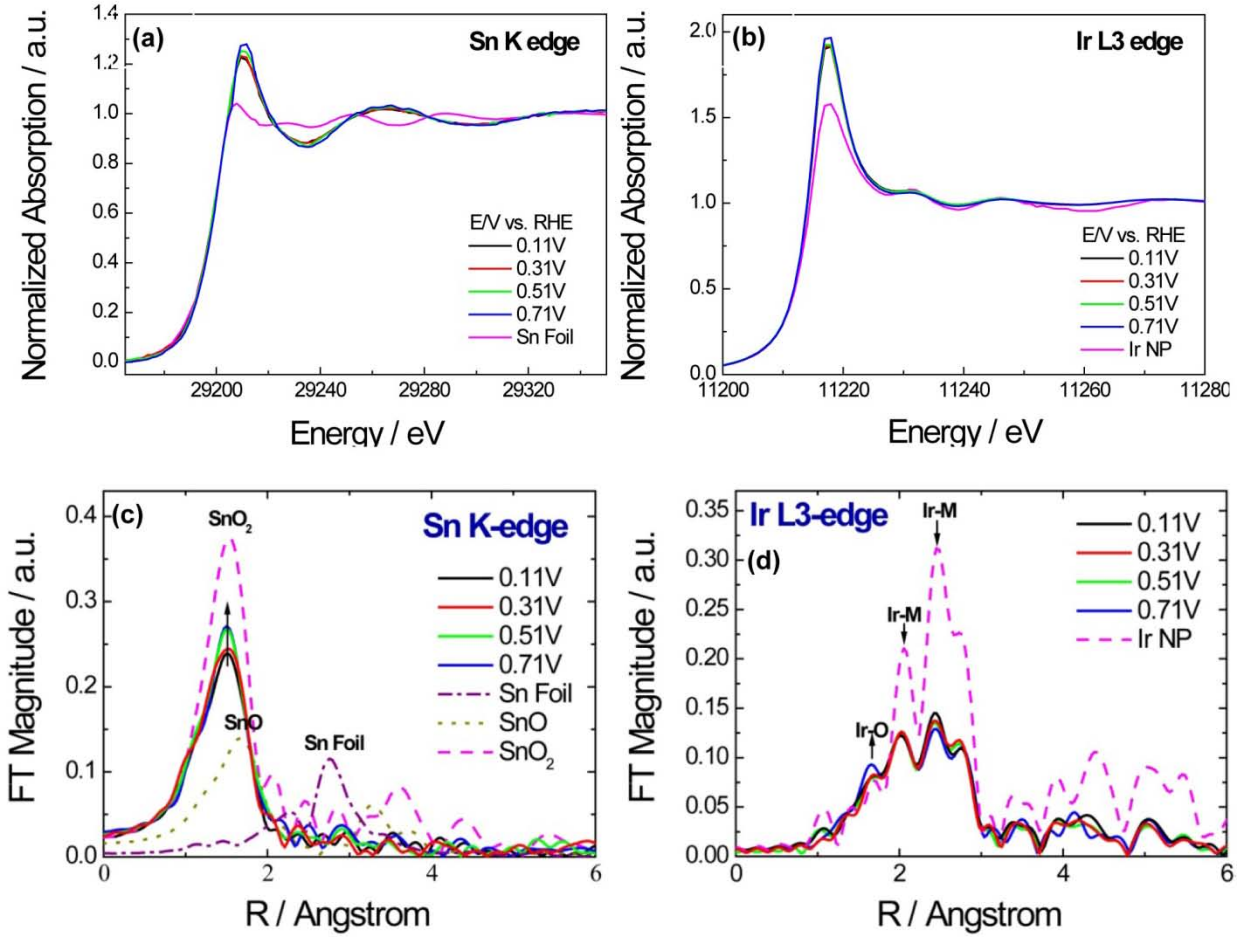

Figure 3.40 *In situ* XANES spectra of Sn K edge (a) and Ir L3 edge (b). FT magnitudes of Sn K edge (c) and Ir L3 edge (d) in Ir_9Sn_1 electrocatalyst.

Figure 3.40 displays the *in situ* XANES spectra of Sn K edge (a) and Ir L3 edge (b). One can find the both elements have little potential dependence when potential is lower than 0.5V vs. RHE. When the potential is higher than 0.5V, both Ir and Sn become slightly more oxidized, as indicated by the increased white line. Sn shows a much higher white line than the reference (Sn foil), indicating an oxidized state. Ir also has a higher white line than the reference (Ir black), suggesting Ir in Ir_9Sn_1 has a more oxidized state than Ir in Ir black. The Fourier transform magnitude of Sn K edge (Figure 3.36c) shows one main peak (Sn-O) in a position same as Sn-O

interaction in SnO_2 nanoparticles, which suggests that Sn stays as SnO_2 in Ir_9Sn_1 catalyst, without metallic Sn^0 existing separately or in alloy with Ir. SnO_2 is a very stable oxide, which explains why Sn is not sensitive to the increasing potential. Figure 3.36d demonstrates there is contribution from both Ir-O and Ir-M in Ir spectra from Ir_9Sn_1, with Ir-M contribution dominated, and it suggested Ir in Ir_9Sn_1 is primarily metallic with partially oxidized surface. Ir-O shows a more profound contribution in Ir_9Sn_1 than in Ir black, indicating Ir in Ir_9Sn_1 is in a higher oxidation state and/or less occupied 4d-electon shell. The insensitivity to potential control in Ir K edge indicates that the existence of SnO_2 stabilizes Ir and alters its electronic structure, which might be account for the enhanced EOR activity possessed by Ir_9Sn_1 catalyst.

3.4.5 Summary

In this section we use a combination of electrochemical methods, *in situ* spectroscopic and structure characterization techniques to improve our understanding of Ir and Ir-based binary electrocatalysts (Ir-Ru and Ir-Sn) in ethanol electrocatalysis. The Ir-based binary electrocatalysts were prepared using a simple thermo-depsotion approach, and the obtained nanoparticle catalysts have an average particle size of 4~5 nm and a relatively broader distribution. We demonstrate that Ir-based electrocatalysts exhibit much higher EOR activity compared to pure Pt nanoparticle electrocatalyst in low over-potential region of 0.1V-0.6V, and the reaction onset potentials on Pt, Ir, Ir-Ru and Ir-Sn were 0.35V, 0.15V, 0.15V and 0.1V, respectively. Ir-Sn displays most profoundly enhanced activity among the Ir-based catalysts. Our *in situ* infrared studies indicate there is no obvious CO poisoning species formation on Ir surface, and this CO-free surface is likely to account for the much lowered onset potential. Ethanol mainly undergoes partial

oxidation pathway to acetic acid on Ir-based catalysts, which suggests that ethanol adsorbs mainly as C2 species. The promotional effect of Sn is likely due to both of the supply of oxygen-containing species (bi-functional effect) and a strengthened bond to CH_3CHO, a precursor to CH_3COOH (electronic effect). The results are of great importance in the exploration of iridium in ethanol electrocatalysis.

3.5 Pt Monolayer Deposited on Au Substrates [188]

Pt Monolayer electrocatalysts, which consist of only one Pt monolayer, or mixed transition metal-Pt monolayer, on suitable carbon-supported metal, or alloy nanoparticles, are a new class of electrocatalysts developed by Adzic et al. [134]. Pt monolayer catalysts hold great potential in fuel cell applications due to the low Pt content and the possibility of fine tuning catalytic properties of Pt by electronic and geometric effects introduced by the substrate metal (or alloy) and the lateral effects of the neighboring metal atoms. In oxygen reduction reaction (ORR) the Pt mass-specific activity of the new Pt monolayer electrocatalysts is up to twenty times higher than the state-of-the-art commercial Pt/C catalysts. Inspired by our success in ORR, we explored the catalytic property of Pt monolayer deposited on gold substrates in the oxidation of alcohols (methanol and ethanol).

Our previous study has demonstrated the enhanced –OH formation on Pt monolayer deposited on Au substrate (Pt_{ML}/Au) due to both geometric effect (tensile strain) and ligand effect, and Au substrates are specifically chosen herein because surface oxygen containing species could facilitate CO removal and potentially improve the kinetics of alcohol oxidation reaction. In this section we study the catalytic property of Pt_{ML}/Au(111) and carbon-supported Au@Pt nanoparticle electrocatalysts using electrochemical and *in situ* spectroscopic methods, taking methanol oxidation reaction (MOR) and ethanol oxidation reaction (EOR) as test reactions.

3.5.1 Pt_{ML}/Au(111) for Methanol Oxidation Reaction (MOR) and Ethanol Oxidation Reaction (EOR)

Au(111) single crystal was prepared by electrochemical polishing followed by flame annealing as discussed in Section 2.1, and Figure 3.41a displays the voltammogram of Au(111) in 0.1M $HClO_4$. Pt monolayer was deposited on Au(111) by galvanic displacing of one underpotentially deposited Cu monolayer, and the Cu UPD curve is also included in Figure 3.41a. Cu UPD on Au(111) in sulfate solution has been well studied [136], and one can find two pairs of characteristic peaks: (i) the first peak marks a first order transition to an ordered phase at 2/3ML Cu overage; (ii) the second deposition peak marks the final stage of the deposition, corresponding to the formation of a full density monolayer which is pseudomorphic with respect to the underlying Au(111) substrate. Platinum monolayer deposited on Au(111) was then obtained by galvanic displacement of the Cu UPD layer. Voltammogram of Pt_{ML}/Au(111) in base electrolyte (Figure 3.41b) shows flat hydrogen adsorption/desorption feature, resembling the feature of Pt(111) single crystal surface, and it suggests the Pt atoms might be epitaxial on Au(111) surface.

The catalytic property of Pt monolayer deposited on Au(111) was examined in the oxidation of methanol and ethanol. The Figure 3.41c and d show the CV curves of Pt_{ML}/Au(111) and Pt(111) in methanol and ethanol containing electrolyte. Pt_{ML}/Au(111) catalyst demonstrates over fourfold increase in peak current compared to Pt(111), and a slightly negative shift in reaction onset potential. The dramatic activity enhancement demonstrates that the catalytic property of Pt is modified by the Au(111) substrate.

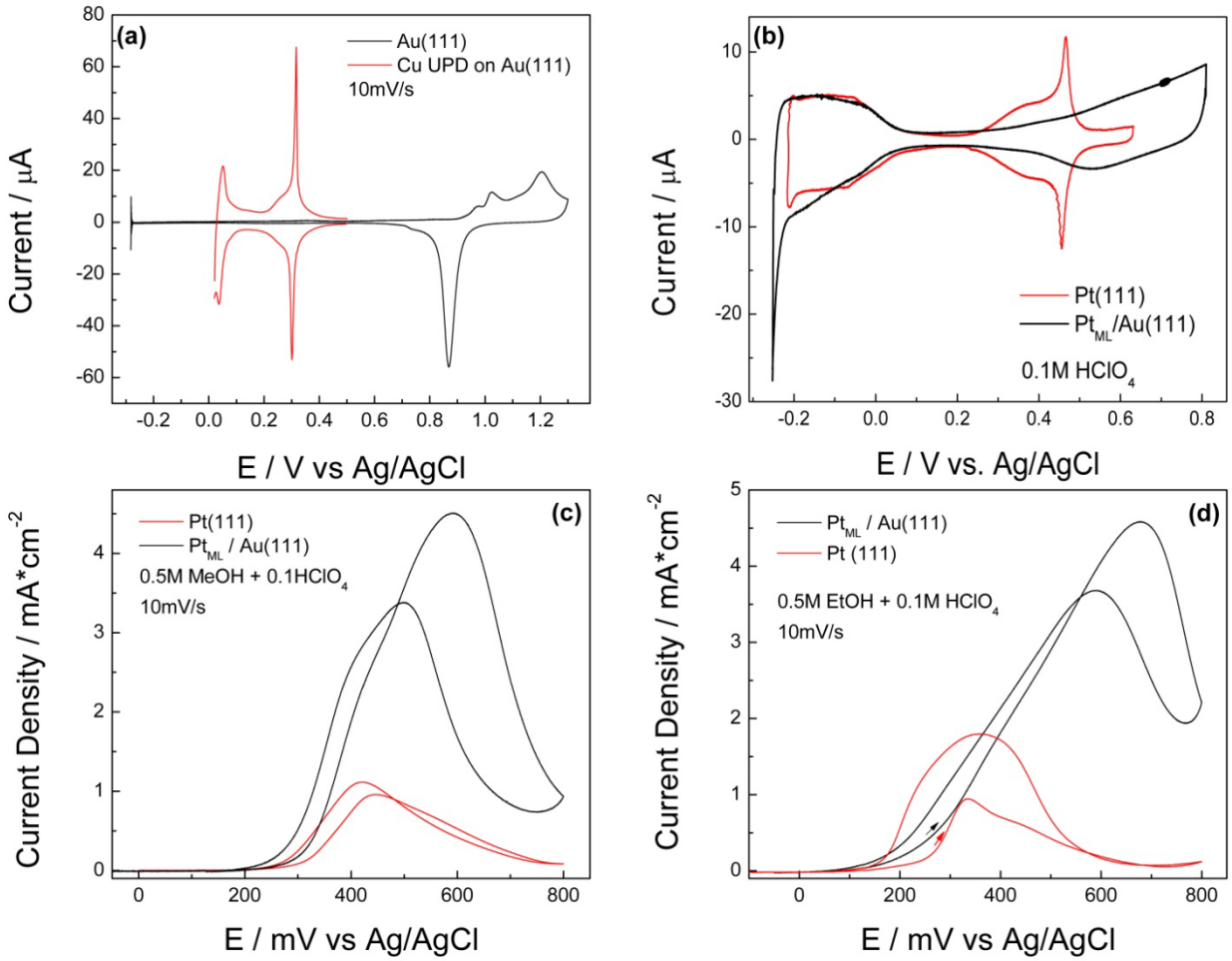

Figure 3.41 (a) Black: CV scan of Au(111) single crystal in 0.1M $HClO_4$ with 10mV/s scan rate; Red: Cu underpotential deposition on Au(111) in 0.05M $CuSO_4$ in 0.05M H_2SO_4 with 10mV/s scan rate. (b) CV scans of Pt_{ML}/Au(111) and Pt(111) in 0.1M $HClO_4$ with 10mV/s scan rate; (c) CV scans of Pt_{ML}/Au(111) and Pt(111) in methanol containing electrolyte of 0.5M methanol in 0.1M $HClO_4$ with 10mV/s scan rate. (d) CV scans of Pt_{ML}/Au(111) and Pt(111) in ethanol containing electrolyte of 0.5M ethanol in 0.1M $HClO_4$ with 10mV/s scan rate. The current density data in (c) and (d) was normalized to ECSA determined from hydrogen desorption charge.

In situ IRRAS study was carried out to identify reaction intermediates and products during MOR and EOR on Pt_{ML}/Au(111), and to gain insight in the mechanism of the greatly enhanced reaction kinetics. Different concentrations of alcohols were employed to investigate the concentration dependence of reaction products distribution. Figure 3.42a displays the *in situ* IRRAS spectra recorded on Pt_{ML}/Au(111) during MOR in 0.1M $HClO_4$ containing 0.1M methanol. The distinct feature in this set of spectra is the absence of adsorbed CO (CO_{ads}) species

(1800~2100cm^{-1}), suggesting the high activity of this catalyst is due to the free of poisoning species. The strong band at around 2434cm^{-1} is ascribed to CO_2, the main product from methanol oxidation. The band at 1640cm^{-1} is attributed to H-O-H from adsorbed water molecules and the growing band at 1110cm^{-1} is due to Cl-O stretching in ClO_4^- ions. The band at 1260cm^{-1} is assigned to some H containing intermediate, possibly COH_{ads} [71, 189-190]. Methanol oxidation on a Pt electrode is usually described as [190]:

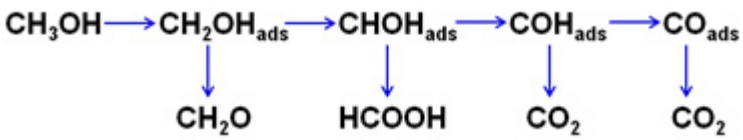

Previous FTIR studies [71, 189] have shown the existence of adsorbed CO (linear bound CO at ~2040cm^{-1} and bridge bound CO at ~1860cm^{-1}), and the formation of formic acid (indicated as the carbonyl group at ~1710cm^{-1}) during MOR on a smooth polycrystalline platinum electrode. Previous research also show Ru adatoms can modify Pt and simultaneously enhance the dehydrogenation of methanol to form CO_{ads} and also the oxidation of CO_{ads} to CO_2. While the absence carbonyl group bands (-CO at ~1710cm^{-1}), as well as the existence of COH_{ads} band (~1260cm^{-1}), indicates that methanol oxidation on Pt_{ML}/Au(111) tends to be further dehydrogenated to COH_{ads}, instead of being oxidized to formaldehyde and/or formic acid. In addition, no CO_{ads} is detected further indicates that COH_{ads} can be oxidized directly to CO_2, rather than forming CO_{ads}. The expanded lattice of Pt monolayer deposited on Au(111) has been shown with increased –OH formation, which could promote the oxidation of COH_{ads}. In summary, we attribute the enhanced MOR activity on this catalyst to the formation of COH_{ads}, instead poisoning CO_{ads}, and the promoted oxidation of COH_{ads} to directly to CO_2. Figure 3.42b shows the IRRAS spectra recorded at higher concentration of methanol (0.5M), the spectra show similar features to the ones at 0.1M methanol (Figure 3.42a), with the absence of CO_{ads} and –CO.

CO_2 band becomes much stronger, due to the higher concentration of reactant. Therefore, MOR products distribution shows no obvious reactant concentration dependence.

The IRRAS spectra collected during EOR at different concentration of ethanol are pesented in Figure 3.42 c and d. One can find both spectra show similar feature, indicating there is no obvious concentration dependence of EOR products from Pt_{ML}/Au(111) catalyst. The downward band at 1044cm^{-1} is the signature peak for the C-O stretching vibration of CH_3CH_2OH, representing the consumption of ethanol by oxidation. The band located around 1705cm^{-1} can be assigned to the stretch vibration of the C=O bond, found in both acetaldehyde and acetic acid. A well-defined band at 1280cm^{-1} is the characteristic absorption of C-O stretching in acetic acid. The bands at 1350cm^{-1} and around 1396-1410cm^{-1} are assigned to CH_3 in-plane bending mode and O-C-O stretching of adsorbed acetate, respectively. These two bands are close and difficult to distinguish. The band observed at 933cm^{-1} is assigned to C-C-O asymmetric stretching of acetaldehyde. The band at 1598cm^{-1} is the H-O-H deformation of adsorbed water molecules. The C-H wagging vibration in CH_3CHO, at 1108cm^{-1}, overlaps with the strong band at 1110cm^{-1} of Cl-O stretching in ClO_4^-. The strong band for ClO_4^- ions is the consequence of its accumulation in the thin layer cell to compensate the increasingly positive electrode potential.

The main feature is the free of both CO_{ads} and CO_2 bands, which shows the ethanol oxidation on Pt_{ML}/Au(111) is mainly following partial oxidation pathway to acetic acid and acetaldehyde, without the cleavage of C-C bond. The Pt monolayer on Au(111) is stretched by more than 4% [92] due to the lattice mismatch between Pt overlayer and Au substrate, and we suspect the formation of Pt nanoclusters. These Pt ensembles consisting of several Pt atoms may not provide enough Pt sites for the full dehydrogenation and C-C bond splitting in the ethanol molecules.

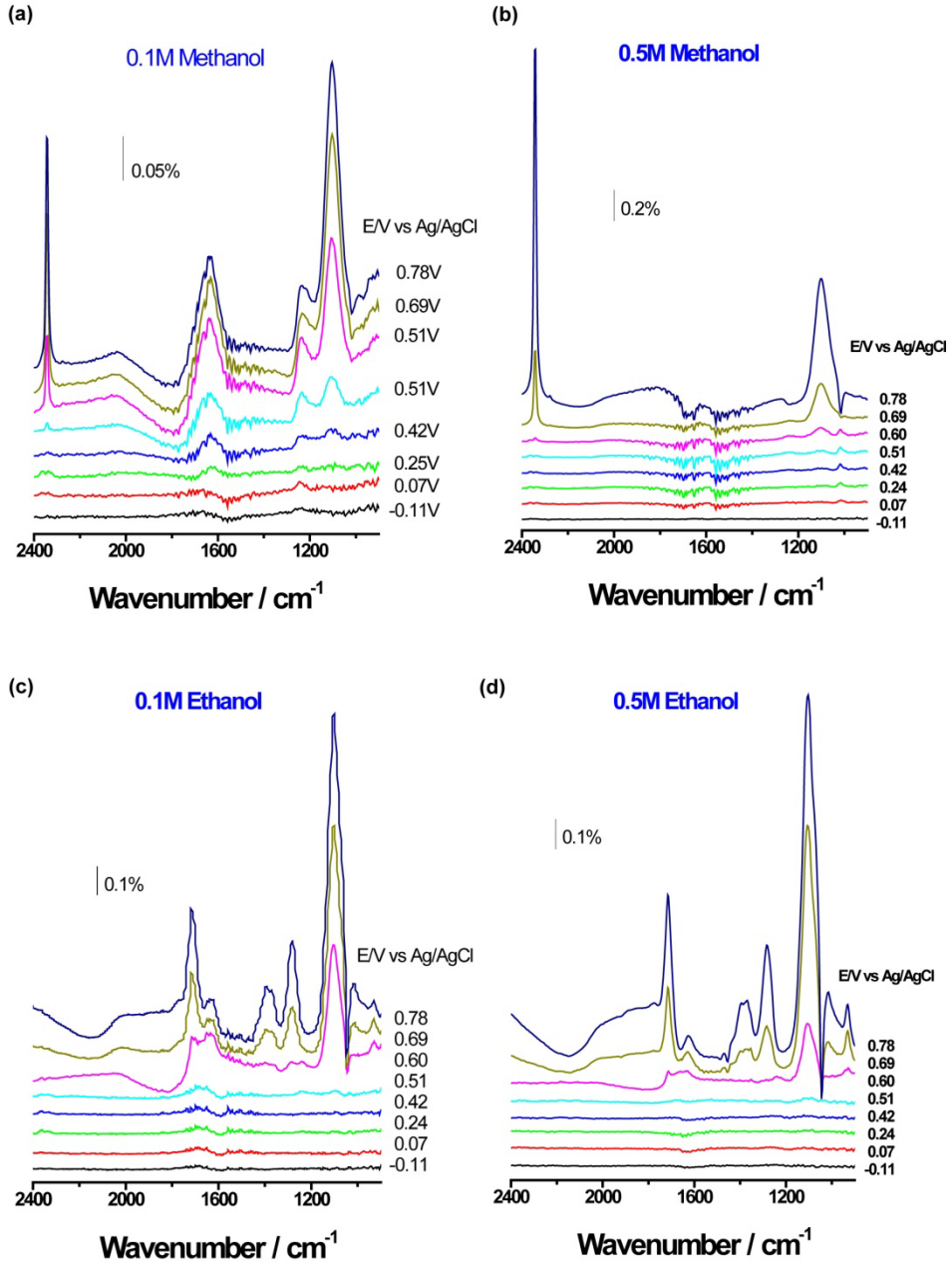

Figure 3.42 *In situ* IRRAS spectra recorded during MOR/EOR on Pt_{ML}/Au(111) in 0.1M $HClO_4$ with different concentration of alcohols. (a) 0.1M methanol; (b) 0.5M methanol; (c) 0.1M ethanol; (d) 0.5M ethanol. Scan rate: 1mV/s. Reference spectra were collected at 0.05V versus RHE in the same electrolyte.

In summary, Pt_{ML}/Au(111) shows greatly enhanced activity in both ethanol and methanol oxidation, as indicated in the over fourfold increase in oxidation current, but it might be considered a better MOR catalyst because it doesn't facilitate ethanol total oxidation to CO_2.

3.1.2 Carbon-Supported Au@Pt Core-Shell Nanoparticle Electrocatalyst

Guided by our success in single crystal based Pt_{ML}/Au(111) electrocatalyst, we prepared carbon-supported Au@Pt core-shell nanoparticle electrocatalysts using microemulsion method. The resulted Au@Pt/C electrocatalyst with atomic ratio Pt:Au of 1:1 is composed of an Au-enriched core and a Pt-enriched shell. Due to the larger radius of Au atoms, we are expecting an expanded Pt lattice in the surface as the Pt monolayer deposited on Au(111).

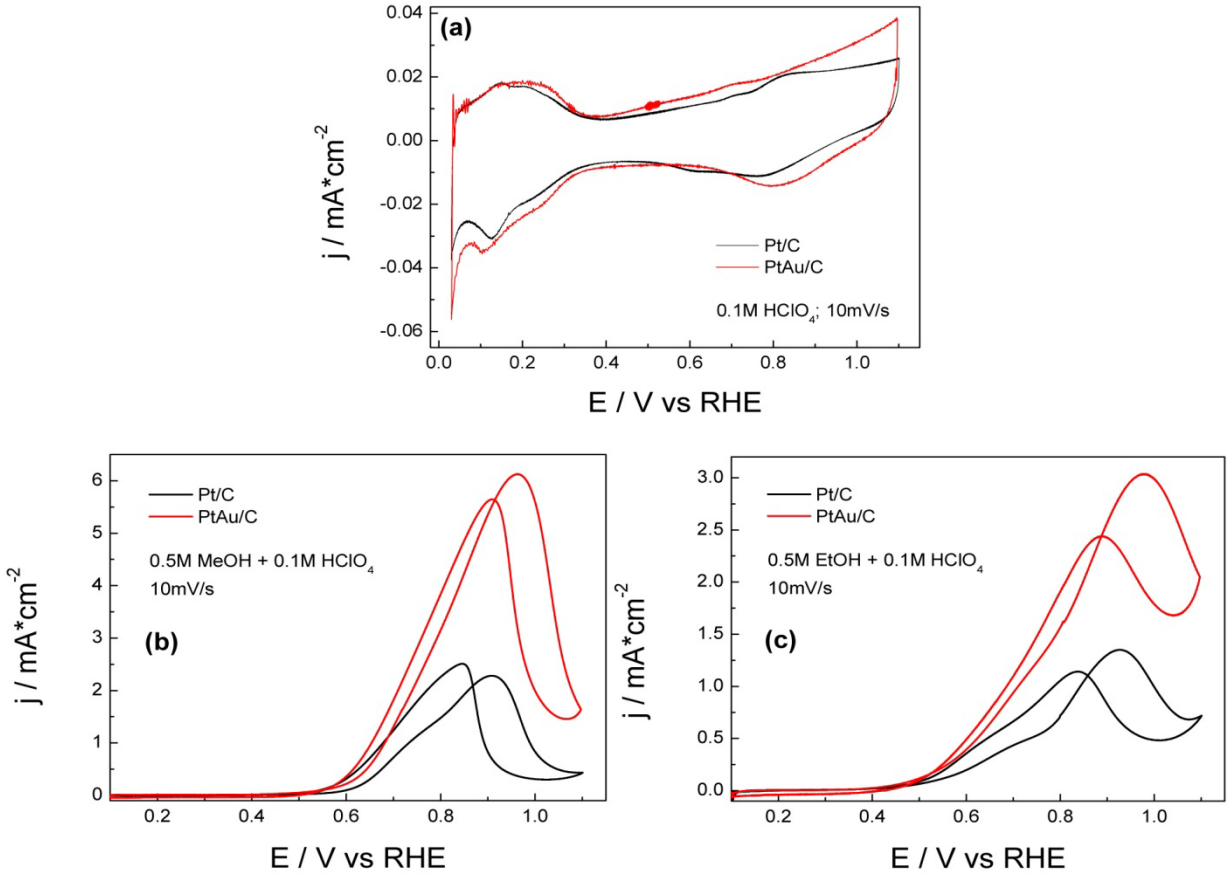

Figure 3.43 (a) CV scans of Pt/C and Au@Pt/C electrocatalysts in 0.1M $HClO_4$ with 10mV/s scan rate; (b) CV scans of Pt/C and Au@Pt/C electrocatalysts in methanol containing electrolyte of 0.5M methanol in 0.1M $HClO_4$ with 10mV/s scan rate. (c) CV scans of Pt/C and Au@Pt/C catalysts in ethanol containing electrolyte of 0.5M ethanol in 0.1M $HClO_4$ with 10mV/s scan rate. The current density data in (b) and (c) was normalized to ECSA determined from hydrogen desorption charge. (With D. Buceta).

Figure 3.43a shows voltammorgrams of both Au@Pt/C and Pt/C electrocatalysts in base electrolyte and one can an enhanced oxide formation feature from the Au@Pt/C catalyst, which confirms our previous hypothesis. Figure 3.43b and c display MOR and EOR curves of both catalysts, and we observe an over twofold increase of the activity on Au@Pt/C compared to pure Pt nanoparticle catalyst. The enhancement is encouraging, but not as great as what was observed in Pt monolayer deposited on the Au(111) substrate, which suggests the morphology and extent of lattice expansion existing the Pt overlayer impact the catalytic property of the Pt overlayer.

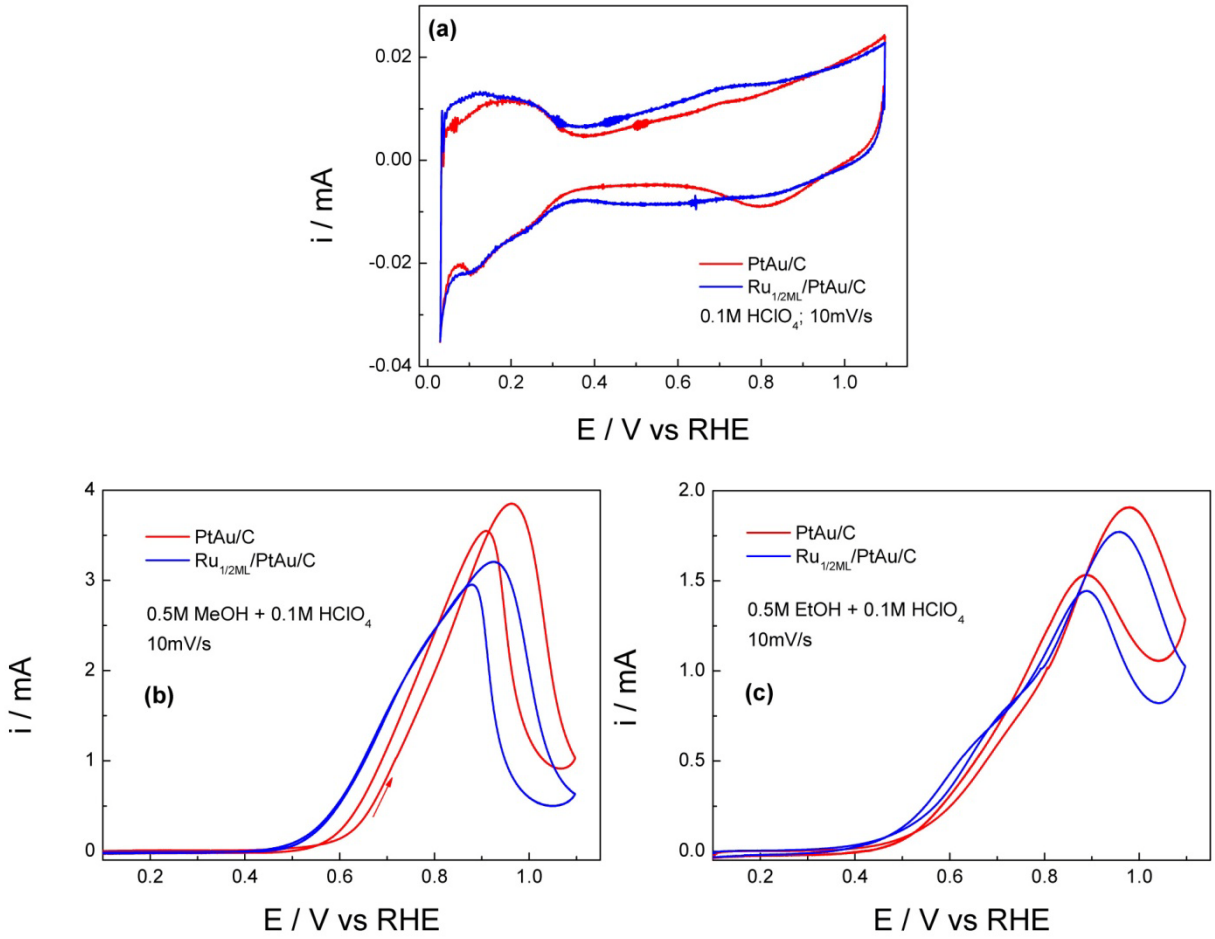

Figure 3.44 (a) CV scans of $Ru_{1/2ML}$/Au@Pt/C and Au@Pt/C catalysts in 0.1M $HClO_4$ with 10mV/s scan rate; (b) CV scans of $Ru_{1/2ML}$/Au@Pt/C and Au@Pt/C catalysts in methanol containing electrolyte of 0.5M methanol in 0.1M $HClO_4$ with 10mV/s scan rate. (c) CV scans of $Ru_{1/2ML}$/Au@Pt/C and Au@Pt/C catalysts in ethanol containing electrolyte of 0.5M ethanol in 0.1M $HClO_4$ with 10mV/s scan rate. The current density data in (b) and (c) was normalized to ECSA determined from hydrogen desorption charge.

Half-monolayer-equivalent amount of Ru was deposited on the Au@Pt/C catalyst to modify the catalyst. Figure 3.44a displays the CV curves in base electrolyte before and after Ru deposition, and one can find the Ru/Au@Pt/C catalyst shows enlarged double layer current and enhanced oxide formation, which all corresponds the existence of Ru adatoms. The addition of Ru improves the catalyst's MOR activity and negatively shifts the reaction by ca. 100mV. The promotional effect of Ru to Au@Pt/C can be attributed to the bi-functional effect, where Ru supplies hydroxyl species and promotes the oxidation of COH_{ads} to CO_2. While the addition of Ru does not show obvious impact on EOR, indicating that the limiting step for EOR is not OH formation.

3.5.3 Summary

Pt monolayer deposited Au(111) substrates and Au@Pt core-shell nanoparticles all demonstrate enhanced activity in the electro-oxidation of methanol and ethanol. We attribute the improved MOR activity to the formation of COH_{ads}, instead of poisoning CO_{ads}. The better EOR activity is likely due to the free of CO_{ads}, and the faster kinetics of ethanol partial oxidation without the cleavage of C-C bond.

The underlying substrates play a significant role in modifying the catalytic activity of Pt overlayer, more detailed study will be carried out to explore the Pt-Au system:

i) Different Au single surfaces will be studied such as high index facets, because stepped Pt surfaces have been proved as effective in splitting C-C bond in ethanol molecules and

facilitate ethanol total oxidation. It will be of great importance to study the epitaxially grown Pt monolayer on these Au single crystal surfaces.

ii) Au/C nanoparticles with different sizes will be prepared, and the catalytic performance of Pt monolayer deposited on these Au nanoparticles will be studied.

Au@Pt/C nanoparticle catalysts with different Pt/Au ratio, thus a different degree of Pt lattice expansion, will be prepared by microemulsion method, and their catalytic performance will be investigated.

CHAPTER 4 CONCLUSIONS

Here are the main conclusions of this dissertation:

(1) We developed a ternary Pt-Rh-SnO_2 electrocatalyst that is capable of splitting C-C bond and oxidizing ethanol to CO_2 with high efficiency. A model catalyst, $RhSnO_2$/Pt(111), was first prepared by depositing Rh and SnO_2 clusters on Pt(111) surface; and then carbon-supported $PtRhSnO_2$ nanoparticle catalysts were synthesized by cation-adsorption-reduction-adatom-galvanic-displacement method. Both show unprecedented activity for ethanol electro-oxidation with the onset of reaction occurring at low overpotentials. *In situ* IRRAS spectra obtained during EOR with both $RhSnO_2$/Pt(111) and $PtRhSnO_2$/C indicate CO_2 is the major product and it also demonstrate that we successfully split C-C bond at room temperature. The DFT investigation of ethanol decomposition was carried out over a model RhPt/SnO_2(110) catalyst, and results suggest the optimal pathway leading to C-C bond breaking is $*CH_3CH_2OH \rightarrow *CH_3CH_2O+H* \rightarrow *CH_2CH_2O+2H* \rightarrow *CH_2+*CH_2O+2H*$. *In situ* XAS study was conducted and the results indicate that the PtRh surface is only slightly oxidized, while tin exists as SnO_2 in the entire potential region. EXAFS fitting results reveal structure information like the particle size and bond distance. These results are corroborated by those obtained using XRD, HADDF-STEM, ICP-OES, EELS and DFT calculations.

(2) We conducted systematic studies on Pt, Rh, PtRh, $PtSnO_2$, $RhSnO_2$ and $PtRhSnO_2$ NP electrocatalysts prepared by a facile polyol approach, and we demonstrate that the EOR activity of above catalysts decreases in the order of: $PtRhSnO_2 > PtSnO_2 > Pt > PtRh > Rh > RhSnO_2$. The catalysts' selectivity towards C-C bond splitting and ethanol total oxidation pathway is

examined using *in situ* IRRAS and the results indicate CO_2 formation decreases in the order of: $PtRhSnO_2$ ~ $RhSnO_2$ > PtRh > Pt > $PtSnO_2$ ~ Rh.

(3) Carbon-supported MM'/SnO_2 NP electrocatalysts comprising SnO_2 NP cores decorated with multi-metallic nanoislands (MM' = PtRh, PtIr, IrRh, PtIrRh) were prepared using a seeded growth approach as synthetic analogues to the PtRh/SnO_2(110) model catalyst in our DFT study. An array of characterization techniques including XRD, HADDF-STEM, EDS mapping and *in situ* XAS, were employed to establish the composition and architecture of the synthesized NPs. Both EOR reactivity and selectivity towards CO_2 formation of several of these M/SnO_2/C NP catalysts are significantly improved compared to Pt/C and Pt/SnO_2/C. Among systems studied, PtRh/SnO_2/C electrocatalysts with a suitable Rh content, i.e. catalysts with atomic ratio Pt:Rh:Sn = 1:1/2:1 and 1:1/3:1, exhibit highest EOR activity and selectivity towards ethanol total oxidation, and we attribute this phenomenon to both ensemble effect and ligand effect. Each constituent in the ternary system plays a specific role: Pt is essential for ethanol adsorption, and the abstraction and oxidation of H atoms, SnO_2 can provide hydroxyl species to oxidize strongly bound intermediates, such as CO, and Rh can facilitate C-C bond splitting. PtIr/SnO_2/C catalyst with highest Ir content, i.e. the catalyst with atomic ratio Pt:Ir:Sn = 1:1:1, shows best activity in three PtIr/SnO_2 samples. The PtIrRh/SnO_2/C electrocatalyst (with atomic ratio Pt:Ir:Rh:Sn of 1:1:1:1) shows lower activity compared to PtRh/SnO_2/C and PtIr/SnO_2/C electrocatalysts, and the IrRh/SnO_2/C electrocatalyst (with atomic ratio Ir:Rh:Sn of 1:1:1) is the poorest one. The CO_2 production efficiency of the above catalysts decreases in the order of: PtRh/SnO_2 (with atomic ratio Pt:Rh:Sn of 1:1/2:1 and 1:1/3:1) > PtIrRh/SnO_2 (with atomic ratio Pt:Ir:Rh:Sn of 1:1:1:1) > PtIr/SnO_2 (with atomic ratio Pt:Ir:Sn of 1:1:1).

(4) Ir-based (Ir-Ru and Ir-Sn) binary electrocatalysts were prepared using a simple thermal

decomposition method. We demonstrate that Ir-based electrocatalysts exhibit much higher EOR activity compared to Pt nanoparticle electrocatalyst at low over-potential region of 0.1V-0.6V, and the reaction onset potentials on Pt, Ir, Ir-Ru and Ir-Sn are 0.35V, 0.15V, 0.15V and 0.1V, respectively. Ir-Sn displays most profoundly enhanced activity among the Ir-based catalysts. Our *in situ* infrared studies indicates there is no obvious CO poison species formation on Ir surface, and this CO-free surface is likely to account for the much lowered onset potential. Ethanol mainly undergoes partial oxidation pathway to acetic acid on Ir-based catalysts, which suggests that ethanol adsorbs mainly as C2 species. The promotional effect of Sn is likely due to both of the supply of oxygen-containing species (bi-functional effect) and a strengthened bonding to CH_3CHO, a precursor to CH_3COOH (electronic effect).

(5) Pt monolayer deposited Au(111) substrate and carbon-supported Au@Pt core-shell nanoparticles electrocatalysts all demonstrate enhanced activity in the electro-oxidation of alcohols (methanol and ethanol). Ru adatoms were placed on Au@Pt/C and further improved its MOR activity. We attribute the improved MOR activity of Pt_{ML}/Au to the formation of COH_{ads}, instead of poisoning CO_{ads}. The better EOR activity of Pt_{ML}/Au is likely due to the free of CO_{ads}, and the faster kinetics of ethanol partial oxidation without the cleavage of C-C bond. The underlying substrates play a significant role in modifying the catalytic activity of Pt overlayer.

REFERENCES

[1] W. Grove, *Phios. Mag., Ser. 3*, 14 (1839) 127.

[2] J. W. Gosselink, *International Journal of Hydrogen Energy*, 27 (2002) 1125-1129.

[3] H.-F. Oetjen, V. M. Schmidt, U. Stimming, F. Tuilla, *J. Electrochem. Soc.* 143 (1996) 3838.

[4] K. Kordesch and G. Simader, (1996) *Fuel Cells and Their Applications*, VCH Verlag GmbH, Weinheim.

[5] C. Lamy, C. Coutanceau, and J.-M. Leger, *The Direct Ethanol Fuel Cell: a Challenge to Convert Bioethanol Cleanly into Electric Energy.* In *Catalysis for Sustainable Energy Production*; P. Barbaro and C. Bianchini, Eds.; WILEY-VCH Verlag GmbH & Co. kGaA, Weinheim, (2009) 1-42.

[6] J. K. Edwards, A. Thomas, B. E. Solsona, P. Landon, A. F. Carley, G. J. Hutching, Catalysis Today 122 (2007) 297.

[7] S. Wasmus, A. Kuver, J. Electroanal. Chem. 461 (1999) 14.

[8] A. J. Appleby, F. R. Foulkes, *Fuel Cell Handbook, Van Nostrand Reinhold*, (1989) New York, pp. 39-122.

[9] P. W. Atkins, *Physical Chemistry*; 5th ed.; Oxford University Press: Oxford, 1994.

[10] J. Larminie, A. Dicks, *Fuel Cell Systems Explained*; John Wiley & Sons: Chichester, 2000.

[11] L. Carrette, K. A. Friedrich, U. Stimming - *Fuel Cells*, 1 (2001) 5-39.

[12] *Handbook of Fuel Cells-Fundamentals, Technology and Applications*; W. Vielstich, A. Lamm, H. A. Gasteiger, Eds.; John Wiley & Sons: Chichester, 2003; Vol. 1: Fundamentals and Survey of Systems, pp 143.

[13] H. P. Dhar. *J. Electroanal. Chem.* 357 (1993), 237.

[14] M. R. Tarasevich, M, A. Sadkowski, E. Yeager, *Comprehensive Treatise of Electrochemistry*, Vol. 7 (1983) (eds B. E. Conway, J. O'. M. Bockris, E. Yeager, S. U. M. Khan and R. E. White), Plenum Press, New York, pp. 301-398.

[15] T. R. Ralph, M. P. Hogarth, *Platinum Metals Review*, 46 (2002) 3-14.

[16] C. Lamy, E. M. Belgsir, J.-M. Leger, *Journal of Applied Electrochemistry*, 31 (2001), 799-809.

[17] C. Lamy, A. Lima, V. Le Rhun, F. Delime, C. Coutanceau, J.-M. Leger, *Journal of Power Sources*, 105 (2002), 283-296.

[18] S. Srinivasan, E. A. Ticianelli, C. R. Derouin, A. Redondo, *J. Power Sources*, 22 (1988) 359-374.

[19] E. A. Ticianelli, C. R. Derouin, A. Redondo, S. Srinivasan, *J. Electrochem. Soc.*, 135 (1988) 2209-2214.

[20] L. W. H. Leung and M. J. Weaver, *J. Phys. Chem.*, 92 (1988) 4019–4022.

[21] S. Song, W. Zhou, Z. Liang, R. Cai, G. Sun, Q. Xin, V. Stergiopoulos, P. Tsiakaras, *Appl. Catal. B: Environ.* 55 (2005) 65.

[22] S. Song, P. Tsiakaras, *Applied catalysis B: Environmental* 63 (2006) 187-193.

[23] S. J. Lee, S. Mukerjee, J. McBreen, Y. W. Rho, Y. T. Kho and T. H. Lee, *Electrochimica Acta*, 43 (1998) 3693-3701.

[24] D. Bevers, N. Wagner and M. V. Bradke, *Int. J. Hydrogen Energy*, 23 (1998) 57-63.

[25] C.-C. Yang, *International Journal of Hydrogen Energy*, 29 (2004) 135-143.

[26] Y. Wang, L. Li, L. Hu, L. Zhuang, J. Lu and B. Xu, *Electrochemistry Communications* 5 (2003) 662-666.

[27] F. Vigier, S. Rousseau, C. Coutanceau, J.-M. Leger and C. Lamy, *Topics in Catalysis*, 40

(2006) 111-121.

[28] T. Frelink, W. Visscher, and J. A. R. Van Veen, *Langmuir*, 12 (1996) 3702-3708.

[29] C. Xu, L. Cheng, P. K. Shen, and Y. Liu, *Electrochemistry Communications*, 9 (2007) 997-1001.

[30] P. K. Shen, and C. Xu, *Electrochemistry Communications*, 8 (2006) 184-188.

[31] P. Bert and C. Bianchini, (2006) *Platinum-free electrocatalysts materials*, European Patent EP 1 556 916 B1.

[32] P. Bert, C. Bianchini, G. Giambastiani, H. Miller, S. Santiccioli, A. Tampucci, and F. Vizza, (2006) *Direct fuel cells comprising a nitrogen compounds and their use*, Republica Italiana Dom. It. FI2006A000160.

[33] Y.-F. Yang, Y.-H. Zhou and C.-S. Cha, *Electrochimica Acta*, 40 (1995) 2579-2586.

[34] J. Prakash, and H. Joachin, *Electrochimica Acta*, 45 (2000) 2289-2296.

[35] S. L. Gojkovic, S. Gupta, and R. F. Savinell, *Journal of Electroanalytical Chemistry*, 462 (1999) 63-72.

[36] S. L. Gojkovic, S. Gupta, and R. F. Savinell, *Electrochimica Acta*, 45 (2000) 889-897.

[37] N. Heller-Ling, M. Prestat, J.-L. Gautier, and J.-F. Koenig, *Electrochimica Acta*, 42 (1997) 197-202.

[38] Y. Hu, Y. V. Tolmachev, and D. A. Scherson, *Journal of Electroanalytical Chemistry*, 468 (1999) 64-69.

[39] V. Rashkova, S. Kitova, I. Konstantinov, and T. Vitanov, *Electrochimica Acta*, 47 (2002) 1555-1560.

[40] J. Ponce, J.-L. Rehspringer, G. Poillerat, and J.-L. Gautier, *Electrochimica Acta*, 46 (2001) 3373-3380.

[41] Mao, L., Sotomura, T., Nakatsu, K., Koshiba, N., Zhang, D. and Ohsaka, T., *Journal of the Electrochemical Society*, 149 (2002) A504-A507.

[42] B. Klapste, J. Vondrak, and J. Velicka, *Electrochimica Acta*, 47 (2002) 2365-2369.

[43] T. Sata, M. Tsujimoto, T. Yamaguchi and K. Matsusaki, *Journal of Membrane Science*, 112 (1996) 161-170.

[44] J. Fang and P. K. Shen, *Journal of Membrane Science*, 285 (2006) 317-322.

[45] L. Li, J. Zhang and Y. X. Wang, *Journal of Membrane Science*, 226 (2003) 159-167.

[46] L. Li, and Y. X. Wang, *Journal of Membrane Science*, 262 (2005) 1-4.

[47] T. Iwamoto, M. Uetake and A. Umeda, (1994) *Hofman degradation of strong base anion exchange resin*, Proceedings of the 68th Autumn Annual Meeting of the Chemical Society of Japan, Nagoya October 1994, pp 472.

[48] M. W. Breiter, *Reaction Mechanism of H_2 Oxidation/evolution Reaction. In Hand book of Fuel Cells-Fundamentals, Technology and Applications*; W. Vielstich, A. Lamm, H. A. Gasteiger, Eds.; John Wiley & Sons: Chichester, 2003; Vol. 2: Electocatalysis; pp 361.

[49] N. M. Markovic, *The Hydrogen Electrode Reaction*. *In Handbook of Fuel Cells-Fundamentals, Technology and Applications*; W. Vielstich, A. Lamm, H. A. Gasteiger, Eds.; John Wiley: Chichester, 2003; Vol. 2: Electocatalysis; pp 368.

[50] J. Heyrovsky, *Recl. Trav. Chim. Pays-Bas,* 46 (1927) 582.

[51] J. Z. Tafel, *Phys. Chem. Stoechiom. Verwandtschaftsl*, 50 (1905) 641.

[52] T. Volmer, M. Z. Erdey-Gruz, *Phys. Chem. Abt. A,*150 (1930) 203.

[53] J. X. Wang, T. E. Springer, R. R. Adzic, *J. Electrochem. Soc.* 153 (2006) A1732.

[54] S. R. Brankovic, J. X. Wang, R. R. Adzic, *Electrochem Solid-State Letter* 4 (2001) A217–A220.

[55] A. Capon, R. Parsons, *J. Electroanalytical Chemistry,* 45 (1973) 205-231.

[56] C. Rice, S. Ha, R. I. Masel, P. Waszczuk, A. Wieckowski and Tom Barnard, *Journal of Power Sources,* 111 (2002) 83-89.

[57] M. Winter, R. J. Brodd, *Chem. Rev.,* 104 (2004) 4245-4269.

[58] W. P. Zhou, A. Lewera, R. Larsen, R. I. Masel, P. S. Bagus and A. Wieckowski, *J. Phys. Chem. B,* 110 (2006) 13393.

[59] J. J. Ge, Y. W. Zhang, C. P. Liu, T. H. Lu, J. H. Liao and W. Xing, *J. Phys. Chem. C,* 112 (2008) 17214.

[60] J. Y. Wang, Y. Y. Kang, H. Yang and W. B. Cai, *J. Phys. Chem. C,* 113 (2009) 8366.

[61] S. G. Sun, J. Clavilier and A. Bewick, J. Electroanal. Chem., 1988, 240, 147.

[62] M. Shibata and S. Motoo, J. Electroanal. Chem., 1985, 189, 111.

[63] L. V. Minevski and R. R. Adzic, J. Appl. Electrochem., 18(1988) 240.

[64] D.-J. Chen, Z.-Y. Zhou, Q. Wang, D.-M. Xiang, N. Tian and S.-G. Sun, *Chem. Commun.*, 46 (2010) 4252–4254.

[65] Chen, Y. X.; Heinen, M.; Jusys, Z.; Behm, R. J., *Langmuir,* 22 (2006) 10399-10408.

[66] G. Samjeské, A. Miki, S. Ye, A. Yamakata, Y. Mukouyama, H. Okamoto, and M. Osawa, *J. Phys. Chem. B,* 109 (2005) 23509-23516.

[67] Neurock, M.; Janik, M.; Wieckowski, A., *Faraday Discuss.* 140 (2008) 363-378.

[68] C. Lamy, J.-M. Leger, S. Srinivasan, and J.O'M. Bockris, (2001) *In Modern Aspects of Electrochemistry*, Vol. 34 (eds B. E. Conway and R. E. White), Kluwer Academic/Plenum Publishers, New York, pp. 53-118.

[69] M. Watanabe, and S. Motoo, *Journal of Electroanalytical Chemistry*, 60 (1975) 267-283.

[70] L. Dubau, C. Coutanceau, E. Garnier, J.-M. Leger and C. Lamy, *Journal of Applied*

Electrochemistry, 33 (2003) 419-429.

[71] T. Iwasita, *Electrochimica Acta*, 47 (2002) 3663-3674.

[72] K. Sasaki and R. R. Adzic, *Journal of The Electrochemical Society,* 155 (2008) B180-B186.

[73] J.P.I. de Souza, S.L. Queiroz, K. Bergamaski, E.R. Gonzalez, F.C. Nart, *J. Phys. Chem. B* 106 (2002) 9825.

[74] T. Iwasita, E. Pastor, *Electrochim. Acta* 39 (1994) 531.

[75] X. H. Xia, H.-D. Liess, T. Iwasita, *J. Electroanal. Chem.* 437 (1997) 233.

[76] B. Bittins-Cattaneo, S. Wilhelm, E. Cattaneo, H.W. Buschmann, W. Vielstich, Ber. Bunsenges, *Phys. Chem.* 92 (1988) 1210.

[77] J. F. E. Gootzen, W. Visscher, J. A. R. Van Veen, *Langmuir* ,12 (1996) 5076.

[78] B. Bittins-Cattaneo; E. Cattaneo, P. Konigshoven, W. Vielstich, *In Electroanalytical ChemistrysA Series of AdVances*; A. J. Bard, Eds.; Marcel Dekker: New York, 1991; Vol. 17.

[79] Wolter, O.; Heitbaum, J. Ber. Bunsen-Ges. *Phys. Chem.* 88 (1984) 6.

[80] N. Fujiwara, K. A. Friedrich, U. Stimming, *J. Electroanal. Chem*. 472 (1999) 720.

[81] T. Iwasita, B. Rasch, E. Cattaneo, W. Vielstich, *Electrochim. Acta* 34 (1989) 1073.

[82] M. H. Shao; R. R. Adzic, *Electrochimica Acta* 50 (2005) 2415-2422.

[83] T. Iwasita, R. Dalbeck, E. Pastor, X. Xia, *J. Electroanal. Chem.* (1994) 39, 1817.

[84] M. R. Tarasevich, A. Sadkowski, and E. Yeager, (1983) *Comprehensive Treatise of Electrochemistry*, Vol. 7 (eds B. E. Conway, J. O'. M. Bockris, E. Yeager, S. U. M. Khan and R. E. White), Plenum Press, New York, pp. 301-398.

[85] R. R. Adzic, (1998) In *Electrocatalysis*; J. Lipkowski, P. N. Ross, Eds.; Wiley: New York, pp 197.

[86] S. Gottesfeld, T. A. Zawodzinski, (1997) In *Advances in Electrochemical Science and*

Engineering; R. C. Alkire, D. M. Kolb, Eds.; Wiley: Weinheim, Vol. 5.

[87] N. M. Markovic, T. J. Schmidt, V. Stamenkovic, P. N. Ross, *Fuel Cells* 1(2001) 105.

[88] M. R. Tarasevich, A. Sadkowski, E. Yeager, (1983) In *Comprehensive Treatise of Electrochemistry*; Conway, B. E., Bockris, J. O. M., Yeager, E., Khan, S. U. M., White, R. E., Eds.; Plenum Press: New York, Vol. 7, pp 301.

[89] H. J. Forman, I. Fridovich, *Science,* 175 (1972) 339.

[90] K. Sasaki, Y. Mo, J. X. Wang, M. Balasubramanian, F. Uribe, J. McBreen, R. R. Adzic, *Electrochimica Acta,* 48 (2003) 3841.

[91] J. Zhang, Y. Mo, M. B. Vukmirovic, R. Klie, K. Sasaki, R. R. Adzic, *J. Phys. Chem. B,* 108 (2004) 10955.

[92] J. L. Zhang, M. B. Vukmirovic, Y. Xu, M. Mavrikakis, R. R. Adzic, *Angew. Chem. Int. Ed.* 44 (2005) 2132.

[93] N.M. Markovic, H.A. Gasteiger, P.N. Ross, X. Jiang, I. Villegas, M.J. Weaver, *Electrochim. Acta* 40 (1995) 91.

[94] S.L. Goikovic, T.R. Vidakovic, D.R. Durovic, *Electrochim. Acta* 48 (2003) 3607.

[95] P.A. Christensen, A. Hamnett, G.L. Troughton, *J. Electroanal. Chem.* 362 (1993) 207.

[96] E. Antolini, *Mater. Chem. Phys.* 78 (2003) 563.

[97] Z. Zhou, S. Wang, W. Zhou, G. Wang, L. Jiang, W. Li, S. Song, J. Liu, G. Sun, Q. Xin, *Chem. Commun.* (2003) 394–395.

[98] C. Lamy, S. Rousseau, E.M. Belgsir, C. Coutanceau, J.-M. L´eger, *Electrochim. Acta* 49 (2004) 3901.

[99] G. A. Camara, R. B. de Lima, T. Iwasita, *Electrochem. Commun.* 6 (2004) 812.

[100] V. M. Schmidt, R. Ianniello, E. Pastor, S. Gonzalez, *J. Phys. Chem.* 100 (1996) 17901.

[101] S. Tanaka, M. Umeda, H. Ojima, Y. Usui, O. Kimura, I. Uchida, *J. Power Sources* 152 (2005) 34.

[102] Z. Wang, G. Yin, J. Zhang, Y. Sun, P. Shi, *Electrochim. Acta* 51 (2006) 5691.

[103] U. A. Paulus, A. Wokaun, G. G. Scherer, T. J. Schmidt, V. Stamenkovic, V. Radmilovic, N. M. Markovic, P. N. Ross, *J. Phys. Chem. B* 106 (2002) 4181.

[104] K. W. Park, J. H. Choi, B. K. Kwon, S. A. Lee, Y. E. Sung, H. Y. Ha, S. A. Hong, H. S. Kim, A. Wieckowski, *J. Phys. Chem. B* 106 (2002) 1869.

[105] A. Oliveira Neto, E. G. Franco, E. Arico, M. Linardi, E. R. Gonzalez, *J. Eur. Ceram. Soc.* 23 (2003) 2987.

[106] A. Kelaidopoulou, E. Abelidou, G. Kokkinidis, *J. Appl. Electrochem.* 29 (1999) 1255.

[107] G. Li, P. G. Pickup, *Electrochim. Acta* 52 (2006) 1033.

[108] M. L. Calegaro, H. B. Suffredini, S. A. S. Machado, L. A. Avaca, *J. Power Sources* 156 (2006) 300.

[109] V. Radmilovic, T.J. Richardson, S.J. Chen, P.N. Ross, *J. Catal.* 232 (2005) 199.

[110] S. Q. Song, W. J. Zhou, Z. H. Zhou, L. H. Jiang, G. Q. Sun, P. Tsiakaras, Q. Xin, V. Leonditis, S. Kontou, P. Tsiakaras, *Int. J. Hydrogen Energy,* 30 (2005) 995.

[111] L. Jiang, G. Sun, S. Sun, J. Liu, S.Tang, H. Li, B. Zhou, Q. Xin, *Electrochim. Acta* 50 (2005) 5384.

[112] Y. Morimoto, E. B. Yeager, *J Electroanal Chem* 441 (1998)77–81.

[113] T. E. Shubina, M. T. M. Koper, *Electrochim Acta* 47 (2002) 3621.

[114] S. Mukerjee, J. McBreen, *J. Electrochem. Soc.* 146 (2) (1999) 600.

[115] W. J. Zhou, B. Zhou, W. Z. Li, Z. H. Zhou, S. Q. Song, G. Q. Sun, P. Tsiakaras, Q. Xin, S. Douvartzides, M. Goula, P. Tsiakaras, *J. Power Sources* 126 (2004) 16.

[116] E.V. Spinace, M. Linardi, A. Oliveira Neto, *Electrochem. Commun.* 7 (2005) 365.

[117] F. Colmati, E. Antolini, E.R. Gonzalez, *Applied Catalysis B: Environmental* 73 (2007) 106–115

[118] S. Rousseau, C. Coutanceau, C. Lamy, J.-M. Leger, *J. Power Sources* 158 (2006) 18.

[119] E. Antolini, F. Colmati, E.R. Gonzalez, *Electrochem. Commun.* 9 (2007) 398.

[120] G. Sine, D. Smida, M. Limat, G. Foti, Ch. Comninellis, *J. Electrochem. Soc.* 154 (2007) B170.

[121] D. M. dos Anjos, K. B. Kokoh, J.-M. L´eger, A. R. de Andrade, P. Olivi, G. Tremiliosi-Filho, *J. Appl. Electrochem.* 36 (2006) 1391.

[122] D. Zhang, Z. Ma, G. Wang, K. Konstantinov, X. Yuan, H. Liu, *Electrochem. Solid State Lett.* 9 (2006) A423.

[123] B. E. Hayden, D. V. Malevich, D. Pletcher, *Electrochem. Commun.* 3 (2001) 395.

[124] J. H. Liu, C. B. Yu, *Chem. J. Chin.* U. 24 (2003) 2263.

[125] K. Drew, G. Girishkumar, K. Vinodgopal, P.V. Kamat, *J. Phys. Chem. B* 109 (2005) 11851.

[126] N. R. de Tacconi, R. O. Lezna, B. Beden, F. Hahn, C. Lamy, *Journal of Electroanalytical Chemistry,* 379 (1994) 329-337.

[127] N. Fujiwara, Z. Siroma, T. Ioroi, K. Yasuda, *J. Power Sources*, 164 (2007) 457.

[128] L. Cao, G. Sun, H. Li, Q. Xin. *Electrochemistry Communications*, 9 (2007) 2541–2546.

[129] Y. Choi, and P. Liu, *Catalysis Today*, in press.

[130] E. Antolini, *Journal of Power Sources*, 170 (2007) 1-12.

[131] Q. Wang, G. Q. Sun, L. H. Jiang, Q. Xin, S. G. Sun,Y. X. Jiang,S. P. Chen, Z. Jusys, R. J. Behm, *Phys. Chem. Chem. Phys*., 2007, 9, 2686–2696.

[132] H. Wang, Z. Jusys, and R. J. Behm, *J. Power Sources* 154 (2006) 351-359.

[133] E. Vesselli, A. Baraldi, G. Comeli, S. Liziti, R. Rosei, *ChemPhysChem* **5**, 1133 (2004).

[134] R. R. Adzic, J. Zhang, K. Sasaki, M. B. Vukmirovic, M. Shao, J. X. Wang, A. U. Nilekar, M. Mavrikakis, J. A. Valerio, F. Uribe, *Top Catal* 46 (2007) 249–262.

[135] D. Buceta et al., Microemulsion Synthesis of Pt-Au nanoparticles. *In preparation*.

[136] N. Vasiljevic, L. T. Viyannalage, N. Dimitrov, K. Sieradzki, *Journal of Electroanalytical Chemistry* 613 (2008) 118–124.

[137] S. R. Brankovic, J. X. Wang, R. R. Adzic, *Surface Science,* 474 (2001) L173-L179

[138] S. R. Brankovic, J. X. Wang, R. R. Adzic, *J.Serb.Chem.Soc.* 66 (2001) 887–898.

[139] K. Sasaki, H. Naohara, Y. Cai, Y. M. Choi, P. Liu, M. B. Vukmirovic, J. X. Wang, R. R. Adzic, *Angew. Chem. Int. Ed.*, 49 (2010) 8602 –8607.

[140] A. Kowal, M. Li, M. Shao, K. Sasaki, M. B. Vukmirovic, J. Zhang, N. S. Marinkovic, P. Liu, A. I. Frenkel, R. R. Adzic, *Nature Materials* 8 (2009) 325.

[141] J. Zhang, L. Gao, *Journal of Solid State Chemistry* 177 (2004) 1425–1430.

[142] L. Jiang, G. Sun, Z. Zhou, S. Sun, Q. Wang, S. Yan, H. Li, J. Tian, J. Guo, B. Zhou, Q. Xin, *J. Phys Chem. B* 2005, 109, 8774-8778.

[143] T. Iwasita, F. C. Nart, (1995) In *Advances in Electrochemical Science and Engineering*; H. Gerischer, C. W. Tobias, Eds.; Wiley-VCH: Weinheim, Vol. 4; pp 126.

[144] A. Bewick, K. Kunimatsu, S. Pons, *Electrochim. Acta,* 25 (1980) 465.

[145] R. J. Nichols, (1992) IR *Spectroscopy of Molecules at the Solid-Solution Interface,* In *Adsorption of Molecules at Metal Electrodes*; J. Lipkowski, P. N. Ross, Eds.; Wiley-VCH: New York.

[146] A. Rodes, J. M. Perez, A. Aldaz, (2003) *Vibrational Spectroscopy*. In *Handbook of Fuel Cells-Fundamentals, Technology and Applications*; W. Vielstich, A. Lamm, H. A. Gasteiger, Eds.;

John Wiley & Sons: Chichester, Vol. 2: Electrocatalysis; pp 191.

[147] P. W. Faguy, N. S. Marinkovic, *Appl. Spectrosc.* 50 (1996) 394.

[148] M. Osawa, *Topics in Appl. Phys.* 81 (2001) 163.

[149] H. Inada, L. Wu, J. Wall, D. Su, Y. Zhu, *Journal of Electron Microscopy,* 58 (2009) 111.

[150] Bradely, D. *J. Chem. Phys*. 92, 508 (1990).

[151] M. Li, A. Kowal, K. Sasaki, N. S. Marinkovic, D. Su, E. Korach, P. Liu, R. R. Adzic, *Electrochim. Acta.* 55 (2010) 4331.

[152] D. C. Papageorgopoulos, Q. Ge, D. A. King, *J. Phys. Chem*. 99 (1995) 17645–17649.

[153] A. F. Lee, D. E. Gawthrope, N. J. Hart, K. Wilson, *Surf. Sci*. 548 (2004) 200–208.

[154] J. L. Zhang, M. B. Vukmirovic, K. Sasaki, A. U. Nilekar, M. Mavrikakis, and R. R. Adzic, *J. Am. Chem. Soc*. 127 (2005) 12480-12481.

[155] M. Batzill, and U. Diebold, *Prog. Surf. Sci.* 79 (2005) 47-154.

[156] P. J. D. Lindan, *Chem. Phys. Lett.* 328 (2000) 325-329.

[157] A. Wieckowski, J. Sobkowski, P. Zelenay, K. Franaszczuka, *Electrochim. Acta.* 26 (1981) 1111-1119.

[158] M. Mavrikakis, and M. A. Barteau, *J. Mol. Catal. A* 131 (1998) 135-147.

[159] H. Idriss, *Platinum Metals Rev*. 48 (2004)105-115.

[160] G. Scott-Jones, M. Mavrikakis, M. A. Barteau, and J. M. Vohs, *J. Am. Chem. Soc.* 120 (1998) 3196-3204.

[161] Batista, E. A. M., Motheo, G. R. P. & Iwasita, A. *J. J. Electroanal. Chem*. 571 (2004) 273-282.

[162] M. Li, W. P. Zhou, Y. M. Choi, R. R. Adzic, "$PtRhSnO_2$ electrocatalyst: the origin of its selectivity towards C-C splitting". *In preparation*.

[163] Sagar Sen Gupta and Jayati Datta, *Journal of Electroanalytical Chemistry,* 594 (2006) 65–72.

[164] A Trovarelli, *Catalysis Reviews*, 4(1996) 439-520.

[165] Shao-Horn Yang et al. *JACS*, 131 (2009) 15669.

[166] S. C. S. Lai, N. P. Lebedeva, T. H. M. Housmans, M. T. M. Koper, *Top Catal* 46 (2007) 320–333.

[167] M. Heinen, Z. Jusys, and R. J. Behm, *J. Phys. Chem. C*, 114 (2004) 9850–9864.

[168] G.A. Camara, T. Iwasita, *Journal of Electroanalytical Chemistry* 578 (2005) 315–321

[169] M. Hansen, K. Anderko, *Constitution of Binary Alloys*, 2nd ed., McGraw-Hill Book Company, New York, 1958.

[170] L.-W. H. Leung, S.-C. Chang, M. J. Weaver, *J. Electroanal. Chem*. 266 (1989) 317.

[171] P. Gao, S.-C. Chang, Z. Zhou, M.J. Weaver, *J. Electroanal. Chem*. 272 (1989) 161.

[172] A. I. Frenkel, *Z. Kristallogr*. 222 (2007) 605.

[173] A. I. Frenkel, C. W. Hills, R. G. Nuzzo, *J.Phys.Chem. B.*, 105 (2001) 12689.

[174] M. Li, K. Sasaki, R. R. Adzic, "MM'/SnO_2 (M = PtRh, PtIr, IrRh, PtIrRh) nanoparticle electrocatalysts for oxidizing ethanol to carbon dioxide". *In preparation*.

[175] S. Alayoglu, A. U. Nilekar, M. Mavrikakis, B. Elchhorn, *Nature Materials* 7 (2008) 333-338.

[176] A. U. Nilekar, S. Alayoglu, B. Eichhorn, and M. Mavrikakis, *J. AM. CHEM. SOC.* 132 (2010) 7418–7428

[177] Z. Peng, H. Yang, *Nano Today* (2009) 4, 143-164.

[178] Z. Peng and H. Yang, *Nano Res* 2 (2009) 406-415.

[179] C. Wang, D. V. D. Vliet, K. L. More, N. J. Zaluzec, S. Peng, S. Sun, H. Daimon, G. Wang,

J. Greeley, J. Pearson, A. P. Paulikas, G. Karapetrov, D. Strmcnik, N. M. Markovic, and V. R. Stamenkovic, *Nano Lett*. 11 (2011) 919–926.

[180] C. Wang, C. Xu, H. Zeng, and S. Sun, *Adv. Mater.* 21 (2009), 3045–3052.

[181] J. M. Jaksic, N. V. Krstaji, L. M. Vracar, S. G. Neophytides, D. Labou , P. Falaras, M. M. Jaksic, *Electrochimica Acta,* 53 (2007) 349–361.

[182] M. Li, R. R. Adzic, "Enhanced catalytic activity of Ir-based electrocatalysts for ethanol electro-oxidation at low over-potentials". *In preparation*.

[183] S. Motoo, N. Furuya, *J. Electroanal. Chem*., 197 (1986) 209.

[184] L. D. Burke, K. J. O'Dwyer, *Electrochim. Acta*, 34 (1989) 1659.

[185] R. O. Lezna, K. Kunimatsu, R. Ohtsuka, N. Sato, *J. Electrochem. Soc*., 134 (1987) 3090.

[186] J. E. Ferrer, L. L. Victori, *Electrochim. Acta,* 38 (1993) 1631.

[187] R. Woods, *Electroanalytical Chemistry and interfacial Electrochemistry*, 49 (1974) 217-226.

[188] M. Li, R. R. Adzic, "Pt monolayer electrocatalysts for ethanol oxidation". *In preparation*.

[189] T. Iwasita, F.C. Nart, *J. Electroanal. Chem.* 317 (1991) 291.

[190] H. Wang, L. Alden, F. J. DiSalvo and H. D. Abruna, *Phys. Chem. Chem. Phys*., 10 (2008) 3739–3751.